THE REFRACTIVE INDEX CHANGE IN GAAS-ALGAAS QUANTUM WELLS PRODUCED BY NEUTRAL IMPURITY INDUCED DISORDERING USING BORON AND FLUORINE

Submitted for the degree of

Doctor of Philosophy

to the

Faculty of Engineering,

University of Glasgow

by

Stein Ivar Hansen

June 1993

ProQuest LLC.
789 East Eisenhower Parkway
P.O. Box 1346
Ann Arbor, MI 48106 – 1346

CONTENTS

Page No

Acknowledgements

The work in this thesis could not have been performed without the multitude of facilities in the University of Glasgow Department of Electronics and Electrical Engineering. Furthermore, this thesis would not have been possible without the help and support of a number of people. I have been particularly fortunate to enjoy a very good relationship with all the technical staff in the department. I have obtained particular assistance from Lois Hobbs and the rest of the cleanroom staff, from Ray Darkin and Dave Clifton at the dry etching facilities and from Douglas McIntyre and the team in the Ultrasmall Structures Lab. Ray Hutchins, Jimmy Young and George Boyle gave me a lot of useful input, and John Cochrane provided me with ever faithful photoluminescence data. The MBE facilities in the Department and at Norwegian Telecom Research Laboratory together with the MOCVD facilities in Sheffield, provided me with high grade material and characterisations. Surrey University performed all my ion-implantations and supplied general PRAL details. I also thank Ken Thomas for showing me the world of holography, even if it wasn't as esoteric as I first had thought.

I also owe a lot to the rest of the Optoelectronics Research Group in the Department, and in particular to the closely co-operating unit led by Richard De La Rue and John H Marsh, my supervisor in this project. Without him, the unfinished version of this thesis would have experienced the turn of this century, and his encouragement and help has been invaluable. I would also especially like to thank Karen McIlvaney, a great friend and colleague for all help and input. Without her singing in the holography lab the gratings would never have come out the way they did.

I would also like to thank Norwegian Telecom for personal financial support.

After all this is said, there is one person I would like to thank the most for her patience and understanding; my wife. And with this I dedicate this thesis to my wife and my newly born son.

List of publications

Papers

S.I. Hansen, J.H. Marsh, J.S. Roberts," Polarization dependence of refractive index of MQW Waveguides.", IEE Part J Optoelectronics Vol.138, No.5, s 309-12 1991.Presented at SIOE-90 in Cardiff.

S.I. Hansen, J.H. Marsh, J.S. Roberts, R. Gwilliam, "Refractive index changes in a GaAs QW structure produced by Impurity Induced Disordering using boron and fluorine", Applied Physics Letters Vol. 58 s 1398, 1991.

S.I. Hansen, J.H. Marsh, J.S. Roberts, R. Gwilliam, "The refractive index of MQW waveguides subject to IID using boron and fluorine", SPIE Proceedings 1361, 1991. Presented in Conf. on Novel Materials and Devices in Aachen, Germany.

J.H. Marsh, S.I. Hansen, A.C. Bryce, R.M. DeLaRue,"Applications of neutral impurity disordering in fabricating low-loss optical waveguides and integrated waveguide devices", Optical and Quantum Electronics, Vol. 23 1991.

J.H. Marsh, S.G. Ayling, A.C. Bryce, S.I. Hansen, S.A. Bradshaw," Neutral impurity disordering of III-V QW structures for optoelectronics", Proceedings of U.S./U.S.S.R. Joint Soviet-American Workshop on the Physics of Semiconductor Lasers, Leningrad May 1991, Am.Inst.of Physics Conf.Proc.240 pp 111-129.

Citable Abstracts

S.I. Hansen, J.H. Marsh, J.S. Roberts, R. Gwilliam, "The use of refractive index changes arising from boron and fluorine IID in optoelectronic integration", presented at the Integrated Phoronics Research Topical Meeting, Monterey, California 1991 and at Norwegian Conference on optics and optoelectronics at Spåtind, Norway 1991.

SYNOPSIS OF THE THESIS

This thesis is concerned with quantum well intermixing in GaAs-AlGaAs multiple quantum well structures due to the impurity induced disordering effect using the electrically neutral impurities boron and fluorine. Particular emphasis is put on the refractive index change induced by the disordering process, and on methods of implementing this technique in the development of novel semiconductor laser structures.

Selective intermixing of quantum wells is a powerful tool in the quest for developing functional integrated photonic structures. The use of impurities to enhance the interdiffusion rate of group III materials in quantum wells and barriers in well defined regions enables the creation of regions with lower optical propagation loss (< 4.5 dBcm^{-1}).This can be utilised in low-loss waveguides for optical interconnects, extended cavity lasers, high efficiency distributed Bragg reflector lasers and more. The introduction of the impurities used in IID leads to an increased interdiffusion rate of the group III materials in the III-V semiconductor quantum well structure when present in volume concentrations above a threshold value ($\approx 10^{18}$ cm^{-3}) and when the structure is subjected to annealing at a temperature (e.g. 890°C) that is close to, but lower than that which induces appreciable self-diffusion in the quantum well-barrier system (>925°C). The diffusion process effectively narrows and squeezes the well, leading to an increase in the bandgap as the quantized levels move away from the bottom of the potential well. The changes in bandgap and exciton transition energies produce a finite change in the refractive index of the material.

In this thesis the refractive indices of as-grown and intermixed quantum well structures are experimentally determined, and the effects of disordering on the dispersive properties of the quantum well materials are studied. The thesis is organised as follows. Chapter 1 is an introduction to the thesis, and chapter 2 provides some theory on the optical properties of multiple quantum well structures. In chapter 3 the process of impurity induced disordering is explained, and this is followed by a treatment of the effective index of semiconductor optical waveguides in chapter 4. Chapter 5 explains the processing steps in the fabrication of the grating couplers used in the determination of the effective refractive indices, and the experimental results obtained are presented in chapter 6. Chapter 7 discusses possible practical implementations of the technique, and presents results obtained in attempts at putting these into practice. The thesis ends with a conclusion in chapter 8, which also give suggestions for further work on the subject.

CHAPTER 1 INTRODUCTION

1.1 Background

The quest for increasingly higher speeds and capacities in information transmission and information processing has exerted great influence on the research effort into optoelectronic and photonic devices and their integration. Optoelectronic integration enables very large scale signal processing and electronic-light conversion to be combined on the same chip. This opens up great possibilities in terms of improved performance over existing separate electronics and optical signal generators, where the parasitic capacitances greatly limit the performance. Additionally, with the advent of true photonic integrated circuits– i.e. devices where the (re)generation of light, information processing and retransmitting are all-optical, –the information capacity increases manyfold over its electronic or even optoelectronic counterparts. The integration on single chips also has the promise of great cost-reduction, since much of the cost of producing circuits arises from the packaging and interconnection of the devices.

Optical integrated circuits represent one of the great research challenges in the optoelectronics field. Optical semiconductor devices have shown immense improvements over the last two decades, and the push for ever higher speed circuits at lower costs have been a major force behind the interest in optical integrated circuits. One of the great stumbling blocks on the way to achieve this goal has been the lack of a simple method to facilitate low-loss optical interconnects. These interconnects have been around for some time in the form of re-grown higher bandgap material, but this is a generally unsatisfactory solution which introduces several additional processing steps which increase processing costs with a potentially low-yield. Many of the regrowth processes that are successfully employed today are performed by LPE, due to the intrinsic fill-in property of this growth process and to the fact that almost no devices requiring overgrowth are completely planar. This process does however not enable the kind of thickness control that is required for many of today's optical devices, specifically when it comes to quantum well devices. This

overgrowth method, which requires a higher temperature than both molecular beam epitaxy (MBE) and metal-organic vapour phase epitaxy (MOVPE), also have a tendency to smear out well defined details such as, for instance, a feedback grating in a distributed Bragg reflector (DBR) laser.

1.2 Impurity Induced Disordering

A solution to the problem arose from the discovery of the impurity induced layer disordering (IILD or IID) in 1981 by W.D. Laidig et al[1]. During attempts at modifying an undoped AlAs-GaAs superlattice by Zn in-diffusion, the layers were found to intermix, giving bulk, undamaged material with an aluminium concentration equal to the material average of the superlattice. The discovery started off a substantial research effort to attempt to understand the intermixing process and to find methods of utilizing the effect. In the process of these studies it was found that several impurities induced layer intermixing with varying degrees of efficiency. Among those with the highest disordering efficiencies were several common dopants: Zn and Si, but also Ge, S, Sn, Se and Mg[2]. A common feature of these dopants is that they are all electrically active in III-V semiconductors at room temperature. Later additions to the list are boron and fluorine, which are not electrically active dopants in this material system at room temperature[3].

Selective quantum well intermixing yields a powerful tool in the quest for developing functional integrated photonic structures. The use of impurities to enhance the interdiffusion rate of group III materials in quantum wells and barriers in well defined regions enables the creation of regions with lower optical propagation loss at the bandgap wavelength of the original structure. Impurities used for IID lead to an increased interdiffusion rate of the group III materials in the III-V semiconductor quantum well structure when present in volume concentrations above a threshold value (typically 10^{17}-10^{18} cm^{-3}) and when the structure is subjected to annealing at a temperature that is close to, but lower than that which induces self-diffusion in the quantum well-barrier system. The diffusion process effectively narrows and squeezes the well, leading to an

increase in the bandgap as the quantized levels move away from the bottom of the potential well. The changes in bandgap- and exciton transition energies produce a finite change in the refractive index properties of the material.

The first few attempts at intermixing used thermal in-diffusion to introduce the impurities, but later studies, to a large extent, rely on ion implantation. Ion implantation has the advantage of creating very sharply defined interfaces between implanted and unimplanted regions. The intermixing efficiency is dependent on the method of introduction.

It was quickly realised that the intermixing process could be used in fabrication, especially with regards to lasers. The discovery opened up the possibility to form lateral injection lasers where the optical mode was confined by the refractive index change resulting from the IID process in the intermixed regions that also doubled as p and n regions of the pin structure[4]. Buried heterostructure lasers could similarly, but not necessarily in the lateral injection configuration, be made using this method, as could lower loss interconnects, which are important for extended cavity lasers, high efficiency distributed Bragg reflector lasers and more. Lower is used here instead of low, since the free carriers associated with the concentration of active dopants ($\approx 10^{18}$ cm^{-3}) necessary for the IID process give a minimum loss value of around[5] 10 cm^{-1}. A related issue in the integration of optical circuits is the electrical isolation needed between e.g. a laser source and a modulator. Interconnecting these two components with a lowered loss waveguide produced by active-dopant IID will, due to the high concentration of dopants needed for IID,create problems in terms of the resulting low electrical resistance between the source and the modulator. Experiments have shown[4] that the electrical resistance needed in interconnection between laser and modulator need to be higher than 100kΩ. These are important points indicating that non-electrically active impurities have clear advantages over electrically active dopants in disordering for integration purposes.

The effect of impurity induced disordering has been utilised in a number of devices, and much attention has been given to studies on the bandgap shifts associated with disordering.

No systematic study has however been performed on the refractive index changes which accompany disordering. This may be due to many of the applications relying on total disordering where the refractive index is assumed to be identical to that of the material average bulk material. This is not always the case, and in particular for low-loss waveguide sections, there is a great desire to use partial disordering to raise the bandgap without perturbing the refractive index too much. An example is a DBR laser with a partially disordered low-loss DBR section where one does not want reflections from the interface between active and passive waveguide region.

1.3 Contents of the thesis

This thesis is concerned with quantum well intermixing in GaAs-AlGaAs multiple quantum well structures due to the impurity induced disordering effect using the electrically neutral impurities boron and fluorine. Particular emphasis is put on the refractive index changes induced by the disordering process, and on methods of implementing this technique in the development of novel semiconductor laser structures.

In this thesis the refractive indices of as-grown and intermixed quantum well structures are experimentally determined, and the effect of disordering on the dispersive properties of the quantum well materials are studied. Chapter 2 is meant to provide some background on the optical properties of multiple quantum well structures, and the process of impurity induced disordering is explained in Chapter 3. The effective index of semiconductor waveguides is discussed in Chapter 4, and Chapter 5 explains the processing steps in the fabrication of the grating couplers used in the determination of the effective refractive indices. The experimental results obtained are presented in Chapter 6. Chapter 7 discusses possible practical implementations of the technique, and presents results obtained in attempts at putting these into practice. The thesis ends with a conclusion in Chapter 8, which also give suggestions to further work on the subject.

[1] W.D. LAIDIG,J.W. LEE,P.J. CALDWELL,"Embedded Mirror Semiconductor Laser", Applied Physics Letters **45**, 485-487 (1984).

[2] D.G.Deppe,N. Holonyak Jr., "Atom diffusion and impurity-induced layer disordering in quantum well III-V semiconductor heterostructures", J.Appl. Phys. Vol.64, 1988, pp R93-R113.

[3] Y. Hirayama, Y. Suzuki, H. Okamoto,"Ion-Species dependence of interdiffusion in Ion-Implanted GaAs-AlAs Superlattices", Journal of Applied Physics Vol.24, No.11 1985 pp 1498-1502.

[4] A FURUYA, M MAKIUCHI, O WADA, T FUJII, "AlGaAs/GaAs Lateral Current Injection Multiquantum Well (LCI-MQW) Laser using Impurity Induced Disordering", IEEE Journal of Quantum Electronics, **QE-24** , 2448-2452 (1988)

[5] J H Marsh,"Neutral Impurity Disordering of Quantum Well Waveguide devices."Ch.9 Waveguide Optoelectronics, NATO AASI Series E:Applied Sciences Vol.226.,Eds. J.H.Marsh and R. De La Rue, Kluwer Academic Press,The Netherlands, pp 185-204

CHAPTER 2

OPTICAL PROPERTIES OF $AL_xGA_{1-x}AS$ MULTIPLE QUANTUM WELL (MQW) STRUCTURES

2.1 Introduction

This chapter is intended to to provide a background for–, and basic understanding of, –the factors that influence the refractive index of quantum well structures and differentiate it from that of bulk material. An informative, less formal approach is deliberately used. This background information is necessary for the understanding of the refractive index modification due to impurity induced disordering discussed in Chapter 6, and for the justification of the models used to describe the wavelength dependence of the MQW refractive index.

2.1.1 General

Even though research in the area of ultrathin heterostructures increased sharply at the end of the 1960's[1], work had been carried out to find lattice matched materials with suitable bandgap differences for quite some time[2]. The advent of quantum well structures was envisaged before the growth technology was sufficiently advanced to fabricate the required low dimensions. At the early stages, liquid phase epitaxy (LPE) was the dominating[3] growth method for III-V materials. However, the high growth rate and nonuniformity of the LPE technique make the fabrication of high-quality, abruptly interfaced heterostructures of dimensions needed for quantum confinement extremely difficult. Even today, when the LPE growth technique has been significantly improved and it has been shown that quantum well structures can be made using this process, the limitations on thickness and uniformity severely limit the usefulness of this exercise. Chemical vapour deposition (CVD) showed more promise, but quantum size effects were not observed until high-accuracy growth methods such as molecular beam epitaxy (MBE) and metalorganic vapour deposition (MOCVD) or metalorganic vapour phase epitaxy (MOVPE) had been developed.

The concept of multiple quantum wells initially arose from considerations of potential barriers and wells thin enough to exhibit resonant tunnelling, and compositional- and doping-modulated quantum structures were proposed. The immediate aim was to show the existence of effects predicted theoretically such as negative differential resistance and Bloch oscillations[1]. This research led to the development of the superlattice (SL), which is a multiple quantum well structure where the barriers are so thin as to allow the evanescent tail of the electron wavefunction in the wells to penetrate them, effectively coupling the wells together. The distinctions between MQWs and SLs will be treated further in later sections.

2.2 Basic properties

Quantum well structures were the first man-made semiconductor microstructures realised. In the case of MQWs, they constitute a binary structure[4] AB with a large number of constant thickness layers of material A alternating with layers of material B. The dimensions of the layers are typically in the region of 100 Å, and certain conditions are imposed on the materials A and B. These usually have to be closely lattice matched (although an important exception is strained layer superlattices, where a finite amount of strain is built into the structure by employing the lattice mismatch, but this will not be considered here) and have a bandgap difference ΔE_g sufficiently large to provide confinement for the electron wavefunction in the well. The degree of confinement depends on well size and material composition as will be shown later. The interleaving of the materials imposes a new periodicity on the material system; $d=L_A+L_B$, which is superimposed on the periodicity of the original materials. From an energy band perspective, this periodic variation produces discontinuities in the Brillouin zone of the starting materials in the direction normal to the layers, whilst the band structure in the direction parallel to the layers remain essentially unchanged.

2.2.1 Energy band structure

As already mentioned, the electronic and optical properties differentiating MQW from bulk material arise from the imposed discontinuities of the host materials' energy bands due to

the abrupt composition changes in the periodic microstructure. Consider the simplest case of a semiconductor single quantum well bound on either side by infinitely high potential barriers.

This is a classical case of the particle-in-a-box problem, where the particle can be represented by an envelope wavefunction. Provided the well width is of the order of the de Broglie wavelength of the electron, quantization of the energy levels will take place in the direction parallel to the layers. This quantization is easiest explained by means of the effective mass approximation[5] (EMA), which uses the basic assumption that any variations in the potential of the material band structure are slow compared with the unit cell size, with the important exception of the underlying periodic potential of the unit cell. Furthermore, the particle has an effective mass associated with it, which is different in the well and barrier regions, and is determined by the diffraction of the particle through the lattice. In the following discussion the z-direction is taken as the growth direction, which is normal to the layers of the quantum well.

In the plane of the layers, the electron and holes can move freely and their energies are governed by the same dispersion law as for the 3-dimensional case of the bulk crystal:

$$E_c(k) = E_g + \frac{\hbar^2}{2m_e}(k_x^2 + k_y^2) \qquad (2.2.1.1a)$$

$$E_v(k) = -\frac{\hbar^2}{2m_h}(k_x^2 + k_y^2) \qquad (2.2.1.1b)$$

where E_C and E_V are the energies of the conduction and hole bands, E_g is the bandgap of the semiconductor making up the layer, $m_{e,h}$ represent the electron and hole effective mass, and $k_{x,y}$ represent the de Broglie wavenumbers in the x and y directions. In the z-direction on the other hand, the energy band discontinuities at the interfaces lead to an exact solution of the Schrödinger wave equation of the electron wavefunction using the boundary

condition that the amplitude of the envelope functions has to be zero at the interfaces, and which gives the eigenenergies:

$$E_j^{\infty} = \frac{\hbar^2}{2m_{e,h}}\left(j\frac{\pi}{L_z}\right)^2 \qquad (j = 1,2,3,) \qquad (2.2.1.2)$$

where L_z is the well width and (j -1) is the number of nodes of the wave function. The eigenenergies thus form an infinite series of 2-dimensional energy sub-bands. The joint density of states form a series of step functions given by:

$$g_{2D}(E) = \frac{\mu}{\pi\hbar^2}\theta\left(E - E_{je}^{\infty} - E_{jh}^{\infty}\right) \qquad (2.2.1.3)$$

where θ is the Heaviside step function and μ is the electron-hole reduced mass given by :

$$\mu^{-1} = m_e^{-1} + m_h^{-1} \qquad (2.2.1.4)$$

The optical transitions associated with the above density of states function are subject to strict selection rules due to the orthogonality of the conduction and valence band envelope functions: $\Delta j = j_e - j_h = 0$.

In reality, the barrier material will impose a finite potential barrier height on the quantum well, and this modifies the boundary conditions for the envelope wavefunctions. In the x,y-plane parallel to the layers, the energy is still governed by the above set of equations 2.2.1.1a ,b. However, in the z-direction, the envelope wavefunction now has a sinusoidal dependence in the well, and an exponential tail in the barrier, giving a penetration depth L_p into the barrier. The boundary conditions now entail that the probability current of the envelope wavefunction must be continuous at the barrier-well interface. It is also worth noting here that the electrons and holes have different effective masses in the well (m_W) and barrier (m_B), and this gives rise to different energies in the two regions. The overall effect of the finite potential barrier height is to reduce the number of bound states in the system. The quantum well system now exhibits a finite number of bound states for the energy range

in which the quantized energy is lower than the potential barrier height, and a continuum above the potential barrier. Furthermore, as the energy bands get closer to the potential barrier height, the penetration depth L_p increases. In a multiple quantum well structure this leads to a coupling between wells when the exponential tails of the envelope wavefunctions overlap; $L_p > {}^1/_2 L_b$, L_b= barrier width. In this case mini-bands of continuous states form in the well regions.

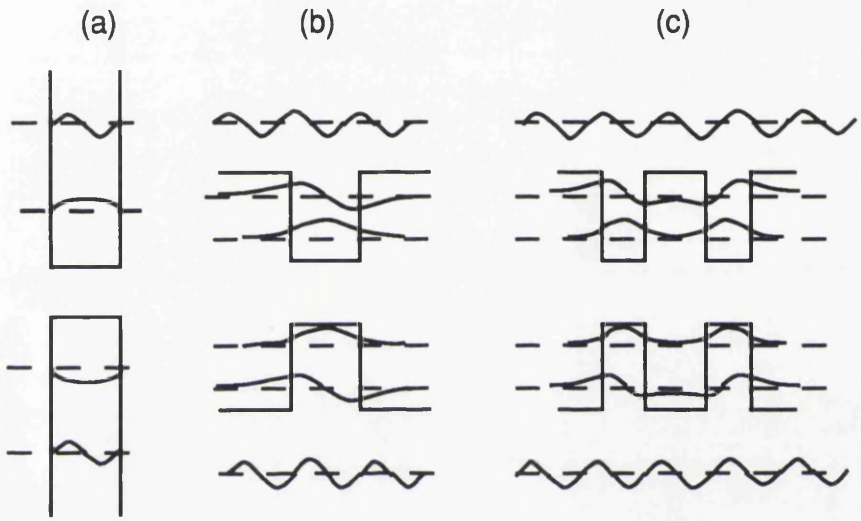

Fig. 2.2.1 Band Structure of layered microstructure in real space. (a) Single Quantum Well with infinite depth, (b) Single Quantum Well with finite depth, (c) MQWS with finite depth close enough to allow significant coupling between adjacent wells. (b) and (c) show two bound states and a continuum resonance in each band. From ref 4.

There will always be at least one bound state in the quantum well structure, and the eigenenergies are solutions of[4]:

$$\sqrt{\varepsilon_j} \times \left[\frac{\cot\left(\frac{\pi}{2}\sqrt{\varepsilon_j}\right)}{\tan\left(\frac{\pi}{2}\sqrt{\varepsilon_j}\right)} \right] = \frac{m_W}{m_B}\left(v - \varepsilon_j\right)^{1/2} \qquad (2.2.1.5)$$

for a symmetric well-barrier system. $\varepsilon_j = E_j / E_1^{\infty}$ and $v = V_{e,h} / E_1^{\infty}$ are the normalized energies and potential discontinuities respectively, where E_j is the bound-state energy of the j^{th} subband and E_1^{∞} is the bound-state energy of the first subband in an infinitely deep well.

The envelope wavefunctions in the conduction and valence bands are still symmetric, but they are no longer orthogonal. They still exhibit a step-like joint density of states, but the selection rules have been relaxed somewhat. The transitions $\Delta j=j_e-j_h=2p+1$ are still forbidden, while transitions corresponding to $\Delta j=2p$,where $p\neq 0$, are allowed.

Although quantum wells have been realised in several III-V semiconductor material systems, the GaAs-$Al_xGa_{1-x}As$ system has been found to be particularly suited to fabrication of quantum well structures. The energy bandgap of the system is easily tuned by changing the Al-fraction, and the lattice mismatch between the two extremes, GaAs and AlAs, is only[6] 7.2×10^{-3} Å. In the region of composition x=0 to $x\approx 0.4$ the $Al_xGa_{1-x}As$ material is a direct bandgap semiconductor which means that in this region both the valence and conduction band wells appear in the same material, yielding a type I quantum well[2]. This is the type of well considered above. For Al-fractions above $x\approx 0.4$ the material goes indirect, giving a type II quantum well, but this case will not be considered here.

The ratio of bandgap discontinuity between the conduction and valence band is of great importance in the calculation of the confinement energies of the electrons and holes in the quantum well structure. This is defined as $\Delta E_c/\Delta E_g$ for the conduction band and $\Delta E_v/\Delta E_g$ for the valence band, and is normally expressed as $\Delta E_c/\Delta E_g$: $\Delta E_v/\Delta E_g$. For the AlGaAs system, the so-called Dingle rule for some time defined a conduction-to-valence band-splitting of 85:15 [7], but other data[8], both preceding and succeeding those of Dingle et al, suggest a ratio of around 60:40.

The simple EMA approach above gives a good agreement with observed transition energies in the case of the electron sub-bands in the quantum well. The situation is somewhat more complicated for the case of the valence band confinement energies. The valence band structure in III-V semiconductors has a four-fold degeneracy, effectively splitting the valence band into the $J=^3/_2$ (upper) valence band multiplet and the $J=^1/_2$ (lower) valence band. The upper and lower valence band multiplets are normally referred to as the heavy- and light-hole valence bands respectively, due to their associated

momentum in bulk crystal. The confinement has the effect of lifting the degeneracy in the direction normal to the layers (z), giving rise to different masses for the heavy and light hole in this direction. However, the confinement also modifies the hole band structure in the xy-plane, resulting in a very complicated system. In the xy-plane close to k=0, the hole corresponding to the uppermost band ($J=^3/_2$) appears lighter than the hole associated with the lower ($J=^1/_2$) band. This can be described by a Luttinger Hamiltonian[9] to give the heavy and light hole masses. This representation does however indicate that the $J=^3/_2$ and $J=^1/_2$ bands cross at some point in the E versus k diagram. This is not so, but is an artifact of the model. The two bands repel each other, giving a non-parabolicity for the states around k=0, and making the heavy hole appear light and the light hole heavy. The two hole sub-bands are mixed away from k=0, but they keep their ±3/2 and ±1/2 character at the zone centre. This is in line with symmetry imposed predictions, and implies selection rules giving transition intensities from the heavy-hole and light-hole sub-bands proportional to 3/4 and 1/4 for light polarized parallel to the layers and 0 and 1 for light polarized along the normal to the layers, the z-direction. These selection rules are believed responsible for many polarization sensitive effects in quantum wells, such as the polarization dependent gain in quantum well lasers[10]. Some controversy does however exist for the states at k=0, due to some polarized photoluminescence measurements performed on modulation doped MQW structures[4]. These indicate significant light emission for the "forbidden" transition from the heavy-hole subband in the case of light polarized along z. The presence of such transitions would dictate some mixing even at k=0,contradicting the present theory.

2.2.2 Excitons

The definition of an exciton states[11] that it is a non-conducting excited electronic state in a perfect insulator, normally a non-magnetic insulator. The concept may be expanded to include similar states in semiconductors, and is most often depicted as bound states of an electron and a hole. The conventional method of modelling this composite particle system is by means of the hydrogen model, with the exciton being assigned a specific radius corresponding to the binding of the electron-hole pair —the Bohr radius. Excitons are

normally divided into two categories: weakly bound or Mott excitons and tightly bound Frenkel excitons. The tightly bound excitons have a radius on the scale of an atomic lattice constant, which means that the probability is high of finding both electron and hole on the same atom. The weakly bound excitons have radii that are large compared to the lattice constant, and thus extend over many atoms.

In bulk semiconductors the Mott exciton radius a_{3D} is given by:

$$a_{3D} = \frac{\varepsilon \hbar^2}{e^2 \mu^*} \qquad (2.2.2.1)$$

where μ^* is the reduced mass of the electron-hole state, taking into account the valence band structure of the semiconductor and incorporating appropriate terms for the description of the influence of the heavy and light hole bands.The other symbols have their usual meaning.

The binding energy E_n of the electron-hole state is expressed in terms of the Rydberg constant R_y as:

$$E_{3D} = -\frac{R_y}{n^2} \quad \text{and} \quad R_y = \frac{e^4 \mu^*}{2\varepsilon^2 \hbar^2} \qquad (2.2.2.2)$$

where n denotes the quantum level. In the case of GaAs, typical values are $R_y = 4.2$ meV and $2a_{3D} = 300$ Å.

The low-temperature absorption spectrum of a semiconductor yields one method of observing excitons. This spectrum consists of a continuum above the band-edge and below this, separated by the binding energy, the exciton absorption peaks can be observed. Theoretically this peak should be infinitely narrow, but interaction with thermal phonons leads to a finite broadening and a Gaussian lineshape. In polar semiconductors the exciton linewidth broadening is mainly due to interactions with LO-phonons. At absolute zero, no phonons are available for this interaction, and even at low temperatures the broadening is

much smaller than the binding energy, allowing the exciton absorption peak to be observed. At room temperature, however, the large concentration of phonons broadens the exciton linewidth considerably, making it larger than the exciton binding energy and hence making it inseparable from the continuum of the absorption spectrum.

The situation is somewhat different for the case of quantum wells. In the case of a bulk semiconductor there is only one exciton below the band-edge, but with quantum wells there are two observable excitons. These arise from the lifting of the degeneracy of the heavy- and light hole bands due to the confinement. Furthermore, excitons are associated with every level in the step-like joint density of states in quantum well structures, resulting in two excitons below each absorption level in the MQW absorption spectrum.

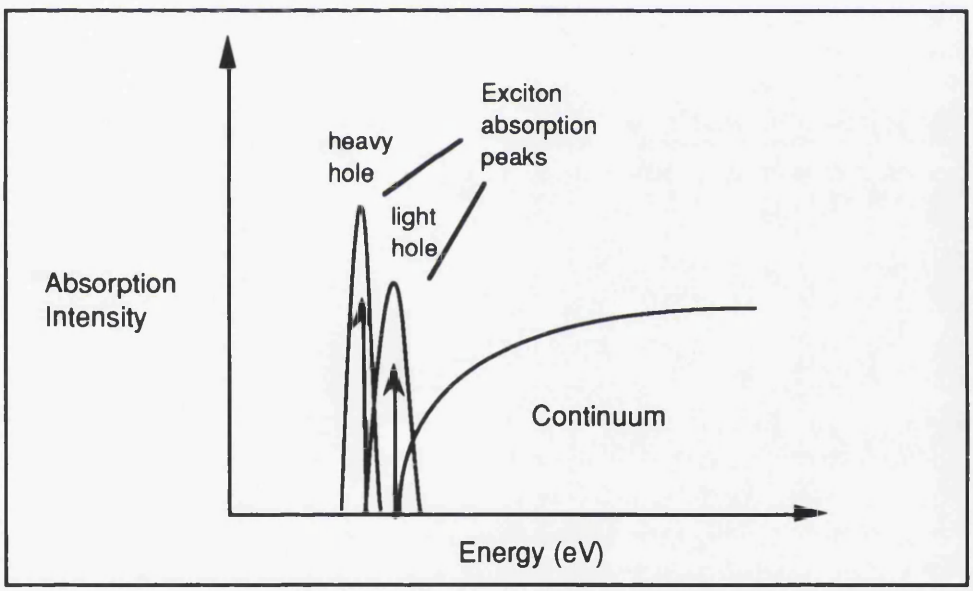

Fig. 2.2.2.1 Schematic diagram of the first (n=1) absorption level of a quantum well structure.

Unlike bulk semiconductor excitons, QW excitons are in general observable at room temperature. This is due to two important factors related to the confinement of the exciton in the well structure. The reduced dimensionality has the effect of compressing the exciton and increasing the overlap between the electron and hole wavefunctions, leading to an increase in the binding energy of the system. Additionally, confinement restricts the

interaction with thermal phonons to GaAs LO-phonons, leading to a smaller linewidth broadening.

The exciton binding energy is greatly dependent on the well size. For well widths L_z of the order of the exciton diameter, nearly 3-D effects are expected but, as L_z decreases, the exciton increasingly takes on a 2-D nature. The binding energy in the 2-D limit is given as[8]:

$$E_n = -\frac{R_y}{(n-\frac{1}{2})^2} \qquad (2.2.2.3)$$

which gives the binding energy $B_{2D} = -4R_y$ for the n=1 level, a fourfold increase from the case of bulk semiconductors. This is however only attainable in the ideal case of a well with infinite potential barriers.

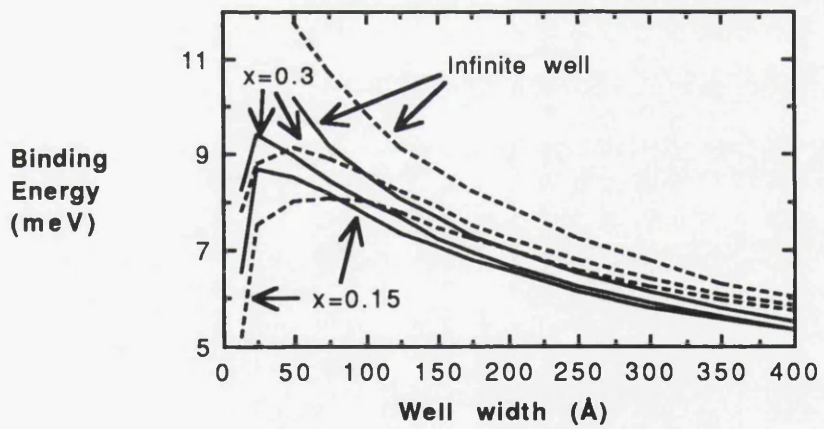

Fig.2.2.2.2 Diagram (with limited no of data points) showing typical variation of binding energy with well width for quantum wells with x=0.15 and 0.30 AlGaAs barriers together with the infinite potential well case.(---) = light hole binding energy, (—) = heavy hole binding energy (data from ref. 2).

In practice, the quantum well will be bound on either side by finite potential barriers and, similarly to the case of the band structure , there will be a non-negligible penetration depth of the wavefunctions into the large gap material. This penetration increases with decreasing well width, and the overall effect is to create a maximum in the binding energy of the exciton, typically in the range $0.5a_{3D} \leq L_z < a_{3D}$. In the GaAs-AlGaAs system this causes

the binding energy to have a maximum value of between -2R_y and -3R_y at a well thickness L_z dependent on the barrier composition and the limit to which the exciton wavefunction can be compressed before spilling over into the surrounding AlGaAs layer.

The energy E corresponding to the absorption line of the exciton is given by the energy of its associated conduction to valence band transition less its binding energy E_{ex} , e.g. :

$$E = h\nu = E_g + E_{1e}(L_z) + E_{1hh}(L_z) - E_{ex}(L_z) \qquad (2.2.2.4)$$

for the case of the exciton associated with the 1s level electron to heavy hole transition in a quantum well of size L_z. Here E_g is the bandgap of the well material and E_{1e} and E_{1hh} are the confinement energies of the 1s electron and heavy hole band respectively.

The half width at half maximum (HWHM) Γ can be measured from the absorption spectrum of a MQW structure giving a measure of the broadening of the exciton linewidth. The variation in linewidth HWHM with temperature can be expressed as[8]:

$$\Gamma = \Gamma_0 + \frac{\Gamma_{ph}}{\left[\exp\left(\frac{\hbar\Omega_{LO}}{kT}\right) - 1\right]} \qquad \text{where} \qquad \frac{\hbar\Omega_{LO}}{k} \approx 428K \qquad (2.2.2.5)$$

where Γ_0 is a constant inhomogeneous term corresponding to the linewidth at low temperatures, Γ_{ph} is a fitting parameter proportional to the temperature dependent LO phonon density and $\hbar\Omega_{LO}$ is the GaAs LO phonon energy. Typical values for the heavy hole exciton when L_z = 102 Å are Γ_0 = 2 meV, Γ_{ph} = 5.5 meV. The linewidth appears to be constant for temperatures below 150K, and thereafter increases exponentially with temperature. At low temperatures the linewidth is mainly governed by interface fluctuations created during growth. Low-temperature exciton linewidth measurements can in this way provide important information about the quality of growth of the QW structure.

Photoluminescence (PL) and photoluminescence excitation (PLE) spectroscopy are two other methods that allow the study of semiconductor excitons. These measurements can be

carried out at low or high temperatures, and have the advantage over absorption measurements in that both the high- and low-energy side of the exciton can be observed. Photoluminescence spectroscopy does not require any particular sample preparation, and is a completely non-destructive process, allowing the study of complete wafers prior to device fabrication.

Photoluminescence has been used extensively in the study of quantum well structures, and particularly in investigations into the effect of monolayer well fluctuations[12,13,14]. Most MQW structures are grown using MBE or MOCVD and, although the growth dynamics for the MOCVD growth process are less understood than for MBE, monolayer formation on the surface of the semiconductor is expected to be effected through a similar process in the two growth methods. The formation of 'islands' of material precedes monolayer formation and, when the the well-barrier interface is grown, any residual islands result in regions of non-uniform thickness in the quantum well (or barrier). For samples grown by MOCVD, an energy shift in the exciton transition has been observed and attributed to interface roughness[15,16]. For MBE-grown material, the monolayer thickness variation has been observed[17] to cause a broadening in the exciton linewidth observed by PL, the amount of which is determined by the lateral size L_S of the growth islands. This is illustrated in fig. 2.2.2.3, which shows that for L_S greater than the exciton diameter, the exciton experiences only one of the confinement energies corresponding to either L_Z or $L_Z \pm a/2$ (a= lattice constant of material, a/2 = 1 monolayer of Ga plus 1 monolayer of As), resulting in three discrete peaks in PLE measurements and, sometimes, in PL at low temperature. Conversely, if L_S is smaller than the exciton diameter, a single peak is observed, with a linewidth corresponding to the well width fluctuations within one exciton diameter, typically a/2. In the case of multiple quantum well structures, it is possible to envisage the presence of a mixture of well thickness fluctuations from layer to layer, and these need not necessarily be limited to single atomic layers. The combination of intra-layer and interlayer well size fluctuations can in this way lead to a continuous broadening of the excitonic

linewidth observed, rather than the discrete peaks observed in single quantum wells. Thermalization effects can also inhibit the observation of the discrete levels.

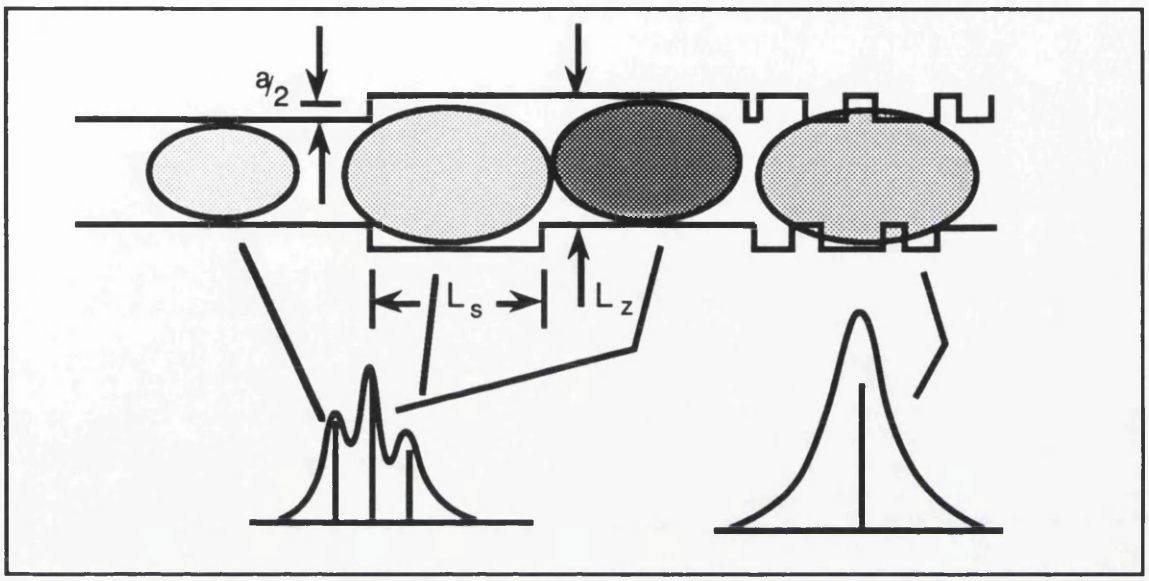

Fig. 2.2.2.3 Diagram illustrating the effect of monolayer fluctuation in a quantum well. When the lateral size of the growth island L_S is smaller than the exciton Bohr diameter, the PL linewidth corresponds to the confinement energy fluctuations experienced by the exciton. Conversely, for large L_S, the exciton experiences only one well width (L_Z, L_Z+a/2 or L_Z-a/2), and discrete PL peaks are observed[18].

2.3 Refractive Index

2.3.1 Real and Imaginary Parts of the dielectric function

The dielectric function ε of a substance is a measure of its interaction with light incident upon or transmitted through it. Although it often is referred to as the dielectric constant of a material, it is a function of the photon energy $E_{ph}=h\nu$ of the incident wave. The dielectric function of a material is a complex number, and its real and imaginary parts ε_1 and ε_2 give rise to the effects of refraction and absorption. The conventional expression for ε is:

$$\varepsilon(\omega) = \varepsilon_1(\omega) + i\varepsilon_2(\omega) \qquad (2.3.1.1)$$

or alternatively, in terms of the complex refractive index $\tilde{n}$, the ordinary refractive index n and the extinction coefficient k:

$$\tilde{n} = n + ik = \sqrt{\varepsilon} \qquad (2.3.1.2)$$

where the extinction coefficient is related to the absorption coefficient α through:

$$\alpha = \frac{4\pi k}{\lambda} \qquad (2.3.1.3)$$

The above expressions are written according to physics convention[19]. Engineering and optic conventions are obtained by complex conjugation.

The refractive index and absorption of a material system form parts of a system of functions that are found to be interdependent. The relationship between them is dealt with in the next section.

2.3.2 Kramers-Krönig

The real and imaginary parts of a response function can, given that certain conditions of linearity and causality are satisfied, be shown to be related through a set of integrals known as the Kramers-Krönig integrals[20]. This relationship is of particular importance when applied to an optical system, where the dielectric function $\varepsilon(\omega) = \varepsilon_1(\omega) + i\varepsilon_2(\omega)$ is the linear response function and the real and imaginary parts of this give rise to the refractive index and the absorption respectively. In this case the Kramers-Krönig integrals take the form[21]:

$$\varepsilon_1(\omega) - 1 = \frac{2}{\pi} P \int_0^\infty \frac{\omega' \varepsilon_2(\omega')}{(\omega')^2 - \omega^2} d\omega' \qquad (2.3.2.1)$$

$$\varepsilon_2(\omega) = -\frac{2}{\pi} P \int_0^\infty \frac{\varepsilon_1(\omega')}{(\omega')^2 - \omega^2} d\omega' \qquad (2.3.2.2)$$

where *P* denotes that the Cauchy principal value is taken. The impact of this relationship on an optical material system is that, for a given change in absorption, there will be a resulting change in refractive index. It is important to note that the relationship is only valid for a linear response function. In semiconductors the relationship remains valid for a system containing a fixed number of carriers[22] such as the case of a semiconductor containing a

fixed number of photogenerated carriers (photocarriers). The change in refractive index Δn associated with a change in absorption Δα can therefore be expressed as[15]:

$$\Delta n(\omega) = \frac{c}{\pi} P \int_0^\infty \frac{\Delta\alpha(\omega')}{(\omega')^2 - \omega^2} d\omega' \qquad (2.3.2.3)$$

It is therefore possible to extract information on the refractive index change in a semiconductor from measured absorption change by transforming it through the Kramers-Krönig relation. This is of great importance in the evaluation of optical properties in semiconductors. Additionally, since the absorption change normally is localised to a small part of the spectrum, the integral can be performed on a restricted integration range only, making the numerical implementation straightforward.

2.3.3 Coulombic screening

The presence of the bound excitonic states described in section 2.2.2 results in a modification of the density of states in the material system. This in turn leads to absorption resonances in the frequency spectrum corresponding to creation of excitons. These resonances are associated with the e-lh and e-hh exciton transitions discussed in section 2.2.2. In MQW material, the dichroism of the material results in the observation of one or two absorption peaks depending on the polarisation of the light. The absorption resonance due to the exciton remains observable even at room temperature for low excitation intensities.

The resonance peak in the absorption in MQW structures is responsible for a major nonlinearity in the refractive index of the material, following the K-K relationship. An exciton is created through the absorption of a photon of energy equal to the excitonic peak. This exciton is thermally ionized within a very short time (0.3-0.4 ps). Ionized excitons give rise to an electron-hole plasma, that is, a population of free electron and hole carriers within the energy bands. In the case of the photons having energies larger than that of the excitonic peak, these free carriers may be created directly. The creation of an e-h plasma

will also lead to a change in the refractive index of the material. This happens by two means. Firstly, the change in the density of carriers will directly lead to a change in refractive index, but also secondly, the increased carrier density will result in a change in absorption which, through the K-K relation will give a modification of the refractive index. At larger photon densities, the effect of the e-h plasma is to effectively bleach the excitonic transition. This is due to bandgap renormalisation, a many-body effect created in the form of a bandgap reduction by the presence of the large concentration of free carriers. Screening of the excitonic transition may effectively remove the absorption peak at this frequency and lower the absorption of the continuum[8]. Another possible effect in semiconductors is the band filling effect or dynamic Burstein-Moss shift, whereby coupling between different k-states through carrier scattering leads to a saturation of a band of states in the energy bands. In this case the bandgap is effectively increased, giving an increase in the absorption band-edge energy.

2.3.4 Refractive index values and models

The AlGaAs material system has been studied extensively and is probably the best characterized system in the III-V semiconductor group. Large amounts of data are available on both electronic and optical-related properties, such as energy band structure, doping effects, as well as optical absorption and refractive indices. A review of the relevant properties can be found in [23]S. Adachi's paper: "GaAs, AlAs, and AlGaAs: Material parameters for use in research and device applications", and several volumes of constants relating to the material system have been published. The database for the refractive index of AlGaAs is however neither complete nor definitive. The optical functions have been measured at discrete points throughout the optical spectrum, but the intervals between points are often large and the values quoted from different sources are not always in agreement. The perhaps most complete set of optical constants for GaAs is presented in the 1985 EMIS datareview RN=15430 through 15438, and is presented by D.E. Aspnes as a compilation of results obtained from his own research and that of a handful of other groups[24]. In the region from 600 nm to 1200 nm there are overlapping measurements at

only two points, with values agreeing to within 1%. For AlGaAs the situation is more severe, in that measurements of optical functions only exist for a limited number of Al-compositions. This makes it difficult to calculate the effective parameters for AlGaAs structures based on reported values alone.

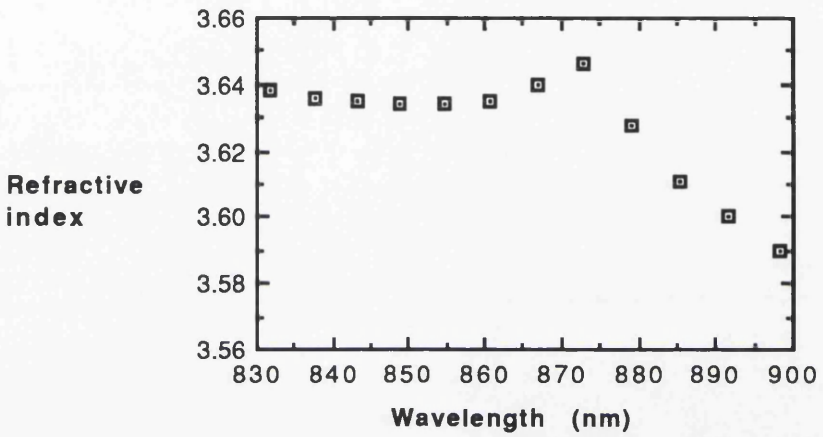

Fig.2.3.4.1 Plot of refractive index of intrinsic GaAs as a function of wavelength in the region around the bandgap (Data from ref 26).

Aspnes[25] et al and Casey[26] et al have presented the most referenced and perhaps the most exhaustive measurements of the dispersion of the refractive index for AlGaAs with variation in aluminium content. These measurements make up data sets of $Al_xGa_{1-x}As$ refractive indices for x=0.0 to x=0.8 (≈0.4 for Casey et al) in increments of approximately 0.1. The measured values have little overlap in the frequency spectrum, but the values that do overlap are in relatively poor agreement. This will be commented upon in Appendix A. Whereas both data sets were obtained through measuring the reflectance of the AlGaAs material, the two groups used different methods for obtaining the indices. Aspnes used the ellipsometric method and obtained the refractive index from the complex reflectance of samples whose AlGaAs layer thickness and material composition were known quantities. Casey assumed the imaginary part of the dielectric function to be negligibly small and obtained the refractive index by comparing the reflectance from AlGaAs of unknown composition with that from a surface of known reflectance, a silver-quartz interface mirror. Both groups used LPE-grown material, but whereas Aspnes used several separately-grown

wafers with layers of AlGaAs that were not intentionally graded, Casey used wafers that were intentionally graded in aluminium content from the surface to the GaAs substrate interface. The determination of the composition was also achieved by different means. The computerised set-up used by Casey et al gave an almost continuous range of measurements and exhibited a peak that was clearly composition dependent. This peak was taken as the bandgap and the composition was derived from a linear interpolation of values of energy-gap versus composition found in the literature (e.g. Onton[27] et al). A later version of the piecewise polynomial fit used by Casey et al is given as:

$$E_0(x) = 1.424 + 1.247x \ \ (eV) \qquad (x \le 0.45) \qquad (2.3.4.1a)$$

$$E_0(x) = 1.424 + 1.247 \times (x - 0.45)^2 \ \ (eV) \qquad (x > 0.45) \qquad (2.3.4.1b)$$

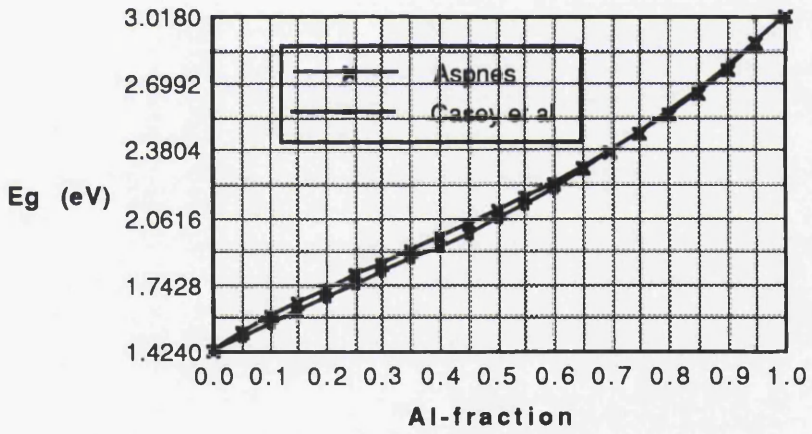

Fig. 2.3.4.2 Diagram of Energy gap as calculated by the two methods given by Casey et al and Aspnes et al.

Aspnes used the more deliberate approach of measuring the bandgap of each wafer by photoluminescence and fitting an interpolation scheme to these data to obtain what they term the 'optically determined composition'. The model fitting took the form of a third order polynomial least-squares fit with the end-point bandgap values (GaAs and AlAs) taken as known restraints. The resulting equation for the E_0 transition energy:

$$E_0(x) = 1.424 + 1.594x + x(1-x)(0.127 - 1.310x)eV \qquad (2.3.4.1c)$$

gave a very good fit to the values measured, including some obtained from MBE-grown control samples.

2.3.4.1 Bulk GaAs Refractive Index Models

For accurate design of AlGaAs optical and optoelectronic structures for specific wavelength regimes with specific guiding properties, knowledge of the dispersion of the refractive index for any chosen composition is essential. However, since the available datasets consist of discrete values, some sort of interpolation or prediction scheme or model has to be devised. The simplest form of this is of course direct linear interpolation between two adjacent values. The interval between the data points are however often quite large, and a linear interpolation scheme will be very inaccurate. Another approach is to design a model based on the energy transitions that affect the optical functions of the material. This approach has been investigated in depth by D.W. Jenkins[28], who devised a model based upon earlier work by Adachi[20]. The model takes into account a series of energy transitions in the AlGaAs system and use interpolation schemes to adjust these for varying Al-mole fraction x. The model is then fitted to experimental data by the use of around 60 fitting parameters. This is clearly quite an involved model, and was devised to enable prediction of the refractive index of any AlGaAs composition throughout the region 1-4 eV.

Such a complicated model is not necessary if only a small wavelength regime is of interest. An alternative is the model developed by Afromowitz[29]. In contrast to the direct interpolation scheme and Jenkins' model, this model does not rely upon curve fitting to the measured refractive index values, but is a semi-empirical calculation of the Sellmeier type. The imaginary part of the complex dielectric function is modelled, and the refractive index values are found from the Kramers-Krönig relationship where the solution forms a power series expansion that incorporates terms related to the main energy band transitions. The energy transitions are, similarly to the model by Jenkins, modelled over the Al-mole fraction range by interpolation schemes. The resulting model, expressed in terms of the susceptibility χ takes the form:

$$\chi(E) = M_{-1} + M_{-3}E^2 + M_{-5}E^4 \times \ln\left[\frac{\left(E_f^2 - E^2\right)}{\left(E_\Gamma^2 - E^2\right)}\right] \qquad (2.3.4.1.1a)$$

with

$$M_{-1} = \frac{\eta}{2\pi}\left(E_f^4 - E_\Gamma^4\right), \qquad (2.3.4.1.1b)$$

$$M_{-3} = \frac{\eta}{\pi}\left(E_f^2 - E_\Gamma^2\right), \qquad (2.3.4.1.1c)$$

$$M_{-5} = \frac{\eta}{\pi}, \qquad (2.3.4.1.1d)$$

$$\eta = \frac{\pi E_d}{2E_0^3\left(E_0^2 - E_\Gamma^2\right)}, \qquad (2.3.4.1.1e)$$

and

$$E_f = \sqrt{\left(2E_0^2 - E_\Gamma^2\right)} \qquad (2.3.4.1.1f)$$

E_Γ is the lowest direct energy transition of the AlGaAs material at the Γ point, and E_0 and E_d are the energy and oscillation strength parameters of the effective oscillator part of the model. E_f and η are fitting parameters arising from solution of the moment equation for the absorption spectrum.

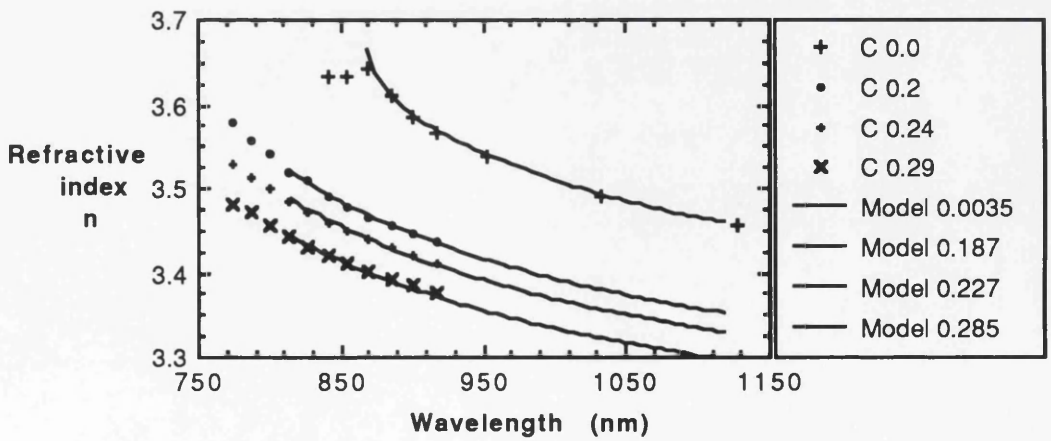

Fig. 2.3.4.1.1 Diagram showing a comparison of GaAs refractive values as measured by Casey et al (C 0.xx) and as calculated by Afromowitz' original model for the aluminium fraction that gave the best fit.

The fit of this model to data presented by Casey et al[20] was, in the case of GaAs, to within 0.1% over the range from 895 nm to 1700 nm. The model could also reproduce data for all the aluminium compositions in that reference to well within the experimental error of the measurements and the Al-fraction determination.

2.3.4.2 Multiple Quantum Well Refractive Index Models

The refractive indices for MQW's and superlattices are less well documented than for bulk material, and fewer models exist. The reduced dimensionality consideration of quantum well structures adds a further difficulty. Both the modification of the band structure due to the quantization of states in the quantum well material and the presence of room temperature excitons contribute to the complexity of the model. Additional factors add to the problem of modelling, such as the anisotropy introduced by the layered structure of quantum well materials. This anisotropy results in a birefringence in the material.

There are of course several approximations that can be made to simplify modelling of the refractive index in MQW materials. The perhaps most obvious solution for such a model consists of taking a refractive index model for bulk material of the same average composition as the quantum well material and modify this to incorporate the effects of quantization. This bulk refractive index model is often taken as a linear approximation of the real refractive index dispersion far away from the bandgap[30]. Another approach disregards the effects of quantization completely and only considers the bulk material optical properties of the components in the MQW material, treating these as a multilayer waveguide configuration. The solutions of Maxwell's equations for such a multilayered structure result in the following expressions for the effective dielectric constants of the two polarization modes for optical waves travelling in the plane of the layers:

$$\varepsilon_{TE} = \varepsilon_{TE}^{0}\left(1+\frac{k^2}{12}\frac{d_a^2 d_g^2}{\left(d_a+d_g\right)^2}\frac{\left(\varepsilon_a-\varepsilon_g\right)^2}{\varepsilon_{TE}^{0}}\right) \qquad (2.3.4.2.1a)$$

and

$$\varepsilon_{TM} = \varepsilon_{TM}^{0}\left(1+\frac{k^2}{12}\frac{d_a^2 d_g^2}{\left(d_a+d_g\right)^2}\frac{\varepsilon_{TE}^{0}\left(\varepsilon_{TM}^{0}\right)^2\left(\varepsilon_a-\varepsilon_g\right)^2}{\varepsilon_a^2\varepsilon_g^2}\right) \qquad (2.3.4.2.1b)$$

d_a, d_g and $\varepsilon_a, \varepsilon_g$ are the thicknesses and material dielectric constants of the two component layers in the structure respectively, k is the wave number and:

$$\varepsilon_{TE}^{0} = \frac{\varepsilon_a d_a + \varepsilon_g d_g}{d_a + d_g} \qquad (2.3.4.2.2a)$$

and

$$\varepsilon_{TM}^{0} = \frac{d_a + d_g}{\left(d_a/\varepsilon_a\right)\left(d_g/\varepsilon_g\right)} \qquad (2.3.4.2.2b)$$

are the dielectric constants for the case where $d_a, d_g << \lambda$. This last set of conditions applies to the case of quantum wells, where d_a, d_g and $\varepsilon_a, \varepsilon_g$ corresponds to thicknesses and material dielectric functions for the wells and barriers respectively.

The latter approach can to some degree account for the birefringence in MQW material, and works well far away from the bandgap of the material. It does however fail close to the bandgap. The presence of room temperature excitons in quantum wells necessitates the inclusion of an additional nonlinear term in the model. The first-mentioned approach does this by including a single effective oscillator term to the "average composition model". A possible implementation of this gives the following expression for the dielectric function ε_{MQW} of the MQW material:

$$\varepsilon_{MQW}(\omega) = \varepsilon_g(\omega) + 4\pi\beta_x \frac{\omega_x^2}{\left(\omega_x^2 - \omega^2 - i\omega\Gamma_x\right)} \qquad (2.3.4.2.3)$$

In the above equation, ε_g represents the background dielectric constant, containing contributions from all interactions except the exciton(s) in question, suffixed 1 for light hole

(lh) and h for heavy hole (hh). ε_g is determined from a linear interpolation of the refractive index n_g of the waveguide composite material away from the bandgap: $n_g=(a\omega+b)$, a and b being fitting parameters. $\beta_{l,h}$ is the oscillator strength of the exciton transition, $\omega_{l,h}$ is the exciton centre frequency and $\Gamma_{l,h}$ is the exciton linewidth. The exciton linewidths and centre frequencies are obtained from room temperature photoluminescence measurements. $ß_l$ and $ß_h$ are the fitting parameters for the model. For the TE excited mode, both lh and hh exciton transitions contribute to the dielectric function, but for the TM excited mode, the lh exciton transition alone contributes to the nonlinear dielectric function.

The refractive index is for both methods found as the square root of the real part of the dielectric function. It is clear that both these methods have their weaknesses, and the best result are probably obtained from a combination of the two methods. The choice of model will in the end depend on compromises between the complexity and required accuracy of the model.

2.4 Summary

Semiconductor quantum well materials have electronic and optical properties differentiating them from bulk semiconductor material. These properties arise from quantization effects due to the abrupt composition changes in the periodic microstructure. Among the effects of quantization compared to bulk material of same average material composition are:

–step-like density of states

–bandgap increase

–lifting of valence band degeneracy

–excitons observable at room temperature
(due to increased exciton binding energy and confinement)

–change in refractive index

–birefringence

–change in absorption

–dichroism

The refractive index and the absorption of quantum well material can be obtained from the real and imaginary parts of the dielectric function of the material respectively, and they are related through the Kramers-Krönig transformation relationship. It is often more convenient to measure the absorption of a structure than the refractive index. Refractive index models are, as a consequence, often based on models of the absorption in the structure. The model of a semiconductor quantum well material need to include terms that account for the rapid increase in the refractive index close to excitonic transitions, together with terms that describe the birefringent behaviour.

[1] L. Esaki," A Birds-Eye View on the Evolution of Semiconductor Superlattices and Quantum Wells", IEEE J.of Q.El. Vol. QE-22 1986, pp 1611-1624.

[2] C. Weisbuch, " Fundamental Properties of III-V Semiconductor Two-Dimensional Quantized Structures: The Basis for Optical and Electronic Device Applications", Semiconductors and Semimetals Vol. 24, Academic Press London, 1987, Ch.1, p1.

[3]H. Holonyak Jr., R.M. Kolbas, W.D. Laidig, B.A. Vojak, K. Hess, R.D. Dupuis, P.D. Dapkus,"Phonon assisted recombination and stimulated emission in quantum well AlGaAs-GaAs heterostructures," J.Appl. Phys. Vol.51, 1980, pp1328-1337.

4 G.Bastard,"Electronic energy levels in semiconductor quantum wells and superlattices", Superlattices and Microstructures,Vol.1, No.3, 1985, pp 265-273.

5 D.S. Chemla, D.A.B. Miller, "Room temperature excitonic nonlinear-optical effects in semiconductor quantum-well structures., J.Opt.Soc.Am.B. Vol.2, No.7,1985, pp1155-1173.

6 S.M.Sze,"Physics of Semiconductor Devices", John Wiley & Sons, New York 1981,p 848.

7 R. Dingle,"Confined Carrier Quantum States in Ultra Thin Semiconductor Heterostructures", Festkoerperprobleme XV, Pergamon/Vieweg, Braunschweig 1975, p. 21.

8 R.C. Miller, D.A. Kleinmann, A.C. Gossard,"Energy-gap discontinuities and effective masses for GaAs-AlGaAs quantum wells", Phys. Rev. B29, 1984, pp 7085-7087.

9 D.S. Chemla,"Quazi-two-dimensional Excitons in GaAs/$Al_xGa_{1-x}As$ Semiconductor Multiple Quantum Well Structures", Helvetica Physica Acta, Vol.56, 1983, pp 607-637.

[10]H. Holonyak Jr., R.M. Kolbas, W.D. Laidig, B.A. Vojak, K. Hess, R.D. Dupuis, P.D. Dapkus,"Phonon assisted recombination and stimulated emission in quantum well AlGaAs-GaAs heterostructures," J.Appl. Phys. Vol.51, 1980, pp1328-1337.

[11]C.Kittel, Quantum Theory of Solids,John Wiley & Sons, New York 1987, p 298.

[12] C. Weisbuch, R. Dingle, A.C. Gossard, W. Wiegmann," Solid State Communications, 39, 1981, p 709.

[13]L. Goldstein, Y. Horikoshi, S. Tarucha, H. Okamoto,".Japanese Journal of Applied Physics, 22, 1983, p 1489.

14 B. Deveaud, J.Y. Emery, A. Chomette, B. Lambert, M. Baudet, " Single monolayer well size fluctuations in the luminescence of GaAs-GaAlAs superlattices", Superlattices and Microstructures, Vol.1, No. 3, 1985, pp 205-208.

[15]D.J. Westland, A.M. Fox, A.C. Maciel, J.F. Ryan, "Optical studies of excitons in $Ga_{0.47}In_{0.53}As$/InP multiple quantum wells", Appl. Phys. Letts. Vol. 50, 1987, pp839-841.

[16]G.Bastard, C. Delalande, M. H. Meynadier, P.M. Frijlink, M. Voos, "Low-temperature exciton trapping on interface defects in semiconductor quantum wells", Phys.Rev.B, Vol.29, 1984, pp7042-7044.

[17]R.F. Kopf, E.F. Schubert, T.D. Harris, R.S. Becker, "Photoluminescence of GaAs quantum wells grown by molecular beam epitaxy with growth interruptions", Appl. Phys. Letts. Vol. 58, 1991, pp631-633.

[18]B.Deveaud, J.Y. Emery, A. Chomette, B. Lambert, M. Baudet,"Single monolayer well size fluctuations in the the luminescence of GaAs-GaAlAs superlattices," Superlattices and Microstructs. Vol.1 (3) 1985, pp 205-208.

[19]D.E. Aspnes,"Optical functions of intrinsic GaAs: General Remarks," EMIS Datareview RN=15430, Chapter 8.1 Properties of GaAs 2nd edition, Inspec,1985.

[20] A.Abragam,"Principles of Nuclear Magnetism", p 93, Clarendon Press 1961.

[21]F.Stern,"Elementary Theory of the Optical Properties of Solids", Solid State Physics Vol.15, p 299, 1963.

[22]D.S. Chemla, D.A.B. Miller, P.W. Smith, A.C. Gossard, W. WIegmann, "Room Temperature Excitonic Nonlinear Absorption and Refraction in GaAs/AlGaAs Multiple Quantum Well Structures," IEEE J.of Q. El. Vol. QE-20, No.3, March 1984.

[23]S. Adachi "GaAs, AlAs, and AlGaAs: Material parameters for use in research and device applications."J.Appl. Phys.58 (3) 1985 ppR1-R29.

[24]D.E. Aspnes,"Optical functions of intrinsic GaAs: General Remarks," EMIS Datareview RN=15437, Chapter 8.1 GaAs and related Compounds 1985.

[25]D.E.Aspnes, S.M. Kelso, R.A. Logan, R. Bhat,"Optical properties of AlGaAs," J.Appl.Phys. Vol.60. No.2 1986, pp 754–767.

[26]H.C.Casey Jr., D.D. Sell, M.B. Panish,"Refractive index of $Al_xGa_{1-x}As$ between 1.2 and 1.8 eV,"Appl. Phys. Letts. Vol. 24, No.2, 1974, pp 63-65.

[27]A.Onton, M.R. Lorenz, J.M. Woodall, Bull.Am.Phys.Soc. Vol.16, 1971 p371.

[28]D.W. Jenkins,"Optical constants of $Al_xGa_{1-x}As$,"J.Appl.Phys Vol.68, No.4, 1990, pp 1848-1853.

[29]M.A.Afromowitz,"Refractive index of $Ga_{1-x}Al_xAs$," Solid State Comms. Vol.15, 1974, pp 59-63.

[30]Y.J. Chen, C. Jagannath, G.M. Carter, E.S. Koteles, S.W. Brown, G.J. Sonek, J.M. Ballantyne,"Optical properties of GaAs/AlGaAs Multiple Quantum Well Waveguides," Superlattices and Microstructures, Vol.3, 1987, pp 287-290.

CHAPTER 3

IMPURITY INDUCED DISORDERING IN ALXGA1-XAS-GAAS QUANTUM WELLS

The concept of impurity induced disordering in $Al_xGa_{1-x}As$-GaAs quantum well structures is explained in this chapter. A review of the current understanding of the disordering process in this material system is also presented.

3.1 Introduction

Impurity Induced Disordering (IID) of III-V quantum well structures was first discovered in 1980 by Laidig et al[1], during an experiment trying to selectively dope an undoped $Al_xGa_{1-x}As$-GaAs superlattice (SL) structure using Zn diffusion. It was found that the layers of the superlattice became unstable when subjected to the Zn diffusion and intermixed to give bulk undamaged homogeneous material of an aluminium concentration equal to the material average of the SL structure. This induced intermixing took place at a temperature much lower than that required for ordinary thermal interdiffusion of the III-V compounds. Since then, many elements have been found to induce intermixing in III-V semiconductors, some of which will be discussed later.

The introduction of various impurities has the effect of lowering the temperature threshold for the intermixing of the quantum well and barrier materials. This is a complex process which is not yet fully understood, but a review of the current understanding follows in section 3.3.2

Consider the simple case of an $Al_xGa_{1-x}As$-GaAs heterostructure: a thin layer of GaAs sandwiched between two layers of $Al_xGa_{1-x}As$ material. An active disordering impurity, such as Si, is introduced into both GaAs and AlGaAs layers. If the system is subjected to high temperature annealing conditions (~800° C), Al will start diffusing into the GaAs layer from the surrounding AlGaAs, substituting for Ga on the group III sublattice. This leads to

an effective narrowing of the GaAs layer. The profile of the Al-indiffusion can be represented by conventional diffusion theory, using a limited plane source diffusion model, and considering the Ga out-diffusion from the thin GaAs layer using an appropriate interdiffusion constant which depends on the impurity species and annealing conditions. The diffusion model for a limited plane source gives the concentration distribution of Ga, $C(z)$ in the form of error functions. The general situation can easily be extended to the case of a quantum well:

$$C(z) = (1-x) + \tfrac{1}{2}x\left[erf\left(\frac{\frac{w}{2}-z}{2\sqrt{Dt}}\right) + erf\left(\frac{\frac{w}{2}+z}{2\sqrt{Dt}}\right)\right] \qquad (3.1.1)$$

The centre of the well is defined as z =0, w is the well (and barrier) width before disordering, t is the annealing time and D is the interdiffusion coefficient of Al and Ga in the presence of the impurity used.

In this case, the interdiffusion of the well and barriers results in an increase in the effective bandgap of the semiconductor. The increase is due to a combination of two factors: 1) bandgap increase at centre of well due to Al in-diffusion, and 2) change in the confinement energy of electron and holes in the well.

3.2 Ion species dependence of IID

Several atomic species have been investigated to ascertain their influence on intermixing rates when used as impurities in MQW structures. Among these are impurities that behave as donors in the III-V material system, e.g. Si, Ge, S, Sn, Se, acceptors; e.g. Zn, Be, Mg and neutrals, e.g. B, F, Kr, Ar. Among the latter are also the elements making up the III-V semiconductor, in the case of AlGaAs, Al, Ga and As. The impurities are mostly introduced into the III-V material either by diffusion or by ion-implantation, but they may also be incorporated during crystal growth.

When the impurities are introduced through conventional diffusion processes, the disordering of the structure is due solely to the effects of the presence of the impurity.

When ion-implantation is used, there is a certain amount of collision intermixing during the implantation stage, and a lot of damage is caused to the crystal lattice. This damage is believed to be almost completely removed after the annealing stage, but it is clear that in the period it takes for the crystal lattice to heal, a certain amount of intermixing will take place. This intermixing comes in addition to the intermixing due to the presence of the impurity.

Of the abovementioned impurities, Si, Ge, S, Sn, Se, Zn, Be and Mg have been shown to induce disordering of varying degrees when introduced by diffusion or when grown into the material structure. Zn, Si and Ge were found to produce a higher degree of intermixing than the rest, given the optimum condition for each impurity. The degree of interdiffusion is greatly dependent on the concentration of impurities present, as well as the annealing conditions. The diagram Fig.3.2.1 shows the time dependency of the IID process in the form of measured photoluminescence (PL) peak shift of the excitonic peak for quantum well samples that have had some of the these impurities introduced.

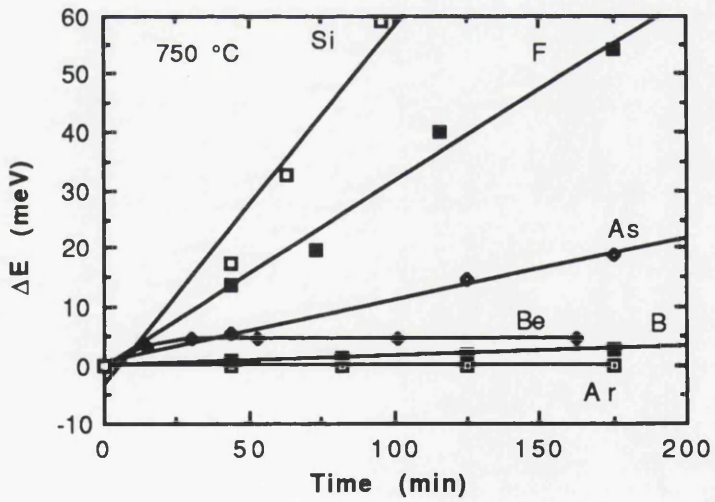

Fig.3.2.1 PL peak shifts as a function of annealing time at 750°C for some of the impurities investigated for the IID effect. From Y. Hirayama et al[2]

With introduction through ion implantation, all the investigated atomic species lead to some intermixing, but in the case of Ga, As, Al, Ar and Be, the disordering observed was small and probably due to collision induced intermixing during ion-implantation, and regeneration during the initial phase of the anneal. This manifests itself in a saturation in the

diffusion process during the annealing process ,with minimal subsequent bandgap shift with increase in annealing time. For the remaining ions, varying degrees of incremental intermixing have been observed, with Zn, Si, Ge and F yielding the highest interdiffusion coefficients.

The majority of the impurities found to induce interdiffusion are electrically active dopants in the III-V material system at room temperature, and indeed, as will be seen in section 3.3.2, the present theory of the disordering mechanism predicts that the creation of free carriers is an integral part of the disordering process. However, for optical device applications, such as waveguides, the presence of free carriers is undesirable, since it greatly increases the absorption losses in the system. Also, for active devices, such as lasers, the high dopant concentrations needed for the disordering process create problems like shunt leakage currents, and, in the case of integrated devices, the low resistivity of the disordered regions makes the electrical isolation of individual components problematic. Of the non-electrically active dopants investigated, the majority induced only small changes in the quantum well structures considered, with two important exceptions: boron and fluorine. Large changes in the bandgap of the structures considered were found for fluorine implantation, and somewhat smaller changes were observed in the case of boron. Since fluorine is a neutral dopant in III-V's at room temperature, it offers great possibilities for the fabrication of low-loss optical interconnects for integration purposes[3]. Additionally, the introduction of the impurity by ion-implantation is believed to increase the resistivity of the material, which is a great advantage for the electrical isolation of integrated devices[4].

3.3 Mechanism of disordering process

The following section is a review of the current understanding of the disordering process of quantum well structures in the III-V material system $Al_xGa_{1-x}As$-GaAs. The processes are not yet fully understood, but evidence suggests the following model, presented by D.G.Deppe et al[5].

3.3.1 Undoped III-V material

If we consider firstly the case of a type III-V heterojunction, eg. GaAs-AlAs, the self-diffusion of the column III lattice atoms, Ga and Al, must proceed through the native defects in the crystal (i.e. substitutional diffusion). Obviously, this means that the self-diffusion rate will be dependent on the concentration of native defects, and on the diffusion rate of these. The concentration of native defects is however very much smaller than the concentration of column III lattice atoms, and it is therefore assumed that the diffusion rate also must be dependent on the requisite crystal defects. For instance for self-diffusion on the column III sublattice through column III vacancies:

$$D_{III} = fD(V_{III})[V_{III}] \qquad (3.3.1.1)$$

where D_{III} is the column III self-diffusion rate, f is a constant containing information about the crystal structure, $D(V_{III})$ is the column III vacancy diffusion rate and $[V_{III}]$ is the concentration of column III vacancies. From the above equation, it can be seen how the disordering is dependent on the defect concentration, as the defect concentration increases, so does the self-diffusion rate. This is important for the case of vacancy disordering processes whereby additional vacancy defects can be created by varying the annealing conditions. It has for instance been shown that capping the sample with thick layers of SiO_2 prior to annealing in As-poor conditions creates column III interstitials as Ga desorbs into the SiO_2 layer. The effect is also evident for uncapped samples in As-poor conditions. In general, what happens is that the crystal during annealing will move towards an equilibrium with the surrounding As pressure, and in doing so will create defects at or close to the surface (e.g. column III vacancy for high As-pressure or column III interstitial for low As pressure). For instance, in the case of low As pressure in a sealed system, this reaction can be described by:

$$0 \leftrightarrow \tfrac{1}{4}As_4(vapour) + I_{Ga} \quad \text{and} \quad [I_{Ga}] = k_2 P_{As4}^{-1/4} \qquad (3.3.1.2)$$

where I_{Ga} is the column III interstitial in the case of a GaAs system, [ ] denotes concentration, k_2 depends on temperature, and P_{As4} is the vapour pressure in the sealed ampoule annealing system.

During the annealing stage, these defects have increased solubility, and are mobile, relaying the defect formation to or from the surface. This dependence on the As overpressure has been observed in disordering experiments[5], yielding a v-shaped curve in the graphical representation of interdiffusion coefficient versus As pressure during the annealing stage. At low As overpressure intermixing is taking place through interstitials and at high pressures intermixing through vacancies is favoured. This is illustrated in fig.3.3.1.1.

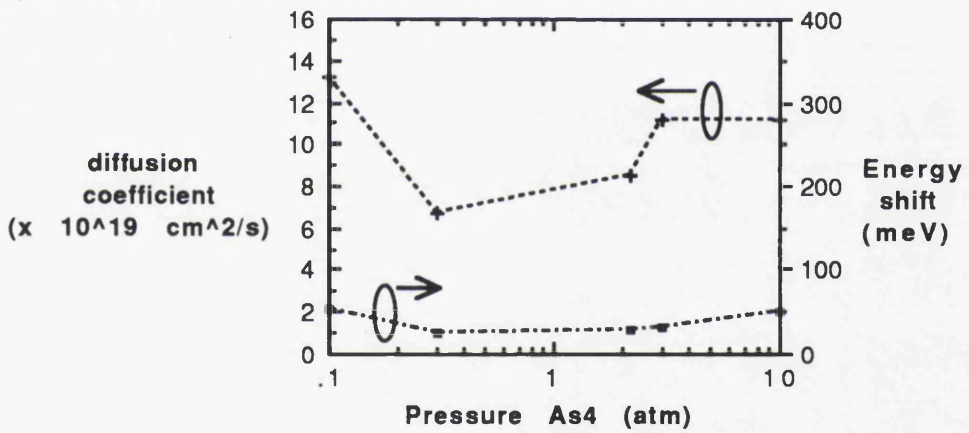

Fig.3.3.1.1 Diagram illustrating the v-shaped dependency of the interdiffusion on As_4 overpressure.(from Deppe et al)

Defects can also be created deep in the semiconductor. Consider for instance the creation of a defect on the column III sublattice by e.g. a Ga atom on the crystal lattice becoming an interstitial and leaving a column III vacancy behind. This is called a Frenkel defect , and the reaction can be expressed as:

$$0 \leftrightarrow I_{Ga} + V_{Ga} \quad \text{and} \quad [I_{Ga}][V_{Ga}] = k_I \qquad (3.3.1.3)$$

where I_{Ga} , V_{Ga} are Ga interstitial and vacancy respectively and k_I is a constant depending on temperature. The creation of Frenkel defects deep in the semiconductor obviously have important consequences for the intermixing rate of the system. Due to the relatively open crystal lattice of the III-V semiconductor, the interstitials are expected to have a diffusion rate much faster than the vacancy diffusion rate. This means that intermixing due to interstitials will take place further into the sample than intermixing due to vacancy intermixing.

The present model requires that the induced diffusion process takes place by the interaction of a lattice atom, an interstitial, and a vacancy. In other words, the lattice atom moves from one position on the crystal lattice to another through an interstitial position. Other mechanisms have been suggested, such as nearest neighbour hopping, but it has been shown that this requires an 11-step process for the vacancy to make one transition on its own sublattice. Furthermore, this divacancy process would be expected to either be independent of, or proportional to the As pressure, and would not exhibit the v-shaped dependency observed. The nearest neighbour hopping process is subsequently not considered important in explaining induced disordering in the III-V system. For the diffusion process in a GaAs-AlAs heterostructure through an interstitial, the following equation illustrates the process for a column III vacancy on its own sublattice:

$$V_{Ga} \leftrightarrow V_{Ga} + (I_{Al} + V_{Al}) \leftrightarrow (V_{Ga} + I_{Al}) + V_{Al} \leftrightarrow V_{Al} \qquad (3.3.1.4)$$

Where $(I_{Al} + V_{Al})$ is the close Frenkel pair for Al on the column III sublattice.

A similar expression illustrating diffusion of column III interstitial defects on their own sublattice and involving Frenkel pairs is given by:

$$I_{Ga} \leftrightarrow I_{Ga} + (V_{Al} + I_{Al}) \leftrightarrow (I_{Ga} + V_{Al}) + I_{Al} \leftrightarrow I_{Al} \qquad (3.3.1.5)$$

These two expressions illustrate how the group III components of a Frenkel pair (interstitial + vacancy) can be substituted so that for instance a Ga interstitial bound to a Ga vacancy

can be exchanged with an Al interstitial (and vice versa) in the diffusion process thought to govern the interdiffusion process in undoped III-V heterostructure systems.

The column III diffusion rate may be expressed in terms of the column III vacancy and interstitial diffusion rates:

$$D_{III} = f_1' D_{V_{III}} P_{As_4}^{1/4} + f_2' D_{I_{III}} P_{As_4}^{-1/4} \qquad (3.3.1.6)$$

where $f'_{1,2}$ correspond to f in equation 3.3.1.1 but with the distinction that it here also contains some information pertinent to the defect in question, and D_X is again the diffusion rate of the column III lattice atom or defect, in accordance with its suffix. Again, a similar expression can be obtained through the consideration of the effect on the diffusion mechanism of column III lattice atoms due to column V vacancies.

3.3.2 Effect of dopants in the III-V system

When dopants are introduced into the III-V material system, the interdiffusion coefficient is altered, and becomes highly dependent on the annealing conditions.It is especially sensitive to the As pressure for a fixed temperature above the level needed for the activation of the impurity. Under As-rich conditions, p-type superlattices are found to remain relatively stable in cases where n-type superlattices are found to intermix completely, and vice versa for As-poor conditions. It has been suggested, by Tan & Gösele[5], that this is similar to the dependence of the equilibrium concentration of point defects on the crystal Fermi level in elemental semiconductors. In this it is assumed that both column III and column V vacancies can be either positively or negatively charged.It has previously been shown[5] that if this is the case, then the equilibrium defect concentrations will depend on the crystal Fermi level. A negatively charged column III or V vacancy in an n-doped structure thus encourages self-diffusion of their respective lattice atoms on their own sub-lattice. The same goes for the case of p-type doping and positively charged vacancies. By way of this hypothesis, intermixing on the column III sublattice takes place due to column III interstitials in the case of p-type doping and As-poor annealing conditions, and due to

column III vacancies in the case of n-type doping and As-rich conditions. A similar reaction is expected for the case of the dependence of column V vacancies and interstitials on intermixing on the column V sublattice. In addition to this, some of the defects created will consist of column III and V antisite defects, which will also contribute to the intermixing.

There are six possible point defects in the $Al_xGa_{1-x}As$ system:

Point defect type	**Notation**	**Energy state in crystal**
Column III Vacancy	V_{Ga}, V_{Al}	Acceptor-like
Column III Antisite	Al_{As}, Ga_{As}	
Column V Vacancy	V_{As}	
Column V Antisite	As_{Al}, As_{Ga}	Donor-like
Column III Interstitial	I_{Ga}, I_{Al}	
Column V Interstitial	I_{As}	

Table 3.3.2.1 Table of possible point defects in $Al_xGa_{1-x}As$ system and their energy-state type in the crystal structure.

From considerations of the free energies of the As vapour and the III-V crystal during annealing conditions, an expression can be derived based on the minimization of the free energy of the total material system. Furthermore, by including the concept of ionized defects, the free energy of the electronic system in the crystal can be introduced and, from this, the expression can be expanded to give the equilibrium concentration of ionized defect states. For example, in the case of strongly n-type material with a column III vacancy, where the vacancy, as seen from table 3.3.2.1 above, becomes ionized due to its acceptor-like behaviour:

$$[V_{III}^{-}] \approx C_1 P_{As_4}^{1/4} \exp\left\{-\frac{[\Delta U_V - (E_F - E_A)]}{k_B T}\right\} = [V_{III}^{x}] \exp\left[\frac{E_F - E_A}{k_B T}\right] \qquad (3.3.2.1)$$

where ΔU_V is the energy cost for the crystal to create a vacancy, E_F is the crystal Fermi energy, E_A is the acceptor level associated with the vacancy, k_B is Boltzmanns constant and T is the annealing temperature. This equation follows from the assumption that the number of charged (ionized) vacancies in the system is very much larger than the number of neutral vacancies, and is based on the charge neutrality condition:

$$[N_d^{+}] \approx n + [V_{III}^{-}] \qquad (3.3.2.2)$$

It is important to note how the position of the Fermi level governs the concentration of vacancies. The basic assumption made is that there is a large separation between the acceptor-like level of the vacancy and the Fermi level of the crystal. This separation is necessary for the crystal to gain enough energy to create and ionize a column III vacancy through an electron dropped from the conduction band to the vacancy acceptor level. Equation 3.3.2.1 shows how an increase in the Fermi level through an increase in the donor impurity concentration induces an increase in the solubility of the column III vacancy defect in the crystal.

Similarly, for the case of the donor-like defects in heavily doped p-type material, the energy difference required for the creation of the ionized impurity state is created by an electron dropping from the impurity level, e.g. the column III interstitial to the crystal Fermi level.

From the above assumptions, the self-diffusion rate of the column III atoms can be expressed in terms of the diffusion rates of column III vacancies and interstitials:

$$D_{III} = f_1'' P_{As_4}^{1/4}\left\{D_{V_{III}^{x}} + D_{V_{III}^{-}} \exp\left[\frac{(E_f - E_A)}{k_B T}\right]\right\} + f_2'' P_{As_4}^{-1/4}\left\{D_{I_{III}^{x}} + D_{I_{III}^{+}} \exp\left[\frac{(E_D - E_F)}{k_B T}\right]\right\}$$

–(3.3.2.3)

This equation contains information about the diffusion due to both neutral (e.g. V_{III}^{x}) and ionized (e.g. V_{III}^{-}) defects, and predicts the observed v-shaped dependence of diffusion constant on As pressure during annealing as well as the n- and p-type doping dependence.

The above equation only takes into account singly ionized states, but the involvement of multiply ionized states is highly probable. Evidence suggests[5] that diffusion due to Si-impurities involves triply ionized vacancy states, but it is very difficult to measure the ionization levels of native defects in III-V crystals, and their dependence on temperature is uncertain. Multiple ionization levels of the defects can be taken into account by including terms in the above equation 3.3.2.3 with a multiplication factor added to the numerator term of the exponential expressions to account for the extra energy needed for ionization, together with a constant to account for the difference in activation energy for each degree of ionization.

3.4 Impurity Introduction

The first experiments of impurity induced disordering took place using impurities introduced through thermally induced in-diffusion. Since then other methods have been investigated. These include laser melting through pulsed laser irradiation of the semiconductor sample surface, on which a thin film layer of an impurity known to induce disordering has been deposited, and ion implantation. Impurities can of course also be introduced during growth, especially those that are normally used for n-and p-type doping.

3.4.1 Diffusion

The process of thermal in-diffusion is an easy and convenient method of introducing impurities. The great advantage of IID lies in its applicability in the lateral modification of the optical and electronic properties of the III-V system. The process of thermal in-diffusion also lends itself to the patterning of disordered regions through conventional and well developed masking techniques. The mask pattern can be made using conventional

photolithography and, since this is inherently a parallel process, a high throughput can be achieved.

This type of impurity introduction can also give a one-step process without the need for subsequent annealing steps, since the temperature used for in-diffusion in some cases is the same as that used for the intermixing. The process is also by nature gentler on the crystal lattice than for instance the ion implantation method, and so is believed to leave the crystal lattice undamaged. This can be of great importance in devices where material of high optical and electrical quality is required.

The process of thermal in-diffusion is a well investigated subject, and the diffusion rates of the dopants are well known for a multitude of material systems. The diffusion depth and the concentration of the dopants can therefore easily be determined, for example assuming a constant surface concentration. The solution to the 1-D diffusion equation is [6]:

$$C(x,\ t) = C_s\, erfc\left\{\frac{x}{2\sqrt{Dt}}\right\} \qquad (3.4.1.1)$$

which is a solution of Fick's equation:

$$\frac{\delta C(x,\ t)}{\delta t} = D\frac{\delta^2 C(x,\ t)}{\delta x^2} \qquad (3.4.1.2)$$

where C is the impurity concentration expressed in terms of depth x (into semiconductor) and time t, D is the diffusion coefficient (approximated constant in the first order approximation but which does have a dependency on temperature and impurity concentration in more precise calculations), and C_s is the surface concentration.

Si_3N_4 is the mask material most commonly used for impurity in-diffusion. It can be patterned using common photolithography techniques and subsequent etching processes, both chemical (buffered hydrofluoric acid) and reactive ion etching (e.g. C_2F_6). It is also preferable to SiO_2 since it is believed to be less likely to induce vacancy-induced disordering due to its higher density. The impurity source is allowed to in-diffuse through

windows defined in the Si_3N_4 layer. In the case of silicon, this entails the deposition of a thin layer of Si (~250 Å), followed by a thicker (~1000 Å) layer of SiO_2, whereas for zinc-induced disordering, a $ZnAs_2$ source is used. After the disordering stage, the source, cap and mask are removed prior to further processing.

Although thermal in-diffusion is a convenient method of introducing impurities into the semiconductor system, it has an important disadvantage in the poor control of the impurity profile. Due to the relatively isotropic nature of the diffusion process, the lateral and vertical diffusion rates will be of the same order. It is also impossible to obtain abruptly defined transitions in the impurity profile. This is easily seen from equation 3.4.1.1, where the graded profile is described by the complimentary error function. It has been shown in section 3.3.2 that the mechanism of impurity induced disordering only can take place for relatively high (~10^{18} cm^{-3}) impurity concentrations. This means that large parts of the graded impurity profile will be of insufficient concentration to cause intermixing, whilst for instance still being large enough to cause enhanced absorption through free carriers.

3.4.2 Laser melting

The application of laser melting in the impurity introduction process facilitates a direct-write process for the disordered sample. The process has been demonstrated for Si-induced disordering[7]. A GaAs-AlGaAs sample was capped with a combination of Si (400 Å) and Si_3N_4 (900 Å), and the pattern was directly written into this cap layer using a tightly focussed cw Ar^+ laser beam. The intense laser beam was found to induce melting in the top layer of the GaAs-AlGaAs material on a micron scale, whilst not being powerful enough to induce dissociation of Si from the Si_3N_4. However, elemental Si present in the Si-Si_3N_4 layer is able to dissolve in the AlGaAs melt in concentrations sufficiently large to induce intermixing. This process was found to induce shallow intermixing (to ~ 1 μm), as the GaAs-AlGaAs system recrystallized to form $Al_xGa_{1-x}As$ in the wake of the scanned beam. The depth of the disordered region can be increased by introducing an additional annealing stage. For this, the capping layer is removed, and annealing is performed under

conditions similar to those for thermal in-diffusion of Si. This method was found[3] to increase the depth of disordering by a factor of 3. The Si diffusion process during the annealing stage is again governed by the solution to Fick's equation, but this time with the imposed condition of a limited source[2]:

$$C(x,\ t) = \frac{S}{\sqrt{\pi D t}} \exp\left(-\frac{x^2}{4Dt}\right) \qquad (3.4.2.1)$$

where S is the total amount of impurities per unit area.

The above method is versatile and eliminates processing steps needed in thermal in-diffusion. However, for commercial applications where high yield and high throughput are required, a less time consuming, more parallel process is needed. This can be achieved by substituting the scanned Ar^+ laser beam with an excimer laser system in combination with pattern masks[8]. Here the pulsed, high energy laser beam is shaped using ordinary photolithographic masks to define the Si -implanted regions. Single and multiple exposures of brief pulse duration (~20 ns), high energy (>200 mJ) laser light (XeCl, λ=308 nm) typically induced melting of GaAs-AlGaAs to a depth of 50-100 nm. This is too shallow for most device applications, and so a subsequent annealing stage is necessary for further diffusion of the Si impurities. The excimer laser induced process therefore merely constitutes a convenient way of introducing a limited source of impurities into the semiconductor system.

Obviously, the laser assisted disordering process suffers the same disadvantages as the thermal in-diffusion process, as far as the impurity profile is concerned. Furthermore, the process involves melting and subsequent recrystallization of the GaAs-AlGaAs material, which inevitably leads to thermally induced damage in the material. This may not be of great consequence if a subsequent annealing stage is used to anneal out crystal imperfections.

3.4.3 Ion implantation

The isotropic nature of the thermal in-diffusion processes makes them unsuitable for applications where abrupt interfaces are absolutely necessary or where impurity distribution profiles of high aspect ratios are needed. Ion implantation is an alternative method of introducing impurities which, due to its anisotropic nature, is far more suitable for integrating applications through the use of IID. Additionally, the ion implantation method does not suffer from the limitations imposed on impurity concentration in thermal in-diffusion processes due to the effective solubility of the impurity in the host material. Higher impurity concentrations can therefore be achieved using ion implantation, although defect clusters may form at very high concentrations. The temperature during the impurity introduction is also well controlled using ion implantation. This gives a far better control over the disordering process during the annealing stage, since both the ion concentration and the effective annealing time are more accurately known. The method also seems ideally suited for the process of IID since the damage induced by the ions on the target compositional structure will give some degree of intermixing during implantation, and since this damage has a diffusion-enhancing effect arising from the crystal imperfections that are created.

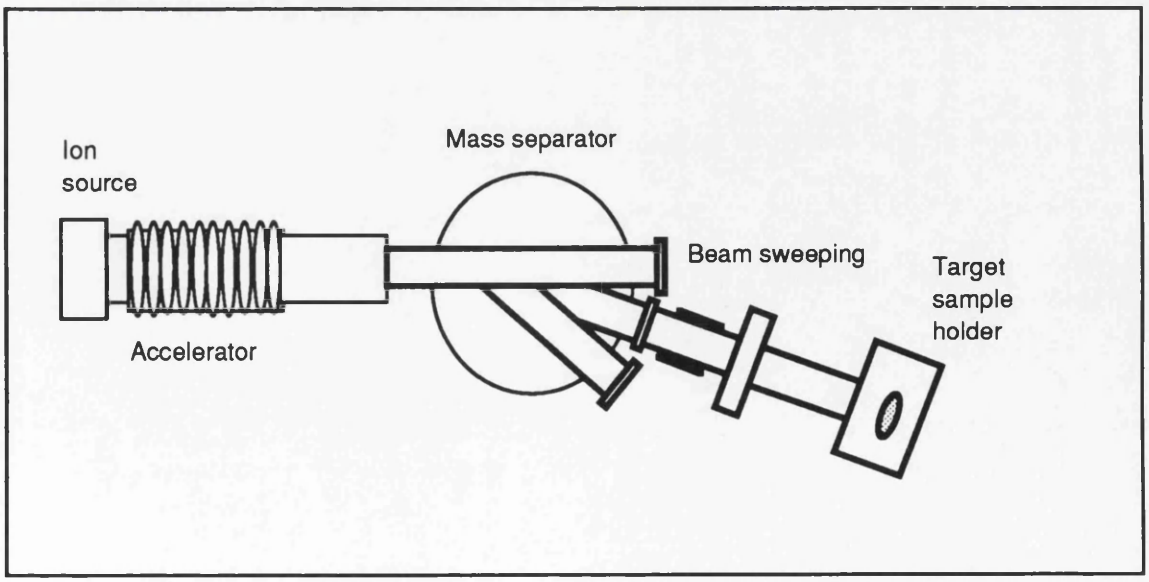

Fig. 3.4.3.1 Diagram illustrating a typical ion implanter.

Ion implantation is the bombardment of a material with high velocity, positively charged ions that have been accelerated through a large dc potential after being extracted from the source material. The ion species can be selectively screened in a mass separator placed between the acceleration stage and the target which is situated some distance from the source. A typical implanter is shown in fig.3.4.3.1

When the ions reach the target a majority penetrate the material, while some ions collide with surface atoms resulting in some reflected ions and sputtered target surface material. The ions that pass through the surface of the target continue some distance into the material before coming to a rest. The range of these ions is determined by the decelerating forces experienced by the ions due to interactions with target atoms.

3.4.3.1 The Physics of implantation

The depth distribution of ion-implanted material is governed by equations based on the energy losses suffered by the ions due to elastic and inelastic interactions with the target atoms. The most widely used method for range estimates for this purpose is based on the theories of Lindhard, Scharff and Schiøtt. It dates back to 1963 and is called the LSS range theory. A number of authors[9] have published computed range-energy tables for a variety of ion-target material systems based upon the LSS range theory, and models exist that predict the ion distribution for multilayered structures of complex material composition. The basic concepts behind the LSS theory will be described here to provide background for understanding the impurity distribution and the associated damage after ion implantation in amorphous materials.

The stopping mechanisms in an ion-target are easiest explained in terms of energy considerations. There is no single event that removes the complete kinetic energy from the incident ion. The stopping action is a continuous exchange of energy whereby the ion gradually loses its momentum and finally comes to rest on or in the vicinity of a lattice site. The differential energy loss suffered by the ion can be described by the following equation:

$$\left(\frac{dE}{dx}\right)_{loss} = \left(\frac{dE}{dx}\right)_{collision} + \left(\frac{dE}{dx}\right)_{ionization} + \left(\frac{dE}{dx}\right)_{exchange} \qquad (3.4.3.1.1)$$

where the three components all are energy dependent and vary in magnitude along the path of the ion. The energy loss term associated with collision losses is often referred to as nuclear stopping and is due to the elastic scattering of the two interacting nuclei, i.e. the ion and the target nuclei. The ionization and exchange terms are likewise referred to as electronic stopping and are inelastic interactions that can be sub-divided into the following categories:

i) direct exchange of kinetic energy through the collision between electrons bound to the ion and target nuclei

ii) excitation of target atoms, whereby strongly bound target electrons are promoted in energy

iii) excitation of weakly bound target electrons

iv) electron capture by the ion.

In general, for an amorphous target material and an ion of sufficiently high kinetic energy, the ionization loss will be at its maximum in the initial stages of the ion path, until the velocity of the ion falls below that of the electrons in the affected shell of the target material atom. As the kinetic energy of the ion is reduced, the ionization loss decreases and the collision loss progressively contributes a larger part of the total differential energy loss of the ion. Part of the explanation for this history dependent energy loss distribution originates in the ionization variation of the ion as it travels through the target material. Whereas the ionization loss is a continuous process, the collision loss is discontinuous and its contribution is therefore dependent upon the time between collisions. This is in turn related to the ionization state of the interacting particles. A degree of correlation is expected to exist between the stopping mechanisms. They are however in general treated as if they are independent of each other, justified by the large averaging over events that is involved in the penetration of a solid. In special cases, such as the qualitative analysis of single collisions or in the case of interactions with very thin targets, the correlation factor would have to be taken into consideration.

The total path length R_{total} covered by the ion can thus be expressed in terms of the difference between the energy of the ion in at entry E_0 and at its final (rest) state ($E=0$) by the use of the equation 3.4.3.1.1 for the differential loss.

$$R_{total} = \int_0^{E_0} \left\{ \frac{-\,dE}{\left(\frac{dE}{dx}\right)_{total}} \right\} \qquad (3.4.3.1.2)$$

At high energies the electronic loss dominates and the ion travels a long distance between collisions, in a straight line, and the collisions that do occur give small deflection angles. It is a very rare event that collisions at high energies give rise to noticeable deflections ($\phi>1°$)[10]. However, as the energy of the incident ion reduces, the mean time between collisions is reduced, whilst at the same time the deflection angles increase. This leads to an effective average implantation depth R_p that is much shorter than the total path length R_{total} of the ion. The early theory of Lindhard and Scharff[11] predicted that these were related by:

$$\frac{R_{total}}{R_p} = 1 + \frac{M_2}{3M_1} \qquad (3.4.3.1.3)$$

where M_1 and M_2 are the masses of the incident and recoiling atoms respectively.The later inclusion of the electronic loss considerations by Schiøtt[12] produced the more sophisticated relationship between total and projected range that forms the basis of the LSS theory.

3.4.3.2 Implant concentration profiles

The calculations based on the LSS theory give a detailed picture of the mechanics of the implantation as well as the range, distribution and damage, but it is worth noting that the scatter in projected range about the mean projected range approximates to a gaussian function. A more general, quantitative estimate of ion concentration distribution can be obtained by using this gaussian approximation. The implant concentration $N(x)$ as a function of depth into the material[5] can be estimated based on an average concentration $\overline{N(x)}$ centred at the projected range and defined as:

$$\overline{N(x)} = \frac{N_D}{(2.5\,\Delta R_P)} \qquad \text{such that} \qquad (3.4.3.2.1)$$

$$N(x) \approx \frac{N_D}{2.5\,\Delta R_P} \exp\left(-\frac{(x - R_P)^2}{\Delta R_P{}^2}\right) \qquad (3.4.3.2.2)$$

where N_D is the number of implanted ions per unit area, x is the depth into the material and R_P and ΔR_P are the projected range and projected straggle respectively. From this equation it is evident that, in order to achieve a deep, uniform implant, several implantation steps are necessary, at different implant energies and doses. The resulting form of the concentration profile is illustrated schematically in fig.3.4.3.2.1, and consists of a plateau at the desired concentration with a small variation superimposed due to the localisation of the implants.

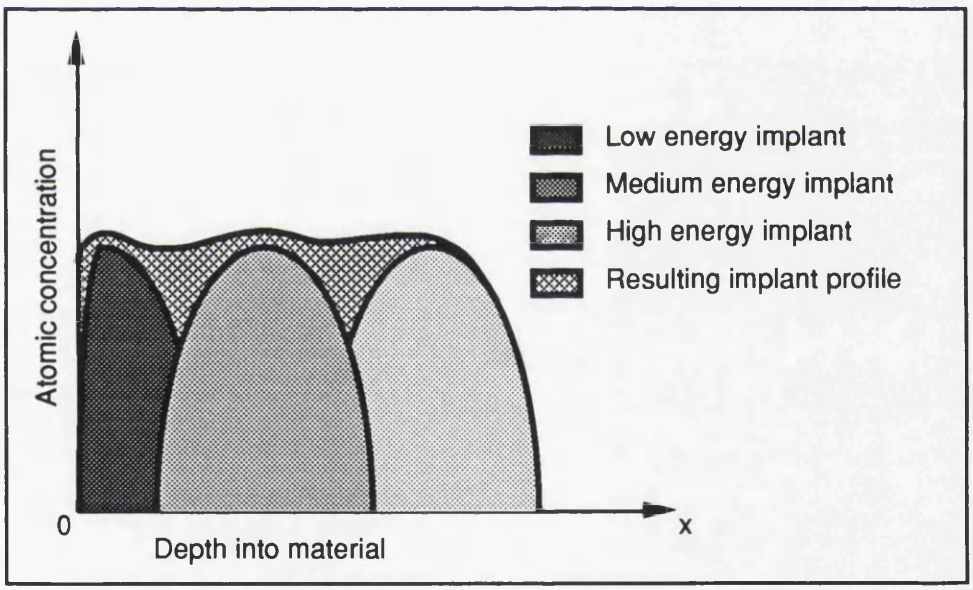

Fig. 3.4.3.2.1 Diagram illustrating effect of multiple implants

This small rippling effect can be smoothed in a separate annealing stage which is commonly performed when the crystal damage associated with implantation is annealed out. It is worth noting here that the diffusion coefficients during a subsequent annealing step will be different from normal thermal diffusion coefficients due to the damage, with an enhancement of the diffusion rate which will be dependent on the extent of vacancies and interstitials in the material. Due to this effect, it is possible to obtain absolutely flat

concentration profiles, since the largest number of vacancies and interstitials are found close to the centre of the doping distribution.

3.4.3.3 Model simulation

It is extremely difficult to derive analytical expressions for the repulsive potential between two ions that are valid for more than a limited number of ion pairs and, because these potentials are related to the effective radii of the particles under investigation, they have a large effect on calculations of scattering angles. Additionally, the dynamic nature of the collision events does not allow probing of the interaction without disturbing the system. This makes it close to impossible to accurately predict the chain of events that take place during implantation. A different approach is to make a statistical computer simulation of the system. If the initial and final states of the system are known (e.g. ion entry point, incidence and energy, and ion distributions following implantation), the chain of events inside the material can be simulated as a succession of history-dependent classical elastic collision events. The state and position of the ion can be modelled in increments until it enters its final state. The computer model described is called a Monte-Carlo simulation and generally suffers from the disadvantage that it is a time consuming process which, in turn, imposes limitations on the complexity of the model. It does however have the advantage of flexibility, enabling the exploration of the effects of variations in implantation energies, direction, binding energies etc., and allows the formation of a complete statistical picture of the state of the material after implantation. TRIM - The Transport of Ions in Matter written by J.F.Ziegler, J.P.Biersack and U. Littmark[6] is such a program which takes into account all the mechanisms considered in the LSS theory, and this program has been used in Chapter 6 to predict the impurity distribution and damage profile after implantation.

3.4.3.4 Channelling effects and radiation damage

So far only amorphous materials have been considered and, although the intentions here have been to use the Monte Carlo simulation method to illustrate the effects of implantation on crystalline material, the TRIM program used does not take channelling into account in its

calculations. Channelling effects must however be borne in mind when considering the ion distribution after implantation in an ordered structure since, for the correct orientation of the incident ion, a significant increase in the range can occur. It is obvious that some ions will experience a reduced rate of energy loss when travelling parallel to the rows or planes, since the mean free path between collisions will be very much longer than in an amorphous material, and to these ions the material will appear to have a degree of transparency. This transparency can however be extended to a larger group of ions, with only small angular deviations from the crystal lattice orientation, because the rows of lattice atoms provide potential walls which guide the ions into a mode travelling in a direction parallel to these rows, —this effect is termed channelling. Through this effect one can envisage ions entering the channelling mode after an elastic interaction with other nuclei. Fig. 3.4.3.4.1 illustrates some possible ion trajectories.

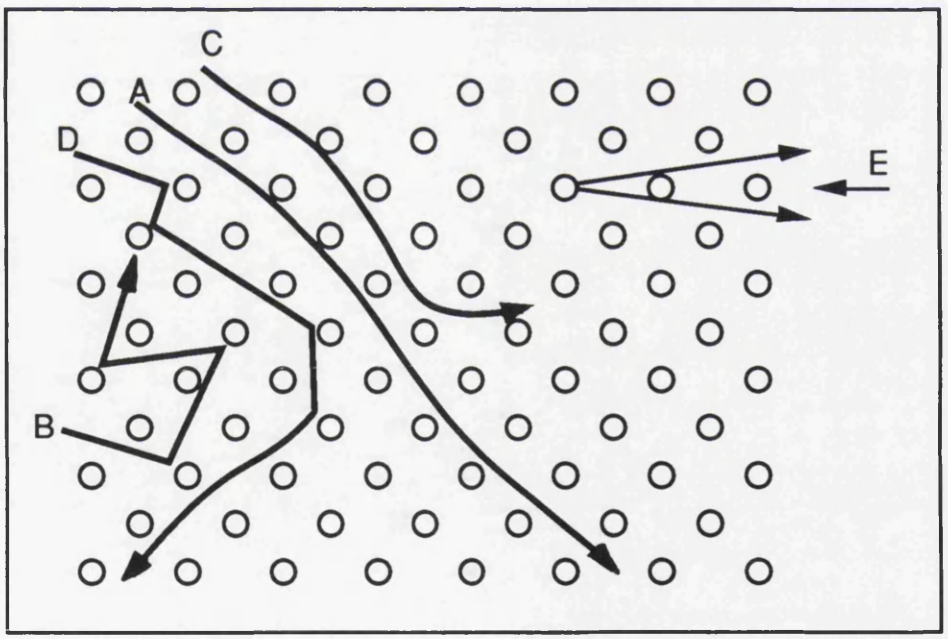

Fig. 3.4.3.4.1 Diagram showing examples of ion trajectories in a crystal lattice. Path A is a channelling direction, B is random, C is quasi-channelled, D is an ion becoming channelled following collision events and E shows the blocking direction for emitted particles.(From Townsend et al [6])

Theoretically an ion moving parallel to the crystal lattice in a perfect crystal should stay channelled forever and only experience electronic losses. In practice the ion would however at some point become unchannelled. This could be due to an elastic collision with an

interstitial atom, with atoms in the lattice in cases of lattice defect imperfections, or as a result of loss of guiding potential sufficient to maintain channelling and subsequent interaction with "sidewall" lattice atoms. (As a direct consequence of this observation, the dechannelling effect of lattice distortion has been utilized in the characterization of crystals by means of observation of the thin film transmitted ion patterns). Obviously, due to the dechannelling effects of interstitials and lattice imperfections the extent of channelling will be a strong function of the degree of damage in the material. The ion beam method of impurity introduction also creates crystal damage through collision events as well as an increased number of interstitials. This effect is termed radiation damage, and will progressively limit the amount of channelling during the implant. The thermal perturbation of the lattice atoms due to phonons created during implantation leads to additional dechannelling. For similar reasons the degree of channelling will be dependent on the history of the material, such as in the case of previous implants. Implantation with Se has for instance been shown[13] to form a damage-induced amorphous layer at the surface of the material, whereas further into the sample the damage takes the form of dislocation loops or defect clusters. Appreciable self-annealing is also thought to take place during high-energy implants, giving a complex picture for the channelling properties of the material with successive implants. The channelling efficiency is found to be greater for heavy, high energy ions[6] due to its dependence on the potential steering mechanisms, and the ions need fairly long distances to stabilize in the channelling mode (several 1000 Å), during which time they are very sensitive to the above dechannelling effects.

3.4.3.5 Implantation masks and annealing caps

The function of the implantation mask is to regionally absorb incoming ions and thereby screen the underlying material from the ion bombardment. The material used for implantation masks can in principle be any material with a suitably high stopping power and thickness, as long as it is stable during the implantation. This is a very general statement, and is just included to show that, theoretically, any material can be used for the implantation mask. The situation is of course different in reality.

The stopping power of a material is a function of the density of the material, and the more dense the material is, the higher is its stopping power. It naturally follows that the use of very low-density material would require impractically thick implantation masks. This is one of the reasons why ordinary photoresist cannot be used for the implantation masks. Also, the mask must not contain any material that would be detrimental to the substrate material if 'knocked into' the material. In high energy implants where one has the problem with obtaining sufficiently high stopping in the mask, mask material atoms can be displaced into the material under the mask. In these cases it would be necessary to check the consequence of this impurity introduction. Additionally, the mask must in most cases be made in such a way that it can be removed after the ion implantation without damaging the underlying material. This can be a problem when using high density masks such as gold on semiconductors, but it can be solved by predepositing a thin layer of e.g. silicon dioxide prior to the gold evaporation. The mask material must also enable patterning, and this is again a potential problem in the use of high density masks on semiconductors. The solution to that problem is to use lift-off procedures to define the pattern. The two latter techniques are described more fully in chapters 4 and 7.

Silicon dioxide or silicon nitride are often quite suitable as mask materials for implantation at lower energies. They do not have very high stopping powers, but they can be deposited in quite thick layers without making post-implant removal impossible. In this respect SiO_2 is the better candidate, since the etch rate of Si_3N_4 is very much lower ($\approx$1/20) than that of SiO_2. Due to the relatively low stopping powers, implantation masks made in these materials have severe limitations on dimensions in the sub-micron range, and are more suitable for masking large, uniform areas. But these materials have other uses too. SiO_2 and Si_3N_4 are often used for capping layers in the post-implant annealing step. This step is intended to anneal out the ion-induced damage to the material and takes place at high temperatures. In (Al)GaAs structure there is a need to stop As-desorption from the surface, and a thin capping layer prevents excess As dissociation from the surface layer.

The annealing step can be a very critical step in the fabrication process. Uncritical use of capping layers can lead to extensive damage to the material. This is especially the case when using Si_3N_4 for the capping layer. Si_3N_4 might be good for stopping As-desorption, but the expansion coefficient is quite different from that of GaAs, and this readily produces cracking and crystal damage to the GaAs material in the rapid thermal ramps of the anneal cycle. As incorporating in the capping material also seem to reduce its etch rate substantially (buffered hydrofluoric acid is used for removal, and this is selective with respect to the $Si_xN_yO_z$/GaAs system). The extended etching time needed for cap removal can damage the GaAs regionally, especially in cases when the cap cracks due to thermally induced stress. Multilayer cap deposition can reduce the stress in the capping layer. This technique has been utilized in semiconductor growth of strained layer systems thicker than the critical thickness of the material. By depositing alternating layers of capping material with different expansion coefficients in a high-low-high-low manner, the overall stress in the film can be reduced, and the capping layer can be made thicker.

3.5 Summary

IID is a complex process that is not yet fully understood. The current understanding has been presented.

Impurities enhance the diffusion rate of column III and column V components of the III-V material system, so that periodic structures such as quantum wells can be selectively intermixed. The process can transform quantum wells into bulk-like material with a composition equal to the material average of the periodic structure.

Most impurities that have been found to induce intermixing are electrically active dopants in the III-V system at room temperature. Two of the exceptions are boron and fluorine. These have the advantages that they can be used to make regions of lower loss and higher electrical resistivity than the electrically active impurities.

Several methods exist for introducing impurities. Ion implantation is one of these, and has many advantages, for instance that it enables formation of deep implants of high concentrations and with abrupt interfaces. The impurity concentration profile after implantation can be measured using SIMS and/or modelled. The most involved models are based on the LSS theories. A Monte Carlo simulation program called Trim-91 exists that can be used to model the distribution of ions and damage, as well as ion trajectories and defect formation.

The choice of masking material for the implantation mask is dependent on the energy of the implant and on considerations such as expansion coefficients and etch selectivity between mask and target material. SiO_2 and Si_3N_4 are regarded as likely candidates for low-energy implants.

[1]W.D. Laidig,N.Holonyak, Jr., M.D. Camras, J.J. Coleman, P.D.Dapkus, Appl. Phys. Letters 38,776,1981

[2]Y. Hirayama, Y. Suzuki, H. Okamoto,"Ion-Species dependence of interdiffusion in Ion-Implanted GaAs-AlAs Superlattices", Journal of Applied Physics Vol.24, No.11 1985 pp 1498-1502.

[3]M.O'Neill, A.C. Bryce, J.H. Marsh, R.M. De La Rue, J.S. Roberts, C. Jeynes, "Multiple quantum well optical waveguides with large absorption edge blue shift produced by boron and fluorine impurity induced disordering." Appl. Phys. Letts.55 (14) 1989 pp 1373-1375.

[4]J.H. Marsh, S.G. Ayling, A.C. Bryce, S.I. Hansen, S.A. Bradshaw," Neutral impurity disordering of III-V QW structures for optoelectronics", Proceedings of U.S./U.S.S.R. Joint Soviet-American Workshop on the Physics of Semiconductor Lasers, Leningrad May 1991, Am.Inst.of Physics Conf.Proc.240 pp 111-129.

[5]D.G.Deppe,N. Holonyak Jr., "Atom diffusion and impurity-induced layer disordering in quantum well III-V semiconductor heterostructures", J.Appl. Phys. Vol.64, 1988, pp R93-R113.

[6] S.M.Sze,"Physics of semiconductor devices",J.Wiley &Sons, NY 1981, pp 66-67.

[7] J.E.Epler, R.D. Burnham, R.L. Thornton, T.L. Paoli, M.C. Bashaw,"Laser induced disordering of GaAs-AlGaAs superlattice and incorporation of Si impurity.",Appl. Phys. Lett. 49(21) 1986, pp 1447-1449.

[8] J.E.Epler, R.L. Thornton, W.J. Mosby, T.L. Paoli, "Low threshold buried-heterostructure quantum well lasere by excimer laser assisted disordering.",Appl.Phys.Lett. 53 (16), 1988, pp 1459-1461.

9 P.D. Townsend, J.C. Kelly, N.E.W. Hartley, "Ion Implantation, Sputtering and their Applications", Ch.2 pp 7-42 , Academic Press Inc.(London) Ltd.1976.

10 J.F.Ziegler, J.P.Biersack, U. Littmark, "The stopping and range of ions in solids", Pergamon Press 1985. Ch.3 pp 66-108.

[11] Lindhard, J., Scharff, M., Phys.Rev. 124 1961 p128.

[12]Lindhard, J., Scharff, M., Schiøtt, H. E., Kgl. Danske Vid. Selsk. Matt.Fys. Medd. 33, No. 14 1963

[13]J. Ralston, G.W. Wicks, L.F. Eastman, B.C. De Cooman, C.B. Carter,"Defect structure and intermixing of ion-implanted $Al_xGa_{1-x}As$/GaAs superlattices." J.Appl. Phys. 59 (1) 1986 pp 120-123.

CHAPTER 4

EFFECTIVE INDEX OF SEMICONDUCTOR WAVEGUIDES

4.1 Introduction

This chapter is concerned with the methods for deriving the effective waveguiding refractive index of a particular semiconductor structure, and shows how measurements can be performed to quantify the modal and material indices of such a structure.

4.2 Experimental determination of the material refractive index of semiconductors

Due to the large absorption and high refractive indices typical of III-V materials only a few of the numerous methods for measuring refractive indices of optical materials can be used. The refractive indices of glass waveguides can, for instance, be measured by means of index-matching oils through experiments based on input and output coupling, loss of guiding and total internal reflection. This is possible because glasses have relatively low refractive indices. No suitable index-matching liquid exists for the high values of refractive index (typically > 3) of III-V semiconductors.

The two most commonly used methods for measuring refractive indices in the III-V semiconductor system are spectroscopic ellipsometry[1] and reflectometry[2]. Both methods have been used to determine the refractive index of $Al_xGa_{1-x}As$ for different Al-fractions x, and they enable measurements to take place beyond the absorption edge of the material.

In the case of spectroscopic ellipsometry, a rotating analyzer spectroellipsometer is used to obtain data of the complex reflectance ratio of the surface of a layered structure semiconductor material. The data obtained take the form of polarisation angles from which amplitude and phase of the reflectance are calculated. If the thickness of the layer is known, the material refractive index can be deduced. The same apparatus is also commonly used

for film thickness measurements in cases where the refractive indices of the film and substrate are known.

Reflectometry relies upon a comparison between the sample surface reflectivity and a mirror of known reflectivity. When the reflectivity is known, the refractive index of the material can be obtained using Fresnel's equation for the the reflectivity R:

$$\overline{n} = \left(\frac{1 + R^{\frac{1}{2}}}{1 - R^{\frac{1}{2}}} \right) \qquad (4.2.1)$$

$\overline{n}$ here signifies that the contribution from the extinction coefficient k in the complex refractive index expression $\hat{n} = n - jk$ has been left out due to its small contribution[2].

The disadvantage inherent in these two methods is that they both assume a perfectly abrupt and film-free surface. This is never obtainable in practice, due to the nonuniform compositions inherent to the growth techniques (particularly in the case of liquid phase epitaxy (LPE)) and the reactiveness of $Al_xGa_{1-x}As$ which results in a thin layer of oxide forming on the surface in a very short time. These factors could be compensated for if all the factors of the surface region were known, such as its abruptness and grading factor and the exact thickness and dielectric function of the surface film, but careful surface preparation is in general preferred in order to make such contributions negligible.

4.3 Two-dimensional waveguide structures

In planar geometry optical structures, the simplest waveguiding structure is the 2-dimensional (2-D) or slab waveguide. This structure consists of a finite thickness layer (guide) of refractive index higher than those of the surrounding (cladding) layers by which it is bound. Light launched into the structure will then propagate in one or more modes bound in one transverse direction given that certain criteria are fulfilled, such as a sufficiently large refractive index step between between guiding and cladding layers and a large enough guide thickness. The effect of confinement of the guided light by the

waveguiding structure results in the guided mode seeing a different refractive index from that of the guiding region itself. The refractive index experienced by the mode is frequently referred to as the modal or effective index of the waveguide.

2-D waveguides can be sub-divided into two groups depending on the relative value of the refractive index difference between the cladding layers. If the cladding layers have the same permittivity, the structure is termed a symmetrical slab waveguide, whereas if they are different, the structure is an asymmetrical slab waveguide. These two structures have different dispersion relations, which for instance in the case of the symmetrical slab waveguides lifts the restrictions on guide thickness with respect to cut-off of the first (zero-order) guided mode. Consider for instance the case of a three-layer slab waveguide as described above. Let the refractive index of the guide layer be n_2, and the refractive indices of the upper and lower cladding layers n_3 and n_1 respectively. This structure will act as a guide for the light in the middle layer only if $n_2 > n_1, n_3$ (there are however also other conditions that have to be satisfied, and these will be looked at later). The waveguide is symmetrical if $n_1 = n_3$ and asymmetrical if $n_1 \neq n_3$. The waveguiding condition and dispersion relationship of this structure can be evaluated both from a ray treatment approach and as a solution derived from Maxwell's equation in an electromagnetic field approach.

The following is a description of the technique used to evaluate the effective index of a three- or four layer slab waveguide in the computer program FourLay written by B. Bhumbra[3] and used in Chapter 6 of this thesis. The technique used here is the transverse resonance condition for constructive interference within a slab waveguide. The theory is treated in detail elsewhere[3,4].

The simplest form of the technique considers the three layer waveguide structure above, where a layer of higher-index material of thickness d with its normal orientated in the x-direction is sandwiched between two layers of lower refractive index. Basic textbook theory using Maxwell's equations can be used to show that a plane-wave mode of light travelling parallel to the layers (the z-direction) and supported by this waveguide structure,

has electromagnetic fields in the guiding layer (region 2) of a standing-wave nature, whereas the fields in the surrounding regions (1 and 3) are exponentially decaying (evanescent). Following this line of reasoning, the electric and magnetic fields (E and H) of a plane wave travelling along z are defined by:

$$\begin{Bmatrix} E(x,y,z) \\ H(x,y,z) \end{Bmatrix} = \begin{Bmatrix} E(x,y) \\ H(x,y) \end{Bmatrix} e^{-jk_z z} \tag{4.3.1}$$

where k_z is the propagation constant in the z -direction. Since a slab waveguide configuration is considered, the field variation is independent of y. It can be shown[5] that for TE modes the fields take the form:

$$E_y(x,z) = \begin{Bmatrix} A_1 e^{-\alpha_{1x} x} \\ A_2 \cos(k_{2x} x + \psi) \\ A_3 e^{+\alpha_{3x} x} \end{Bmatrix} e^{-jk_z z} \qquad \begin{vmatrix} x > d/2 \\ |x| \le d/2 \\ x < -d/2 \end{vmatrix} \tag{4.3.2a}$$

and

$$H_z(x,z) = \begin{Bmatrix} \dfrac{-j\alpha_{1x}}{\omega\mu_1} A_1 e^{-\alpha_{1x} x} \\ \dfrac{-jk_{2x}}{\omega\mu_2} A_2 \sin(k_{2x} x + \psi) \\ \dfrac{+j\alpha_{3x}}{\omega\mu_3} A_3 e^{+\alpha_{3x} x} \end{Bmatrix} e^{-jk_z z} \qquad \begin{vmatrix} x > d/2 \\ |x| \le d/2 \\ x < -d/2 \end{vmatrix} \tag{4.3.2b}$$

where the transverse wavenumbers are defined by $\alpha_{ix} = \sqrt{k_z^2 - \omega^2 \mu_i \varepsilon_i}$ and $k_{2x} = \sqrt{\omega^2 \mu_2 \varepsilon_2 - k_z^2}$, A_i are the field amplitudes, μ_i and ε_i are the permeabilities and permittivities of the layers respectively, ω is the angular frequency and ψ is a phase constant defined by the boundary conditions at $\pm d/2$.

The boundary conditions are that the tangential fields must be continuous at the interfaces at ±d/2, and this yields:

$$E_{\tan}:\ A_1 e^{-\alpha_{1x} d/2} = A_2 \cos(k_{2x} d/2 + \psi) \qquad \text{and} \tag{4.3.3a}$$

$$H_{\tan}:\ A_1 e^{-\alpha_{1x} d/2} = \frac{\mu_1 k_{2x}}{\mu_2 \alpha_{1x}} A_2 \sin(k_{2x} d/2 + \psi) \tag{4.3.3b}$$

for the +d/2 interface. Eliminating A_1 and A_2 gives the following expression:

$$\tan(k_{2x} d/2 + \psi) = \frac{\mu_2 \alpha_{1x}}{\mu_1 k_{2x}} \tag{4.3.4}$$

and, matching the boundary conditions at -d/2 the same way gives:

$$\tan(k_{2x} d/2 - \psi) = \frac{\mu_2 \alpha_{3x}}{\mu_3 k_{2x}} \tag{4.3.5}$$

these two equations can be rewritten as a sum of angles using the periodicity of the tan function $\tan(x) = \tan(x \pm n\,\pi)$ $n = 0,1,2,\ldots$, giving:

$$k_{2x} d/2 + \psi = \tfrac{1}{2}\Phi_1^{TE} \pm n\pi \qquad \text{and} \qquad k_{2x} d/2 - \psi = \tfrac{1}{2}\Phi_3^{TE} \pm m\pi \tag{4.3.6}$$

where $m,n = 0,1,2,\ldots$

$$\Phi_1^{TE} = 2\tan^{-1}\left(\frac{\mu_2 \alpha_{1x}}{\mu_1 k_{2x}}\right) \qquad \text{and} \qquad \Phi_3^{TE} = 2\tan^{-1}\left(\frac{\mu_2 \alpha_{3x}}{\mu_3 k_{2x}}\right) \tag{4.3.7}$$

Eliminating ψ gives the relation:

$$2k_{2x} d - \Phi_1^{TE} - \Phi_3^{TE} = 2p\pi \qquad p = 0,1,2,\ldots \tag{4.3.8}$$

which is the general guiding condition for TE modes in a waveguide. The TM mode case yields a similar equation for the guiding condition:

$$2k_{2x} d - \Phi_1^{TM} - \Phi_3^{TM} = 2p\pi \qquad p = 0,1,2,\ldots \tag{4.3.9}$$

where:

$$\Phi_1^{TM} = 2\tan^{-1}\left(\frac{\varepsilon_2\alpha_{1x}}{\varepsilon_1 k_{2x}}\right) \qquad \text{and} \qquad \Phi_3^{TM} = 2\tan^{-1}\left(\frac{\varepsilon_2\alpha_{3x}}{\varepsilon_3 k_{2x}}\right) \tag{4.3.10}$$

There is a well known phenomenon named the Goos-Haenchen shift that results in an effective thickness of the waveguide that differs from its physical thickness. The Goos-Haenchen shift is an angularly dependent phaseshift that is associated with reflections at dielectric boundaries.

The effective thicknesses d_{eff}^{TE} and d_{eff}^{TM} as seen by the TE and TM modes are given by[6]:

$$d_{eff}^{TE} = d + \frac{1}{\alpha_{1x}} + \frac{1}{\alpha_{3x}} \tag{4.3.11}$$

and

$$d_{eff}^{TM} = d + \frac{q_1}{\alpha_{1x}} + \frac{q_3}{\alpha_{3x}} \tag{4.3.12}$$

where

$$q_1 = \left[\frac{k_{2x}^2 + \alpha_{1x}^2}{k_{2x}^2 + \left(\frac{\varepsilon_2}{\varepsilon_1}\right)^2 \alpha_{1x}^2}\right]\frac{\varepsilon_2}{\varepsilon_1} \qquad \text{and} \qquad q_3 = \left[\frac{k_{2x}^2 + \alpha_{3x}^2}{k_{2x}^2 + \left(\frac{\varepsilon_2}{\varepsilon_3}\right)^2 \alpha_{3x}^2}\right]\frac{\varepsilon_2}{\varepsilon_3} \tag{4.3.13}$$

for the two interfaces at ±d/2.

For the GaAs-AlGaAs system in particular and most materials suitable for integrated optics in general, $\varepsilon_1/\varepsilon_2 \approx 1$ ($\varepsilon_3/\varepsilon_2 \approx 1$) which gives $q \approx 1$ and a thickness increment due to the Goos-Haenchen shift close to the 1/e penetration depth of the evanescent fields[6].

To simplify the expressions for the guiding condition and to get rid of some suffixes, the dispersion relations are rewritten as:

$$k_1^2 = \beta^2 - n_1^2 k_0^2 \qquad k_2^2 = n_2^2 k_0^2 - \beta^2 \qquad k_3^2 = \beta^2 - n_3^2 k_0^2 \tag{4.3.14}$$

where k_i are the transverse wavenumbers and β is the longitudinal wavenumber. The layers are assumed to have the same permeability, and the identity $k_0 \equiv \omega\sqrt{\mu\varepsilon_0}$ has been used for the free-space wavenumber.

The criteria for constructive interference in the waveguide, and hence guiding, can now be expressed as:

$$k_2 d_2 = \tan^{-1}\left[\frac{\eta_1 k_1}{\eta_2 k_2}\right] + \tan^{-1}\left[\frac{\eta_3 k_3}{\eta_2 k_2}\right] + M\pi \qquad M = 0,1,2,\ldots \tag{4.3.15}$$

for both the TE and TM modes, using the weighting factor η_i to account for the additional terms in the TM case:

$\eta_i = 1$ for TE modes in the waveguide, and (4.3.16a)

$\eta_i = \frac{1}{n_i^2}$ for TM modes. (4.3.16b)

The refractive index for layer i is n_i, β and k_0 are the modal and free space propagation constants respectively, d_i is the thickness of layer i and M is the mode number. The effective index n_{eff} of a guided mode is given by :

$$\beta = k_0 n_{eff} \tag{4.3.17}$$

The modal index of a mode in a slab waveguide of known composition and dimensions can be obtained by numerically solving equation 4.3.15. The program FourLay does exactly this, but for a four layer structure. This is achieved by adding an additional term:

$$k_4^2 = \beta^2 - n_4^2 k_0^2 \tag{4.3.18}$$

to the above collection of equations. The constructive interference criterion now takes the form[3]:

$$k_2 d_2 = \tan^{-1}\left[\frac{\eta_1 k_1}{\eta_2 k_2}\right] + \tan^{-1}\left[\frac{\eta_3 k_3}{\eta_2 k_2} \cdot \frac{\exp(k_3 d_3)(\eta_3 k_3 + \eta_4 k_4) - \exp(-k_3 d_3)(\eta_3 k_3 - \eta_4 k_4)}{\exp(k_3 d_3)(\eta_3 k_3 + \eta_4 k_4) + \exp(-k_3 d_3)(\eta_3 k_3 - \eta_4 k_4)}\right] + M\pi \quad (4.3.19)$$

From the above it can be seen that the value of the effective index of a guided mode lies somewhere in the region $n_1, n_3 < n_{eff} < n_2$.

4.4 Three dimensional waveguides

A three-dimensional dielectric waveguide is one where propagating modes are bound in both transverse directions, so-called because this confinement makes it necessary to consider field variations in all three orthogonal directions. In other words, the optical fields are confined in both x- and y-directions for a wave travelling in the z-direction. The main types of the several variants of 3-D waveguides are shown in fig.4.4.1, and are the strip and buried strip (a), rib or ridge (b) and strip loaded waveguides (c). The guiding mechanism of the strip and embedded strip structures can be analysed in the same manner as for the 2-D waveguide using the simplified view of the 'bouncing beam' concept, since the guides in these cases are totally surrounded by regions of lower permittivity. For the other types of structures however, the apparent lack of intuitively observable transverse confinement in the lateral direction necessitates the use of a slightly differing concept, such as the effective index method.

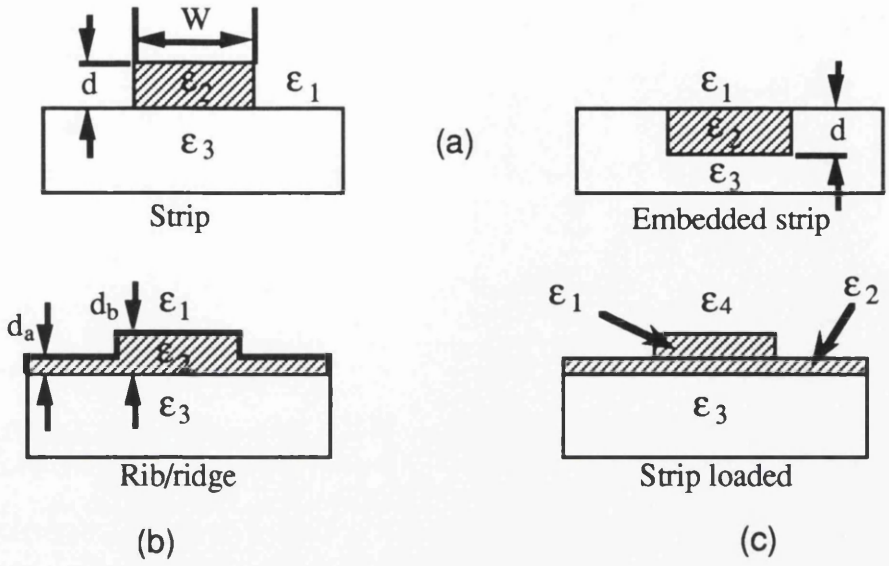

Fig.4.4.1 Diagram showing the main types of threedimensional semiconductor waveguides (from D.L.Lee[5])

The 3-D waveguides are of particular importance for optical integrated circuits (OIC) due to their ability to maintain high optical irradiances over relatively long distances and because they facilitate a method to obtain single mode guiding through the proper choice of the confinement parameters.

4.4.1 Numerical methods for the effective index of waveguides

In the above treatment of the slab or 2-D waveguide, one of the basic assumptions made was that there was no variation of the electric or magnetic fields in the transverse direction (y-direction). For the 3-D waveguide this is not the case, and an exact analytic solution is no longer possible. To obtain the effective indices of these types of waveguides numerical techniques are used. Below is a short description of some of the methods applicable to the semiconductor waveguide system.

4.4.1.1 Effective Index Method

The effective index method (EIM) is basically an extension to the three- or four-layer resonance method described for the slab waveguide above. The basic concept of the method is to divide the 3-D waveguide into three sections; one each for the regions either side of the guide region, and one for the guide region itself. The transverse resonance

method is applied to each of these regions in turn. The effective (slab-) indices obtained are then used to calculate the effective index of a hypothetical slab structure consisting of a guide layer of thickness equal to the width of the 3-D guide and refractive index equal to the effective index obtained for the guide-region slab waveguide above. The structure is bound either side by cladding layers of indices given by the effective (slab-) indices found for the side regions as explained above. The polarisation for this second calculation is chosen as the opposite of the one used for the first (slab) effective index calculation to conform with the choice of polarisation of the light travelling in the guide.

The EIM is well suited for calculating the effective index of buried, planar surface waveguides, but does not work well with raised ridge waveguides. This is mainly because the method relies on breaking down the transverse field variation into rapidly and slowly varying component functions in an orthogonal system, and that this assumption becomes invalid in the case of the discontinuity resulting from the surface contour. It has also been found[7] that the EIM overestimates the propagation constant, especially in the case of modes that are close to cut-off. This error becomes smaller with increasing optical confinement.

4.4.1.2 Finite Difference Method

The finite difference method (FDM) is another approach that is particularly useful for numerically solving the field distribution and effective index of waveguiding structures. Its matrix formulation makes it a natural candidate for the vectorised computational powers of computers.

The method works as follows. A representation of the cross-section of the waveguide is enclosed in a rectangular box of finite dimensions (X,Y), and with boundaries at which the modal field ϕ=0. The area inside the box is divided into a fine mesh, defining cells in which the dielectric function is assumed constant. The basis for the FDM is that an optical mode in the waveguide must satisfy Helmholtz' equation[5] for any point in the waveguide:

$$\nabla_{xy}^2\boldsymbol{\phi} + \left[k^2\boldsymbol{\varepsilon}_r(x,y) - \boldsymbol{\beta}^2\right]\boldsymbol{\phi} = 0 \qquad (4.4.1.2.1)$$

where k is the wavenumber, β is the propagation constant of the mode and $\varepsilon_r(x,y)$ is the permittivity distribution. The object is therefore to determine $\phi(x,y)$ and β for a given permittivity distribution. This is done in a stepwise process. Firstly, an initial guess for the field distribution is discreticised and assigned to meshpoints. This initial guess can for instance be obtained from use of the effective index method. Discretisation of the Helmholtz equation and the finite-difference representation of its derivative are thereafter used to describe the field at any one meshpoint in terms of the field values at the adjacent meshpoints. Lastly, the continuity of the modal field and its derivative are used in conjunction with the boundary conditions in repetitive iteration procedures for both mesh directions. The convergence of these iteration procedures yields a field distribution that approximates the exact solution to an estimated accuracy defined in the reiterative subroutines.

The inaccuracies associated with this method arise mainly from the approximate form of the differential equations and from use of boundary conditions at infinity being used on a finite-sized system (box). The accuracy can be increased by ensuring that there are sufficiently many mesh points at any point in the box, and that the box is large enough that the boundary conditions stay valid. If a rectangular, uniform grid is used, this would imply a massive cost in terms of computing time, and excessive calculations at points where the field remain essentially unchanged. The solution to this is the use of a dynamic grid, whereby a relatively large mesh spacing is used in areas of slow variation in ϕ, and a progressively decreasing mesh spacing is used as the variation in ϕ becomes more rapid.

4.4.1.3 Finite Element Method

The finite element method (FEM) is similar to the FDM in the discretisation of the problem. The two methods share the approach of meshpoint assignment but, whereas the FDM works with a finite number of difference values at each meshpoint, the FEM uses a finite number of trial functions assigned to the meshpoints. An approximation to the exact solution is obtained from combinations of these trial functions. The trial functions can be

special to the the particular problem or they can be general functions such as piecewise polynomials. The latter case particularly lends itself to numerical computation, in that the computer itself can generate the trial functions to fit the geometry of the problem and solve for these. The use of case-peculiar trial functions may on the other hand be impractical and difficult to implement in computer models. The end-product of the finite-element computation is again an approximation to the real solution at the meshpoints.

The finite element-method is more exact than the finite difference method[8], but it is slower and more costly in terms of computing time. The finite difference method is faster, easier to to program and more suited for initial value problems.

4.5 Direct determination of effective index

It has been shown above how the material refractive indices for the layers in a waveguide structure can be used to determine the effective refractive index of a mode by the use of numerical methods. This is normally the approach used to design dielectric waveguide systems.In multiple quantum well (MQW) waveguide systems however, the strong nonlinearities of the MQW's together with a scarcity of data and inherent uncertainties in the quantum well uniformity and quality makes effective index calculations difficult and results suspect. In these cases the effective index of a waveguide structure may be determined directly or indirectly using various techniques, –for instance by measuring the mode spacing (especially of laser structures) in a Fabry-Perot cavity, or by measuring the absorption of the waveguide and performing a Kramers-Krönig transformation on the results to give the real part of the permittivity. The most accurate methods are however those that derive the refractive index from angular data found from the mode matching conditions between (unguided) free-space and guided modes with the aid of some intermediate medium, i.e. the techniques of prism and grating coupling.

4.5.1 Prism coupler

The prism coupler technique is one of the most important diagnostic tools for characterizing dielectric waveguides in terms of their propagation properties. Unfortunately one of the requirements for this technique to work is that the refractive index of the prism is higher than that of the waveguide. This requirement in general precludes the use of this technique on III-V semiconductors. The technique does, however, have enough similarities with the grating coupler technique, both in terms of the analytical interpretation of the physics involved and the experimental procedure for waveguide characterization to warrant it being mentioned here.

In its simplest form, the prism coupler consist of a high-refractive-index prism placed in close proximity to a slab waveguide. The efficiency of the coupler depends strongly on the size of the resultant air gap between the waveguide and the coupler. For a uniform gap the optimum theoretical coupling efficiency is ≈81.4 %[9]. The use of a nonuniform gap could theoretically increase this efficiency to 100%. This technique is therefore by far the most efficient for waveguide mode excitation, avoiding the problems of mode-size mismatch and Fresnel-reflection-limited transmission experienced in, for instance, end-fire coupling.

A single prism can be used for both input and output coupling, where the explanation for the output coupling effect follows from that of the input coupling by reciprocity. The most usual set-up does however involve two separate but identical prisms for the input and output coupling separated by some distance. In the input coupler, an optical beam is passed through the prism onto its base at an angle exceeding the critical angle. The evanescent fields extend outside the prism, through the air-gap and into the waveguide. Here the resulting 'wavelets' add up in phase to give rise to a guided mode in the waveguide assuming a phase-matched waveguide-supported mode exists. In terms of light ray theory, this transfer of power through an air gap from a beam exceeding the critical angle is labelled frustrated total internal reflection. The condition for coupling light of wavenumber k_p into a waveguide mode of wavenumber k_m is given as:

$$k_p \sin \theta_i = k_m \sin \theta_m \qquad (4.5.1.1)$$

where θ_i is the angle of incidence of light in the prism medium with respect to the normal of the waveguide surface and θ_m is the bounce angle for the m^{th} waveguide mode. This is simply the phasematching condition of the prism coupler and, for measured values of the reciprocal output coupling angles at the second prism for a pair of excited modes (e.g. m=0 and m=1), the material refractive index n_2 and thickness d of the guide are easily obtained from the modal indices of the pair of modes $(n_{eff})_m$ using:

$$k_m \sin \theta_m = (n_{eff})_m \qquad (4.5.1.2)$$

and

$$k_0 d\left[n_2^2 - (n_{eff})_m^2\right] = \psi_m[n_2, (n_{eff})_m] \qquad (4.5.1.3)$$

where

$$\psi_m = m\pi + \tfrac{1}{2}\phi_1[n_2, (n_{eff})_m] + \tfrac{1}{2}\phi_3[n_2, (n_{eff})_m] \qquad (4.5.1.4)$$

and ϕ_1 and ϕ_3 are the phase shifts due to total internal reflection at the upper and lower interfaces of the waveguide. This set of equations does not give any analytical solution for n_2 and d, but these values are easily found by iterative methods.

4.5.2 Grating couplers

Optical gratings, —fine periodic structures with periods comparable to optical wavelengths— have proved to be extremely useful and versatile components in waveguide structures. Only the input/output grating coupler is considered here, but gratings are also used for codirectional couplers (e.g. used for mode conversion: up-down, TE-TM etc.), contra-directional couplers (e.g. used in distributed feedback for lasers and in band-stop filters) and for coplanar couplers (e.g. used for guided-beam splitters). The various types of grating couplers have been treated in detail by a number of authors[10], most using the

concept of coupled mode equations for the theoretical aspect. Grating couplers for input/output coupling have likewise been examined in detail elsewhere[6,11].

4.5.2.1 Phase matching

The prism coupling method proves unsuitable for most semiconductor material systems due to their high refractive indices and large absorption. For efficient excitation of waveguide modes, the phase matching between the free-space light and the guided mode in a semiconductor waveguide therefore has to be achieved by other means. A convenient method of achieving this efficient mode matching was demonstrated by M.L. Dakss et al in 1970[12], where a phase grating defined directly in the thin film waveguide provided the incremental horizontal wavevector component needed for the phase matching.

The exact theory of wave-grating interactions is rather involved, but the underlying physics is readily understood. Consider, for instance, the case of a two-dimensional waveguide with light propagating in the x-direction and with its normal in the y-direction. A grating of pitch Λ is defined in the top layer of the waveguide structure, and light of free-space wavelength λ is incident on the grating at an angle ϕ. The horizontal component $\mathbf{k_x}$ of the wave vector $\mathbf{k}$ of the incident light is then, in terms of the free space propagation constant k_0, given by:

$$k_x = k_0 \sin \phi \qquad \text{where} \qquad k_0 = \frac{2\pi}{\lambda_0} \qquad (4.5.2.1.1)$$

The propagation constant of a guided mode in the waveguide is given by:

$$k_g = \frac{2\pi}{\lambda_g} = \frac{2\pi}{\lambda_0} n_{eff} \qquad (4.5.2.1.2)$$

where n_{eff} is the effective index of the waveguide at wavelength λ_0. The grating is now assigned a Bragg wave vector k_B given by:

$$k_B = \frac{2\pi}{\Lambda} \qquad (4.5.2.1.3)$$

The incident light can now be coupled to the waveguide mode provided:

$$k_0 \sin \phi + mk_B = k_g \qquad (4.5.2.1.4)$$

In terms of quantum mechanics and the concept of momentum changes due to the interaction between the optical wave and the grating, this equation describes how the incremental horizontal component of momentum needed for phase matching between the incident and guided light is supplied by integer multiples of the momentum associated with the grating structure.

The above equation can be written as:

$$\frac{2\pi}{\lambda_0} \sin \phi + m\frac{2\pi}{\Lambda} = \frac{2\pi}{\lambda_0} n_{eff} \qquad (4.5.2.1.5)$$

where m is the order of diffraction (m = 0,1,2,...). From this it naturally follows that the effective index of the guided mode in the waveguide structure can be expressed in terms of the grating pitch Λ and the input coupling angle ϕ:

$$n_{eff} = \sin \phi + m\frac{\lambda_0}{\Lambda} \qquad (4.5.2.1.6)$$

4.5.2.2 Diffracted orders and power distribution

The relationship between guided and radiative modes that follows from a grating coupler being used as either an input or an output coupler can be analysed using the Lorentz reciprocity theorem. From this it follows that when a grating is used as an input coupler, the fraction of incident power coupled to a waveguide mode from an input beam at a given angle with the grating is equal to the the fraction coupled out of the waveguide from the same waveguide mode and at the same angle with the grating for the case where the grating is used for output coupling, but multiplied by a mismatch function which accounts for the difference between the beam profile and the aperture function of the grating[9]. Hence, the

properties of a grating input coupler can be fully characterized from measurements obtained from the device when used as an output coupler.

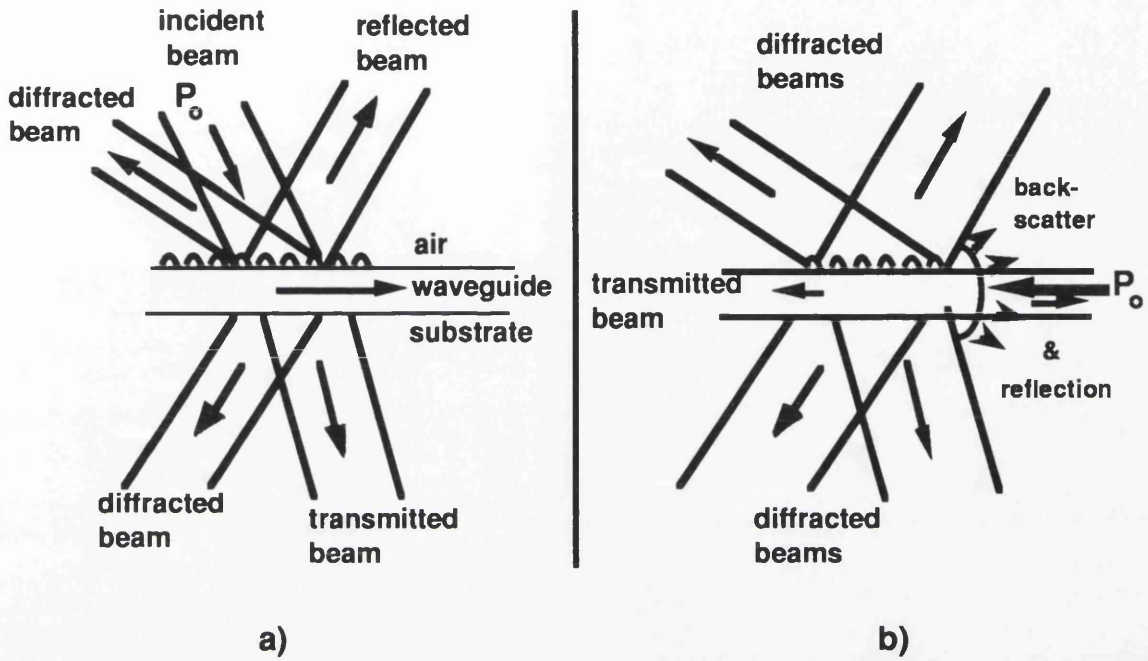

Fig.4.5.2.2.1 a) Grating coupler used as input coupler.b) Grating coupler used as output coupler. P_0 is used to denote input beam power in both cases.

The power distribution in the diffracted order(s) can also be analysed using the reciprocity of the coupler. When used as an input coupler, the light incident on the coupling region will be distributed between reflected, coupled, diffracted and transmitted beams of light. This is illustrated in fig.4.5.2.2.1 a). Similarly, for the case of output coupling, the light entering the grating coupler region will follow the reciprocal paths but, in addition, some guided light will be scattered or reflected at the edge of the grating region by the impedance discontinuity between the waveguide and grating sections. The latter case is illustrated in fig.4.5.2.2.1 b). The pitch of the grating dictates the number of diffracted orders and, for maximum coupling, only one order of diffraction should be present. In the case of the output coupler this will under normal circumstances mean that there will be one (useful) diffracted order emitted through the surface of the material, and one (unwanted) through the substrate. It is possible to obtain one single output beam by restricting output coupling to the order that is emitted through the substrate, but in many applications the theoretical limit of 50% coupling into the useful first order mode proves sufficient.

4.6 Summary

Characterisation of the refractive index of a semiconductor is more difficult than for materials with lower refractive indices. The refractive index can be obtained from ellipsometry or reflectometry measurements , and the waveguide index can be calculated using numerical methods. The waveguide index of a slab waveguide can, alternatively, be obtained directly. This is possible using the grating coupler method. The material refractive indices of the component layers of the slab waveguide can then be derived from the waveguide index.

1D.E. Aspnes, S.M. Kelso, R.A. Logan, R. Bhat,"Optical Properties of $Al_xGa_{1-x}As$", J. Appl. Phys., Vol. 60, No. 2, 1986, pp 754-767.

[2] H.C. Casey Jr., D.D. Sell, M.B. Panish, " Refractive Index of $Al_xGa_{1-x}As$ Between 1.2 and 1.8 eV", Appl. Phys. Lett. Vol. 24, No. 2, 1974, pp 63-65.

[3] B. Bhumbra, "Nonlinear optical waveguide devices in GaAs/AlGaAs",Ph. D. Thesis Glasgow University 1990 pp 27-30.

[4] T. Tamir (Ed.), "Integrated Optics", opics in Applied Physics, Vol.7, Springer-Verlag, 1975.

[5]D.L.Lee,"Electromagnetic principles of integrated optics", J. Wiley & Sons, 1986, pp77-92.

[6]D.L.Lee,"Electromagnetic principles of integrated optics", J. Wiley & Sons, 1986, p96.

[7]R. Baets, P. Kaczmanski, P. Vankwikelberge,"Design and modeling of passive and active optical waveguide devices," Waveguide Optoelectronics, Kluwen Academicas Publishers, 1992, Ch.2 pp 21-71.

[8]G.Strang,"Introduction to applied mathematics",Ch.5 pp 367-470.

[9]D.L.Lee,"Electromagnetic principles of integrated optics", J. Wiley & Sons, 1986, p166.

[10]H. Nishihara, M. Haruna, T. Suhara, "Optical Integrated Circuits", Chapter 4, McGraw-Hill, 1989, pp 63-95.

[11]D.G. Dalgoutte, C.D.W. Wilkinson,"Thin grating couplers for integrated optics: an experimental and theoretical study", Applied Optics Vol.14, No.12 1975, pp 2983-2998.

12 Dakss, M.L., Kuhn, L., Heidrich, P.F., Scott, B.A., "Grating Coupler for Efficient Excitation of Optical Guided Waves in Thin Films.", Applied Physics Letters Volume 16 No.12, 15. June 1970, pp 523-525.

CHAPTER 5

FABRICATION OF GRATING COUPLER

5.1 Introduction

This chapter describes the fabrication of the grating couplers used for the refractive index measurements, the measurement set-up used.

The grating coupler method described in chapter 4 was realised using laser holography to define the diffraction grating. Other methods for producing periodic sub-micron patterns exist, such as electron beam lithography, but these are generally time-consuming and subject to severe restrictions on uniformity over large areas. Holography can make uniform patterns over large areas, and it is a less time consuming, parallel process.

5.2 Diffraction Grating

The definition of the diffraction grating is the most critical step in the fabrication of the grating coupler. The grating must be well defined over a large area, and aligned with one of the $[0\bar{1}1]$ or $[01\bar{1}]$ crystal planes. This is achieved by the use of laser holography.

5.2.1 Laser Holography

There are several possible set-ups presently being used for grating fabrication by laser holography, and these have been treated in detail elsewhere[1]. These include:

—the corner cube arrangement using a single mirror[2] and utilizing the divergence of a laser beam acting as a point source

—the three mirror interferometer[3] with spatial filter and collimated beams

—and the symmetrical arrangement[4] using two mirrors and two spatial filters

The symmetrical interferometer arrangement was chosen, shown in fig. 5.2.1.1. In this set-up the output light from the laser is split up into two beams of equal intensity using a

50-50 beam splitter. The two beams are incident on mirrors which are equidistant from the beam splitter and which are separated by the interferometer baseline a. At the mirrors the beams are reflected through an angle ϕ such that they interfere at the sample surface. This places the sample at a distance c from the mirrors and b along the normal to the baseline at its midpoint.

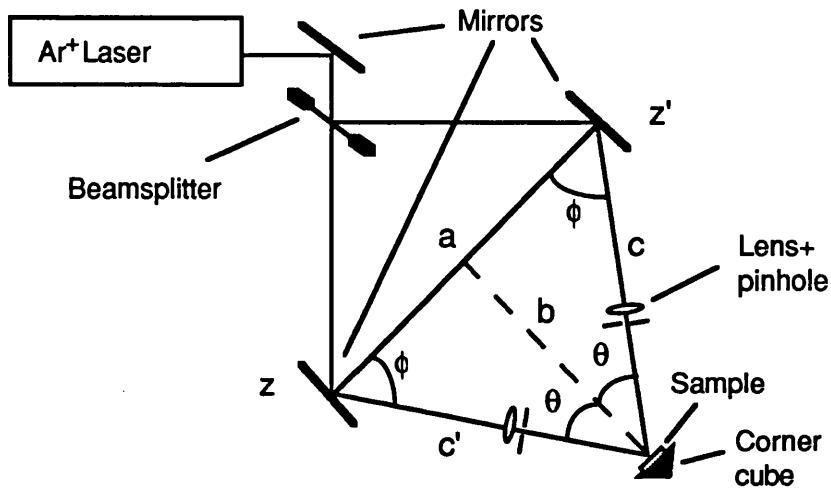

Fig.5.2.1.1 Diagram showing the holography recording set-up.

The symmetrical interferometer has the advantage of enabling easy rearrangement of the incidence angle on the sample surface, thereby facilitating grating period adjustments, without altering the baseline of the interferometer. Also, the optical path length difference between the two unexpanded beams in the interferometer can be made arbitrarily small, thereby relaxing the requirements on the temporal coherence of the laser source. The major disadvantage with the symmetrical set-up is that any wavefront imperfections are compounded due to the asymmetry in the number of lateral inversions of the beams in the two beam paths before the interference at the sample surface. To minimize this effect, spatial filters were placed immediately after the two high flatness mirrors (λ/20) used for the beam steering.

The laser used was a Spectra Physics 165 Argon ion laser producing 4 Watts cw when in all-line operation. The laser was wavelength selectable when a rear mirror prism assembly was included, giving as many as nine lines with output powers sufficient for grating

holography. The line chosen for the diffraction grating definition was the 457.9 nm line, with an output power of approximately 200 mW. The factors governing this decision include considerations on wavelength dependence of photoresist responsivity, desired grating period and limitations on interferometer set-up, both practical and fundamental[1]. The laser operated simultaneously in the TEM_{00} and TEM_{01} modes, however, and for the fabrication of holographic gratings it was necessary to restrict oscillations to the TEM_{00} mode due to the requirements of spatial coherence of the wavefronts. This was achieved by means of an aperture within the laser. The reduction of this aperture has the effect of increasing the losses for the higher order mode whilst leaving the lower order mode unaffected, forcing the laser into TEM_{00} operation.

From standard textbook theory the period of the interference fringes, Λ, is given as:

$$\Lambda = \frac{\lambda_0}{2n \sin \theta} \qquad (5.2.1.1)$$

where λ_0 is the free-space wavelength of the two beams of light incident on the sample, each at an angle θ symmetrically about the normal to the sample, and n is the refractive index of the medium in which the angle θ is measured, usually air. From this equation it is evident that, for the interferometer set-up used here, the smallest pitch obtainable is half the wavelength of the laser line used (at $\theta=90^\circ$), but this cannot of course be realised in practice. It was believed[1] that gratings could not be written with angles θ much larger than 45° due to the resulting phase errors, but gratings have been made using angles up to 70° in the present system[1]. Smaller pitch gratings are possible using an incident medium of high refractive index, for instance by immersing the sample in high index liquid or through novel techniques such as the front-prism method[5].

5.2.2 Photoresist gratings.

5.2.2.1 Dependence on reflectivity

The photoresist used was Hoechst AZ 1450 J, which gives a typical thickness of 1.76 μm when spun at 4000 rpm for 30 seconds. The resist can be used in a diluted solution by introduction of a thinner supplied by the manufacturer to give the required thickness. Photoresist gratings can be made using the undiluted product, but these are of no practical use for the grating periods and pattern transfer methods considered here, due to the difficulties involved in removing the photoresist in the troughs down to the substrate.

The procedure of making photoresist gratings is complicated by the finite reflectivity of the substrate on which the photoresist is spun. For photoresist gratings on glass slides, the reflection at the resist-glass interface is small enough not to have any significant effect on the grating quality. The reflection arising from the rear glass-air interface of the slide is, however, an order of magnitude larger. This tends to deteriorate the grating through light scattering and the support of vertical standing waves in the photoresist-glass system. The effect can be suppressed through the inclusion of a prism with its two rear surfaces painted matt black, placed with its front surface in contact with the rear surface of the glass slide through a layer of index-matching oil. The problem is more complex in the case of photoresist gratings on a semiconductor substrate. Semiconductors have in general a very high reflectivity, which immediately causes problems for holographic fabrication of gratings. Vertical standing waves are supported in the photoresist-substrate system, leading to a vertical spatial variation in the intensity of the lateral standing wave pattern used for the grating definition. This gives incomplete exposure. Additional scattering of light from the surface result in further deterioration of the holographic pattern. Furthermore, the refractive index of a semiconductor is complex, and so introduces a finite phase shift difference compared to that experienced from an insulator. The latter means that the nodes of the vertical standing wave pattern are displaced slightly with respect to the case of an insulator with similar real part of the reflectivity. One method of suppressing the deteriorating effects

of the vertical standing wave formation in photoresist on reflecting substrates is to carefully control the thickness of the photoresist and make sure that it exactly mismatches an integral number of vertical standing wave periods. This type of grating is referred to as a thin resist grating and has been achieved[1]. Experience shows though, that it is very difficult to reliably control the thickness of photoresist over larger areas to the accuracy needed. This is a result of the many factors influencing the viscosity and flow patterns of the resist during spinning, such as temperature, humidity, age of photoresist and thinner, filtration efficiency and substrate geometry. A better solution to the problem is to suppress the light reflected from the semiconductor surface. Suppression can be achieved by the use of an antireflection coating or by using a highly absorptive medium deposited on the semiconductor surface prior to application of the resist. Both methods have been used[1], but with the availability of a spin-on absorptive medium of resist-like properties supplied by Brewer Science Ltd., the latter is more preferable. The resulting grating is then referred to as a thick resist grating.

5.2.2.2 Thick resist gratings. Fabrication.

Although the possibility existed for making thin resist gratings, experience suggested that this would be an uncertain process giving low yield, as well as not being applicable to the lift-off process required for transferring the pattern to the semiconductor surface. Thick resist gratings allow the use of lift-off processes where the maximum metal thickness for successful lift-off is roughly one third of the photoresist thickness. If a thicker layer of metal is evaporated on to the photoresist, the metal on top of the photoresist tends to link up with the metal in the exposed areas, making selective removal very difficult. Thick photoresist gratings should also, in theory, be less susceptible to the interference of light backscattered from the surface of the substrate due to the absorption in the resist. In practice however, it is found that thick resist gratings also suffer from the effects of vertical standing waves. By using ARC-XL©, a commercially available antireflection antireflection coating for spin-on application, the vertical standing wave effect was removed. This medium works in a different way from what is normally termed an antireflection coating

such as a quarter wavelength dielectric. It is in fact a polyimide-based product with a very high absorption in the wavelength range used for exposure of most photoresists. The film thickness when spun at 5000 rpm for 90 seconds was determined to be 0.2 μm, and the manufacturer quote a transmittance of only 1.6% of the incident light through this thickness at a wavelength of 436 nm. After application, the coating was baked at 135° for 30 minutes and allowed to cool down before application of the thinned photoresist. Two resist thicknesses were used, corresponding to photoresist/thinner ratios of 2:1 (66%) and 1:3 (25%), giving thicknesses of 0.68 and 0.16 μm respectively when spun at 4000 rpm. The thicker resist-solution was used for making metal gratings developed for use as implantation masks, and the more dilute solution was found to be particularly reliable for use in the process of transferring the grating pattern to the semiconductor surface.

5.2.3 General procedure

The pitch of a holographically defined grating is altered by changing the incidence angle at the sample surface, and is governed by the above equation 5.2.1.1. The output/input coupling angle of a grating coupler is given by equation 4.2.1.6. From considerations on the accuracy of the measured values, it is obvious that the region of maximum variation in the output coupling angle ϕ should be chosen. Since the relationship between the output coupling angle and refractive index of the material is a sine function, the maximum change is in the region close to $\phi = 0°$. In addition, due to experimental set-up considerations, it was necessary to have forward output coupling. These factors, together with a knowledge of the estimated approximate values of the refractive indices of the couplers governed the choice of 285 nm as the grating period. The Ar^+ laser used had a strong emission line at 457.9 nm, and the calculated incidence angle at the sample surface at this wavelength for this pitch is 53.45°; well within the range for useful grating holography and also in the range compatible with the photoresist.

The angle between the two beams incident on the sample surface can be set with a high degree of accuracy, typically to much better than 0.25° by the use of geometric construction

techniques. This produces very small errors in the grating pitch. An expression for the error in the period is obtained from equation 5.2.1:

$$\frac{\delta\Lambda}{\Lambda}(\%) = 100 \times \cot\ \theta \times\ \delta\theta \qquad (5.2.3.1)$$

This gives a percentage error of 0.16% in the case of an angle of 53.45°, corresponding to $\delta\Lambda$ of 4.6 Å. In practice the error was found to be smaller than this, typically less than 2Å.

5.2.3.1 Interferometer construction

One of the largest problems experienced in holography is that of vibration in the system. Any mechanical disturbances during the exposure leads to fringe instability and blurring of the written pattern. This is readily observed in any interferometric set-up. To reduce the effect of vibrations transferred from the floor, the optical table was placed on gas-filled columns. No active stability control was used, since the damping in the columns proved adequate in the damping of low frequency vibrations from the building. There was however at intervals still some noise present in the system. This was due to the pressure fluctuations in the water-cooling system for the laser when the Nd-YAG laser in the adjacent room was running. The YAG laser ran off the same watercooling system, and took in water intermittently. Grating recording was consequently only performed when the other laser was turned off.

All mirrors used for the interferometer had a specified flatness of better than $\lambda/20$. The laser beam was deflected by one mirror in order to fit the set-up on the optical table. The beam was then divided into two equal intensity parts by the use of a 50-50 beamsplitter. The beamsplitter ratio was sensitive to the angle of incidence of the laser beam, and consequently this angle had to be carefully set whilst monitoring the power in the two arms during the set-up of the front part of the interferometer. The beam-splitter angle does not directly affect the choice of grating periods available, apart from limitations imposed on the system due to the table top area available for the set-up. The two beams were steered onto the sample through an angle ϕ by the use of two mirrors placed equidistant from the

beamsplitter, these arms corresponding to the lines x and y in fig. 5.2.1. Between these two mirrors the diagonal a in the interferometer was drawn, giving the baseline of the interferometer, and the midpoint of this diagonal was used in conjunction with calculated values for c, c' and b in the above diagram to set the value of ϕ and consequently of θ. Set-squares were used for the alignment of the beam paths, and a black metal target with a white cross hair was used for setting the height of the laser beam above the table. The sample holder, in the form of a goniometer-controlled stage, was inserted with a reflective target in place of the sample. The target had the same thickness as the sample. The exact position of the sample holder was marked when:

—the sample surface was at the point of intersection of the incident beams and

—the back-reflected spots on the beam-steering mirrors were on a line that was normal to the optical table and which went through the incident beam spot of the steering mirrors.

This enabled accurate positioning of the samples prior to exposure.

5.2.3.2 Spatial filters

Although it is possible to write grating patterns with an unexpanded beam, these gratings would be of little practical use, due to their area being limited to that of the beam spot size. The beam therefore had to be expanded to yield large area gratings (>1 cm^2). Also, in a real system, laser noise and wavefront imperfections lead to a deterioration of the grating quality. By using a lens-pinhole arrangement, these factors can be alleviated. The lens is used to expand the beam and, in its focal plane, the Fourier transform of the incident beam can be used to remove the beam imperfections by utilising the higher spatial frequencies of the imperfections compared to the gaussian laser mode. The filter is used to block out the higher spatial frequencies and takes the form of a pinhole situated in the focal plane of the lens. Its diameter is large enough to let the gaussian mode through but too small for the higher frequency components, thus acting as a low bandpass filter. The spatial filter set-up

used here consisted of a 16 mm focal length quartz microscope objective lens and a 30 μm pinhole, mounted on controllable x,y,z-mounts.

The spatial filters were placed at a distance of 25 cm from the point of intersection of the two beams, giving an effective grating area the order of 2 cm^2. The exact grating area was found to depend on:

—the reflectivity of the sample surface
—the thickness of the photoresist
—laser power
—exposure and development time.

Regional variations in the thickness of photoresist, for instance in the form of build-up due to surface tension at the sample edges for smaller samples, was found to severely limit the area over which a grating of uniform quality could be obtained. For this reason, the sample should always be made larger than the area in which the grating is to be formed.

5.2.3.3 Alignment prior to holographic recording

The alignment of the set-up was always checked and, if necessary, adjusted prior to each holography session. For each of the spatial filter assemblies, the lens and the pinhole were taken out of their holders and the alignment of the unexpanded beam was checked and centred on the target as described above. The lens was thereafter reinserted and the positioning adjusted so as to give an expanded beam with the same centre on the target as the unexpanded beam. The pinhole was inserted and positioned in the focal plane of the lens. This was easiest performed by initially keeping the distance between lens and pinhole larger than the focal length of the lens, making the spot size larger than the pinhole aperture and creating diffraction patterns in the target plane. The separation was reduced while scanning the pinhole in the x and y directions to keep the diffraction pattern as central and well defined as possible. As the distance between the pinhole and the focal plane of the lens was reduced, the radius of the diffraction rings were observed to increase until, as the pinhole entered the focal plane of the lens, they disappeared, leaving the bright central spot.

Minute adjustments were now made to yield a well defined spot without traces of diffraction along any part of its periphery. Finally, the positions and points of intersection of the two expanded spots were checked using a small sized white paper card in the plane of the sample holder. If the overlapping area was found to be centered and well defined, the spatial filter system was defined as set, and the set-up was now ready for grating recording.

5.2.4 Holographic recording

The power emitted by the laser was monitored throughout the setting up procedure and at intervals during the recording using a United Detector Technology integrating sphere power meter. This power meter was calibrated against a Coherent Model 210 black body power meter to give readings in milliwatts. The output power of the laser was kept at 90 mW, giving a power density at the sample surface of approximately 20 mW cm^{-2} for an overlap area 2 cm in diameter[1] after losses in mirrors and spatial filters. This power density resulted in exposure times ranging from 30 to 50 seconds for the photoresist thicknesses used here, and using an AZ developer to deionized water mixture of ratio 1:2. The exposure times could be reduced by increasing the development time, but the strongest gratings were formed when the exposure time was of the order of twice the development time for this power density.

After each resetting of the holography set-up, the grating quality obtainable and the resulting pitch were checked in a holography session using photoresist spun onto glass slides. This option was chosen because of the relative ease with which these gratings could be produced compared to the normal procedure of coating semiconductors with the antireflection substance. Reflection problems do exist with the use of glass slides, but here they occur at the rear glass-air interface and could be overcome by the use of indexmatching oils and a rear prism with matt black painted rear faces[1]. These gratings were much easier to record, and the grating quality obtained could be used for fault-finding in the set-up. When a strong, well defined grating was obtained, it was used in a reflection grating mode

to determine the pitch. The data from these measurements were used to check the accuracy with which the angles in the interferometer were set . If necessary, the set-up was adjusted to yield the correct pitch.

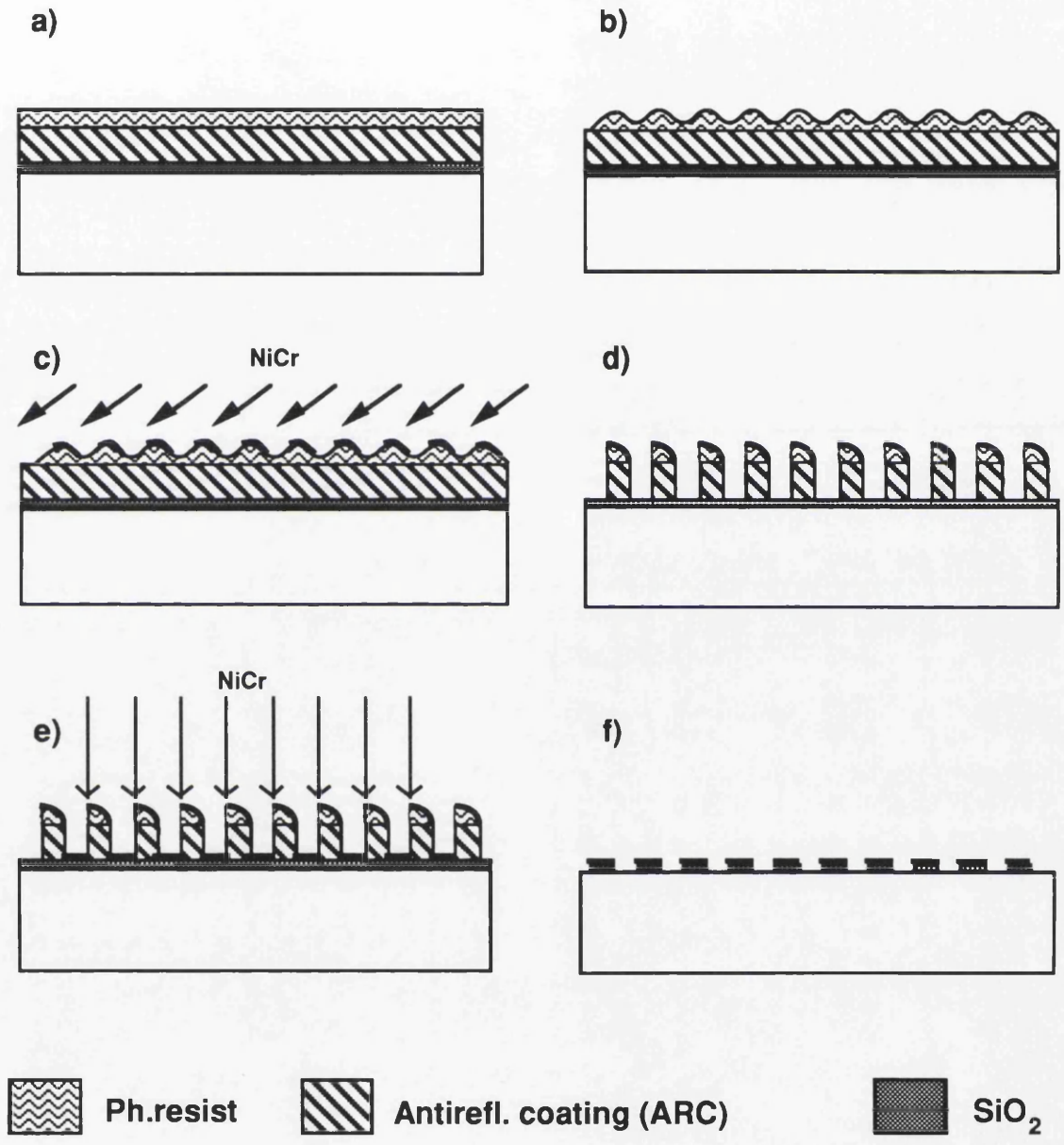

Fig.5.2.4.1 Diagram showing the sequence of processing steps in the fabrication of the grating couplers.

Conventionally, a grating coupler is incorporated in a semiconductor material by the periodic removal of semiconductor material using anisotropic etching methods through a grating mask defined by laser holography or electron beam lithography. The removal of

semiconductor material in this way modifies the material structure, and may therefore affect the modal index of the waveguide. This problem can be overcome by using a thin film of low-refractive index material to form a grating on top of the semiconductor. Silicon dioxide is a good candidate for the output grating. It has a relatively low refractive index, is resistant to solvents (important for cleaning the couplers) and mechanical abrasions and can be selectively removed in RIE processes that do not affect the semiconductor.

It is possible to form the low-refractive-index grating coupler directly in the SiO_2 annealing cap present on top of the slab waveguides, in which case the thickness of the SiO_2 layer should be chosen to optimize the output coupling efficiency[6]. The etch rate of the SiO_2 capping layer was however found to change dramatically after annealing in the presence of the As overpressure, which meant that, due to fabrication considerations such as depth control, a better solution was to completely remove the cap and redeposit a 1200 Å layer of SiO_2.

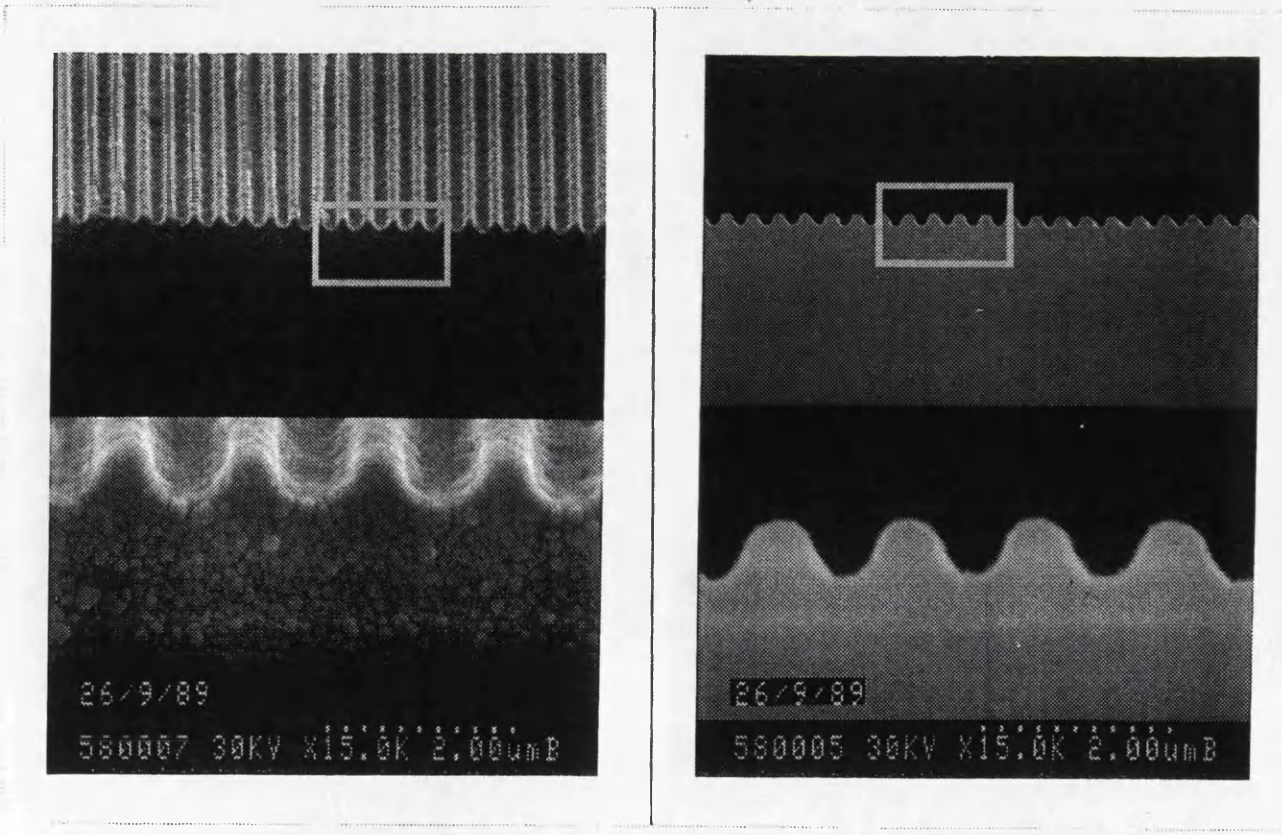

Fig.5.2.4.2 Near sinusoidal grating formed in photoresist on top of ARC-XL™. The coarser texture of the spin-on antireflection coating makes it distinguishable from the photoresist.

The grating pitch of 285 nm was designed to give output coupling angles in the region of 10° to 45° to the normal to the sample. A grating of pitch 285 nm was defined in photoresist by laser holography using the procedure described in the preceding sections.

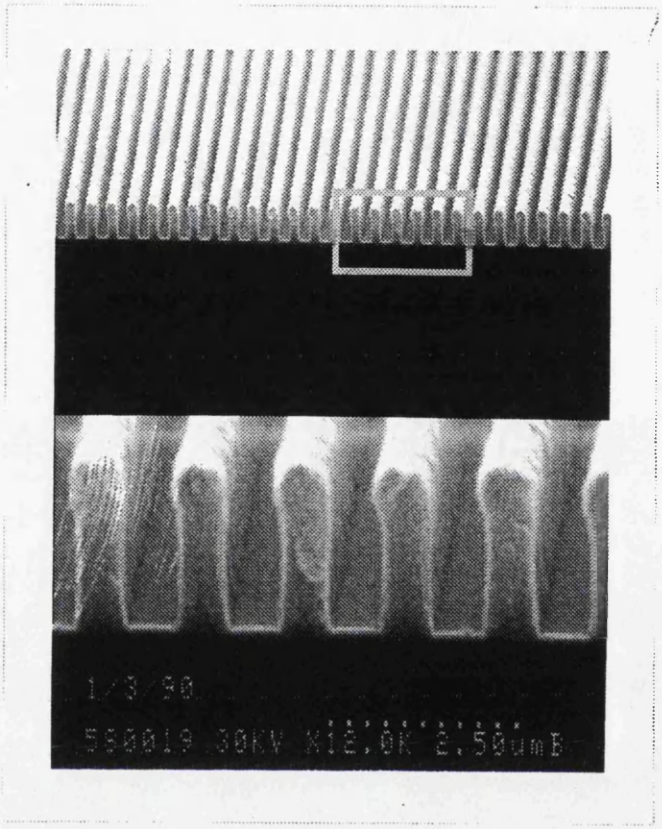

Fig.5.2.4.3 SEM photograph of the high aspect ratio grating columns.

The grating pattern was transferred from the photoresist to the SiO_2 using a multistep process. These process steps are illustrated in Fig.5.2.4.1 a-f). The first two steps, shown as a) and b) in the diagram, involve the deposition of photoresist and ARC-XL on top of the SiO_2 layer covering the semiconductor. The next step is shown in c), where the grating crests are shadowmasked by evaporating a 20 nm layer of NiCr onto the photoresist grating at an angle of 60° (chosen to give a 1:1 mark-space ratio). In this way the NiCr layer covers the top and one side of each grating crest. It is used as an etch mask in the subsequent O_2 reactive ion etch to protect the photoresist and ARC below each crest, whilst allowing the complete removal of the photoresist/ARC in the valleys of the photoresist grating down to the SiO_2 layer. The very high (7:1) aspect ratios that can be achieved using this technique

are illustrated in d) and can also be seen in the SEM photograph, fig.5.2.4.3. A second evaporation of 15 nm NiCr, at normal incidence to the sample surface, was used to transfer the grating mask pattern to the SiO_2. This step is illustrated in e), where also the composition of the grating columns is shown. The photoresist/ARC columns were then completely removed by boiling in acetophenone in a reflux condenser, leaving a NiCr grating mask on top of the SiO_2. Using this mask, the exposed SiO_2 was completely removed by CHF_3/O_2 dry etching, leaving a low-index, SiO_2 grating on top of the semiconductor waveguide (f).

Inspection of the grating structure by scanning electron microscopy showed that the above procedure produced a perfectly rectangular grating (Fig.5.2.4.4). This was also confirmed by observing the Fourier spectrum of the grating output when used as a reflection grating at normal incidence.

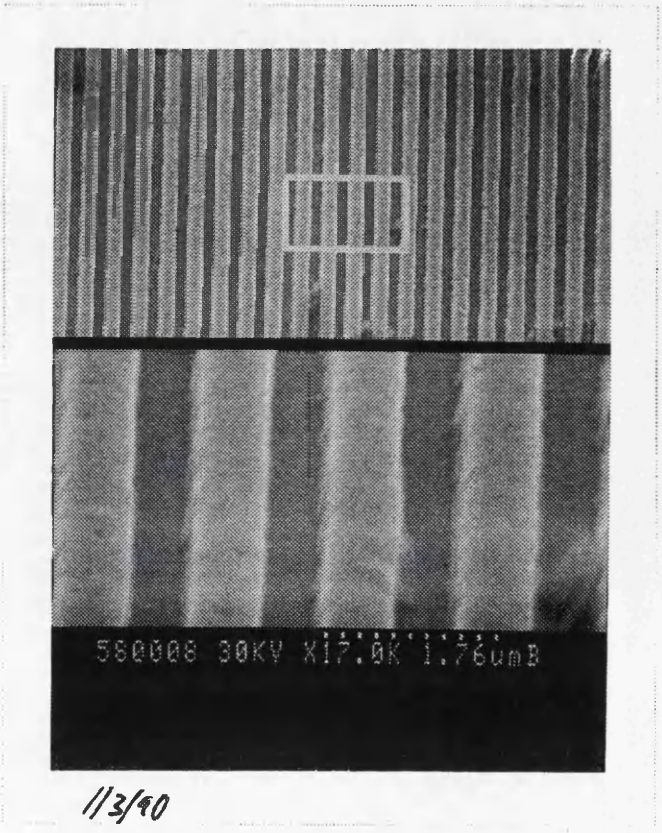

Fig.5.2.4.4 Electron micrograph of the SiO_2 grating.

The grating coupler region was defined by conventional optical lithography prior to SiO_2 chemical etching, and consisted of a 150 μm wide stripe parallel to the lines of the grating pattern. The structure was cleaved into individual devices of 1 mm width and 3 mm length as shown in fig.5.2.4.5. Fabry-Perot effects were suppressed by the use of a mirror cleave at the input coupling facet and a disruptive cleave at the opposite facet . The length of the slab waveguide between the input facet and the grating was designed to be at least 2 mm in order to strip off leaky modes. The pitch of the grating period was verified by monitoring the reflection from a test sample using the 457.9 nm line of an Ar^+ laser.

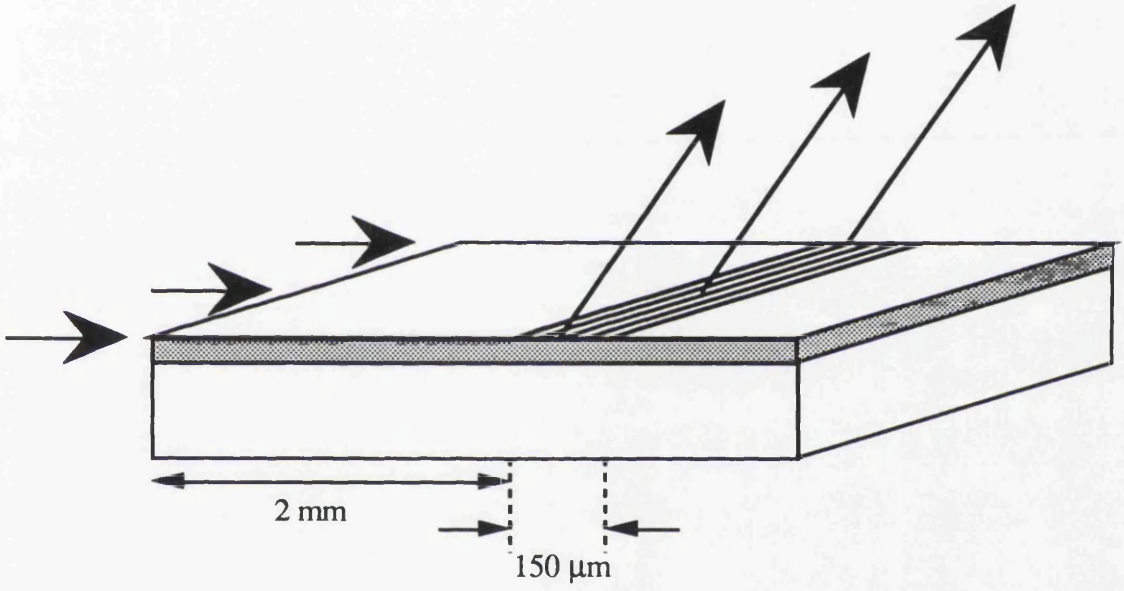

Fig.5.2.4.5 Diagram illustrating the output coupler device (from ref[7]).

5.3 Summary

There exist several possible set-ups suitable for grating holography. The symmetrical arrangement was used here, and thin and thick photoresist gratings were produced. Vertical standing wave interference was eliminated using an absorbing spin-on polyimide.

Grating couplers made in a low-index material on top of a semiconductor waveguide influence the refractive index of a waveguide less than when a grating is etched directly into the waveguide material. SiO2 was found to be suitable for this purpose. The holographically defined photoresist grating pattern was transferred to the underlying SiO_2

layer by a combination of lift-off pattern transfer and dry etching. 150 μm long grating regions were produced using conventional photolithography and chemical etching. Output grating couplers, 3mm long and 1mm wide, were fabricated by scribing and cleaving the sample. The pitch of the gratings was verified using the gratings in reflection mode.

[1] K.M. Thomas "Sub-micron holographic grating masks replicated by X-ray contact printing for integrated optics", Ph.D Thesis Glasgow University,1989.

2 S.H. Zaidi, S.R.J. Brueck,"High aspect ratio holographic gratings", Applied Optics Vol.27, 1988 pp 2999-3002.

3 D.G. Dalgoutte, C.D.W. Wilkinson, "Thin grating couplers for integrated optics: an experimental and theoretical study", Appl. Optics Vol.14 1975, pp 2983-2997.

4 E.Y.B Pun,"Thin film Bragg deflection gratings for integrated optics", Ph.D thesis, Glasgow University 1983.

5 C.V. Shank, R.V.Schmidt,"Optical technique for producing 0.1 micron periodic surface structures", Appl. Phys. Letts. Vol.23, 1973, pp 154-155.

[6] Streifer, W., Scifres, D.R., Burnham, R.D.,"Analysis of grating-coupled radiation in GaAs:AlGaAs lasers and waveguides", IEEE Journal of Quantum Electronics, QE-12, 422-425, 1976.

[7]J.H. Marsh, "Neutral Impurity Disordering of Quantum Well Waveguide Devices",Waveguide Optoelectronics,Chapter 9, Eds. J.H. Marsh and R.M. DeLa Rue, Nato ASI Series, Kluwer Academic Publishers, 1992, pp185-203.

CHAPTER 6

EXPERIMENTAL RESULTS/MODELS

6.1 Introduction

This chapter presents the main experimental results in this thesis. The waveguide refractive indices in this chapter are measured using the grating coupler method described in Chapter 4, with grating couplers fabricated as shown in Chapter 5. Waveguide– and material refractive index values are presented for bulk GaAs and AlGaAs waveguides, as-grown GaAs quantum well waveguides and partially and completely disordered waveguides.

6.2 AlGaAs refractive index

6.2.1 Background

The continuous range of AlGaAs refractive index values that were used in the calculations were obtained from the modified version of Afromowitz' model (section 2.3.4.1 and appendix 1). This model showed very good agreement with the refractive index values as published by Aspnes et al[1]. Aspnes' values were considered more accurate in terms of aluminium-concentration estimate than those of Casey et al [2]. This conclusion was reached after a comparison of the method applied to determine the aluminium concentration in the two instances, combined with consideration of the methods used for the measurements. The reasoning is more extensively explained in appendix 1 of this thesis.

The structures used for the MQW experiments were designed to be single-moded and preliminary calculations of the expected waveguide indices proved the as-grown structure to be quite sensitive to the refractive index of the cladding layer in terms of cut-off wavelengths. When refractive index values from Casey et al were used in calculations with the resonance criterion, the results indicated that the structure should stop guiding at the longer wavelength end of the measurement range. This loss of guiding was not observed.

Using Aspnes' refractive index values the calculations indicated guiding over the whole wavelength range of interest.

A study of the bulk refractive index of $Al_xGa_{1-x}As$ around x= 0.1 - 0.3 was performed due to the apparent uncertainty in the exact refractive index of AlGaAs at these compositions. Three different structures were grown, with guiding layer composition ranging from GaAs to $Al_{0.2}Ga_{0.8}As$ and cladding layers from $Al_{0.15}Ga_{0.85}As$ to $Al_{0.3}Ga_{0.7}As$. The layers were nominally undoped and grown on semi-insulating GaAs substrates. The $Al_xGa_{1-x}As$ composition was measured using the x-ray diffraction (XRD) method. This method measures the change in the lattice constant between GaAs and $Al_xGa_{1-x}As$ in terms of orders of diffraction of incoming directional x-rays. The resulting angular measurements can then be converted into a percentage aluminium content of the semiconductor crystal using known values of the lattice constants for GaAs and $Al_xGa_{1-x}As$. This is claimed to be the most accurate method for determining the composition of $Al_xGa_{1-x}As$.

6.2.2 AlGaAs waveguide material structure

The waveguide structure A578 had a 0.5 μm GaAs guiding layer and a 2.5 μm $Al_{0.17}Ga_{0.83}As$ cladding layer (17.1 % Al as determined by XRD) and supported a single vertical transverse mode. The two AlGaAs waveguides A375 and A374 had 1 μm guiding layers of $Al_{0.15}Ga_{0.85}As$ (14.6 % by XRD) and $Al_{0.2}Ga_{0.8}As$ (19.6 % by XRD), and 2.5 μm cladding layers of $Al_{0.19}Ga_{0.81}As$ (18.8 % by XRD) and $Al_{0.29}Ga_{0.71}As$ (28.9 % by XRD) respectively. A374 supported two modes and A375 supported a single vertical transverse mode.

6.2.3 Waveguide index measurements

The procedure described in chapter 5 was used to fabricate grating couplers of the GaAs-AlGaAs samples to facilitate determination of the waveguide index. The slab waveguide configuration was used. Since the absolute dimensions of the layers were known, the

material refractive indices could easily be obtained from iterative procedures which fitted the solutions to Maxwells equations for a slab waveguide to the measured waveguide indices.

The grating couplers were designed to be approximately 3mm long and 1mm wide, with a 2mm slab waveguide section between the input section and the grating section in order to strip off leaky modes. The set-up used for the measurements is shown in the diagram fig.6.2.3.1 and combines a simple set-up procedure with measurements of high accuracy and repeatability.

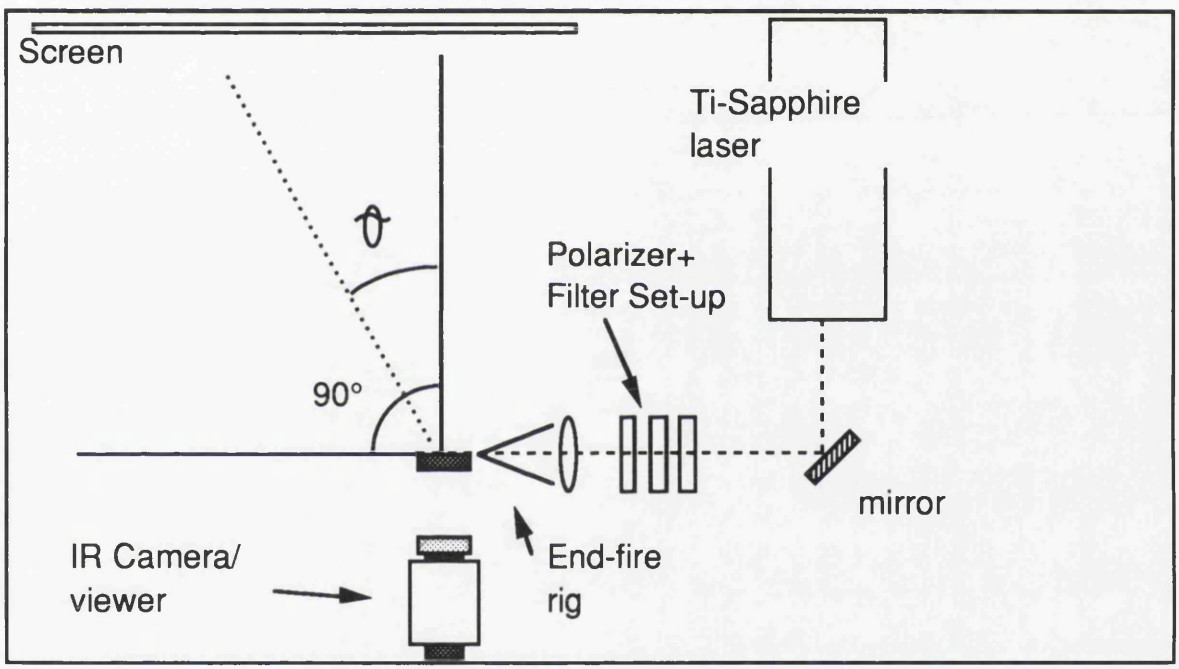

Fig.6.2.3.1 Diagram showing the set-up used in the measurement of effective index

Output coupling angles were measured for both TE and TM polarisations in the range 820 to 920 nm using a tunable laser. An Ar^+ pumped dye laser was used in the initial stages of the project , but this was exchanged for a solid-state titanium:sapphire laser that exhibited a much larger tuning range and which had far more reproducible emission intensities. The wavelength tuning of the titanium:sapphire laser was calibrated using a double 1/4 meter monochromator. Fig.6.2.3.2 shows the calibration curve obtained together with the linear interpolation fit obtained from the measurements.

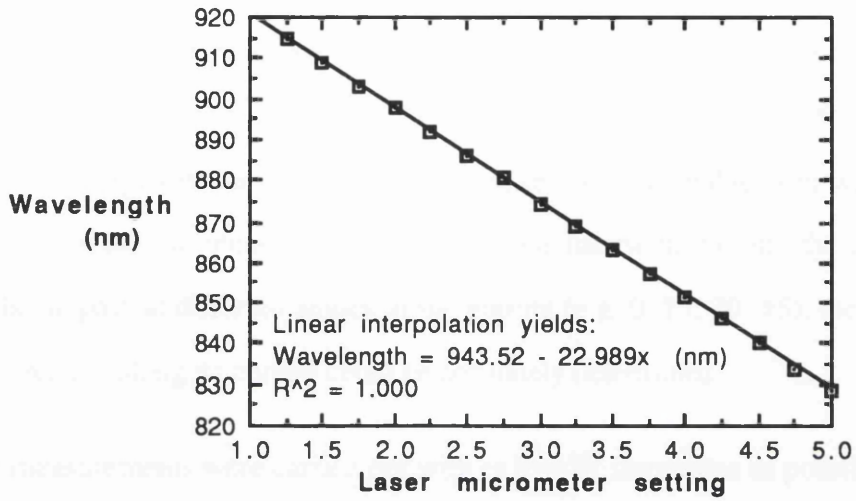

Fig.6.2.3.2 Wavelength calibration curve for the solid-state Ti-sapphire laser.

The light was steered by the use of telescopic mirror sets to be parallel to the optical table and at the same height as the end-fire rig. A polarizer, a quarter-wave plate and a neutral density filter were placed between the end-fire rig and the mirror set to facilitate TE and TM selection. The grating coupler was mounted on a vertical holder with no effort made to provide a heat sink. The coupler was carefully aligned with the incident beam to obtain maximum end-fire coupling into the slab-guided mode and a sharply defined streak of IR light was observed at the output screen. This method differs from conventional grating coupler measurement set-up in that the couplers frequently are used for coupling light into a waveguide mode and the output from a cleaved facet (or a second grating) is used to detect the point at which the waveguide mode is excited. The conventional method obviously, due to the wavelength dependency of the coupling angle, requires the grating coupler to be rotated and the optics to be realigned for each separate wavelength measurement. This makes it a very time consuming and elaborate technique. Using the above set-up however, no re-alignment is needed as the wavelength is changed, only the position of the detector is moved as the output angle changes.

The position and orientation of the grating coupler were accurately determined by means of a low-power visible helium-neon laser at 1 m distance from the grating coupler and with its

beam incident upon the top surface of the coupler. The position and orientation of the laser was adjusted until the (diffracted) spot reflected from the grating coupler surface was coincident with the aperture of the He-Ne laser. Fine adjustment was carried out by minute positional adjustments to collapse the central lobe feature of the diffracted light (reflected off the grating) with the He-Ne output beam centre. The visible laser was thereafter moved around and used to obtain several pin-point line intersections with the grating. By marking the beam path at different angles to the grating (e.g. 0, 15, 30, 45), the grating position in the direction along its normal could be accurately determined.

The measurements were carried out with as low IR intensities as possible to avoid heating and nonlinear effects in the grating coupler. The output light from the tunable laser was typically held at 20 mW, giving approximately 1.5 mW at the waveguide input side of the end-fire rig. This was more than sufficient to observe the coupled-out line 1-2 meters from the grating. Measurements were carried out at several higher power settings over the whole wavelength range in order to make sure that no heating effects could be observed, and no variation was found for output powers from the tunable laser in excess of 90 mW (this was equally true for the MQW waveguides in the following section 6.3).

Measurements of output coupling angle were carried out in the range 820 to 920 nm in steps of 5 nm or less, depending on cut-off wavelength and absorption edge position in the structure measured. The wavelength dependent output power of the tunable laser necessitated monitoring and appropriate adjustment of the pump laser intensity at each measured wavelength to give a flat power response over the whole of the tuning range. Measurements were performed on several grating couplers and on average 8 measurements were taken for each wavelength on one grating coupler and for each polarization. This rigorous measurement procedure was adopted in order to minimize the total errors of the system. The contributing errors were introduced in the determination of output coupling angle, exact position and orientation of the grating coupler, and in the accuracy with which the output wavelength of the tunable laser could be set. The errors arising from the divergence of the output-coupled light were found to be negligible for the distance at which

the measurements were taken. The contribution from the divergence to the full width at half maximum of the output beam was estimated using an expression[3] for the angular FWHM ϕ_{FWHM}:

$$\phi_{FWHM} = \frac{2\alpha}{k_0 \cos\theta_0} \qquad (6.2.3.1)$$

which follows from the Lorentzian far field diffraction pattern for a uniform coupler with an exponential aperture function exp(-αx) and with far field amplitude A varying as [4]:

$$A \propto \frac{1}{\alpha + jk_0 \cos\theta_0 \sin(\theta_0 - \theta)} \qquad (6.2.3.2)$$

for a radiated beam making an angle θ_0 with the grating normal. The above equation is valid for cases where the decay constant α is much less than the free space wavenumber k_0. This gives, as a worst case approximation, an angular divergence resulting in a FWHM at 1 m distance of 0.14 mm for an output coupling angle of 10°. Combining the divergence and the physical length of the grating section gives a maximum value of ~ 0.3 mm, which corresponds to an angular error of 0.0084°, less than the resolution of the readings.

The angular data sets were used to find the effective refractive indices of the slab waveguides using equation 4.5.2.1.6. By using the collective data obtained for each waveguide material system it was possible to minimize the contribution from the data points with the largest degree of inaccuracy. A weighting procedure was used to select the best-fit values to form a single set of data for further processing. A sample of the results of these measurements is shown in the diagram fig.6.3.3.1.

The results of the grating measurements and calculations are presented in fig.6.2.3.3 together with the refractive index models for the Al-fraction inputs that gave the best fit. The starting point was the calculation of the cladding refractive index of the GaAs waveguide. It is assumed that the uncertainty in the published refractive index values arise from the measurement of the exact aluminium content of the material. On this basis the refractive indices of GaAs in the literature are assumed to be correct. Consequently, a high-

accuracy polynomial fit of the dispersion of the refractive index of GaAs was used as the basis for the calculation of the AlGaAs indices. The calculations based on the GaAs waveguide (A578) coupler results give a Modified-Afromowitz Model (MAM) fit of x_{MAM} =15.5%. This compares to the XRD value of 17.1% for the Al composition of the GaAs waveguide cladding layer. The MAM therefore seem to have an offset of 1.6% at this Al-fraction. This offset was used as a basis for calculating the refractive indices of the guiding and cladding layers of A375 in two separate operations. The guiding layer of A375 was 14.6% AlGaAs and this gives x_{MAM} =13% when subtracting the 1.6% offset. This model value gave refractive indices for the cladding layer corresponding to x_{MAM} =17.4%, or x=17.4 +1.6 =19%. Using 18.8%-1.6%=17.1% for x_{MAM} and solving for the guide refractive index gave x_{MAM} =13%. The values agree very well with the XRD values of 14.6 and 18.8 % for the cladding and waveguide layers for this waveguide, and confirms the validity of the 1.6% offset. Similar measurements and calculations were performed for A374 using both guided modes for calculation. The XRD value for the guiding layer, x=19.6%, was used as a known factor in the calculations. On the background of the results obtained from A578 and A375, this is taken to correspond to x_{MAM} =18% for the modified Afromowitz model. Cladding layer refractive index results corresponding to x_{MAM} =26.5% were calculated. This corresponds to x= 28.1% and compares with the measured XRD value of 28.9%.

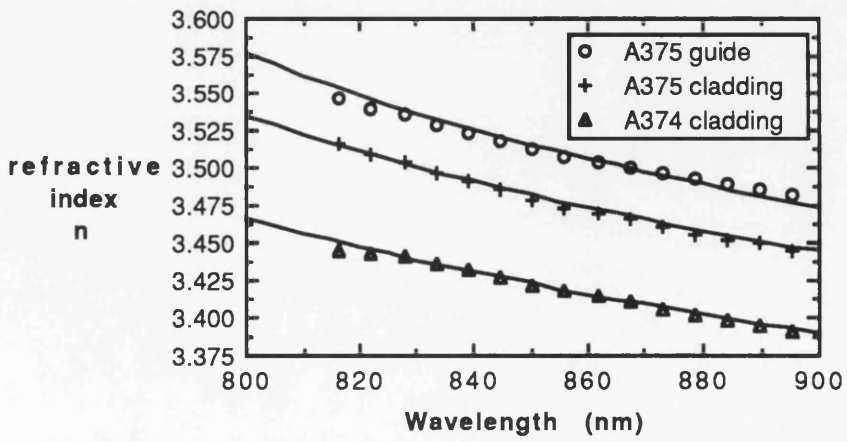

Fig.6.2.3.3 Plot of the measured material refractive indices of AlGaAs waveguides together with MAM model fits. The MAM model Al-percentages are 26.5%, 17.4% and 13% for the lower, middle and upper whole lines respectively.

The conclusion of this study of the refractive index model MAM and the real refractive indices is that the model works very well for these values when using the offset of 1.6% for the fit with values reported here, 0% for the fit with Aspnes' values and ≈4% for Casey's values. Considering uncertainties involved in the accuracy of a model based on either of Aspnes' or Casey's data in the wavelength range of interest, it was found best to use the results from this study in the present calculations. The uncertainty in the refractive index of AlGaAs is therefore to a great extent limited to the accuracy of the XRD method of determining the aluminium content of the material.

6.3. Multiple quantum well refractive indices

6.3.1 MQW material structure

For the investigation of the refractive index changes produced by IID, a MQW waveguide structure was designed. The design criteria were that the structure should support a single vertical slab mode, that a large part of the optical field be close to the semiconductor-air interface and that the structure be optimized for the implantation process and for analysis by photoluminescence spectroscopy.

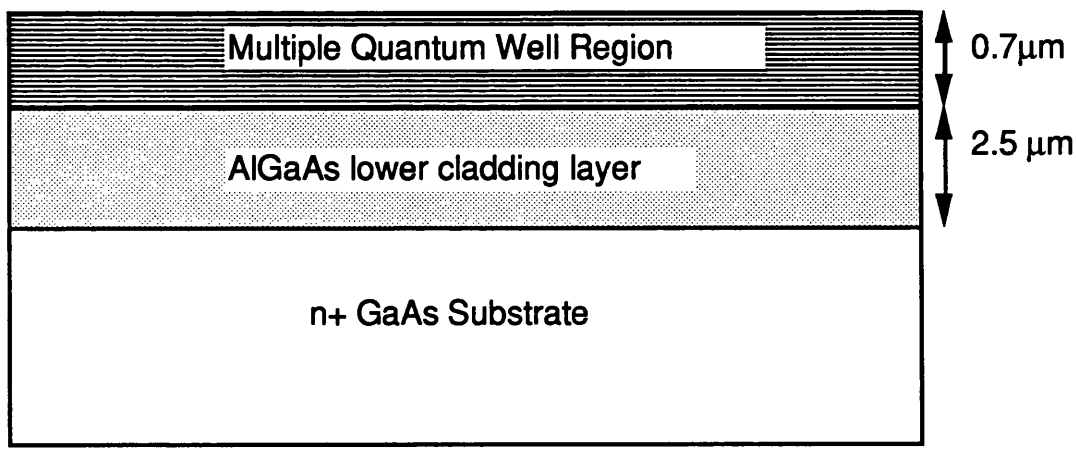

Fig. 6.3.1.1 Diagram showing the material structure of the MQW waveguide.

The structure is shown in fig. 6.3.1.1 and consisted of a nominal waveguide thickness of 0.7 μm (the exact thickness being dependent on the well-barrier thickness) with *n* periods of GaAs quantum wells and $Al_{0.26}Ga_{0.74}As$ barriers grown with a 2.5 μm $Al_{0.2}Ga_{0.8}As$

lower cladding layer on an n^+ GaAs substrate. By growing the structure without an upper cladding layer the above requirements were fulfilled, and the MQW-air interface acted as an upper cladding for the optical waveguide.

This material structure was grown at Sheffield University using MOVPE at low-pressure (100 Torr). The details of the different quantum well structures are shown below in table 6.3.1.1. The lower cladding layer composition was measured using the x-ray diffraction (XRD) method.

Material	Well Width Lz (Å)	Barrier Width L_B (Å)	No of periods n	Cladding Al (%)	Waveguide Thickness (μm)
QT18	60	60	54	22.6	0.648
CB364	100	100	35	20 [*]	0.70
CB365	40	60	70	19.3	0.70

Table 6.3.1.1 MQW waveguide parameters ([*] –higher uncertainty.due to broadened XRD peak)

6.3.2 Quantum well material characterisation

Electrochemical etch profiling was used to characterise the MQW structure, together with photoluminescence at ambient (room) and low temperature. The electrochemical etch profiling was performed with a Biorad Model 4200 instrument with an integrated photovoltaic spectrometer PVS Model 4250. Measurements showed the MQW regions of the waveguide structures to have a p-type background doping concentration of around 1×10^{16} cm^{-3}. PVS measurements are frequently used to give an estimate of the Al-concentration in bulk AlGaAs material, and are an important tool in determining composition and interface positions in a semiconductor structure. They can also be used to yield the exciton centre frequencies of MQW material in a quick and easy manner.

Photovoltaic spectroscopy was employed to determine the exciton peak resonances at room temperature for the virgin materials, and the results were confirmed using photoluminescence measurements at room temperature.

Photoluminescence spectroscopy (PLS) was performed using a customized set-up which employed a visible wavelength laser for excitation (exchangeable helium-neon 632.8 nm or argon 514 nm), a cryogenic cell for temperature variation, a 1 meter monochromator, and a high-sensitivity detector-amplifier system with a hardcopy facility. The photoluminescence measurements were also used to obtain information about the full width at half maximum (FWHM) of the exciton resonances. This value cannot be directly read from a PLS plot, since the heavy and light hole resonances are relatively closely spaced and hence cannot be discretely resolved by PLS. The values for exciton linewidth therefore have to be found from a model fitting to the spectral data from the PLS. The model used for empirical linefitting to photoluminescence resonances take the form of an oscillator lineshape, and can be based on either a Lorentzian or a Gaussian oscillator. Fig.6.3.2.1 illustrates the fitting model in the case of room temperature photoluminescence measurements for CB364 virgin material, and shows the results of fitting with a Lorentzian oscillator . The gaussian oscillator fitting model gave a larger deviation from the measured values.

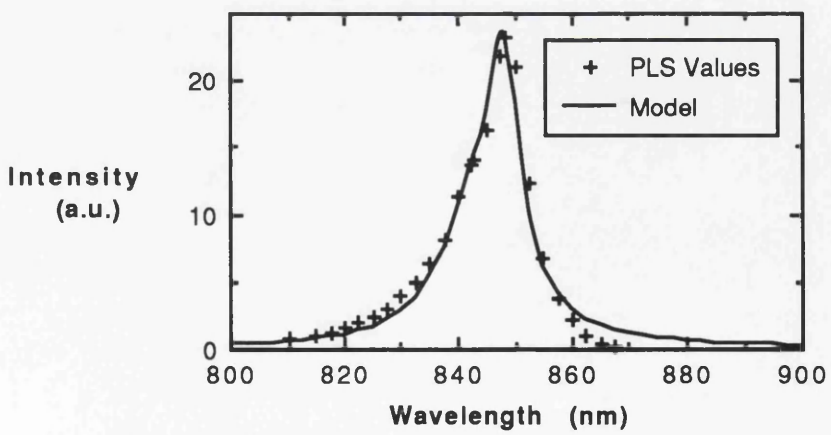

Fig.6.3.2.1 Lorentzian lineshape fitting for heavy and light hole exciton resonances for 100Å Lz/Lb MQW material CB364.

Although neither of the lineshapes exactly reproduces the exciton resonance, the Lorentzian model provides a better fit. This is in line with other publications[5] on the subject of excitons, where a better model is described as comprising a Gaussian lineshape on the low-wavelength side of the peak and a Lorentzian lineshape on the high wavelength side. This lineshape model was attempted, but it was found that although the deviation over the whole wavelength range was decreased by this method, the change had a negligible effect on the FWHM values.

Material	**Exciton resonance**		**FWHM Linewidth**	
	e-lh	e-hh	e-lh	e-hh
QT18	832.6 nm 1.4887 eV	822.6 nm 1.5068 eV	17 meV	10 meV
CB364	848.3 nm 1.4612 eV	842.8 nm 1.4707 eV	18.5 meV	8.5 meV
CB 365	816.8 nm 1.5175 eV	804.5 nm 1.5407 eV	21.9 meV	15.9 meV

Table 6.3.2.1 Table of virgin material exciton resonance parameters obtained from Gaussian oscillator model lineshape fitting.

The Lorentzian lineshape model was therefore used throughout for the assignment of FWHM values to the exciton resonances observed. The room temperature results are shown in the table. 6.3.2.1 .

6.3.3 Material refractive index

Grating couplers were fabricated on the MQW waveguide structures using the same procedure as for the GaAs-AlGaAs waveguides, and the measurement procedure described in section 6.2.3 was used to obtain the waveguide indices.

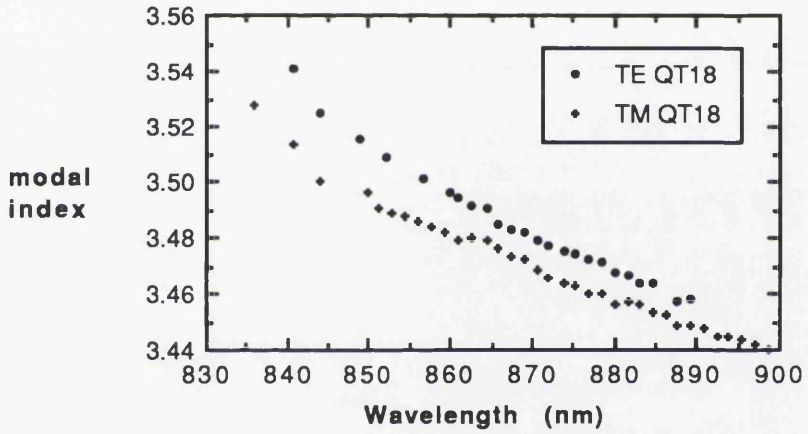

Fig. 6.3.3.1 Typical single set of measured values for the wavelength dependency of the effective refractive index of GaAs multiple quantum well material waveguide.

The waveguide index results were used to find the material refractive index of the MQW waveguide core. The technique employed is based on the transverse resonance condition described in section 4.3. It forms the basis of a Turbopascal computer program where the procedure extracting the constructive interference condition of the waveguide is used iteratively to yield one unknown factor in a system where all other parameters are known. In this way the program can find the refractive index of any layer of a slab waveguide consisting of up to four layers providing the waveguide index of the waveguide and all the dimensions and material refractive indices of the other layers are known.

The results obtained were then fitted to a Lorentzian single electron oscillator model of the nonlinear refractive index, which took excitonic contributions into consideration[8]. The

basic form of this model has previously[6] been used for the modelling of MQW waveguide refractive indices:

$$\varepsilon_{MQW}(\omega) = \varepsilon_g(\omega) + 4\pi\beta_x \frac{\omega_x^2}{(\omega_x^2 - \omega^2 - i\omega\Gamma_x)} \qquad (6.3.3.1)$$

In the above equation, ε_g represents the background dielectric constant, containing contributions from all interactions except the exciton(s) in question. $\beta_{l,h}$ is the oscillator strength of the exciton transition, $\omega_{l,h}$ is the exciton centre frequency, $\Gamma_{l,h}$ is the linewidth of the exciton, and $\varepsilon_{MQW}(\omega)$ is the dielectric constant for the MQW material. The exciton centre frequencies and linewidths had been obtained from photoluminescence measurements at room temperature and confirmed by low temperature measurements with the energy shifts and exciton broadening due to the temperature difference accounted for. For the virgin material these are the values displayed in the table 6.3.2.1 above. To model ε_g, the semi-empirical Sellmeier-type equation described in section 2.3 was employed to calculate the dielectric constant of $Al_XGa_{1-X}As$. $4\pi\beta_{l,h}$, the oscillator strengths of the exciton transitions, were used as the fitting parameters of the model. The model fitting was realised in a Turbopascal program called ElectronOscillator (see Appendix 2), and used a conventional least-square-fit approach optimised for the number of input parameters.

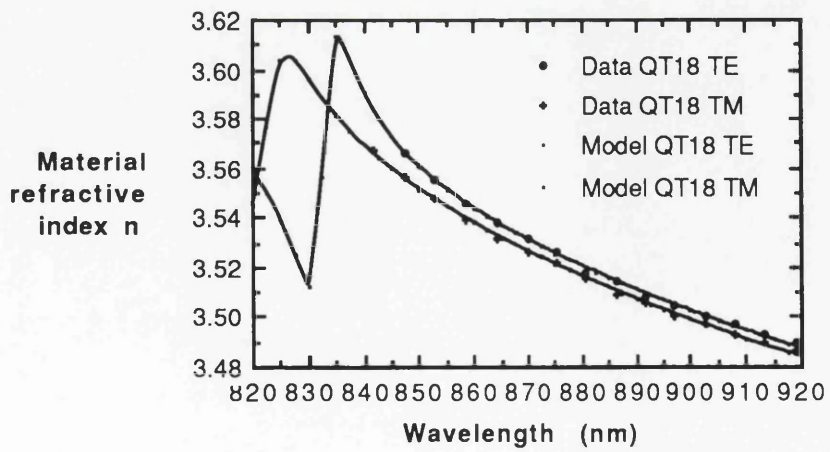

Fig.6.3.3.2 Plot of the dispersion of the refractive index of 60 Å quantum well material.

The TE and TM material refractive indices for the as-grown 60Å quantum well material are shown in fig. 6.3.3.2 .

Plots of the birefringence of the quantum well materials QT18 and CB365 materials are shown in fig.6.3.3.3. The birefringence is observed to increase rapidly in the vicinity of the bandgap. The birefringence of the 40Å well material is larger than that of the 60Å well material at long wavelengths, but in the region 835-855 nm the 60Å well material has the larger birefringence. This is due to the rapid increase close to the bandgap resulting from contributions from the excitonic transitions.

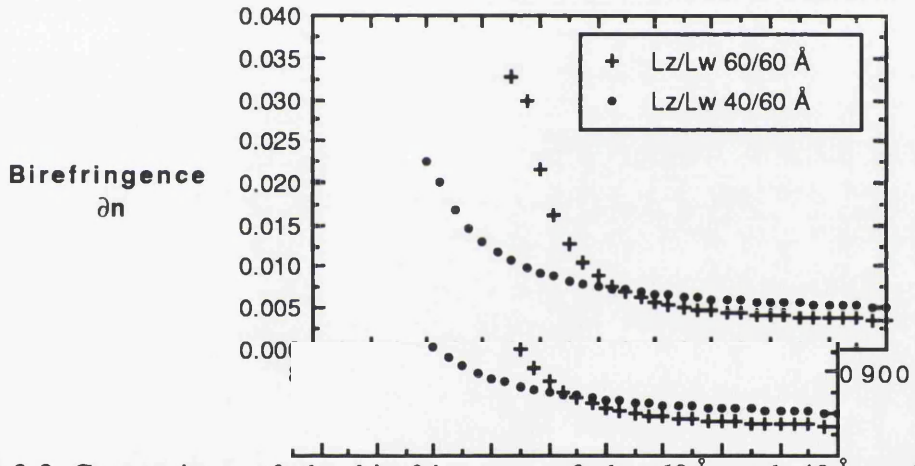

Fig.6.3.3.3 Comparison of the birefringence of the 60Å and 40Å well material waveguides.

The 40Å well material does not appear to reach the same maximum value as the 60Å well material, but this may be an artefact of the model fit used for the measured refractive indices and cannot be confirmed since there are no measured values close to the bandgap. The above results shows a larger difference between 40 Å and 60 Å compared to results estimated from the birefringence model presented in chapter 2 of this thesis. It is also obvious that the birefringence model only holds true for wavelengths well away from the GaAs bandgap. The model fails if the GaAs refractive index values from above the bandgap are used.This is illustrated in fig.6.3.3.4, where the measured birefringences are plotted together with the model-calculated birefringence.

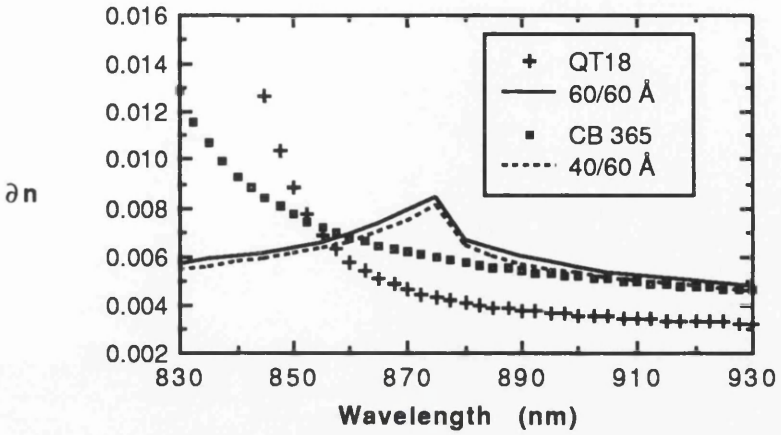

Fig.6.3.3.4 Comparison of measured birefringence (discrete points) and periodic-layer birefringence model results (lines) for 40Å and 60Å quantum well material.

6.4 Refractive index of disordered MQWs

6.4.1 Impurity Induced Disordering

The effect of boron and fluorine impurity induced disordering on the refractive indices of MQW waveguides was to be examined. Investigation of optimum implant doses and annealing temperatures had previously been carried out at the Optoelectronics Research Group at Glasgow University[7], employing low temperature (18K) photoluminescence measurements. A sample of these PL spectra is shown in fig.6.4.1.1. In this process the features associated with recombination at the bandgap (b) were compared[8] in intensity to those associated with damage (d), and an optimum combination of implant dose and annealing temperature was found; around 10^{18} cm^{-3} and 890° C respectively. For doses of 3 x 10^{17} cm^{-3} and lower the induced disordering decreased progressively and for temperatures above 910° C the thermal intermixing of the quantum well structure became significant. For higher implant doses and for longer annealing times at lower temperatures the photoluminescence peaks associated with damage showed increased intensity and their width increased. The peaks in fig.6.4.1 1 labelled (a) are due to transitions in the AlGaAs layer and the ones labelled (c) are due to band to band recombination in the GaAs layer (at 819 nm) and transitions via carbon acceptors (at 830 nm). The continuation of these studies

yielded the relationship between energy shift in the bandgap with annealing time, and from these results the annealing conditions used here were projected.

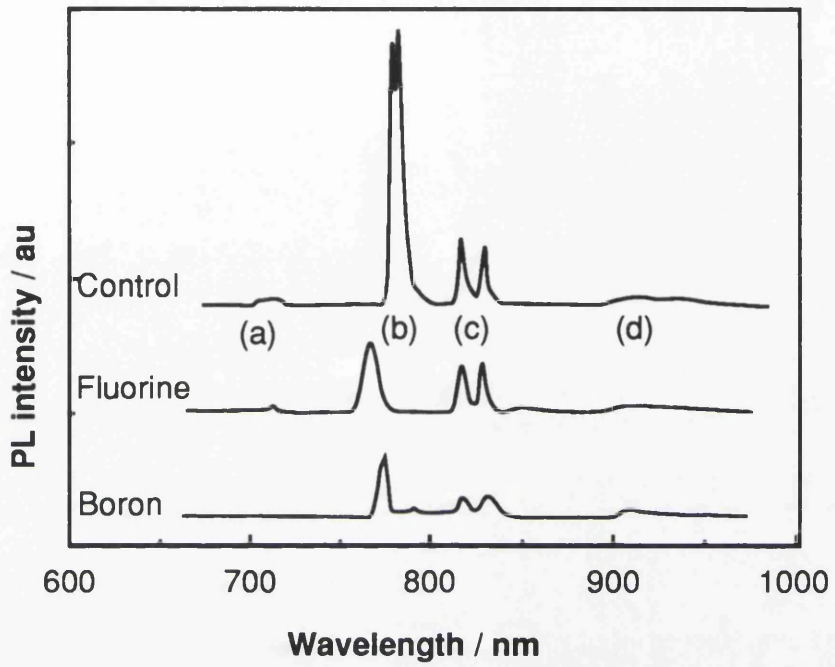

Fig.6.4.1.1 Photoluminescence spectra at 18 K for starting material, a fluorine-disordered sample, and a boron-disordered sample (from ref.6)

The implantation of boron and fluorine was performed by the University of Surrey. Samples of area about 1 cm^2 were implanted with boron or fluorine ions of different aggregate doses and energies selected to give a uniform impurity concentration from the surface down to a depth of about 1 μm. Due to the localized nature of ion beam implantation, as discussed in section 3.4.3, implantations at three separate energies were required. The implant doses and energies were estimated from calculations based on Projected Range ALgorithm (PRAL), discussed in chapter 3. For fluorine, the implantation doses and energies were: 1.53 x 10^{13} cm^{-2} at 80 keV; 3.3 x 10^{13} cm^{-2} at 260 keV; 5.1 x 10^{13} cm^{-2} at 700 keV, and for boron: 1.8 x 10^{13} cm^{-2} at 50 keV; 3.3 x 10^{13} cm^{-2} at 170 keV; 4.9 x 10^{13} cm^{-2} at 400 keV.

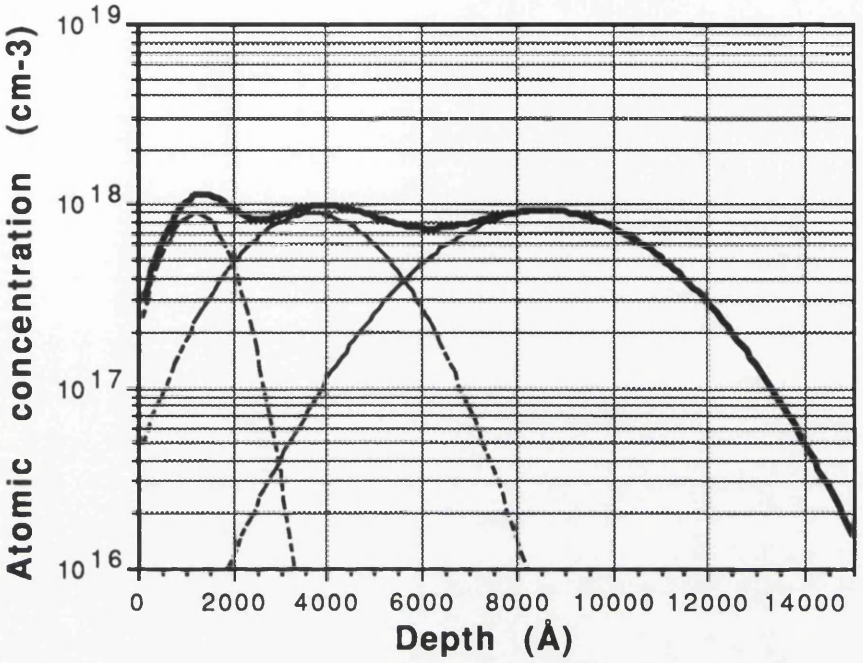

Fig.6.4.1.2 Diagram showing the Fluorine impurity distribution in the material after a triple implant procedure as calculated by PRAL (Projected Range ALgorithm). The dashed lines show the impurity concentration for each of the implant energies and the full line is the resulting impurity profile.

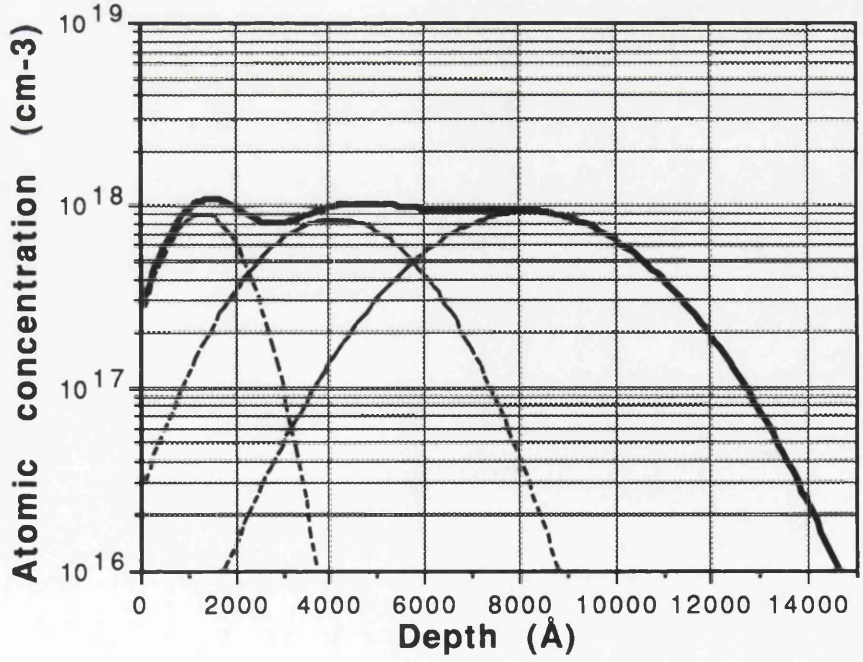

Fig.6.4.1.3 Boron implantation profile as calculated by PRAL for three separate implants at 50, 170 and 400keV.

The calculated impurity profiles for the fluorine and boron implants are shown in figs. 6.4.1.2 and 6.4.1.3 respectively. Implanted test samples were investigated using Secondary Ion Mass Spectroscopy (SIMS) to verify the implant profiles of boron and fluorine. The results showed good agreement with the distribution profiles calculated by PRAL. A diagram showing a plot of impurity concentration as a function of depth into the material for a fluorine implanted (but unannealed) sample is shown in fig. 6.4.1.4. The SIMS profile shows a tail in the concentration below the predicted implantation range. This may be due to channeling, an effect that has not been taken into consideration in the PRAL and TRIM-91 calculations, but which may be of considerable importance when implanting into structures with additional quantum wells below the implant region.

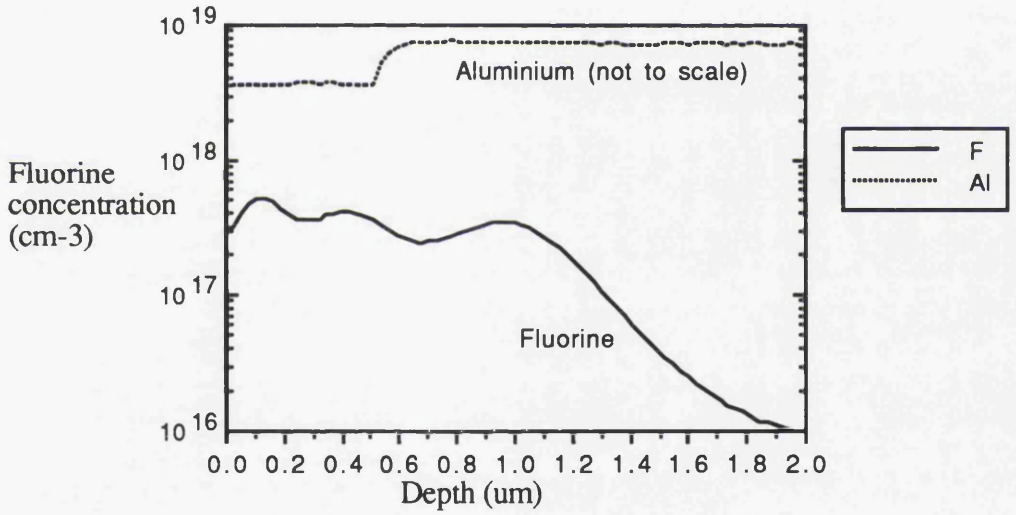

Fig, 6.4.1.4 Diagram showing the SIMS profile of the fluorine implanted sample prior to the annealing stage.

The Monte-Carlo simulation program TRIM-91 mentioned in Chapter 3 was used to model the interaction between impurity ions and target material lattice atoms. The loss mechanisms consist, as explained in Chapter 3, of ionization and collision events. Fig. 6.4.1.5 shows the energy loss due to ionization as a function of depth in the target material for the three implant sequence of fluorine used here. Included is also the ionization energy loss of the recoils due to the ion-atom interaction. The ionization loss is seen to decrease with increasing depth in the material.

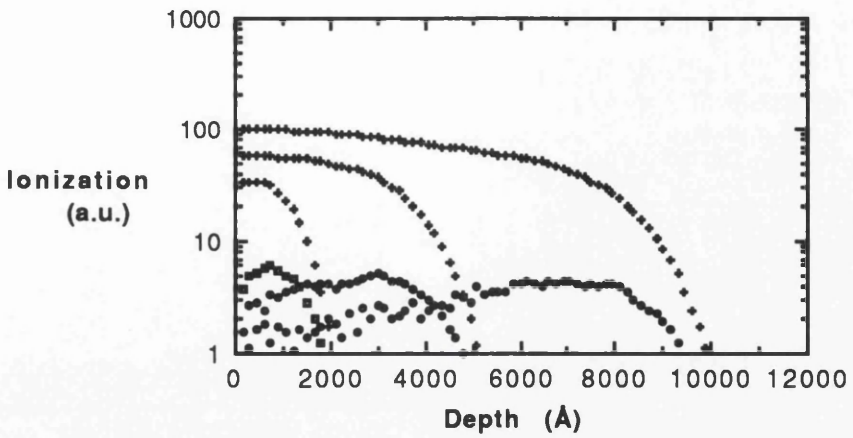

Fig.6.4.1.5 Monte-Carlo simulation of the depth-dependent ionization energy loss for the three-implant sequence in the case of fluorine (80, 260 and 700 keV).The upper curves are for incident ion interactions, the lower curves are for recoil interactions.

Fig.6.4.1.6 shows the corresponding plot of the energy loss due to phonon generation as a function of depth for the three-implant sequence. The phonon generation is seen to increase with depth until it reaches a maximum at about the same depth as that of maximum impurity concentration. This is because the ions to a large extent are prevented from direct collisions with the lattice at high energies (cf. Chapter 3) and need to lose most of their kinetic energy before they can participate in phonon generation. It is worth noting that the energy loss mechanisms here are plotted against real depth in the target material rather than the ion range. This means that some of the phonon energy seen at shallow depths is contributed from ions which have travelled a distance comparable to the mean projected range, and does not necessarily imply that the phonons are generated in the initial stages of the ion traverse.

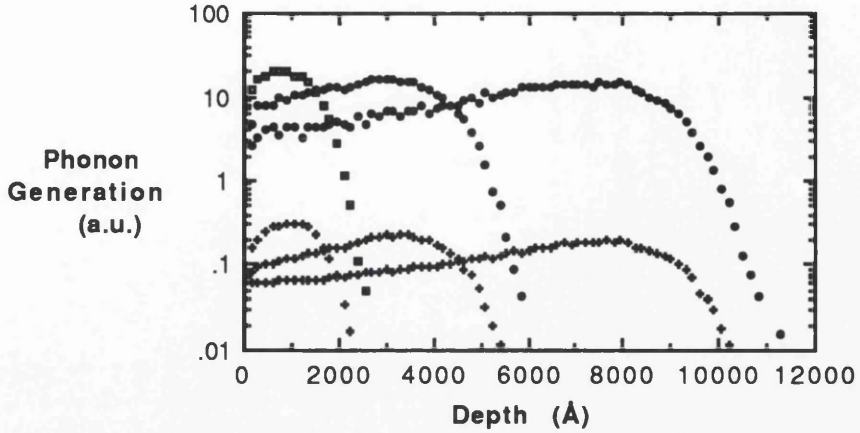

Fig.6.4.1.6 Diagram showing Monte-Carlo simulation of the depth-dependent energy loss resulting from generation of phonons for the three-implant sequence in the case of fluorine (80, 260 and 700 keV). The upper curves are for incident ion interactions, the lower curves are for recoil interactions.

The relative intensities of the two loss mechanisms are shown more clearly in fig.6.4.1.7. This graph shows a more detailed plot of the 260 keV fluorine implant. The ionization energy loss clearly constitutes a larger part of the total loss than the energy loss due to phonon generation, illustrating again that only a small part of the initial energy is resulting in vacancies through direct collisions and, consequently, phonons.

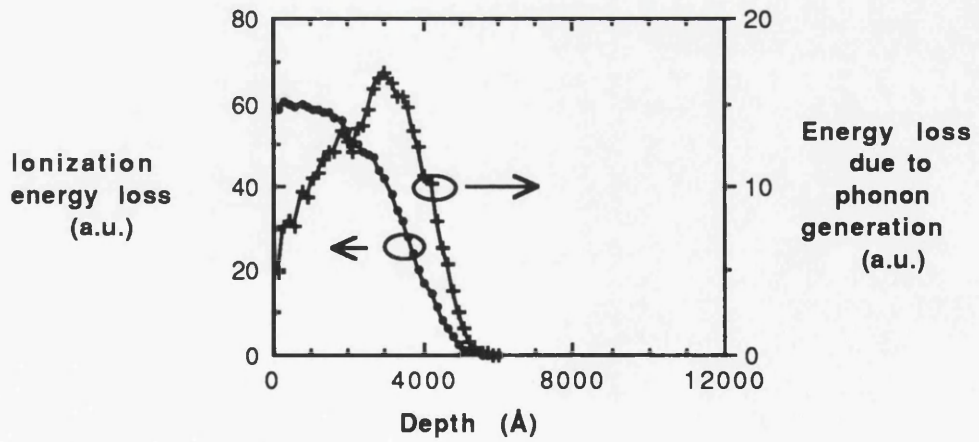

Fig.6.4.1.7 Diagram of energy loss mechanisms as a function of depth into target material for 260 keV fluorine implantation.

The direct proportionality between the phonon-related energy loss and the number of vacancies created is illustrated in fig. 6.4.1.8. The single-implant case is again shown here.

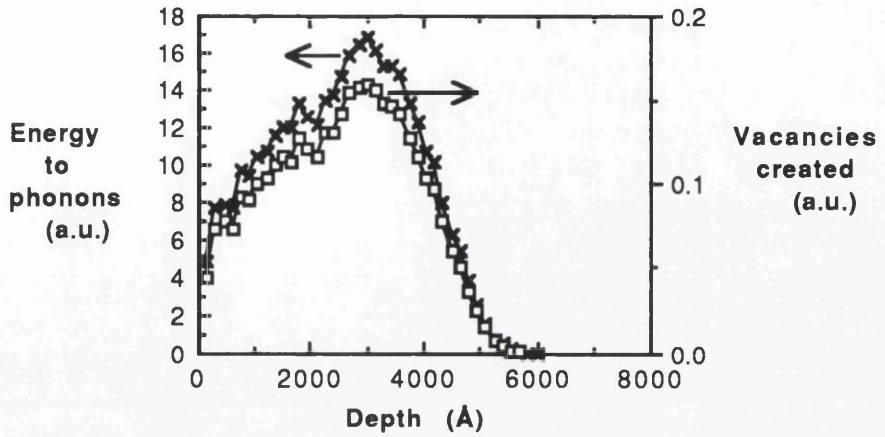

Fig.6.4.1.8 TRIM calculation of energy transferred to phonons (x) and vacancies generated (open squares) plotted against depth for 260 keV fluorine implant.

The depth distribution of fluorine resulting from each implant energy was used to obtain a Monte-Carlo simulation of the concentration profile. This is shown in fig.6.4.1.9.

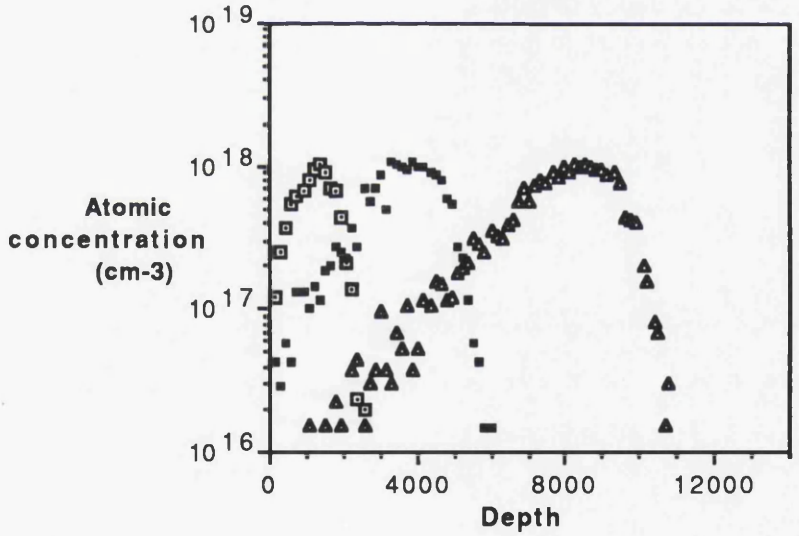

Fig.6.4.1.9 Diagram showing the ion concentration as a function of depth for the triple implant of fluorine. Concentrations are calculated from an average concentration at the projected range in the Trim-91 simulation.

Boron implantation yields similar results for the general nature of the loss mechanisms.

The depth (or ion path-length-) dependency of the loss mechanisms have an impact on the technique of impurity induced disordering with ion implantation. Because the intermixing effect in part is dependent on the concentration of vacancies, the intermixing coefficient will

be larger in regions with more induced damage. This has previously been confirmed by experiments (cf. section 3.2) involving disordering using ion implantation with impurities known to be inert with respect to impurity induced disordering. The shift in energy found in these cases corresponded purely to disordering due to the induced damage. In cases where active disordering impurities are used, the vacancies created through the collisions can be expected to increase the local rate of disordering. Also, since the maximum initial concentration of vacancies coincide with the localised maximum impurity concentration, a further increase in the localised behaviour of the ion-implanted impurity induced disordering process can be expected. However, for the three-implant sequence used here, the resulting vacancy profiles are quite flat over the depth range of interest, and negligible variation in intermixing with depth is expected.

A conventional diffusion furnace with a high-purity nitrogen flow atmosphere was used for the annealing. The samples were mounted in a high-purity graphite box. Protection against As desorption was provided by the inclusion of a small volume of Ga loaded with GaAs to produce a high local As vapour pressure, and also by capping the samples with a layer of plasma-deposited silicon dioxide prior to annealing. Annealing experiments using silicon nitride capping had been proven to give very similar results, but silicon dioxide was favoured because it was much easier to remove. It had also been established[8] that any contribution to intermixing from vacancies created by diffusion of gallium into the SiO_2 capping layer[9] was small using our deposition and annealing conditions. In the case of the 60 Å well material the abovementioned projection of annealing conditions indicate an annealing temperature of 890 °C for times of 90 minutes for the fluorine sample and 120 minutes for the boron implanted sample to give bandgap shifts in the region of 60 meV. The difference in annealing times is due to the slower disordering process in the boron compared to the fluorine system, where fluorine typically results in a group III interdiffusion coefficient an order of magnitude larger than boron. The annealing conditions estimated above were used as the starting parameters for the disordering experiments, and

the annealing times were later extended to 4 hours in the case of the 60Å well material QT18 to examine the effect of longer annealing times.

The degree of disordering is frequently measured in terms of the terms of the shift in bandgap energy after annealing, and this shift was measured for the disordered samples used here. The photoluminescence efficiency proved to be much lower for the boron implanted material than for fluorine implanted material, and the exciton peak position and linewidth at room temperature could not always be properly resolved in the case of boron implanted material. This was especially a limiting factor for the CB364 and CB365 materials, in which cases only the exciton peaks for the fluorine implanted and annealed samples were used. Typical results from the photoluminescence on the 60 Å quantum well material are shown in the diagram fig.6.4.1.10 below.

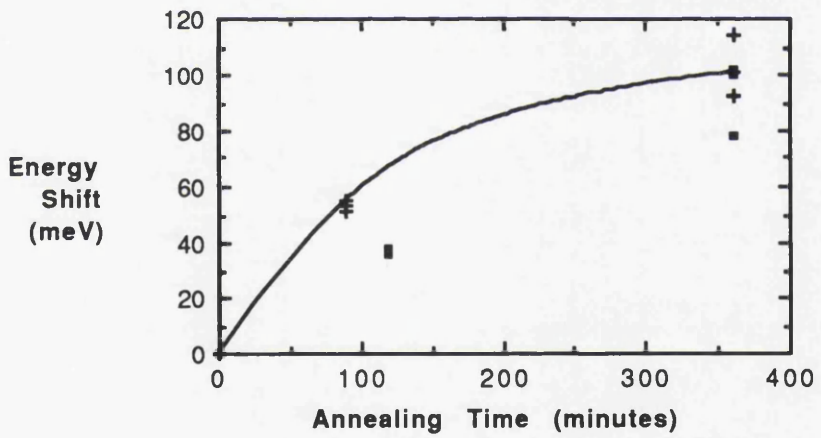

Fig. 6.4.1.10 Diagram showing energy shift in 60 L_z material with disordering for the times used for the grating coupler structures. + denotes fluorine implanted material and the small squares are for the boron implanted material. The line is only drawn to guide the eye and is not an attempt at modelling the energy change with disordering.

Both unimplanted virgin material and implanted and annealed samples were examined using SIMS to investigate the intermixing and diffusion effects. Fig.6.4.1.11 shows the SIMS profile of Al and Ga in the control sample. The quantum wells show up as a periodic modulation in the fractional content of Ga and Al in the material. The longer period

modulation that can be observed results from the sampling frequency of the SIMS system, and is not a real material modulation.

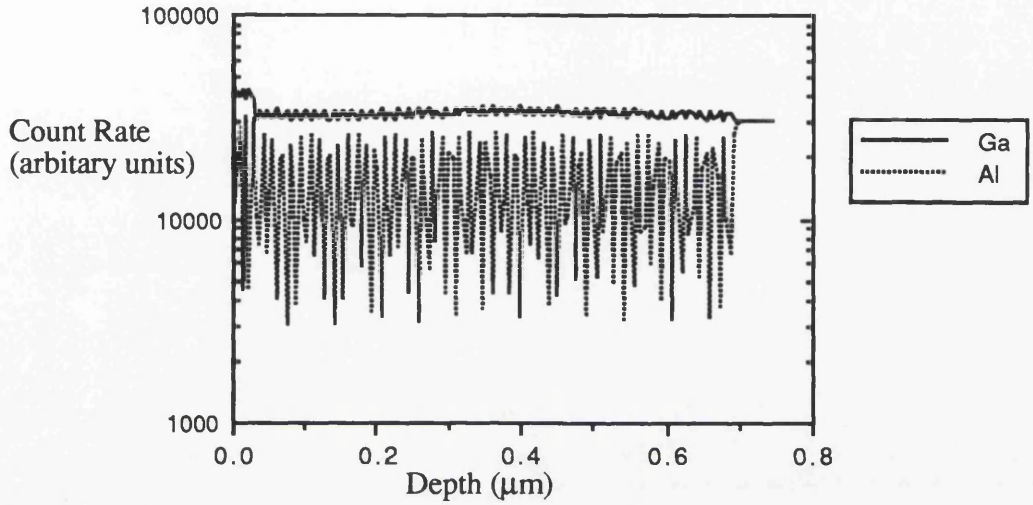

Fig.6.4.1.11 Diagram showing the SIMS profile of as-grown MQW material.

Fig.6.4.1.12 below, shows the SIMS profile of the MQW material after implantation with fluorine and subsequent annealing at 890° C for 90 minutes. The fluctuations in gallium and aluminium are here observed to be much smaller than in the case of the as-grown material, reflecting the smoothing-out of the quantum wells by the IID process.

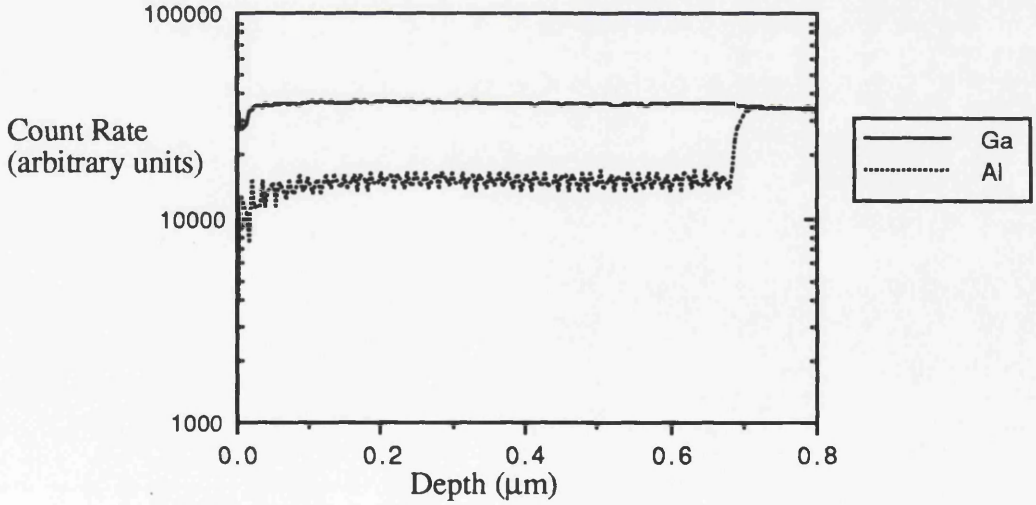

Fig. 6.4.1.12 Diagram showing the SIMS profile of MQW material after fluorine implantation and annealing at 890° C for 90 minutes.

The SIMS analysis also provided details of the distribution of fluorine and boron before and after annealing. The pre-anneal distribution had been modelled by PRAL and TRIM-91 analysis before the implantation, and the SIMS analysis could be used to confirm the accuracy of the predictions. The impurity distribution as found by SIMS agreed well with the models used, although the peak concentration per unit volume was found to be slightly lower than predicted in the case of the fluorine implant and slightly higher in the case of the boron implant. The observed difference may be due to a combination of the choice of the average concentration at the projected range for equation 3.4.3.2.2 in section 3.4.3 and also the accuracy of the measured values, but no detailed analysis of the accuracy of the SIMS method is going to be entered into here.

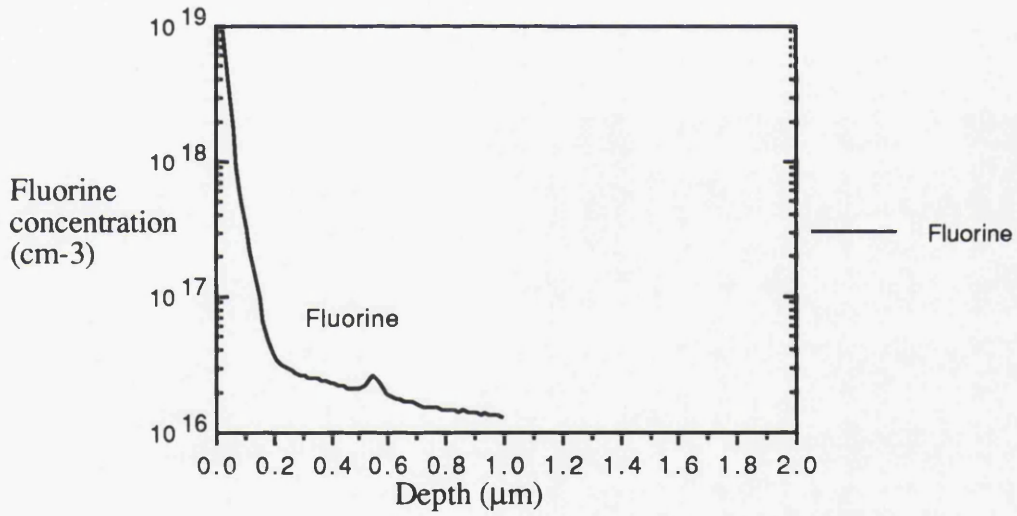

Fig.6.4.1.13 Diagram showing the SIMS profile of the fluorine implanted sample after annealing at 890° C for 90 minutes. The impurity concentration is seen to be highest at the surface of the sample.

It is well known that some dopants have greater diffusion coefficients than others, and this can be a problem in the growth and processing of some semiconductor devices needing well defined interface regions in highly doped p-n junctions. The SIMS analysis of the impurity distribution after the annealing stage allowed for the study of the diffusion of the impurities within the semiconductor. The boron was found to be very stable, and no appreciable difference was observed in the distribution before and after annealing at 890° C for 2 hours. The fluorine did however have a very high diffusion rate, and this is illustrated

in figs.6.4.1.4 and 6.4.1.13. Here the distribution before and after annealing is shown, and the fluorine is seen to diffuse into the substrate and out to the surface.

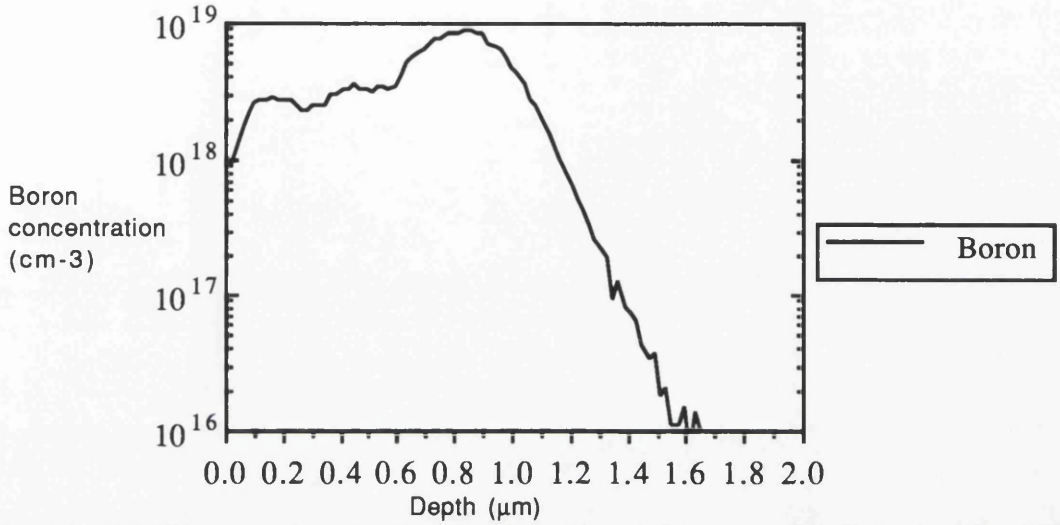

Fig.6.4.1.14 Diagram showing the SIMS profile of the boron distribution after annealing at 890°C for 120

The high diffusion rate of the fluorine impurities is clearly a problem for this application, especially since the IID process depends on the local fluorine concentration. The decrease in concentration at depths larger than 0.1 μm observed in the above SIMS plot leads to a self-limiting effect on the degree of disordering that can be achieved, and the uniformity of the disordering will also be affected for longer annealing times. This will also manifest itself in a broadening of the observed photoluminescence peaks, making it difficult to distinguish a single peak. Additionally, since there is no reason to expect any directionality in the diffusion process, any patterning of the implant will have a reduced effect. A possible way around this problem may be to use a rapid thermal annealing process, whereby the disordering may be achieved in a timespan too short for any appreciable impurity diffusion to occur.

Electrochemical profile plots were also obtained from these samples to establish the level of active dopants in the implanted and annealed material. The resulting plots of doping concentration versus depth are shown in fig. 6.4.1.15. There is little contribution to the doping level from the implanted impurities, confirming that boron and fluorine are not active dopants in the GaAs-AlGaAs material system at room temperature.

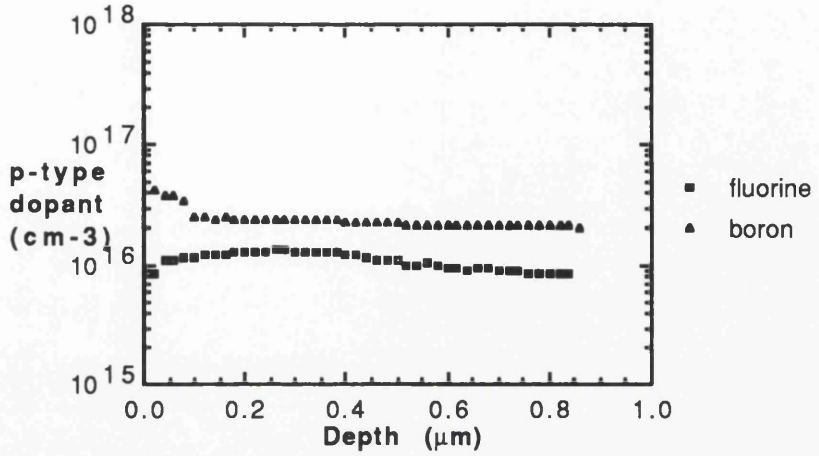

Fig. 6.4.1.15 Electrochemical etch profiling plot of dopant concentration versus depth for materials that have been implanted with boron and fluorine and annealed at 890° C.

6.4.2 Material Refractive index of IID MQW

The implanted and annealed 60Å well material samples were made into grating couplers using the same method as described for the virgin material couplers. The waveguide refractive index was thereafter measured and the material refractive index calculated from the data obtained. The results of these measurements and calculations are shown in the subsequent figures.

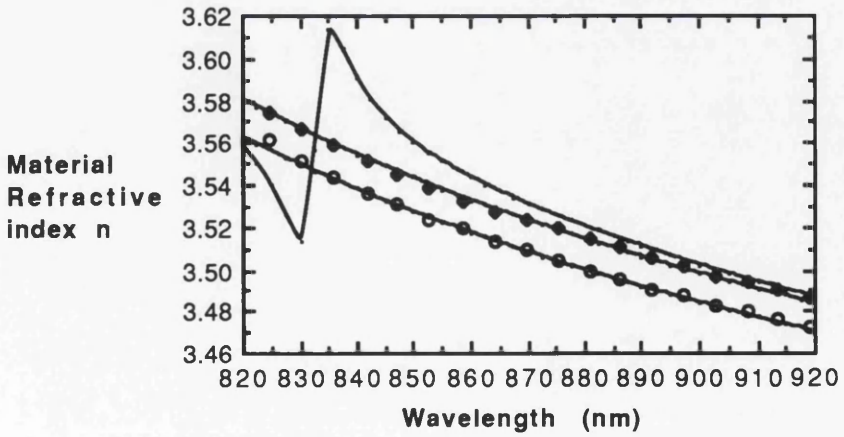

Fig.6.4.2.1 Plot of TE material refractive index versus wavelength for partial (diamonds) and complete disordering (circles) using fluorine for the 60 Å quantum well material system.

The effect of further disordering was examined by using longer annealing times following implantation. Samples of the QT18 material were implanted with the same doses of boron and fluorine and annealed for 4 hours at 890° C and processed into grating couplers. The resulting dispersion curves of the refractive index for the two polarisations are shown in figs.6.4.2.1 through 6.4.2.4, where they are plotted together with the corresponding curves of virgin material and partially disordered material.

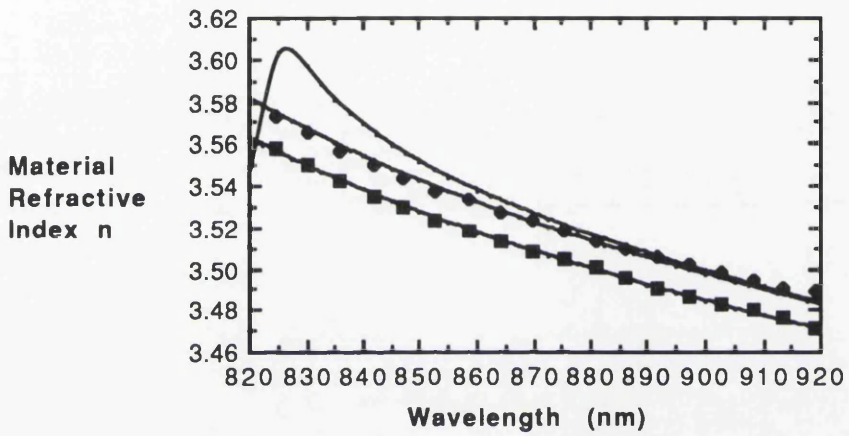

Fig.6.4.2.2 Plot of TM material refractive index vs wavelength for partial (diamonds) and complete disordering (squares) using fluorine for the 60 Å quantum well material system.

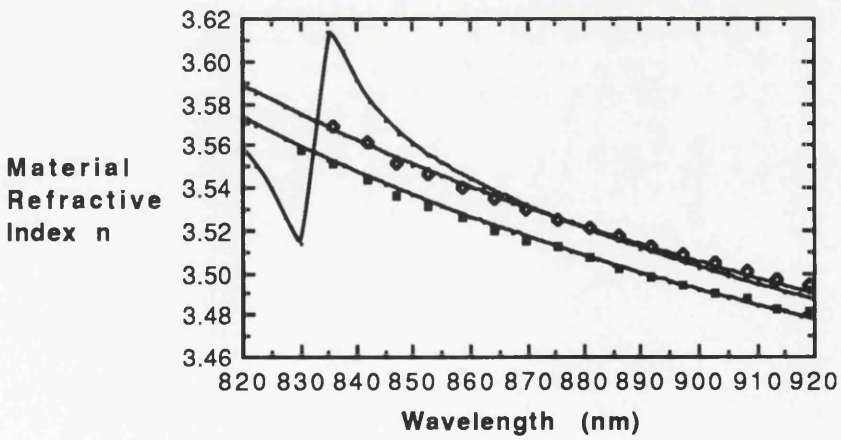

Fig.6.4.2.3 Plot of TE material refractive index versus wavelength for partial (diamonds) and complete disordering (squares) using boron for the 60 Å quantum well material system.

The slope of the refractive index is observed to be less steep following disordering, and from a modelling point of view it departs from the single oscillator model for quantum well material and approaches the case of the AlGaAs dispersion curve for the samples annealed for 4 hours.

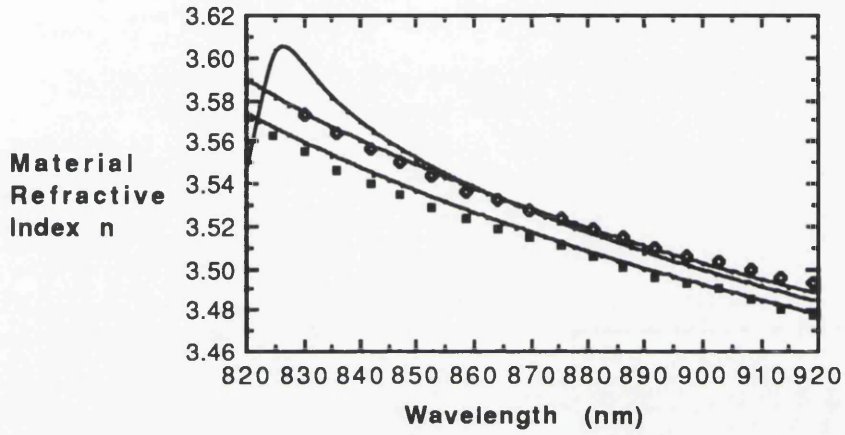

Fig.6.4.2.4 Plot of TM material refractive index vs wavelength for partial (diamonds) and complete disordering (squares) using boron for the 60 Å quantum well material system.

The refractive index change produced by IID using boron is much smaller than for IID using fluorine for comparable disordering times. This is shown more clearly in figs. 6.4.2.5 and 6.4.2.6, where the net refractive index changes produced by IID using boron and fluorine on the 60Å well system are shown for the TE and TM polarisations respectively. The annealing times are 90 minutes for the fluorine containing sample and 120 minutes for the boron containing sample, but the induced change is still smaller for the boron case. The tendency compares well with the measured shifts in the photoluminescence peaks with disordering in the two cases, where fluorine implanted material annealed for 90 minutes showed a PL peak shift nearly 20 meV larger than boron implanted material annealed for 120 minutes.

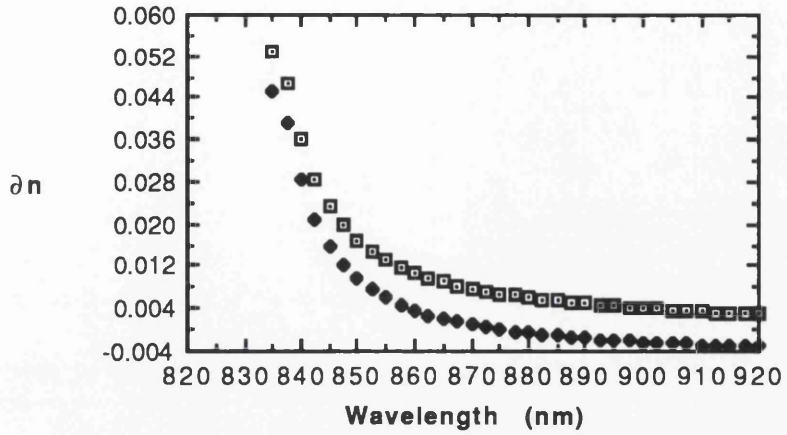

Fig.6.4.2.5 The TE refractive index change produced by IID using fluorine (squares) and boron (diamonds) for 90 and 120 minutes respectively.

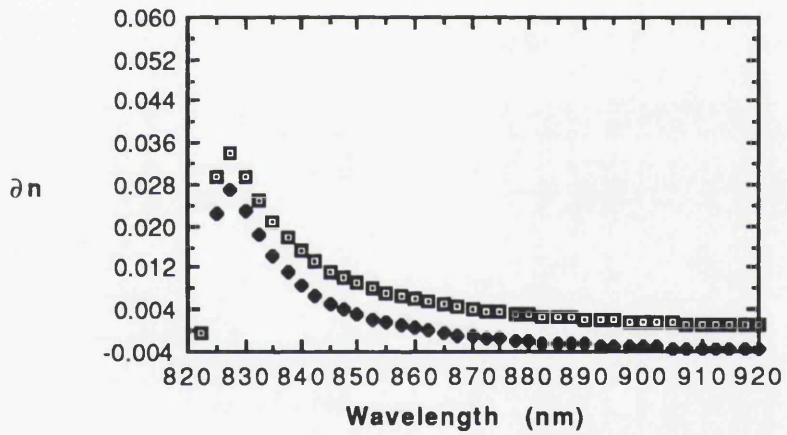

Fig.6.4.2.6 The TM refractive index change produced by IID using fluorine (squares) and boron (diamonds) for 90 and 120 minutes respectively.

The same tendency in the degree of refractive index change was observed when samples implanted with boron were annealed for 4 hours and their net refractive index change compared with results from fluorine implanted material annealed using the same annealing conditions and -time. Comparisons of the net change in refractive index for TE and TM polarised light in the case of 4 hour anneals are shown in figs. 6.4.2.7 and 6.4.2.8.

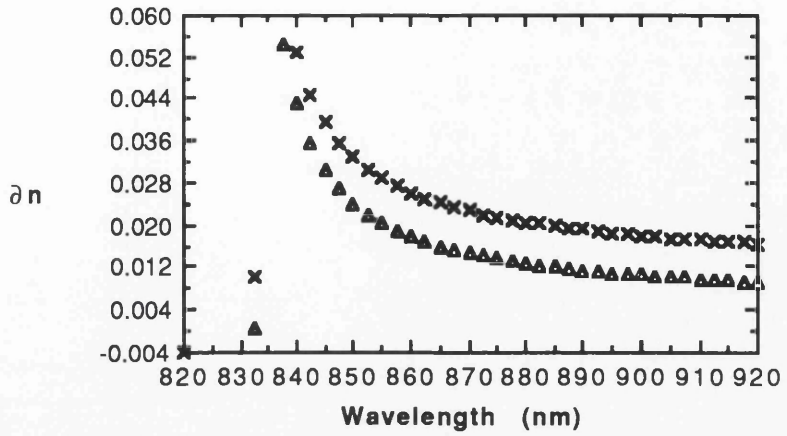

Fig.6.4.2.7 The TE refractive index change produced by IID after implantation with fluorine (x) and boron (Δ) and subsequent annealing for 4 hours.

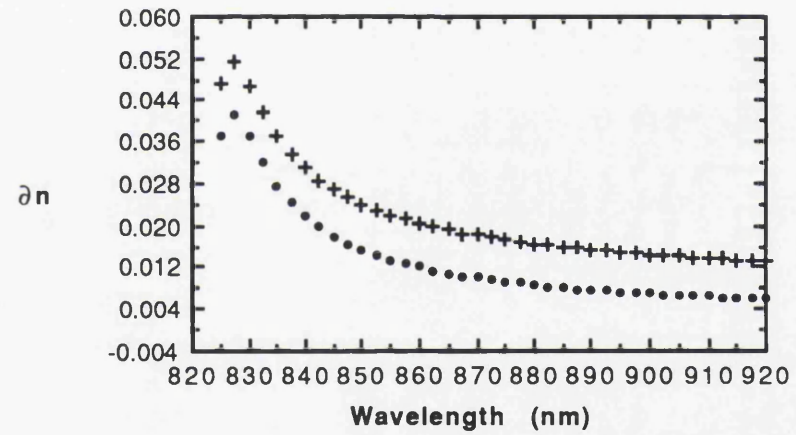

Fig.6.4.2.8 The TM refractive index change produced by IID after implantation with fluorine (+) and boron (circles) and subsequent annealing for 4 hours.

The birefringence is found to decrease dramatically after disordering. The birefringence of the as-grown 60Å well material is shown in fig. 6.4.2.9 together with that of fluorine implanted and annealed material. Annealing times were 90 and 360 minutes. The birefringence is reduced substantially in the material after annealing for 90 minutes, and after 360 minutes there is no discernable birefringence (not shown in diagram).

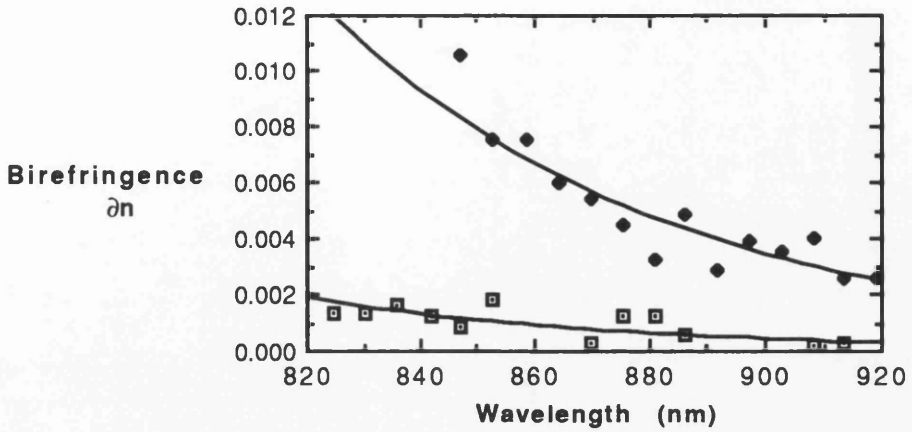

Fig. 6.4.2.9 Diagram of birefringence ∂n of 60 Å quantum well material before (filled diamonds) and after (open squares) partial disordering using fluorine.

This reduction in birefringence is due to two effects. Firstly, the disordering process is seen to both move the excitons to shorter wavelengths, and to reduce the intensities of the transitions.

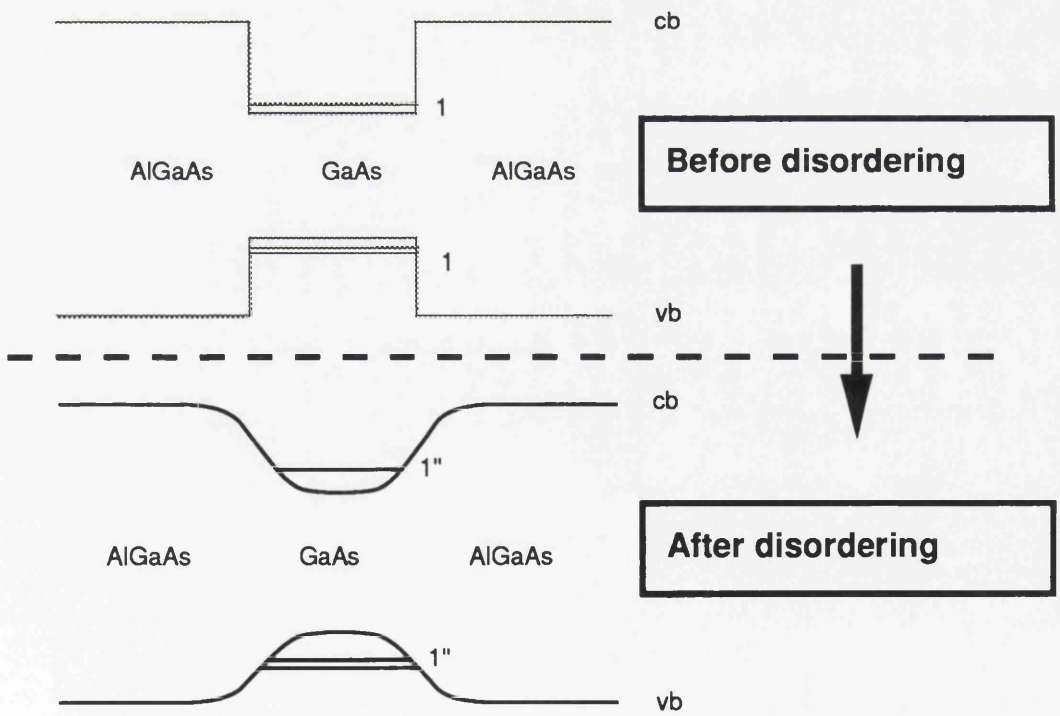

6.4.2.10 Diagram illustrating effect of disordering on quantum well potential.

The apparent reduction in transition intensity and consequently oscillator strength, is observable at low temperatures but is perhaps most evident at room temperature. Secondly, the distribution within one period of the structure is changed by the disordering process.

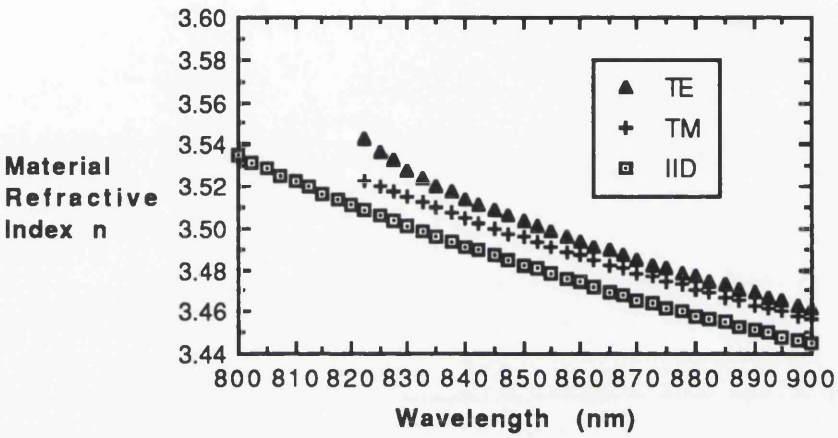

Fig.6.4.2.11 Dispersion of the refractive indices of as-grown and `completely disordered' 40Å well material.

The boundary conditions for the TE and TM modes change as the interfaces between well and barrier material become 'smeared out' as illustrated in fig.6.4.2.10. The effective widths of the well and barriers change, as does the modulation depth of the well as aluminium diffuses in. Figs. 6.4.2.11 through 6.4.2.13 show comparative results for 40 Å well material.

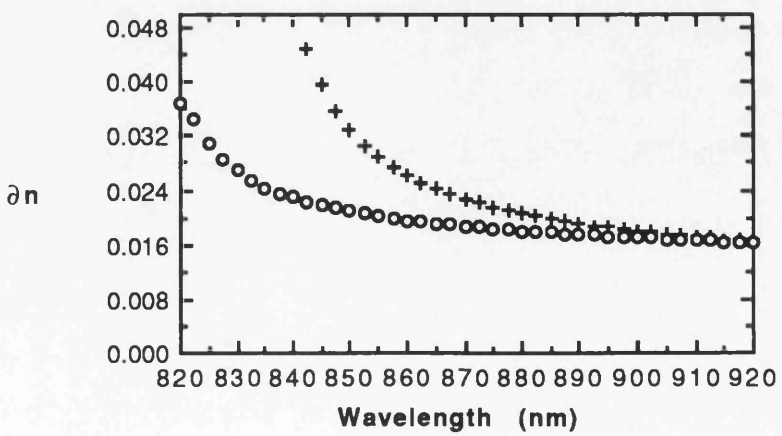

Fig.6.4.2.12 Comparison of the dispersion of the TE refractive index change for the two structures assumed to be totally disordered (o) 40Å well material annealed for 90 mins. and (+) 60Å well material annealed for 4 hours

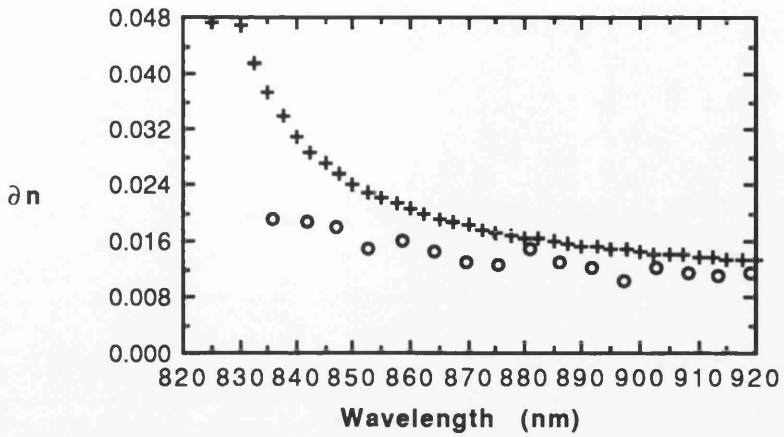

Fig.6.4.2.13 Comparison of the dispersion of the TM refractive index change for the two structures assumed to be totally disordered (o) 40Å well material annealed for 90 mins. and (+) 60Å well material annealed for 4 hours

6.4.3 Theoretical calculations

Independently from the work of this thesis, A. Meney also at the University of Glasgow, had written a computer program for calculation of energy band structures in quantum well structures[10]. The program used the finite difference method to calculate the energy bands in near-arbitrarily shaped quantum wells, and incorporated routines to yield the absorption coefficient of the material (based on the energy band calculations), from which the refractive index could be deduced.

The creator of the program customised it to accomodate a potential well model suited for the impurity induced disordering well shape. The model took the form of a set of error functions to represent the diffusion of aluminium from the barriers into the wells, and was based on a method proposed by Kash et al[11]. The aluminium concentration profile in the barrier-well system after disordering was taken as[12] $1-C(z)$ with the gallium concentration profile $C(z)$:

$$C(z) = (1-x) + \tfrac{1}{2}x\left[erf\left(\frac{\frac{w}{2}-z}{2\sqrt{Dt}}\right) + erf\left(\frac{\frac{w}{2}+z}{2\sqrt{Dt}}\right)\right] \qquad (6.4.3.1)$$

The centre of the well is defined as z=0, w is the well (and barrier) width before disordering, t is the annealing time and D is the interdiffusion coefficient of Al and Ga in the presence of the impurity used. The potential profile V(z) of the well/barrier was modelled using the above Al concentration profile and by choosing V(z=0)=0. A conduction/valence band offset ratio of 65/35 was used, giving:

$$V(z) = V_0 x\left[erf\left(\frac{w}{4\sqrt{Dt}}\right) - \left\{ erf\left(\frac{\frac{w}{2}-z}{2\sqrt{Dt}}\right) + erf\left(\frac{\frac{w}{2}+z}{2\sqrt{Dt}}\right)\right\}\right] \times \begin{Bmatrix} 65\%(conduction-band) \\ 35\%(valence-band) \end{Bmatrix} \qquad (6.4.3.2)$$

V_o is the total barrier height (conduction and valence band) for the as-grown quantum well, and the shift in the bandgap at z=0 due to Al in-diffusion ΔE_g is given by:

$$\Delta E_g = V_0 x\left[1 - erf\left(\frac{w}{4\sqrt{Dt}}\right)\right] \qquad (6.4.3.3)$$

The relationship between the shift in exciton transition energy and amount of disordering could now be derived. The energy shift was plotted as a function of diffusion length $L=\sqrt{Dt}$ and also versus interdiffusion coefficient D_{int}. The plot of the energy shift versus the interdiffusion coefficient for constant time is shown in fig.6.4.3.1.

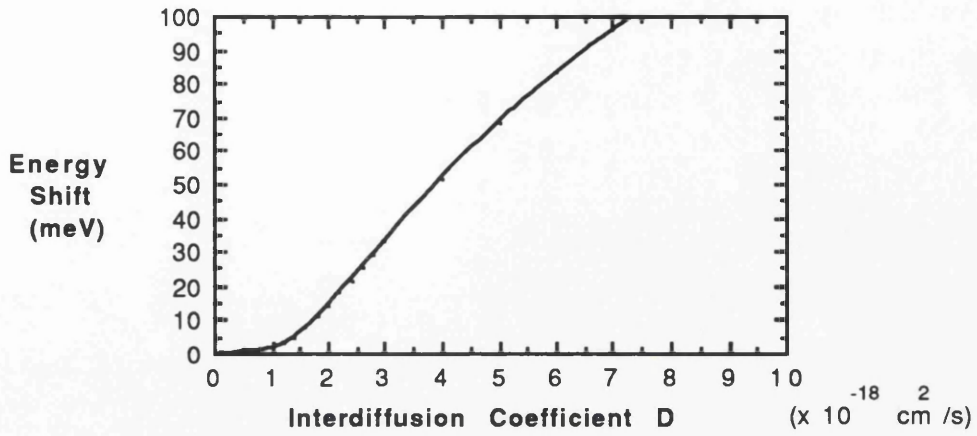

Fig.6.4.3.1 Plot of the relationship between the n=1 heavy-hole to conduction band transition energy shift with diffusion and the interdiffusion coefficient D_{int} calculated using the finite difference method in ref.7.

Using preliminary results from this thesis, the interdiffusion coefficient was estimated at 2.5 x 10^{-18} cm^2s^{-1}. These were early results, and later processing induced larger energy shifts, typically ≈50 meV for fluorine implanted material after 90 minutes annealing and ≈35 meV for boron implanted material annealed for 120 minutes.

By using these later values for the energy shift after 90, 120 and 360 minutes, new estimates were obtained for the interdiffusion coefficient of boron and fluorine implanted materials. These were 4 x 10^{-18} cm^2s^{-1} for fluorine and 3.35 x 10^{-18} cm^2s^{-1} for boron. These values compare to published experimentally obtained data of 3 x 10^{-18} cm^2s^{-1} and 1 x 10^{-19} cm^2s^{-1} for fluorine and boron respectively, when annealed at 800°C. These values are in very good agreement considering that the annealing for the published results took place closer to the activation energy needed for disordering by the two impurities. The values obtained were used to plot the photoluminescence peak energy shift versus time for both boron and fluorine IID. These results are shown in fig.6.4.3.2, together with the experimentally determined datapoints from fig.6.4.1.10.

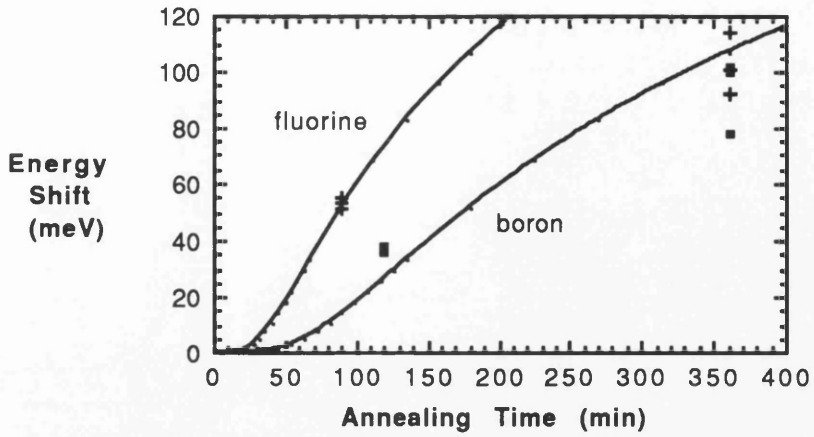

Fig. 6.4.3.2 Energy versus annealing time with included calculated graphs based on D(interdiffusion) of 4x10-18 cm^2s^{-1} for fluorine and 3.35x10-18 cm^2s^{-1} for boron.

The energy shifts of fluorine implanted at long annealing times are obviously overestimated here. The energy shift of the fluorine implanted samples after 360 minutes annealing are comparable to those of the boron implanted samples with the same annealing time. This supports the findings from the SIMS investigation, indicating that the disordering due to the fluorine impurity slows down markedly as diffusion depletes the fluorine concentration in the MQW region. The effect of fluorine diffusing out of the MQW region will probably be noticeable even after 90 minutes, and the initial interdiffusion coefficient may therefore be higher than that estimated here.

It is naturally difficult to accurately state what the exact interdiffusion coefficient is for the two cases. In the case of boron the measured energy shift after 90 minutes is larger than that predicted by the model. This can however be explained by the damage-induced disordering that is believed to take place in the initial part of the annealing stage. Investigations on ion species dependence of the IID process[13] have shown that even non-disordering impurities give rise to a damaged-induced energy shift (e.g. ≈5 meV for Be) in the initial stages of the annealing process. The damage was believed to be almost totally annealed out after 30 minutes, and would not add to the energy shift after this time. It is not unreasonable to assume that such a damage-induced energy shift should be larger for an active disordering impurity such as B than for, say, Be since the rate of disordering is

thought to be dependent on the concentration of defects (cf. Chapter 3). This effect could therefore account for the difference between the model for boron and the measured values after 120 minutes annealing at 890°C, and it will of course further complicate making an accurate estimate of the true interdiffusion coefficient of fluorine.

A. Meney used the preliminary results to calculate the total band structure of the fluorine implanted and annealed system for various degrees of disordering. Although these data are underestimating the actual disordering in this later work, they should yield coefficients that are very close to the boron and the fluorine implanted systems. The absorption of the partially disordered material was derived from the energy band data of the computer model.

6.4.4 Absorption measurements

An independent method of determining refractive index shifts exists in the Kramers-Krönig transformation technique explained in section 2.3.2. This method relies on transforming the imaginary part of the dielectric function (absorption) to yield the real part of the function (-> refractive index). The imaginary part of the dielectric function can be obtained through absorption (transmission) measurements.

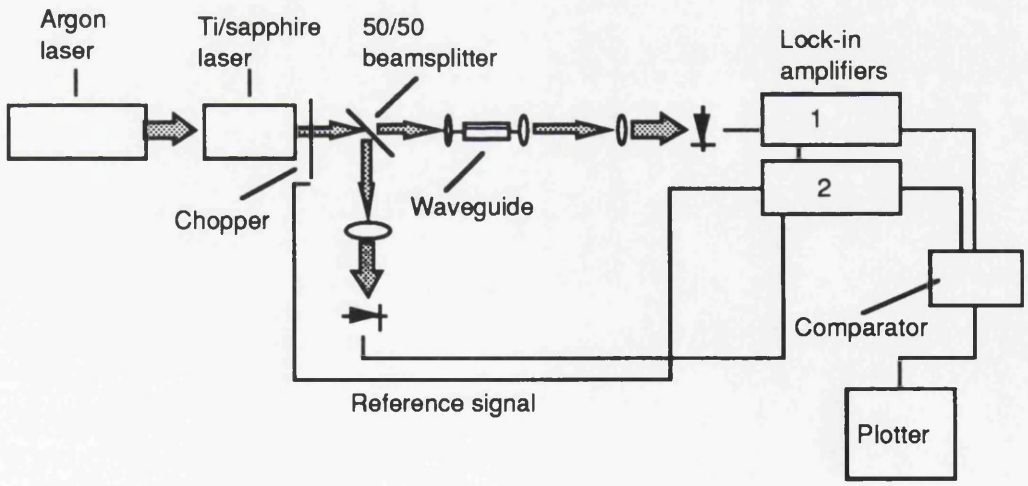

Fig.6.4.4.1 Diagram showing schematically the set-up used for the absorption measurements.

Waveguides were made from all the unimplanted and implanted and annealed samples, and the transmission was measured as a function of wavelength using the set-up illustrated in fig.6.4.4.1.

The set-up used the same tunable laser as was used for the grating coupler measurements, a beam splitter, an end-fire rig, collimating and focussing optics and two silicon photodiodes. The photodiodes were separately connected to two lock-in amplifiers and the outputs from the amplifiers were combined in a comparator before being output to an analogue x versus time plotter.

The tunable laser was scanned using a 1 rev/second motor, giving 5.65 nm/s scan speed. Start and stop points were indicated by short electric pulses to the plotter. The laser beam was split by a 50/50 cube beam splitter, and the input power was monitored by one of the photodiodes. The undiverted beam was used to excite waveguide modes in the suitably cleaved sample, and the output power was monitored by the second photodiode. Neutral density filters were used to keep the intensity below the saturation level of the photodiodes. The laser beam was chopped by a 1 kHz chopper which had a reference output connected to the lock-in amplifiers. TE-TM selection was facilitated by the inclusion of a half-wave plate and a polarizer in front of the chopper.

The wavelength-dependent responses of the two photodiode/lock-in amplifier systems were calibrated prior to the measurements, as were the losses in the components making up the set-up, including neutral density filters, lenses, beam splitter and the losses incurred by the end-fire coupling. The latter was determined using a combination of Fabry-Perot and conventional loss measurements as well as with a theoretical estimate of the losses involved. In the wavelength regime of interest, 800-900 nm, the calibrations obtained were as follows. The neutral density filters had transmissions of 2.3%, 11.8% and 30.3%. The 50% beamsplitter ratio was confirmed, and a beamsplitter input loss of 4% was measured. The intrinsic transmission of the end-fire coupling set-up was estimated to 11% for coupling through a lossless ridge waveguide.

Using the above set-up, plots of the absorption (transmission) of slab waveguides were obtained for both TE and TM polarisations in the range 780 to 920 nanometers. Both linear and logarithmic plots were obtained.

The waveguide optical absorption per unit length can be obtained from measurements of the intrinsic optical loss in a waveguide of known length d . Disregarding input and output coupling losses, the input I_{in} and output I_t powers are related through the absorption coefficient α::

$$I_t = I_{in} \exp(-\alpha d) \qquad (6.4.4.1)$$

The real input and output powers are found using the calibration values obtained before the transmission measurements were performed. To further calibrate the system, Fabry-Perot absorption measurements were performed on ridge waveguide structures at wavelengths below the absorption band-edge. Absorption values for wavelengths above the absorption edge were taken from previous experiments in the material system. When these factors were all known, the absolute absorption coefficient could be determined for any point on the transmission curve.

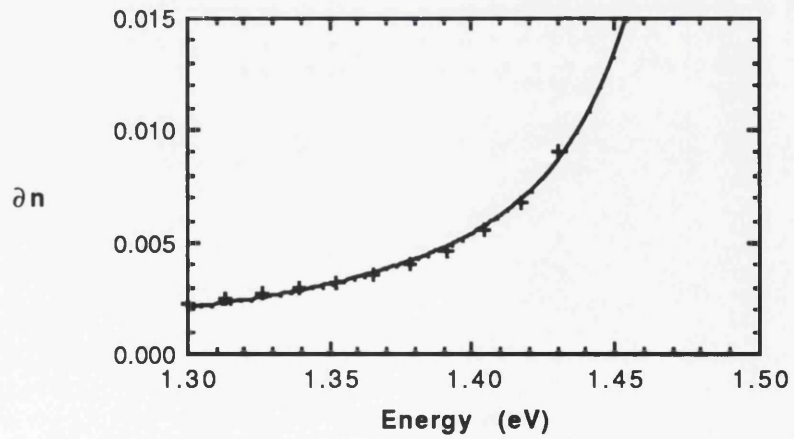

Fig.6.4.4.2 Plot of the TE refractive index difference ∂n between partially disordered (using fluorine) and as-grown material (whole line) for 60Å well material together with calculated values (discrete points) from Kramers-Krönig relations.

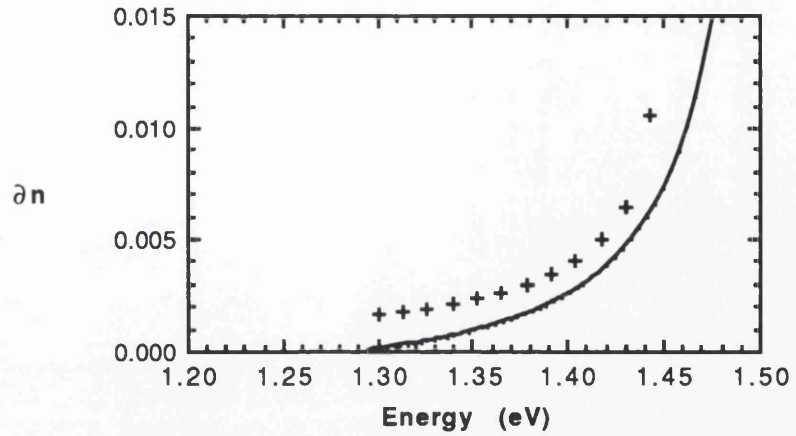

Fig.6.4.4.3 Plot of the TM refractive index difference ∂n between partially disordered (using fluorine) and as-grown material (whole line) for 60Å well material together with calculated values (discrete points) from Kramers-Krönig relations.

The absorption data were used to obtain the changes in absorption ($\Delta\alpha$) due to the neutral impurity induced disordering process. These data were subsequently used to obtain the changes in refractive index from the Kramers-Krönig transformations (equation 2.3.2.3). The results from these calculations on the 60Å quantum well material are shown in figs.6.4.4.2-7.

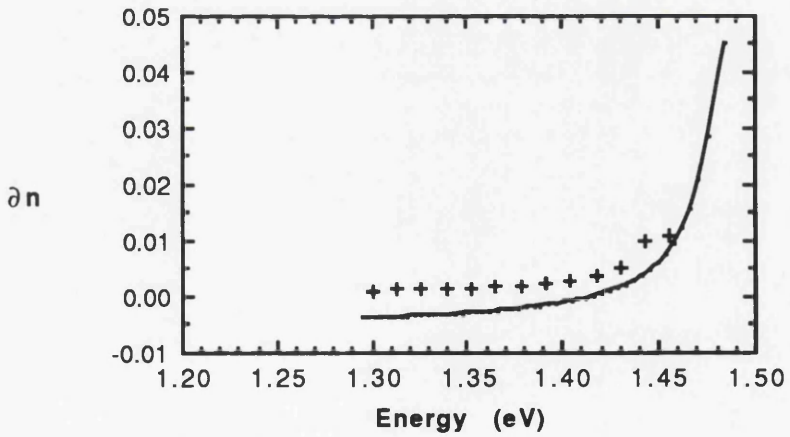

Fig.6.4.4.4 Plot of the TE refractive index difference ∂n between partially disordered (using boron) and as-grown material (whole line) for 60Å well material together with calculated values (discrete points) from Kramers-Krönig relations.

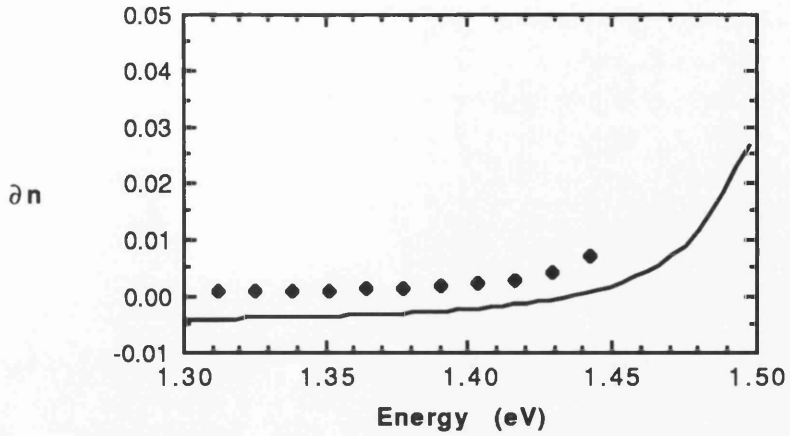

Fig.6.4.4.5 Plot of the TM refractive index difference ∂n between partially disordered (using boron) and as-grown material (whole line) for 60Å well material together with calculated values (discrete points) from Kramers-Krönig relations.

The above plots show that the Kramers-Krönig transformation on the absorption data from the partially disordered material generally gives values in excess of those measured by the grating coupler method. On the other hand, for the totally disordered case, the Kramers-Krönig transformations give a lower refractive index change than the grating coupler method. This discrepancy may in part arise from one or both of the following:

i) errors in the input refractive index for the cladding layer of the structure

ii) incorrect estimate of the absorption in the disordered material after disordering through contribution from radiation damage/defects, impurities or from disordering-related quantum size effects.

—Cladding layer refractive index:

The accuracy of the refractive index of the cladding layer has been ascertained in section 6.2 and these values are therefore not considered to be uncertain factors for the waveguides used here.

—Impurities:

Impurities that are dopants in semiconductors contribute to the refractive index of the semiconductor through the generation of free carriers. This effect is not expected from electrically neutral dopants. The impurities boron and fluorine have

been associated with deep levels in GaAs, and could theoretically have some effect on the material properties. The electrochemical etch profile of the implanted and annealed IID material however supports the assumption that neither boron nor fluorine contribute greatly to the free carrier population. Only a modest increase in the hole concentration was observed, comparable in magnitude to the experimental error in the profiling method. It is therefore improbable that the impurities themselves contribute to the refractive index of the material through the effect of free carrier generation.

—Radiation damage/Vacancies:

The method of ion implantation is known to produce large amounts of crystal damage. The damage takes the form of lattice imperfections involving interstitials and vacancies. These defects can act as donors or acceptors in the structure, depending on the type of defect, the type of host material and, in the case of interstitials, the impurity associated with the defect.

The damage introduced by ion implantation has been studied by different methods[14] to provide data on the regrowth of crystal lattice after implantation. On the basis of these studies the implanted material was assumed to be damage-free after relatively short annealing times at high temperatures (30 mins, 800°C in conventional furnaces). Ion implantation into GaAs-AlGaAs material has however been shown[15,16] to give dislocation loops at the edge of the implant range[16]. These loops are created during the implantation. The dislocation loops are types of radiation damage that involve several defects and are known as extended defects. Other types of these defects form during the annealing cycle, and extended defects can trap other defects, such as interstitials. Common to the extended defects is that they are more resistant to crystal healing than other localised defects, and require a higher temperature to anneal out. This is explained in the mechanism through which lattice defects are exterminated. The 'de-activation' energy used to remove a defect

comes from the lattice vibration. A single defect will not have a great influence on the vibration frequency, whereas extended defects can significantly reduce the frequency. Extended defects therefore alter the energy of the phonons in the material. This will influence the temperature and annealing time required for the crystal healing. Previous measurements on implanted material have indicated[14,15] that radiation damage has been almost completely healed after short anneal times (15 min, 800°C), but these measurements were performed by Rutherford backscattering and only probed the top 100nm region of the material. There is reason to believe that the dislocation loops extend deeper than this[14], and that the degree of radiation damage increases with implantation energy. These two points give support to the idea that there may still be significant damage in the form of extended defects after the initial stages of the anneal. This damage may then contribute to the real and imaginary parts of the dielectric function of the material, and could explain the results from the partially annealed samples. It is worth remembering that the implantation of the MQW waveguide structures in this thesis entailed three stages, which therefore would result in three regions of dislocation loop formation. The deeper (higher energy implant) region would be extending into the lower cladding layer. This could possibly have led to a sheet of locally altered refractive index that would yield a slightly different value for the refractive index of the partially disordered guide region. This could be a contributing reason for the observed higher index at longer wavelengths. Conversely, it may be argued that the effect of radiation damage on the hole and electron population is too small to significantly influence the dielectric function of the material. The scattering loss arising from the damage may however contribute to the observed losses without contributing to the refractive index of the material. This would result in an overestimated refractive index when this is calculated through Kramers-Krönig transformation on values obtained from absorption measurements.

In reality it is unlikely that the above constitute the real reasons for the anomalous behaviour of the long-wavelength refractive index in the partially disordered samples. If, for instance, the defects were responsible for the increased refractive index (through an increase in the absorption), then this would mean that the waveguide would exhibit great losses at long wavelengths. This has been shown not to be the case. Also, the annealing times and temperatures are such that it is unlikely that large concentrations of defects remain.

—Influence of quantum well shape:

The explanation is more likely found in changes to the quantum well arising from the disordering process. The long-wavelength increase in the refractive index of partially disordered quantum wells has been observed by other groups[17,18]. As a consequence of this, Li et al[19] performed model calculations on the electronic transitions in hyperbolically shaped quantum wells. The results from these calculations were used to determine theoretically the dielectric properties of a partially disordered quantum well structure. The dielectric function was studied as a function of the degree of intermixing r_d. r_d was defined as the ratio L_d/L_z, where L_d was the diffusion length and L_z the well width. The model results showed that for large degrees of intermixing ($r_d > 0.4$), the refractive index of the quantum well structure decreased with intermixing until it reached a value consistent with that of bulk material of composition equal to the material average of the well/barrier system. This was exactly as expected. A special case was however found for the combination of wide wells and small degrees of intermixing ($r_d < 0.4$). In these cases both the refractive index and the absorption were higher in the disordered wells than in the square wells. The consequence of this is that the quantum well profile is more important than the well width in terms of the variation in the dielectric constant.

This last item is very interesting, and offers a very good explanation for the apparently anomalous results found for the partially disordered samples here. The diffusion length $L_d=\sqrt{Dt}$ for the fluorine samples annealed for 90 minutes at 890°C is: $\sqrt{(4 \times 10^{-18}\ cm^2s^{-1} \times 5400s)} = 1.47 \times 10^{-7}$ cm (14.7 Å), and for boron annealed for 2 hours at the same temperature L_d is 15.5 Å. These diffusion lengths give intermixing ratios r_d of 0.25 and 0.26 for the two cases respectively. These values are much lower than the r_d crossover value of 0.4 found from the hyperbolic well model, and they are consistent with the observed disordering-induced refractive index increase at longer wavelengths.

The considerations of the dependence of the dielectric function on the well shape can also be used to explain the difference in refractive index values found from Kramers-Krönig transformation and measured values. The calculations performed here were based on the assumption that the maximum value of the absorption would be the same before and after disordering. The model calculations by Li et al clearly show that this is not a valid assumption. The hyperbolic well approximation shows that the maximum absorption for a partially disordered quantum well can be more than 20% higher than for the square well. Similarly, the maximum absorption of the completely disordered well structure is seen to be only 25% of the maximum absorption of the as-grown well.

A consequence of the hypothesis is that, after long annealing times (e.g. 4 hours), the IID material should have a refractive index comparable to that of bulk AlGaAs with an aluminium content equal to the material average of the MQW material. This gives $\bar{x}$=13% in the case of $L_z=L_b$ (QT18,CB364) and $x_{barrier}$=26%, and $\bar{x}$=15.6% in the case of L_z/L_b=40/60 (CB365).

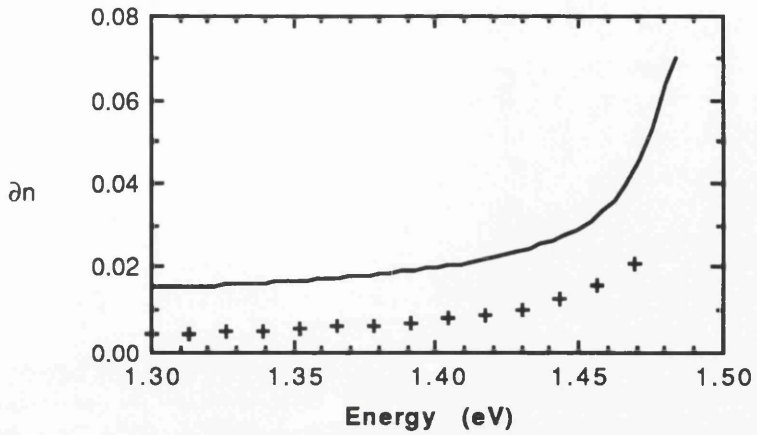

Fig.6.4.4.6 Plot of the TE refractive index difference ∂n between completely disordered (using fluorine) and as-grown material (whole line) for 60Å well material together with calculated values (discrete points) from Kramers-Krönig relations.

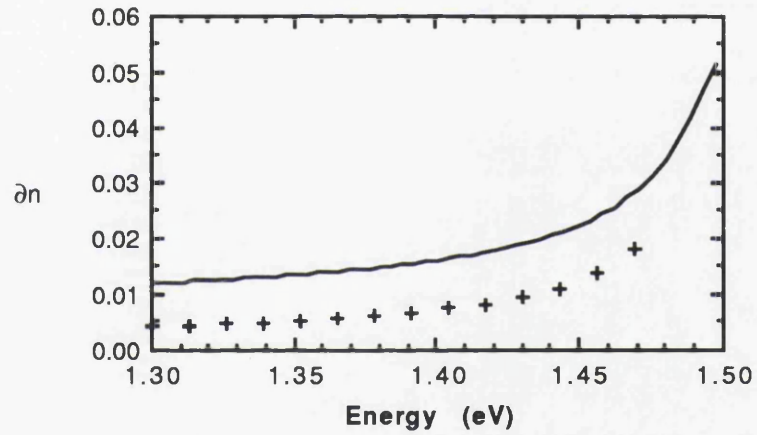

Fig.6.4.4.7 Plot of the TM refractive index difference ∂n between completely disordered (using fluorine) and as-grown material (whole line) for 60Å well material together with calculated values (discrete points) from Kramers-Krönig relations.

The refractive indices of the 4 hour annealed samples are shown in fig.6.4.4.8 together with the best-fitting MAM value for x. The x_{MAM} values for fluorine and boron disordered samples were 11.5% and 10.5% respectively. When the previously determined offset of 1.6% is added to these values, the aluminium percentages corresponding to the best fit become 13.1% and 12.1%, in excellent agreement with the theoretically predicted value. The boron implanted sample is seen to have slightly higher corresponding x-value than fluorine. This is consistent with the progressive disordering results, and may indicate that the presence of boron as an impurity influences the refractive index of the material. The fluorine implanted material shows no such tendency. This is consistent with both the

electrochemical profile and the SIMS analyses, the first of which showed a lower free carrier concentration in fluorine implanted material than for boron implanted material, and the latter of which showed that the fluorine rapidly diffused out of the quantum well region during annealing.

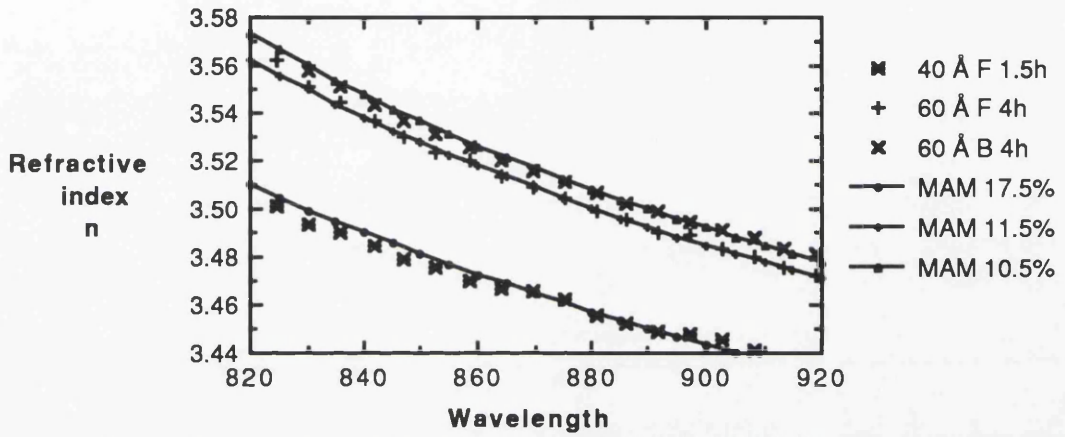

Fig. 6.4.4.8 Plot showing the material refractive index of the fluorine and boron implanted 60 Å well material after annealing for 4 hours, the fluorine implanted 40Å well material after 90 minutes annealing and the best-fitting MAM curves.

The comparison of the 40Å well material annealed for 90 minutes with the MAM curves gave a value x_{MAM} =17.5%. This corresponds to $\bar{x} \approx 19\%$, compared to the expected value of $\bar{x} = 15.6\%$. This indicates that the material has not been completely disordered and/or that the extended defects have not been annealed out, consistent with the arguments above. The shape of the refractive index dispersion curve and the photoluminescence measurements on the disordered 40Å well material indicated that the material was bulk AlGaAs. This may however reflect more on the fact that there were no excitonic transitions at room temperature. The room temperature excitons may in turn have been suppressed by crystal damage (increased phonon interaction) and the remaining band-edge variation may have influenced the dielectric properties of the material. The result of this could be that the optical properties of the material is decided by the effective band-gap of the material, meaning an energy band gap averaged over free space[20] and with a dependency on the depth of the bandgap modulation. This would result in an apparent aluminium content higher than the real material average of the quantum well structure.

6.5 Summary

This chapter has presented a systematic study of the effect IID has on the refractive index of MQW waveguides. In the process, the waveguide refractive indices were determined in the wavelength range 800-900 nm for AlGaAs waveguide material, with the aluminium composition ranging from 0 to 30%, and for GaAs multiple quantum well material, with well widths 40, 60 and 100Å and $Al_{0.26}Ga_{0.74}As$ barrier composition.The measurements were performed using the grating coupler method. The material refractive indices were obtained from the waveguide refractive indices through solutions of Maxwell's equations for a 2-D waveguide.

The AlGaAs refractive index results differed somewhat from published results from the most referenced sources[1,2] (of AlGaAs refractive indices) in the literature. The present results confirmed the apparent overestimate (≈2-2.5%) in the Al-composition by Casey et al[2] in the region 0-30% that has previously been reported[21].Comparison with reported data from Aspnes et al[1] is made difficult by the scarcity of data in the presently used wavelength regime. The few points that are in this wavelength range do however indicate a somewhat lower (≈1.5%) aluminium content.

The results found from the first part of this chapter were used for the calculations throughout. MQW waveguides of well widths 40, 60 and 100Å were measured before and after disordering using the non-electrically active dopants boron and fluorine. This rigorous approach made it possible to determine accurately the change in refractive index with progressive disordering. Partial and complete disordering was studied in detail for the 60Å well material, and complete disordering was achieved after annealing for 4 hours at 890°C for both boron and fluorine impurities.

Waveguide optical absorption measurements were performed on as-grown and disordered material. Kramers-Krönig transformation was then used to obtain the refractive index change with disordering for reference purposes.

In the region close to the bandgap, both partial and complete disordering resulted in a decrease in the refractive index (negative Δn), with a maximum projected refractive index change of 2% for complete disordering. Complete disordering also gave a negative refractive index change at long wavelengths. For the partly disordered 60Å well material, and at long wavelengths, the refractive index was observed to increase slightly (positive Δn). This was unexpected, but through a literature search it was found that the results were consistent with that of other groups[17,18]. The positive refractive index change at long wavelengths has been suggested[19] to arise from the non-square potential bands of quantum wells as a result of the intermixing process.

The positive Δn was not seen in the K-K transform results, but this may arise from the assumptions made for the maximum absorption before and after disordering. The exact absorption could not be measured above the bandgap of the semiconductor in the set-up employed. The above bandgap maximum absorption was estimated from published values, and assumed not to change with disordering. This was later found to be an inaccurate assumption.

After complete disordering the material was shown to have a bulk-like refractive index dispersion. The composite equivalent aluminium composition after complete disordering was shown to give a refractive index dispersion equal to that of the material average of the original quantum well structure.

[1]D.E. Aspnes, S.M. Kelso, R.A. Logan, R.Bhat, "Optical properties of $Al_xGa_{1-x}As$", J.Appl.Phys. Vol.60,1986, pp 754-767.

[2]H.C. Casey Jr., D.D. Sell, M.B. Panish, "Refractive index of $Al_xGa_{1-x}As$ between 1.2 and 1.8 eV", Appl. Phys. Letts.Vol.24 1974, pp 63-65.

[3] D.G. Dalgoutte, C.D.W. Wilkinson,"Thin grating couplers for integrated optics: an experimental and theoretical study", Applied Optics Vol.14, No.12 1975, pp 2983-2998.

[4] D.G. Dalgoutte, C.D.W. Wilkinson,"Thin grating couplers for integrated optics: an experimental and theoretical study", Applied Optics Vol.14, No.12 1975, pp 2983-2998.

[5] D.S.Chemla,"Quazi-two-dimensional Excitons in $GaAs/Al_xGa_{1-x}As$ Semiconductor Multiple Quantum Well Structures", Helvetica Physica Acta, Vol.56, 1983, pp 607-637.

[6]SONEK, J., BALLANTYNE, J.M., CHEN, Y.J., CARTER, G.M., BROWN, S.W.,KOTELES, E.S., SALERNO, J.P.,"Dielectric properties of GaAs/AlGaAs Multiple Quantum Well waveguides", IEEE Journal of Quantum Electronics, QE-22, No.7, pp 1015-1018, July 1986.

[7]O'NEILL, M., BRYCE, A.C., MARSH, J.H., DE LA RUE, R.M., ROBERTS, J.S., JEYNES, C.,"Low Loss MQW Optical Waveguides with Large Absorption Edge Blue-shift Produced by Boron and Fluorine Implantation", Applied Physics Letters **55**, 1373 (1989).

[8]J H Marsh,"Neutral Impurity Disordering of Quantum Well Waveguide devices."Ch.9 Waveguide Optoelectronics, NATO AASI Series E:Applied Sciences Vol.226.,Eds. J.H.Marsh and R. De La Rue, Kluwer Academic Press,The Netherlands, pp 185-204

[9]J.D. RALSTON, S. O'BRIEN, G.W. WICKS and L.F. EASTMAN, Appl Phys Lett **52** (1988) 1511.

[10]A.Meney,"Effects of impurity induced disorder on the index of refraction in GaAs-AlGaAs quantum wells," Superlattices and Microstructures, Vol.11, No.1,1992, pp 47-53.

[11]K. Kash, B. Tell, P. Grabbe, E.A. Dobisz, H.G. Craighead and M.C. Tamargo, "Aluminium ion-implantation enhanced intermixing of GaAs-AlGaAs quantum well structures," J. Appl. Phys. 63 (1) 1988, pp190-194.

[12]A.Meney,private communications.

[13]Y. Hirayama, Y. Suzuki, H. Okamoto,"Ion-Species dependence of interdiffusion in Ion-Implanted GaAs-AlAs Superlattices", Journal of Applied Physics Vol.24, No.11 1985 pp 1498-1502.

[14]G.D.Alton,L.O. Love, "Radiation damage and substitutional chemical impurity effects in single-crystal germanium bombarded with 40-keV B^+,Al^+,Ga^+,Ge^+,P^+,As^+, and Sb^+ ions", Can.J.of Phys. Vol.46, 1968, pp 695-704.

[15]Ralston, G.W. Wicks, L.F. Eastman, B.C. De Cooman, C.B. Carter, "Defect structure and intermixing of ion-implanted $Al_xGa_{1-x}As$/GaAs superlattices", J.Appl.Phys. Vol.59, 1986, pp 120-123.

[16] K. Matsui, T. Takamori, T. Fukunaga, T. Narusawa, H. Nkashima, "Ion-implantation induced damage in $Al_xGa_{1-x}As$ and superlattices studied by Rutherford backscattering.", Jap.J. of Appl. Phys. Vol.26, 1987, pp 482-486.

[17]T.Wolf, C-L. Shieh, R. Engelmann, K. Alavi, J. Mantz, "Lateral refractive index step in GaAs/AlGaAs multiple quantum well waveguides fabricated by impurity-induced disordering", Appl. Phys. Letts. Vol.55 1989, pp 1412-1414.

[18]E. Kapon, N.G. Stoffel, E.A. Dobisz, R. Bhat, Appl. Phys. Letts. Vol. 52 1988, p 351.

[19]E.H. Li, B.L. Weiss, "Dielectric properties of nonsquare AlGaAs/GaAs single quantum wells at photon energies below the band gap", Appl. Phys. Letts. Vol.59, 1991, pp 3312-3314.

[20]E.F. Schubert, K. Ploog,"Free and bound excitons and the effect of alloy disorder in MBE grown $Al_xGa_{1-x}As$,"J.Phys.C: Solid State Physics Vol.18, 1985 pp 4549-4559.

21B.Jensen,"Calculation of compound semiconductors below the bandgap", Ch.6, Handbook of Optical Constants of Solids, E.D. Palik, Ed. Vol 2, Academic Press Orlando ,1991, pp 141-147.

CHAPTER 7

DEVICE IMPLEMENTATION

7.1 Introduction

The technique of Impurity Induced Disordering using boron and fluorine has proved to be a powerful process for use in the fabrication of photonic and optoelectronic devices, and in particular in the field of circuit integration. By exploiting the bandgap-altering mechanism to its full extent, various devices can be both implemented and integrated on the same substrate. This has previously been attempted using various impurities for the IID process, such as mentioned in Chapter 3 e.g. Si or Zn. However, for many device configurations that would benefit from the technique of bandgap engineering via IID, low optical absorption and high electrical resistance are required. This is where the use of impurities that are electrically active in semiconductors at room temperature can be unfavourable. Because the IID process has a threshold impurity concentration of around 10^{18} cm^{-3}, the reported absorption coefficients for disordered material using electrically active impurities are very high, e.g. for Si around[1] 43 $dBcm^{-1}$. For the application of waveguides as interconnects, for instance between a laser and a modulator or switch (fig.7.1.2 a), there is also very often a need for electrical isolation. It is however unlikely that the electrically active IID impurities can give the required isolation resistance, reported to be larger than 100 kΩ[2]. Optical interconnects fabricated by IID using boron and fluorine are on the other hand expected to have an isolation resistance that is more than 200 times that of the Si or Zn IID material[1]. This is due to the waveguide material being essentially undoped, as shown by the electrochemical profile plots in Chapter 6. The total propagation loss in fluorine implanted and disordered waveguides has additionally been measured[3] to be as low as 4.7 $dBcm^{-1}$, nearly a factor of 10 lower than results reported for Si IID. There are possible optoelectronic applications for IID where it can be advantageous to have an electrically conductive region of lower refractive index than the surrounding material. This would however be the exception rather than the rule, since free carriers then would be present in

what would effectively be the cladding region of the structure. One such application is the fabrication of an antiguided array laser structure, where the advantages of antiguiding can be combined with a dopant-free optical guide layer. A schematic diagram of this type of structure is envisaged in fig. 7.1.1

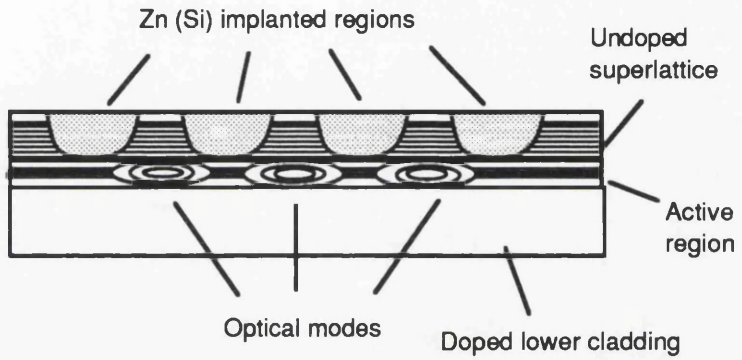

Fig. 7.1.1 Diagram illustrating antiguide laser made using IID

There are a number of possible applications for IID using electrically inactive impurities, and these have been the subject of several publications[4,5]. The simplest realisation of a component for integrated optics using IID is the fabrication of a low-loss waveguide for use in optical interconnects in an integrated optical circuit. The situation today is that the techniques for making the separate devices needed in such an integrated circuit are maturing, but there is still a problem in the high loss intrinsic to the III-V semiconductor materials in the region of the bandgap. This is also the region in which many devices such as modulators and switches have to operate because of the strong dependency of the refractive index modulation properties on the absorption, illustrated through the Kramers-Krönig relationship between the refractive index of the material and its absorption. One way to overcome the problem is to fabricate the devices in isolated "islands" on the substrate and then overgrow the structure with a larger bandgap material, in which the interconnects can be defined. This is the technique that is being used today in several multiple section laser structures, especially in the InP based system. The overgrowth method does however lead to several extra processing stages and is a very demanding

process. The IID process yields a method for engineering the bandgap of the material in specific, well defined regions post-growth and without the need for subsequent regrowths.

By integrating a passive optical waveguide with a laser (fig.7.1.2 b), a reduction in linewidth can be achieved. Linewidth narrowing is today frequently achieved by operating the lasers in external cavities, which are subject to bulky optics and alignment problems[1]. The linewidth reduction obtained by integrating the laser with a passive optical waveguide is achieved with a relatively small penalty in the threshold current of the original laser.

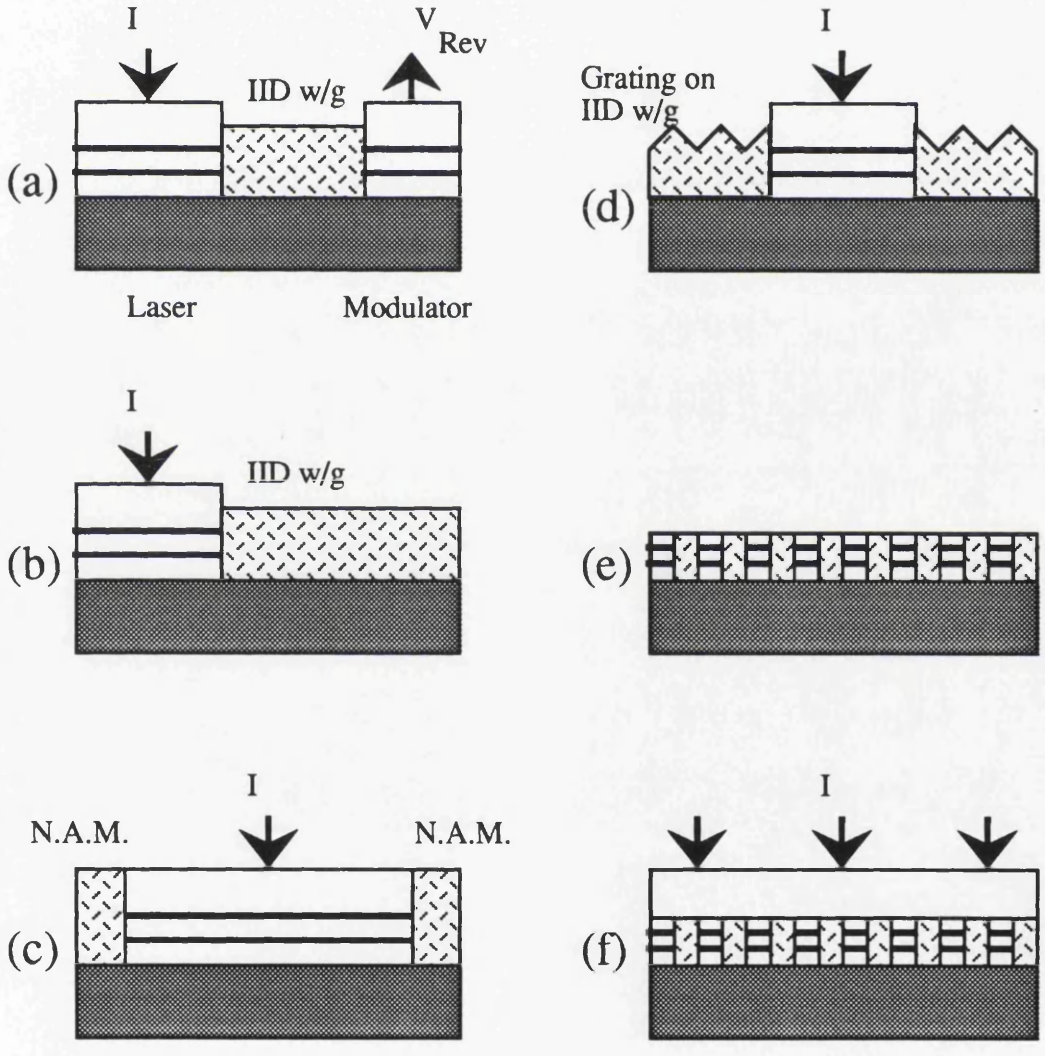

Fig.7.1.2 Examples of the potential applications of IID in devices for coherent optics: (a) integrated laser and modulator, (b) extended cavity narrow linewidth laser, (c) high power laser with non-absorbing mirrors, (d) DBR laser, (e) grating formed by IID and (f) DFB laser with index and gain gratings.(From ref.[6])

The IID process also opens up the possibility of engineering the bandgap of a laser structure in the region of the facets (fig.7.1.2 c). One of the most common failure modes in high-power quantum well lasers is catastrophic damage due to facet melting. Several studies have been performed on the subject, and the process is found to be material dependent and especially prominent in the AlGaAs-GaAs and AlGaAs-InGaAs quantum well systems. In all cases the effect is believed to be caused by the bandgap narrowing at the end facet due to surface states, but in these two systems there is potentially a two-component interdependent effect. The argument behind this is a) that the facet oxidation rate is found to be temperature dependent, and b) that the absorption at the surface is due to a combination of bandgap narrowing and Al-oxide formation. The absorption due to the bandgap narrowing leads to a localised temperature rise at the facet. This increases the facet oxidation rate which, in turn, leads to an increased absorption since the lasing wavelength lies within the absorption peak of AlO_2. The increased absorption induces a further rise in the temperature, which then further narrows the bandgap at the facet and increases the facet oxidation rate, leading to a runaway situation. The result is that the localised temperature melts the facet and laser action is inhibited. From the above it is clearly seen that the situation can be avoided by increasing the bandgap at the facet to counteract the effect of the surface states. It is also clear that IID provides the technique for achieving this increase, and that a non-dopant impurity such as boron or fluorine would be preferable for this application.

IID also facilitates fabrication of single frequency lasers in the DBR configuration without the need for regrowth. One of the main disadvantages of the DBR configuration in semiconductor lasers today is that the losses in the passive section of the device are prohibitively high, with the consequence that half[1] or more of the output power of the laser is absorbed in the distributed feedback section before the facet. By using IID to enlarge the bandgap in the passive section of the device the absorption can be reduced, and a low-coupling coefficient grating can be etched onto the waveguide producing a stable narrow-linewidth source . This is illustrated in Fig.7.1.2 d.

Gratings can also be directly defined by IID instead of being fabricated through an etching process[7]. The IID process modifies the dichroic and birefringent properties of quantum well materials and alters the spectral distributions of the refractive index and absorption. This property can be used to periodically modify a quantum well waveguide structure to yield a refractive index grating. This type of grating can be used for fabricating grating couplers, wavelength multiplexers or DBR lasers (Fig.7.1.2 e).

Gratings produced by IID can also be used in DFB lasers. These lasers are today generally made by etching a grating in a layer in the vicinity of the active region and subsequently overgrowing this to complete the laser material structure. Overgrowing this non-planar structure is not completely straightforward and not necessarily compatible with all material systems and growth methods.Overgrowth also tends to smear out the etched gratings, making it difficult to predict the properties of the grating, such as the coupling coefficient. Implanting and diffusing the active quantum wells periodically along the longitudinal direction of the laser can be used to fabricate a simultaneous gain and phase grating (fig.7.1.2 f). The increased resistivity of the implanted region and the bandgap modulation serves to channel the carriers and concentrates the gain at the points of maximum optical intensity in the longitudinal direction of the laser. This is expected to reduce the threshold current of the device, and also leaves a planar surface for subsequent regrowth. By taking this further and reducing the pitch of the grating, quantum wires can be fabricated. Quantum dots are also achievable through the use of crossed-grating or electron/ion-beam-defined implantation masks.

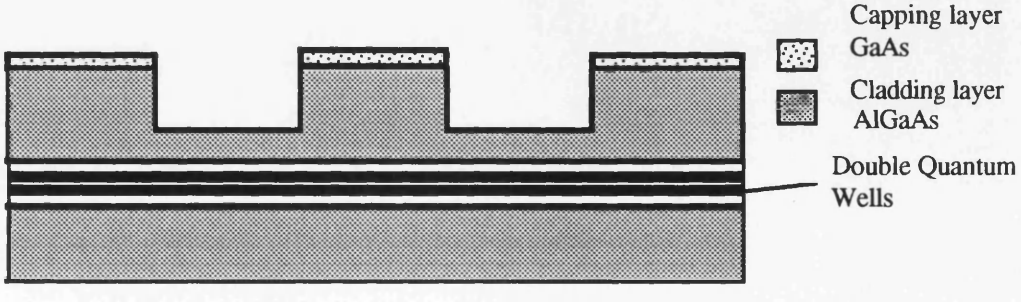

Fig.7.1.3 Diagram illustrating conventional etched ridge waveguide laser structure.

On a larger scale and, similarly to the case of the antiguiding structure, the non-dopant IID process can be used simply to define a "buried" ridge waveguide structure. The conventional ridge structure is made by the removal of semiconductor material on both sides of a previously defined and suitably masked region. The resulting thickness variation creates an effective waveguide through the refractive index steps it produces. This conventional structure can in turn be made into a buried ridge by effectively 'filling in' the trenches either side of the ridge with material of lower refractive index than the ridge in a subsequent overgrowth step in the fabrication process. Alternatively, IID can be used on a suitably defined material structure to give the refractive index variation directly on the sides of the ridge. This can also help reduce current spreading in the regions adjacent to the ridge due to the increased resistivity produced by the IID process.

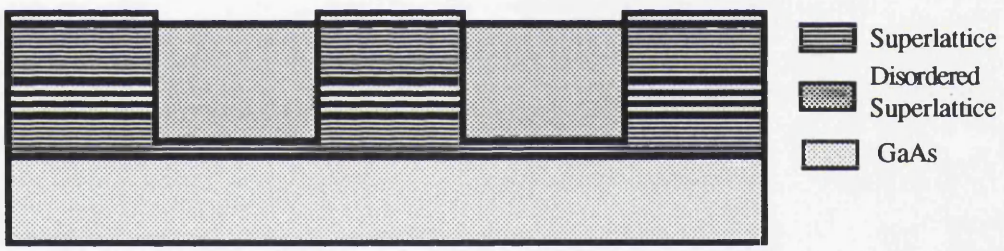

Fig. 7.1.4 Diagram illustrating 'buried ridge' structure fabricated by IID.

7.2 Realised structures

7.2.1 Material structure

An attempt was made at realising some of the laser structures outlined above, such as the buried ridge laser structure of fig.7.2.1.1, together with the DBR and DFB lasers made by IID. The material structure developed for this purpose is shown in fig.7.2.1.1. The double quantum well structure previously used by the Optoelectronics Research Group at Glasgow University was used as the starting point for the structure. The composition of the

superlattice in the cladding layers was chosen to give 'bulk' material with an average Al-content of 40% when completely disordered.

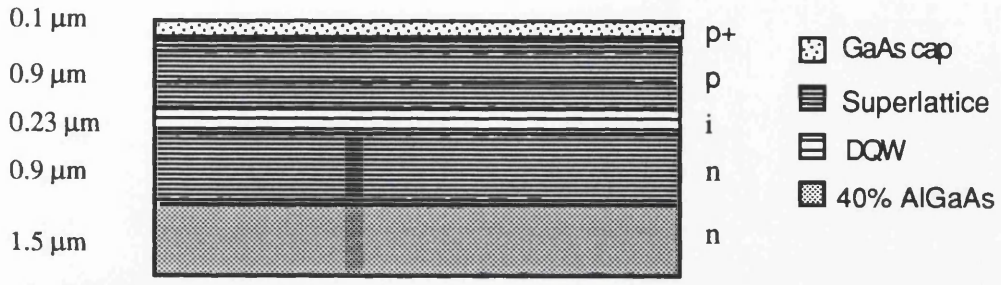

Fig.7.2.1.1 Diagram of the SuperLattice Cladding Layer Double Quantum Well (SLCL DQW) material structure designed for the purpose of fabrication of novel lasers by IID. The Double Quantum Well region is undoped and contains two GaAs quantum wells with L_Z=L_B=100Å in a 20% AlGaAs confinement region.

Investigations were carried out to examine the degree of lateral optical confinement that could be expected from a buried ridge structure of this composition, compared to that of a conventional type ridge waveguide laser structure. The effective index method was used on the IID buried ridge structure, and a finite difference program was used for the conventional ridge waveguide. The assumption was made that the superlattice would be totally disordered in the implanted regions and unaffected elsewhere. From these calculations the conventional ridge structure was found to have much lower lateral optical confinement (≈39%) than the IID buried structure (≈99%).

The refractive index values of superlattices used in the investigations into the suitability of the superlattice structure were found from recent publications on the subject[8]. The refractive index step resulting from total intermixing of the superlattice was found from data on the refractive index of bulk $Al_xGa_{1-x}As$. The average composition $\bar{x}$ of a superlattice with well and barrier widths L_Z and L_B respectively, was used for the Al-content x in the above expression:

$$\bar{x} = \frac{L_B}{L_B + L_Z} \qquad (7.2.1.1)$$

in the case of an AlAs-GaAs superlattice. The expected bandgaps of superlattices of different periods and compositions were also estimated. From these considerations a superlattice was designed with AlAs L_B≈30Å, GaAs L_Z≈45Å, with actual widths being 11

monolayers (31.1Å) and 16 monolayers (45.3Å) respectively. The wells were deliberately made as wide as possible to achieve as large refractive index step as possible when making the IID buried structure.

The wafers were grown by MOCVD at Sheffield University, one consisting of the complete laser structure and one with growth stopped after the separate confinement layer.

Control samples were used to fabricate broad area lasers. This was necessary to characterize the lasing performance of the structure. The broad area laser structures were found to emit light, but no definite laser action was observed before they broke down, as illustrated in the power versus current plot in fig.7.2.1.2. To find the cause of the poor result, some characterisations of the material were carried out. A current versus voltage (I-V) measurement was carried out to find the diode characteristics of the structure, and electrochemical profile etching and PVS measurements were carried out to examine doping levels and absorption peaks in the different layers.

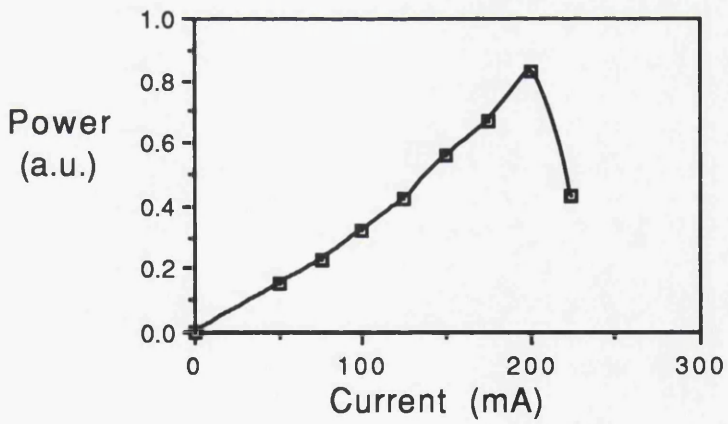

Fig.7.2.1.2 Plot of light versus current characteristics of CB 356 SLCL broad area laser structure.

The electrochemical profile plot showed the doping levels and types to be correct throughout the structure. The PVS measurements in the superlattice cladding layers did however reveal a room-temperature absorption peak centred at 860 nm, the expected lasing wavelength of the structure. The diode characteristics of the sample further confirmed the presence of a low

bandgap transition in the superlattice. A very low and poorly defined reverse breakdown voltage (≈ 0.5V) indicated poor electrical confinement in the SCH structure.

From the experience with the first SLCL structure, several improvements were made to the structure design. These were as follows:

–introduced aluminium into superlattice wells to increase bandgap

–narrowed wells and barriers in the superlattice whilst retaining $\bar{x}$=0.4 to improve carrier transport

–lowered aluminium content in SCH layer from 0.2 to 0.15 to enhance optical confinement

Introducing Al into the wells of the superlattice changes the equation for average aluminium content (7.2.1.1) to:

$$\bar{x} = \frac{L_B + aL_Z}{L_B + L_Z} \qquad (7.2.1.2)$$

where a is the Al-fraction of the quantum well. From these considerations, the superlattice was redesigned to have 28.3Å (10 monolayers) $Al_{.04}Ga_{.96}As$ wells and 16.98Å (6 monolayers) AlAs barriers, thus retaining $\bar{x}$=0.4. The wells and barriers were narrowed both to lift the energies of the minibands and to improve the tunnelling of carriers through the barriers. Aluminium was introduced to increase the bandgap in the SL further. The exact value of 4% was decided upon from considerations of successful structures used for embedded mirror devices, and it raises the SL miniband energy level by the same amount as the difference between the DQW n=1 level states and the GaAs band edge. Decreasing the Al-content of the SCH layer gives a higher optical confinement and also increases the potential barrier between SCH layer and SL layer.

The new structure was grown both by MOCVD at Sheffield and by MBE at Norwegian Telecom Research in Kjeller, Norway. The MOCVD material CB 439 had Sn n-type doping to a level of 6 x 10^{17} cm^{-3} in the lower SLCL and Zn p-type doping 5 x 10^{17} cm^{-3} in the upper SLCL. The active quantum wells were estimated to have L_Z = 103Å from PVS measurements at Sheffield. The MBE grown laser GaAs100 had nominally 5 x 10^{17} cm^{-3} Si n-type and Be

p-type doping. The reverse breakdown voltages for the structures were 9.3 Volts and 11.3 Volts for GaAs100 and CB 439 respectively.

Broad area lasers 300 x 400 μm were made from both laser structures. The CB439 structure was observed to have a laser threshold current density $J_d \approx 330$ A/cm2 and an overall differential quantum efficiency of around 35% per facet. The lasing wavelength was 863 nm. The GaAs100 structure had much the same threshold current density, but lower quantum efficiency, and a lasing wavelength of 858 nm.

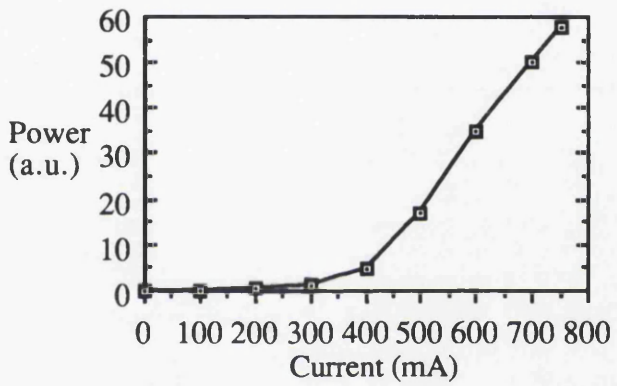

Fig.7.2.1.3 Power versus current characteristics of CB439 SLCL DQW SCH broad area (300 x 400 μm) laser.

The two wafers, even though grown to the same specifications, do not have identical SL structures. In order to grow the thin $Al_{.04}Ga_{.96}As$ wells by MOCVD, the trimethylaluminium gas flow had to be very small, and the flow was ramped up and down to form the superlattice. This resulted in wells and barriers that were graded. The MBE method did, on the other hand, use shutters, resulting in sharply interfaced rectangular wells. This difference in the two material structures may explain some of the difference in laser characteristics.

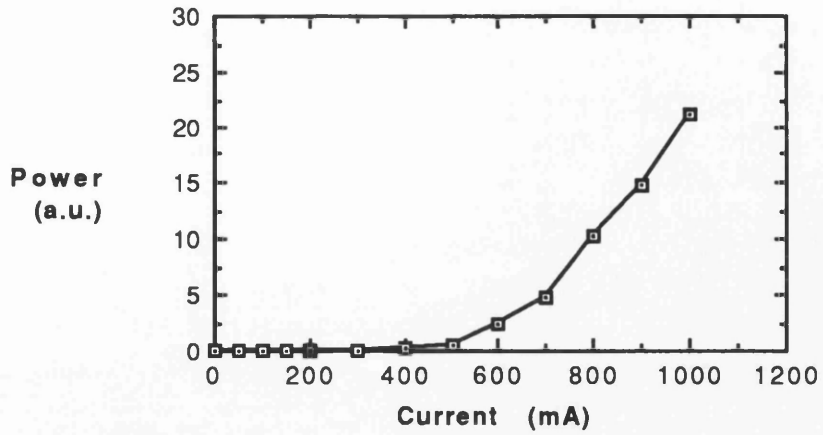

Fig. 7.2.1.4 Power versus current characteristics of TF GaAs100 SLCL DQW SCH broad area (300 x 400 μm) laser.

The MOCVD-grown material gave the better performance, and this material was subsequently chosen for the attempts at making a DBR laser structure. The MBE-grown material was used for the 'buried-ridge' IID experiments.

7.2.2 Buried heterostructure laser

The MBE-grown material was cleaved into 1 x 1 cm samples. These were then cleaned and a 2.5μm layer of SiO_2 was deposited on top of the GaAs cap. Conventional lithography was used to define a ridge-type pattern in photoresist on the SiO_2 and, using CHF_3 reactive ion etching, the areas either side of the stripe pattern were opened up down to the semiconductor surface. The GaAs cap was selectively removed in these windows, using an etch mixture consisting of 1:50 parts NH_4OH:H_2O_2. The SiO_2 was used as a mask in the subsequent implantation with fluorine. The implantation, performed at Surrey University, followed the same recipe as with the MQW waveguide (Chapter 6) to give a uniform impurity concentration down to approximately 1 μm. After the implantation the SiO_2 mask was removed in buffered HF. A new capping layer of 1000Å SiO_2 was thereafter redeposited to act as a capping layer in the annealing stage. The samples were annealed in the conventional furnace described in Chapter 6 at 890°C for 90 minutes, together with capped and patterned, but unimplanted, control samples.

The capping layer was removed in buffered SiO_2. The capping layer could of course have been used for the isolation layer in the subsequent laser processing, but after the annealing process the etch rate of SiO_2 is found to reduce substantially. To avoid any uncertainty in the SiO_2 etch rate, newly deposited SiO_2 was used. The samples were given a 1700Å coating of plasma deposited SiO_2. Some of the samples were thereafter processed into lasers following the standard procedure[9] of contact window opening, sample thinning, metallisation and subsequent cleaving into individual lasers 300 x 400 μm. The remaining samples were prepared for TEM inspection.

The lasers were tested in pulsed mode, using 250 nanosecond pulses at 1: 1000 duty cycle (4 kHz repetition rate), using a Hewlett-Packard pulse generator. The current was measured using a current probe and the power using an HP integrating power detector with a Si detector head. This was part of a standard laser test system. No laser action was observed at room temperature. Low intensity emission could be detected from some devices, but all devices failed rapidly.

7.2.3 Distributed Bragg Reflector DBR Laser

An attempt was made of fabricating DBR laser structures define by IID. The idea is outlined in 7.1.

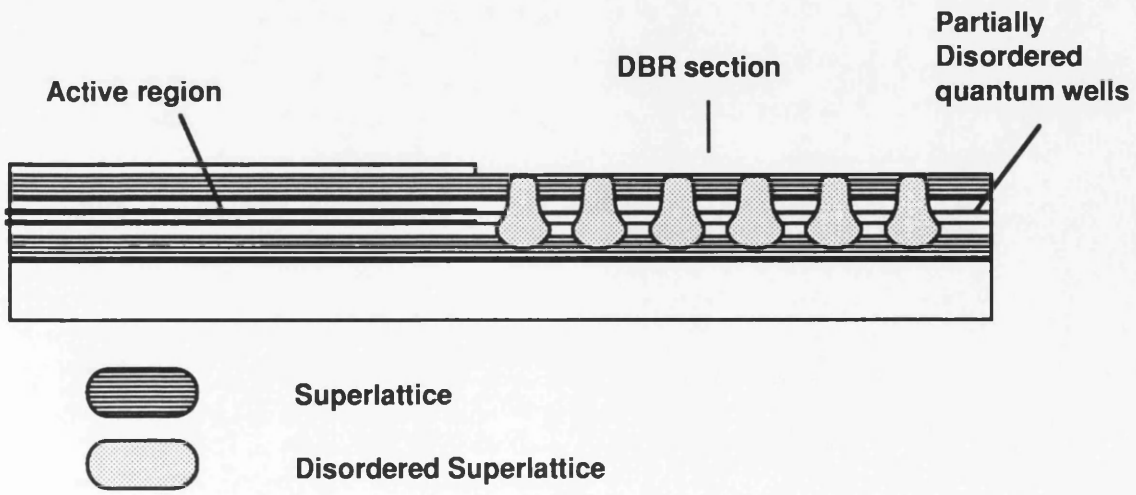

Fig.7.2.3.1 Diagram showing DBR by IID laser.

Contrary to using the IID only to lower the absorption in the Bragg reflector area, IID was to be used also for the definition of the grating itself, as illustrated in fig.7.2.3.1. This meant that a grating-type implantation mask had to be realised.

Calculations had shown that SiO_2 implantation masks had to be more than 2 μm thick, and for a grating pitch in the region of 300 nm, this mask structure would not be feasible. The alternative mask material was gold, where calculations showed that 0.3 μm gold would be sufficient to stop fluorine ions penetrating to a depth of 0.5 μm in GaAs. The disadvantage with using gold was that it could not be selectively removed in etching processes the way SiO_2 could. The grating mask therefore had to be realised using a lift-off process. This is a standard process and is described in detail elsewhere[10]. Here it involves metallising a pattern of grating columns defined in photoresist on semiconductor material and thereafter dissolving the photoresist to leave columns of gold on the semiconductor surface.

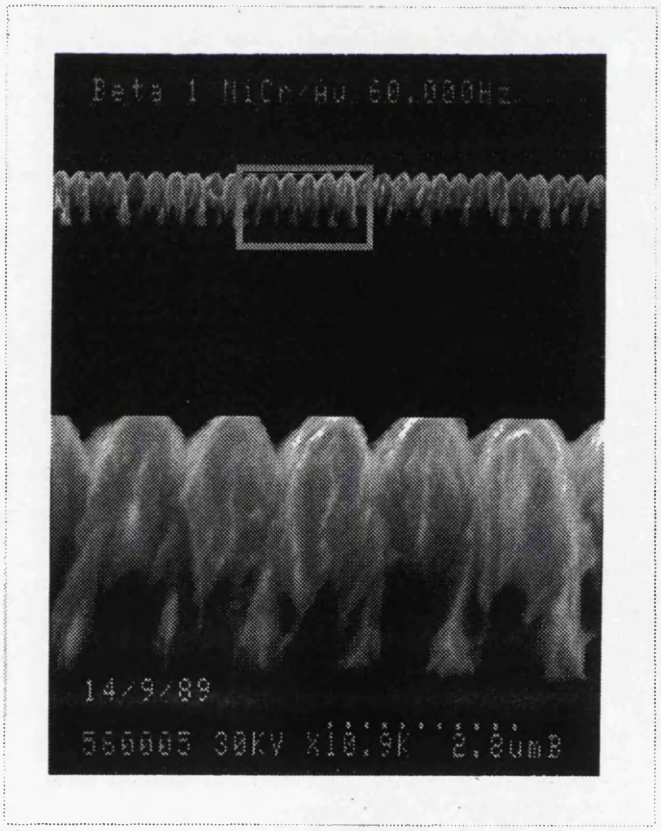

Fig.7.2.3.2 SEM photograph showing unsuccessful lift-off due to excessive gold deposition.

A severe limitation of this process is that the thickness of gold cannot be more than 1/3 of the photoresist thickness. If the gold columns were to be taller, the gold would start forming 'bridges' to the gold on top of the photoresist columns, resulting in unsuccessful removal of the gold on top of the columns. This is illustrated in the SEM photograph fig. 7.2.3.2, where erroneous calibration of the gold deposition rate lead to 0.45 μm gold being deposited on a 0.8 μm thick grating.

The tallest reproducible photoresist columns were 0.85 to 0.9 μm with a mark-space ratio of 1:1 and realised using a 1:2 solution of photoresist thinner to Shipley AZ1450J photoresist spun at 3000 rpm. Fig. 7.2.3.3 shows an electron micrograph of the high aspect ratio columns. Experiments using thicker photoresist coatings resulted in collapsing columns.

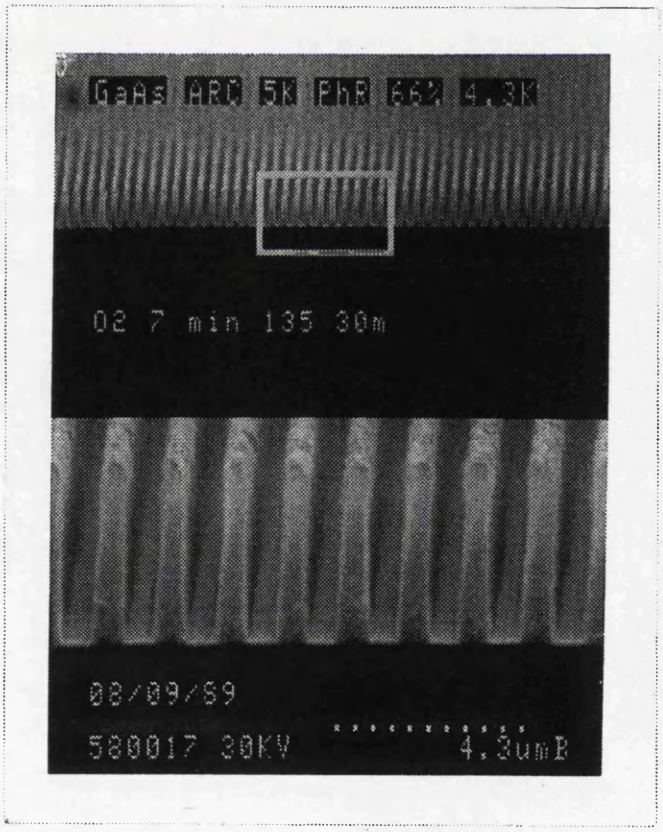

Fig.7.2.3.3 SEM photograph of high aspect ratio photoresist columns used for grating mask fabrication.

This limited the mask thickness to approximately 0.3 μm, corresponding to implantation to 0.5 μm in the semiconductor. This would obviously not be sufficient on its own using the laser structure designed for this exercise, particularly since the capping layer alone was 0.1 μm thick. To compensate for this, it was decided to use the 0.3 μm gold grating mask and etch trenches between the grating columns. In this way the implanted fluorine gets closer to the active layer of the structure, enabling partial disordering also of the DQW region and hence lowering the losses in the DBR region. The DBR laser would therefore have a reflector made up partially by a conventional etched grating and a disordered grating. The hope was that the channelling effect on the one hand and the angular divergence of the implantation on the other together would give impurity distributions of varying concentrations leading to a partially disordered Active region and to modulated grating structures above and below the SCH region of the structure.

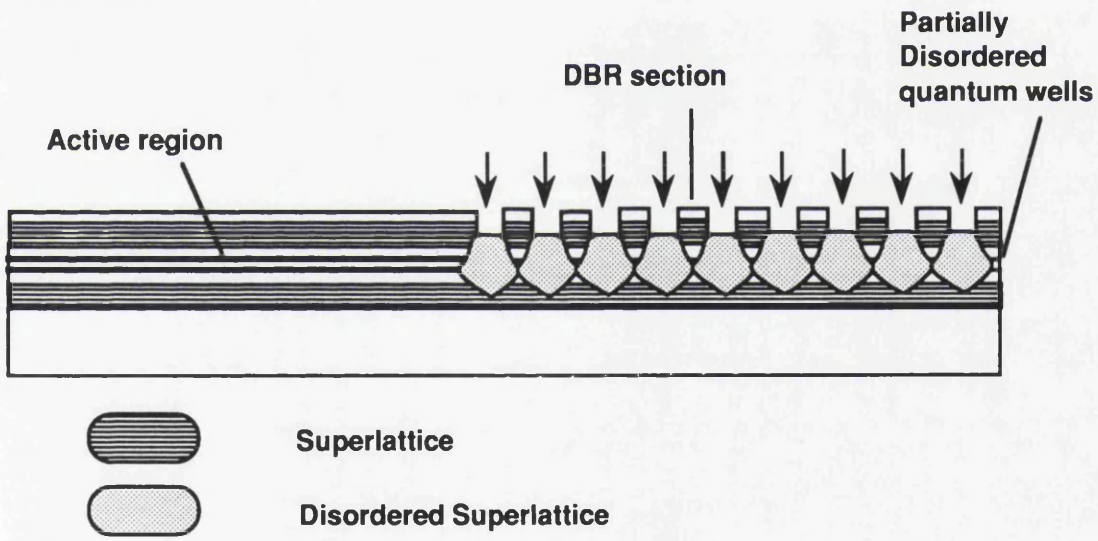

Fig.7.2.3.4 Diagram showing the reconsidered DBR structure.

The required grating pitch was calculated from known values of lasing wavelength and values of group refractive index calculated by the finite difference method. From these considerations a third order grating of pitch 380 nm was defined in gold by the combination of holography and lift-off explained above.

Fluorine implantation was carried out at Surrey University. The samples were then annealed using the same conditions as for the IID BH structure.

Laser devices were processed from the material and tested under pulsed conditions, but failed to work as lasers.

7.2.4 Distributed Feedback DFB Laser

The DFB lasers also needed an implantation mask pattern defined by lift-off, but due to the close proximity of the active wells to the surface, the mask did not have to be as thick as with the DBR lasers. There was however another problem inherent in the removal of the gold grating prior to overgrowth. Leaving the gold grating on the passive section of the DBR lasers was not considered a problem. In the case of the DFB's the gold would have to be removed without damaging the surface of the semiconductor. The solution was to deposit a thin layer of SiO_2 prior to defining the grating mask and, due to the adhesion of gold to SiO_2 being poor, evaporating a thin layer of nickel-chromium prior to the gold evaporation. This SiO_2 layer could be left there during implantation, since previous investigations had shown only small amounts of Si being introduced from a capping layer during implantation at low energies. Buffered HF could then be used to selectively etch the SiO_2 and effectively lift off the gold grating, leaving a smooth surface for overgrowth.

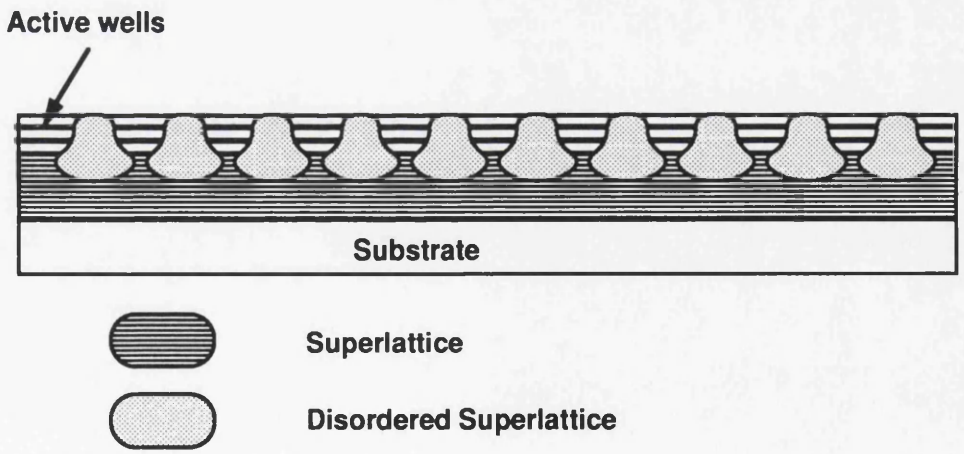

Fig.7.2.4.1 Diagram showing distributed feedback laser fabricated using IID

A grating with the same pitch as for the DBR structure was defined in NiCr/Au on SiO_2. The lasing wavelength for this laser would therefore not be the same as for the DBR. Because a DFB made with partially reflective facets and a grating without $\lambda/4$ phaseshift will have a

tendency to lase in one of two sidemodes either side of the bandstop provided by the grating, the laser was expected to suffer from mode instability. This was however not viewed as important in this experiment.

The implanted structure was overgrown with a 0.9 μm p-type 40% AlGaAs cladding layer and a 0.1 μm p^+ GaAs cap by MOCVD at Sheffield University, then annealed at the same conditions as for the implanted DBR laser structures.

Laser devices were processed from the material and tested under pulsed conditions, but failed to work as lasers.

7.3 Evaluation of devices/results

The three different device structures were all processed in parallel due to the time limitation imposed by the project. Had time allowed, much could have been learnt from the failure of the structure first discussed here, the BH IID laser.

Clearly, since the original material structure was found to yield working lasers, the clue to the failed laser structures must be found in changes in the structure due to part(s) of the further processing, i.e. changes to the material during the IID process.

In order to examine in detail the material structure before and after the IID process, transmission electron microscopy was employed. This is a method that can be used to examine layered GaAs–AlGaAs structures by utilising their differing electron transmission efficiency. AlGaAs transmits electrons better than GaAs, and GaAs wells in AlGaAs material are therefore observed as dark regions on a lighter background.

The sample preparation and microscopy was performed at the University of Trondheim in Norway. As-grown samples, annealed control samples and implanted and annealed samples were investigated, all of which were grown by MBE, and all of which had been given the same patterning (IID BH implantation mask).

The as-grown material is shown in the photograph figure 7.3.1. Parts of the superlattices above and below the separate confinement heterostructure region are shown together with the active wells. The well- barrier interfaces are abrupt and very well defined, with a good contrast to the surrounding AlGaAs material. The wells and barriers are also very uniform (the apparent widening of the AlGaAs barriers is an artefact of the microscopy, as can be seen when the point of focus of the imaging system is moved).

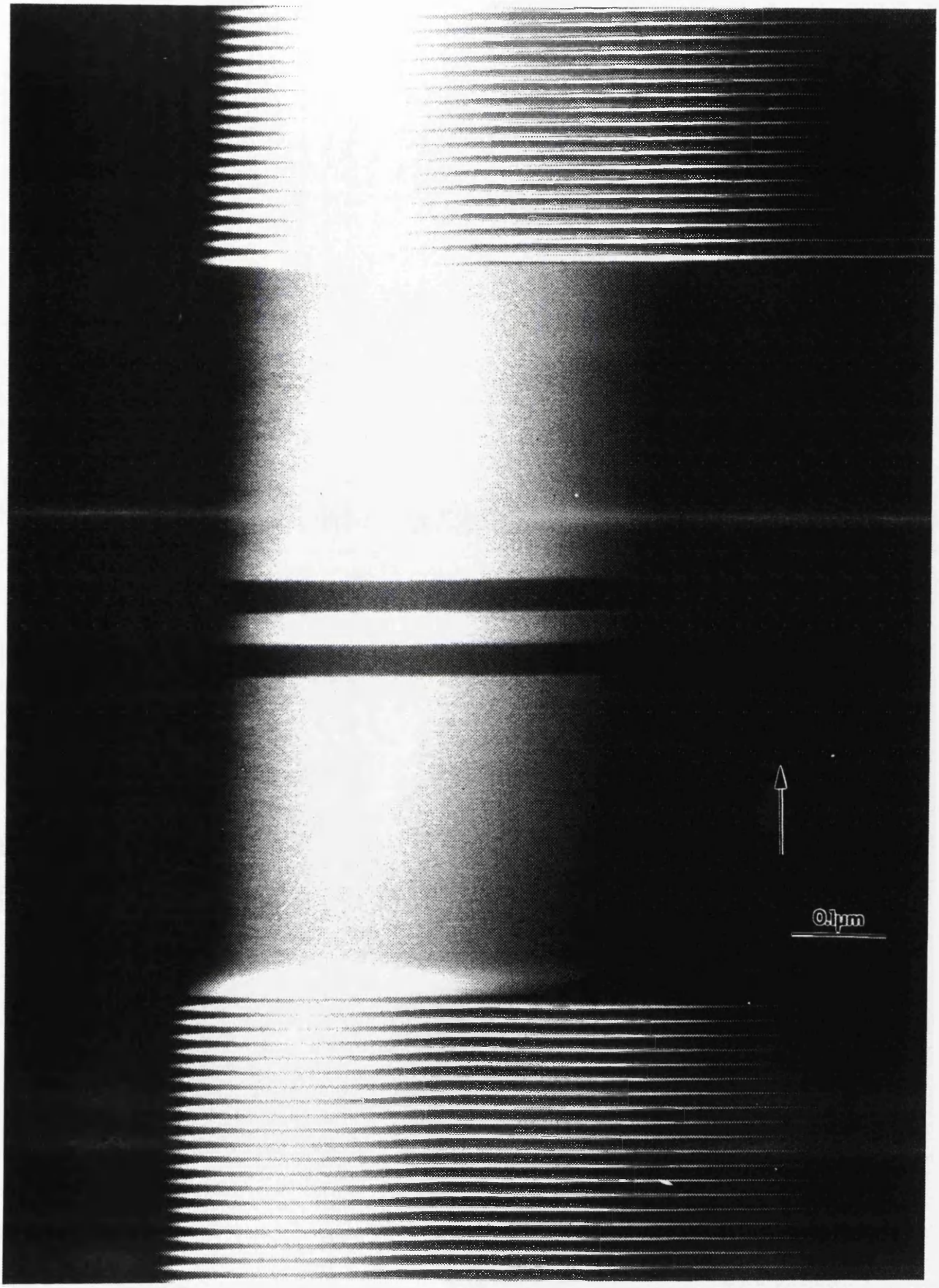

Fig.7.3.1 TEM photograph showing SLCL DQW SCH virgin material grown by MBE. The arrow indicates the growth direction.

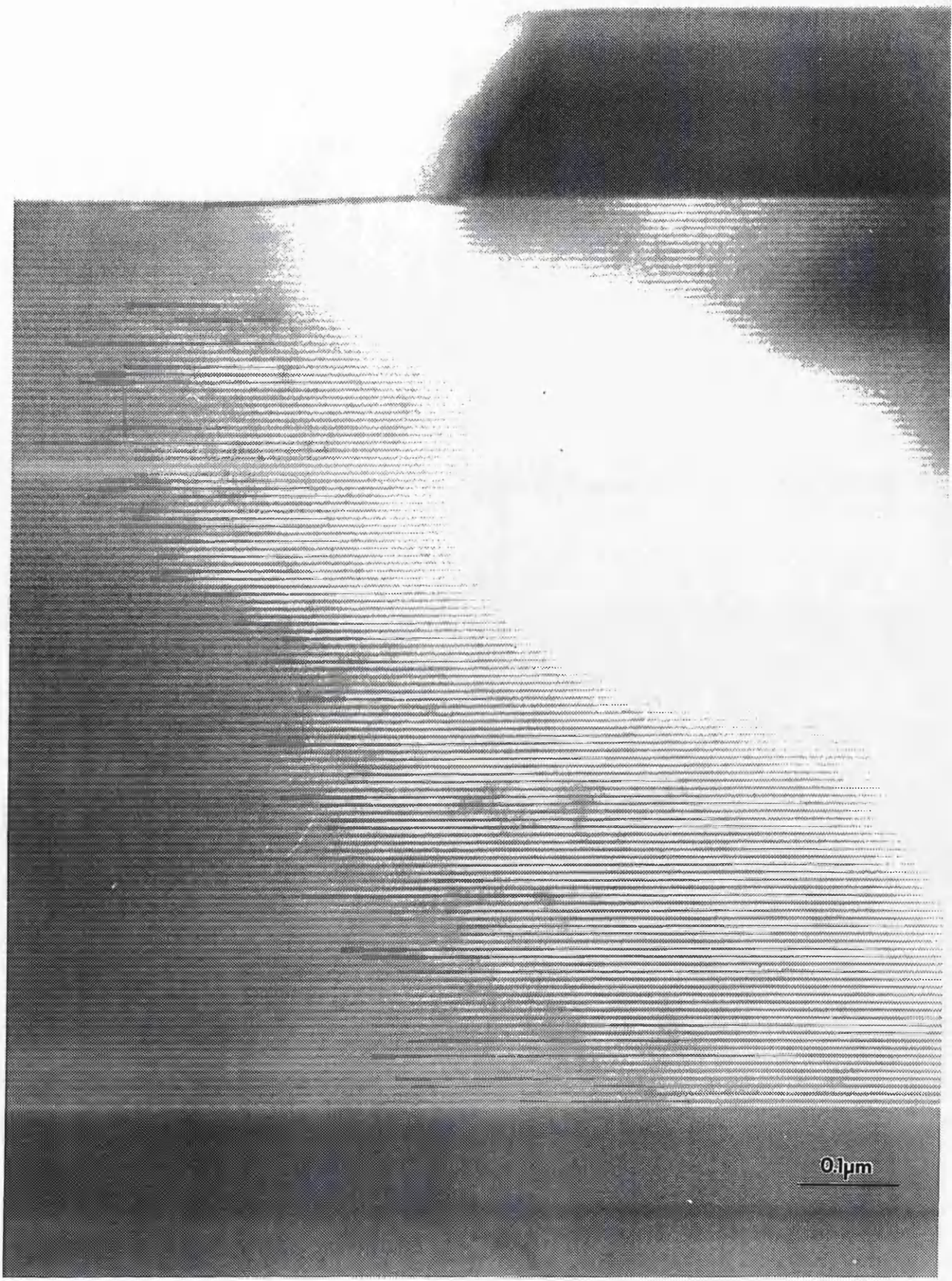

Fig. 7.3.2 TEM photograph showing top part of superlattice cladding layer and the remaining GaAs cap indicating the position of the implantation mask.

The top part of the patterned superlattice structure is shown in fig.7.3.2. The selective GaAs and SiO_2 etchants used to pattern and remove mask and cap materials are seen to have induced negligible damage to the superlattice structure.

A region of the unimplanted but annealed material is shown in fig.7.3.3. The arrow indicates the growth direction of the material. The lower superlattice cladding layer has been totally intermixed; no periodic variation in the Al-content can be found. Examination of the material composition by auger spectroscopy showed the material to have 40% aluminium content. The upper superlattice is observed to be unchanged and has not been affected by the 90 minute annealing at 890° C. The two active wells in the SCH-region are on the other hand observed to have less abrupt interfaces, indicating partial intermixing of wells and surrounding (barrier) material. The interface between the SCH region and the n-type (lower) cladding layer is also seen to be smeared out.

There had been no attempt at processing the unimplanted but annealed material into lasers. If this had been done, the resulting lasers would most probably have worked, since the intermixing of the lower cladding layer should have little effect on the lasing performance of the material and since the active wells still seem reasonably well defined. The lasers would however probably have been emitting light at significantly shorter wavelengths than for the virgin material, due to increased bandgap following the partial intermixing of the wells.

A TEM photograph of the corresponding section of the sample that had been implanted with fluorine prior to annealing is shown in fig.7.3.4. The arrow again indicates the growth direction. The left arrowhead indicates the transition region between implanted and unimplanted region (corresponding to the implantation mask edge), and the right arrowhead indicates the region under the implantation mask.

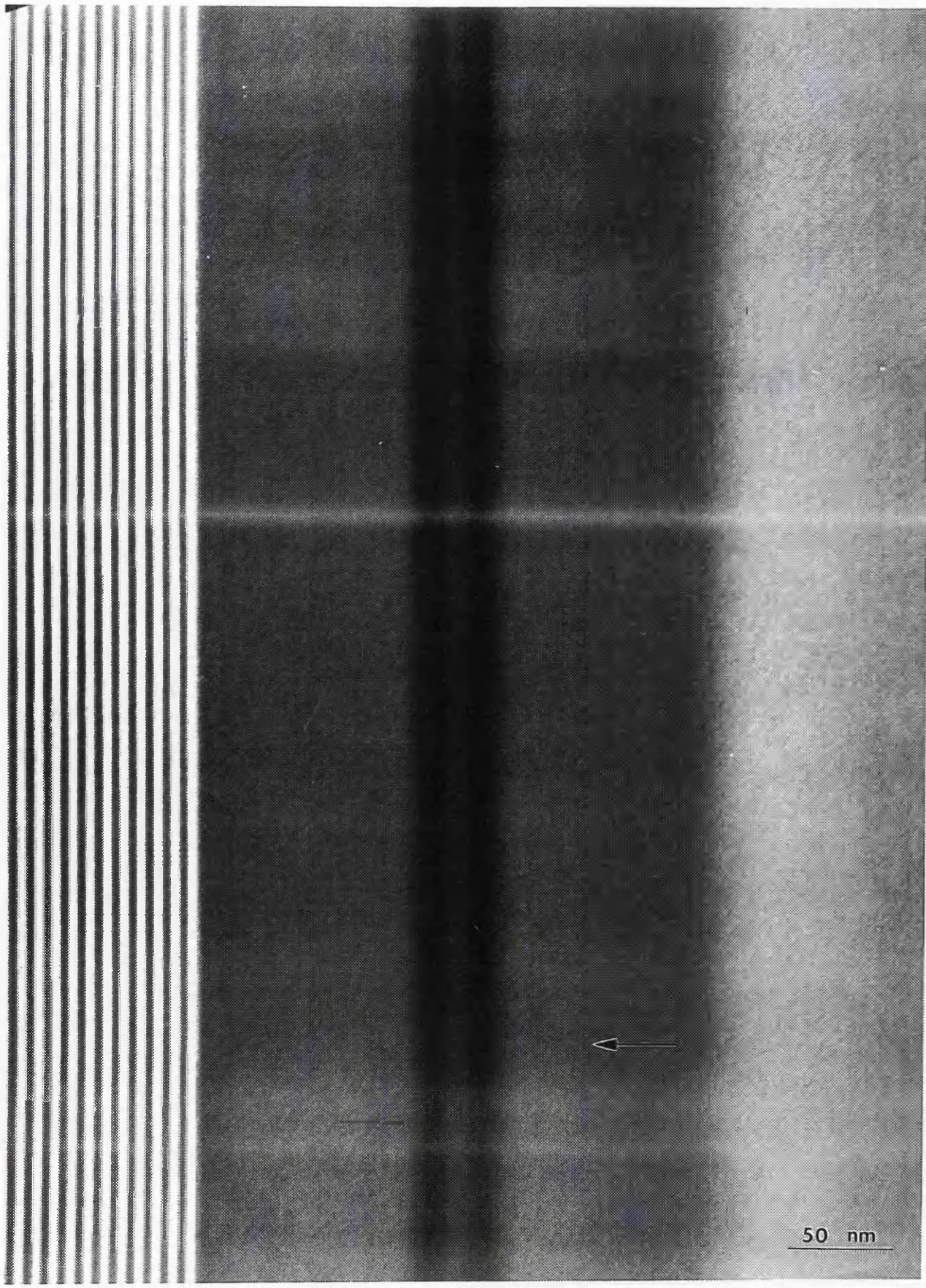

Fig.7.3.3 TEM photograph showing section around the SCH region of unimplanted but annealed SLCL DQW SCH material.

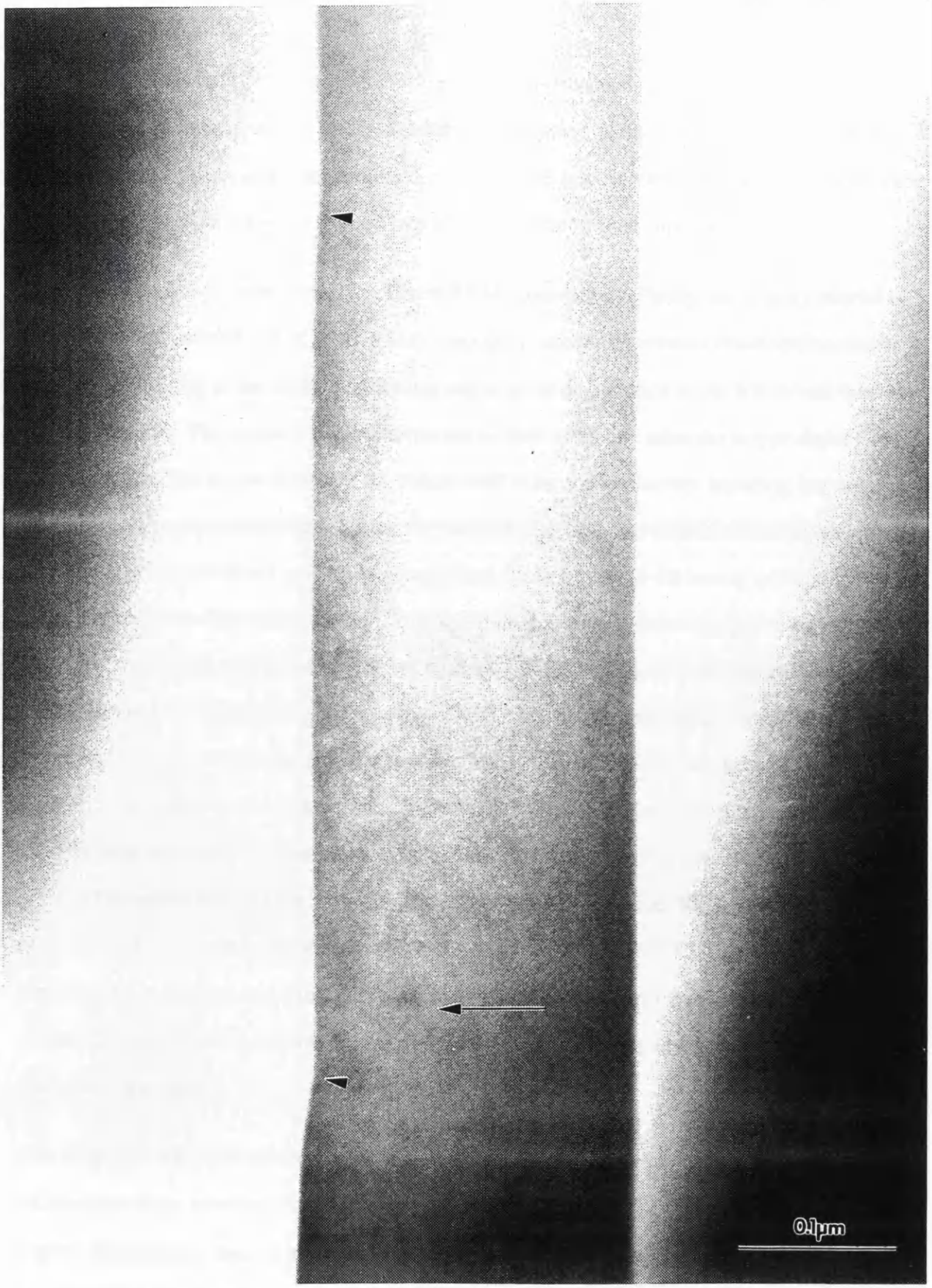

Fig.7.3.4 TEM photograph showing section around the SCH region of SLCL DQW SCH material following fluorine implantation and furnace annealing.

The first obvious feature to be observed is that there is no trace of any quantum wells at all, indicating total intermixing of both superlattices and active wells over the whole region and without regard to implanted and masked regions. The next interesting feature is the extra widening of the SCH-region at the interface with the former p-type superlattice layer.

Several conclusions can be drawn from these TEM observations. Firstly, the virgin material is seen to be well defined and of good quality. Secondly, annealing without implantation clearly leads to intermixing of the n-type superlattice and to some degradation in the active well-barrier interface quality. The reason for this intermixing is clear when one takes the n-type dopant into consideration. The n-type dopant is Si, which itself is an active disorder inducing impurity at temperatures comparable to those used for the fluorine IID. The diffusion and disordering times previously published generally quotes times far in excess (8-10 hours) of the diffusion times for fluorine disordering though, and it was hoped that in this case the relatively low (5×10^{17} cm^{-3}) impurity concentration would have inhibited significant intermixing in the timespan used for the fluorine disordering. The TEM photographs readily explain why the implanted and annealed samples failed to work. The active wells have disappeared completely both in the unmasked and masked areas. The weak light that was observed during testing of the IID BH laser structures will therefore probably have been spontaneous emission from the SCH region. The explanation for the indiscriminate intermixing of the upper SL layer (and the active quantum wells) is to be found in the rapid diffusion of fluorine at 890° C. The SIMS results for the fluorine implanted and annealed material in Chapter 6 confirm that the fluorine rapidly diffuse during annealing and that the distribution after the annealing stage is radically different from the initial state.

The TEM photograph of the implanted and annealed sample appears to show a widening of the SCH region at the interface with the upper cladding layer. This can be interpreted as a region of higher disordering than is the case for the rest of the structure, and may be due to a combination of higher fluorine concentration in the initial stages of the disordering (before the fluorine had time to diffuse away), and of damage induced during implantation enhancing the disordering in that region.

7.4 Conclusion

The conclusion drawn from the above processing results was that the processing steps for the IID process would have to be re-examined. New methods for masking would be desirable in order to block implantation into masked regions totally, and a rapid thermal process would need to replace the conventional furnace annealing to limit fluorine diffusion. It would be possible to use a combination of SiO_2 and gold as masking material for the IID BH structure and, in the case of the IID DBR laser structure, the gold thickness that could be deposited could be increased by using a combination of cured polyimide and photoresist for the lift-off process. The material structure could also be redesigned. Unless a non-disordering n-type dopant could be found, the lower superlattice cladding layer could be replaced by bulk 40% AlGaAs. The undoped SCH layer could also be extended towards the n-type cladding to reduce degradation of the active wells due to the n-type dopant (this would probably not be necessary though, since the application of a rapid thermal process would lead to only small amounts of dopant diffusion). It may also be necessary to use boron as the disordering impurity rather than fluorine. Even though boron here has been found to induce less rapid disordering, it does possess a remarkable stability during annealing, with negligible diffusion. This may be a crucial factor in the choice of disordering impurity .

[1] R.L. Thornton, W.J. Mosby and T.L. Paoli, IEEE Journal of Lightwave Technology, LT-6 1987 p786.

[2]M. SUZUKI, H. TANAKA, S. AKIBA, Y. KUSHIRO, J. Lightwave Technol **6** (1988) 779.

[3]M. O'NEILL, J.H. MARSH, R.M. DE LA RUE, J.S. ROBERTS and R. GWILLIAM, Electron Lett **26** (1990) 1613-5.

[4] J. H. Marsh, S.I. Hansen , A.C. Bryce, R.M. De La Rue , Optical and Quantum Electronics**24** (1991) S1—S17.

[5]J. H. Marsh, S.G.Ayling, A.C. Bryce, S.I. Hansen and S.A. Bradshaw Proceedings of U.S /U.S.S.R Academies of Science Meeting on Heterostructure Lasers,Leningrad May 1991.

[6]J H Marsh,"Neutral Impurity Disordering of Quantum Well Waveguide devices."Ch.9 Waveguide Optoelectronics, NATO AASI Series E:Applied Sciences Vol.226.,Eds. J.H.Marsh and R. De La Rue, Kluwer Academic Press,The Netherlands, pp 185-204

7J.D. RALSTON, L.H. CAMNITZ, G.W.WICKS and L.F.EASTMAN GaAs and Related Compounds 1986 (Inst Phys Conf Ser No 83), pp.367-372

[8]K.B. Kahen, J.P. Leburton, "Index of refraction of GaAs-$Al_xGa_{1-x}As$ superlattices and multiple quantum wells", Superlattices and Microstructures, Vol.3, 1987, pp251-256.

[9] S.I. Hansen "Fabrication of MCRW DQW SCH stripe lasers", Thesis submitted for the degree of M.Sc. in Optical Information Technology , University of Glasgow 1988.

[10]K.M. Thomas "Sub-micron holographic grating masks replicated by X-ray contact printing for integrated optics", Ph.D Thesis Glasgow University,1989.

Chapter 8

Conclusions and future work

8.1 Summary of the thesis

This thesis has reported investigations on quantum well intermixing in GaAs-AlGaAs multiple quantum well structures due to the impurity induced disordering effect using the electrically neutral impurities boron and fluorine. Particular emphasis was put on the refractive index change induced by the disordering process, and on methods of utilising this technique in the development of novel semiconductor laser structures.

The refractive indices of as-grown and intermixed quantum well structures have been experimentally determined, and the effect of disordering on the dispersive properties of the quantum well materials were studied. Large refractive index changes ($\approx 2\%$) were obtained for completely intermixed structures. The quantum well structures were shown to lose their birefringence and the material was found to behave increasingly like bulk AlGaAs material as the disordering progressed.

The results of the refractive index measurements were tied up with independent theoretical calculations and shown to be in excellent agreement. The experimental findings were also confirmed by an alternative method for determining the refractive index of semiconductor materials; the Kramers-Krönig transformation of experimentally obtained absorption data.

The disordering technique was implemented in practical laser applications in Chapter 7. Some of the problems associated with the technique were uncovered, and suggestions for future work on the subject were put forward.

8.2 Conclusions

The main object of this thesis was to study the effect of IID on the refractive index of quantum well structures in the GaAs-AlGaAs material system and to investigate how it

correlated with previously obtained findings on the energy gap shift and absorption change. Additionally, an attempt was to be made at making laser devices where the IID technique was employed to regionally modify the material properties, and in the progress examine the feasibility of the processes.

To facilitate investigation of the refractive index of the semiconductor quantum well structures, the grating coupler method was chosen. Effective grating couplers were successfully fabricated. Holographically defined photoresist gratings were used in a pattern-transfer technique to form gratings in plasma-deposited silica on top of the waveguide. This ensured that only the evanescent field was coupled out of the waveguide, and calculations showed that this method ensured a higher degree of accuracy compared to that achieved with conventional grating couplers defined by periodic removal of parts of the waveguide material.

Measurements were performed with a simple set-up using end-fire excitation to excite the waveguide mode(s) and using the grating in an output-coupling configuration. This facilitated easily repetitive measurements with a high degree of accuracy and without the need for re-adjustment and realignment of the grating coupler for every wavelength. The measurements were performed in the wavelength range 800-920 nm, with the data range being limited at the lower wavelength end by the absorption edge of the material, and upwards limited by the tuning range of the tunable excitation laser.

The material refractive index was extracted from the waveguide refractive index using a reiterative computer procedure based on the resonance condition. Measurements were performed on as-grown material and on material that had been implanted with either boron or fluorine impurities and annealed in an IID process. The effects of both partial and complete intermixing were examined, with complete intermixing typically being achieved after 4 hours annealing at 890°C. The results obtained from the as-grown and intermixed materials were compared. Refractive index changes at the order of 2% were achieved after complete intermixing, with substantial changes > 1% observed even after partial

disordering. There was a clear relationship between the energy shift and the refractive index change, and this was particularly noticeable in the birefringence of the material. The progressing disordering was found to quickly reduce the birefringence of the material, fully in line with the theoretical expectation. Comparison of the refractive index data with data obtained from Kramers-Krönig transformation on the absorption of the structures gave good agreement. After complete disordering the refractive index of the (former) MQW material had a dispersive behaviour similar to that of bulk AlGaAs, and with absolute values equalling those of bulk AlGaAs with an aluminium content the material average of the MQW layer.

A clear connection was observed between the refractive index change and the interdiffusion coefficient for the two impurities. Fluorine was found to have a larger interdiffusion coefficient ($\approx 4 \times 10^{-18}$ cm^2s^{-1}) than boron ($\approx 3.25 \times 10^{-18}$ cm^2s^{-1}), and showed a larger refractive index shift over the whole range of annealing times. Fluorine did however also have a higher diffusion coefficient, and the fluorine impurities were found to diffuse out of the implanted region (into the substrate and out to the surface), leading to a depletion of the volume concentration in the MQW region. This constitutes a self-limiting effect that will be more obvious in wider quantum wells. Boron had a slower interdiffusion coefficient, but also had a greater stability and showed no appreciable diffusion after annealing. This is in good agreement with results published elsewhere, and may be of great importance for practical use of the disordering mechanism using these impurities.

The feasibility of using this process in practical applications was studied. A laser structure was specially designed for this purpose. The design criteria called for a device with great potential for refractive index and band-to-band transition energy modification by IID both in the active and cladding layers, low threshold current density and high gain. The resulting structure was a superlattice cladding layer laser with a double quantum well active region. The structure was realised and tested as a broad area laser. With minor modifications a threshold current density of 330A/cm^2 was achieved for a 400 μm long device. Patterning procedures were employed to facilitate regional implantation of the F impurity to make

buried heterostructure and distributed Bragg reflector lasers from the complete structure, and distributed feedback lasers from half-grown versions of the same structure. This work uncovered some of the limitations of the disordering process developed here. The fluorine impurity had been chosen because it gave the largest refractive index change, and since the details of the diffusion rate had not been ascertained at the time. The high diffusion rate of fluorine in combination with an annealing procedure using a conventional furnace led to intermixing in both patterned and unpatterned regions. Intermixing was also found to take place in the n-type cladding region for the unimplanted control samples (with some interface smearing also being noticeable in the originally intrinsic active layer). This was found to be due to the n-type dopant being used, Si, which also is an active IID agent and which has a diffusion rate similar to fluorine.

The study into the feasibility of device implementation clearly shows that the effect of the impurity diffusion has to be limited. This can be achieved by the use of a rapid thermal annealing system, whereby the annealing time is reduced substantially. Experiments have shown that the IID induced energy changes can be obtained in a fraction of the time required if a conventional furnace is used. It is believed that the shorter annealing time will greatly improve the stability of the impurities (and maybe altogether remove the unwanted effect of the dopant impurity), but it is probably also necessary to use boron instead of fluorine. Furthermore, there does not seem to be anything to gain from using a superlattice in the lower cladding layer (partially due to the intermixing effect of the n-type dopant), so this could be made in bulk AlGaAs. To reduce the effect of the n-type dopant on the active wells further, the n-type doping concentration could be graded to give a concentration lower than that required for IID in that system in the region close to the active layer. Better masking techniques can also be developed, enabling higher energy implants for use in the DBR structure.

Appendix 1

An implementation of Afromowitz' model for the refractive index of AlGaAs for x=0.0 to 1 is shown in the Pascal subroutine AlGaAs below. The subroutine uses the original equations given by Afromowitz in his paper in Solid State Communications 1974. The model there turns out to have a discrepancy from the experimental values corresponding to an offset in aluminium fraction of 0.02.

General comments:

1) In this original version of Afromowitz' model, the E_Γ energy transition was taken to be 1.424 eV for GaAs , and 2.95 eV for AlAs.

2) The E_Γ transition energy variation for AlGaAs was assumed to be defined as:

$$E_\Gamma = 1.424 + 1.266x + 0.26x^2 \qquad \text{(A1.1)}$$

From this, the coefficients E_0, and E_d were defined as:

$$\begin{aligned} E_0 &= 3.65 + 0.871x + 0.179x^2 \\ E_d &= 36.1 - 2.45x \end{aligned} \qquad \text{(A1.2)}$$

where $E_0 = A + BE_\Gamma$ and A =2.67 and B =0.688.

3) The refractive index values published by Casey et al[1] were not in very good agreement with results published elsewhere[2]. This is illustrated in fig.A1.1, where reported values for the dispersion of the refractive index of AlGaAs is shown for x=0 to x=0.4, (from Casey et al[1] and Aspnes et al[3].)

Stein I Hansen

```
Function  AlGaAs(Wavelength,Percentage:Real):Real;

        {** Function to return material refractive indices for Al(x)Ga(1-x)As  **}
      {** for a specified wavelength.  Theory from Afromowitz Solid St.Comms 1974  **}

 Const
  CNVRT=1239.5
  Var
   Energy,SqEnergy,Logpart,FEnergy,GEnergy,SqFNRJ,SqGNRJ,DEnergy,M1,M3,
  OEnergy,SqONRJ,EtaPi,EChi,Permi:Real;
 Begin
  Energy:=CNVRT/Wavelength;
  SqEnergy:=Sqr(Energy);
  OEnergy:=3.65+0.871*Percentage+0.179*Sqr(Percentage);
  DEnergy:=36.1-2.45*Percentage;
  GEnergy:=1.424+1.266*Percentage+0.26*Sqr(Percentage);
  SqONRJ:=Sqr(OEnergy);
  SqGNRJ:=Sqr(GEnergy);
  SqFNRJ:=2*SqONRJ-SqGNRJ;
  EtaPi:=DEnergy/(2*SqONRJ*OEnergy*(SqONRJ-SqGNRJ));
  M1:=EtaPi*(Sqr(SqFNRJ)-Sqr(SqGNRJ))/2;
  M3:=EtaPi*(SqFNRJ-SqGNRJ);
  LogPart:=Ln((SqFNRJ-SqEnergy)/(SqGNRJ-SqEnergy));
  EChi:=M1+M3*SqEnergy+EtaPi*Sqr(SqEnergy)*LogPart;
  Permi:=EChi+1;
  AlGaAs:=Sqrt(Permi);
 End;
```

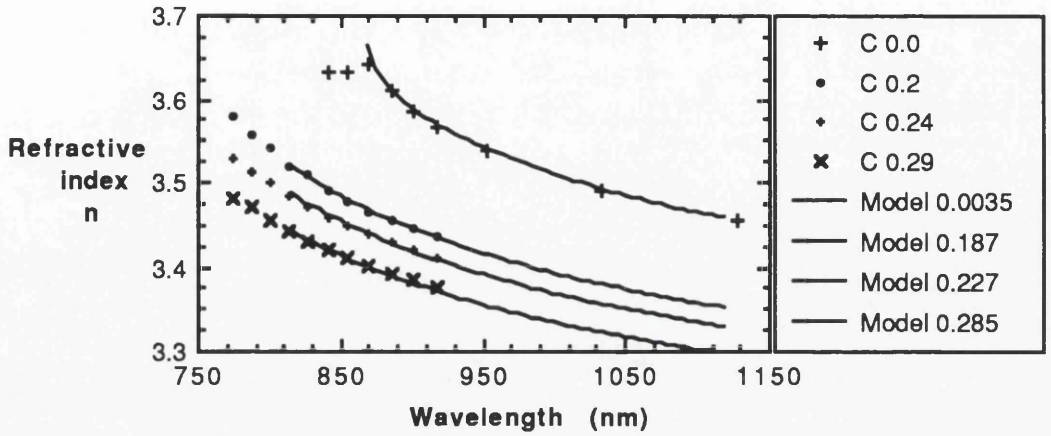

Fig.A1.1 Dispersion of the refractive index of AlGaAs (Casey et al), shown with Afromowitz original model calculations.

The model in this form turned out to have large discrepancies with refractive index data published elsewhere[2]. The bandgap transition data for AlAs was also different from later publications [3].

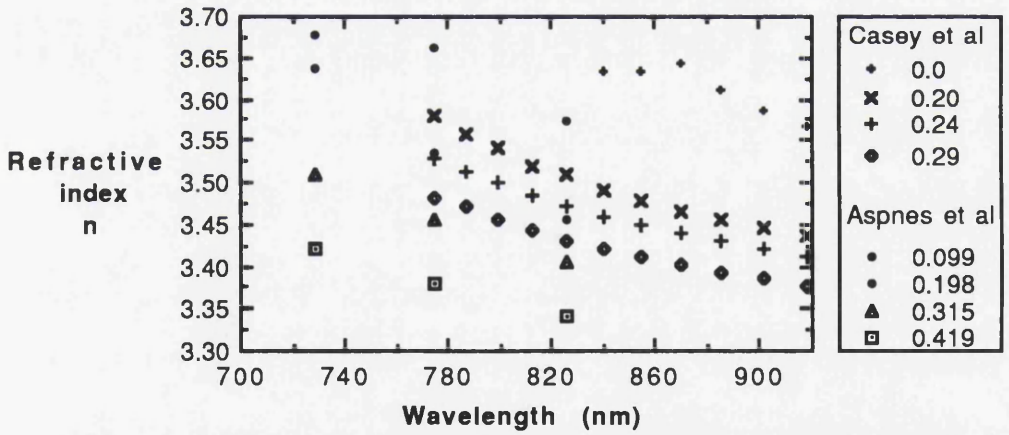

Fig.A1.2 Dispersion of the refractive index of AlGaAs from the literature (data from Casey et al and Aspnes et al.)

The diagram illustrates the difference existing between reported values of AlGaAs refractive indices. It can be seen that some of the values reported by Aspnes et al for $x \approx 0.2$ coincide with the values reported by Casey et al for $x \approx 0.24$.

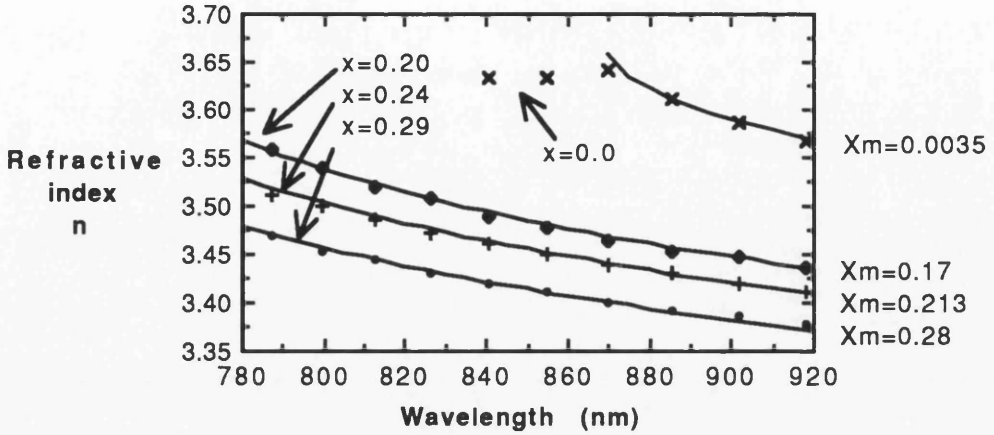

Fig. A1.3 Plot of the refractive index of AlGaAs (casey et al) and modified Afromowitz model calculations for best fitting x-values.

More recently published data[3] with the transition energy of 3.018eV for AlAs were used to modify the model. Aspnes et al expressed the Γ–valley bandgap energy variation with Al-composition as:

$$E(x) = 1.424 + 1.594x + x(1-x)(0.127 - 1.310x)eV \qquad \text{(A1.3)}$$

This gives coefficients A=2.712 and B=0.6587 when computing for known boundary conditions, and:

$$E_0 = 3.65 + 1.05x + x(1-x)(0.08367 - 0.863x)$$
$$E_d = 36.1 - 2.45x \qquad \text{(A1.4)}$$

These changes were made to the subroutine above. Fig.A1.4 shows the close agreement between the refractive index values calculated from the modified Afromowitz model and those reported by Aspnes et al.

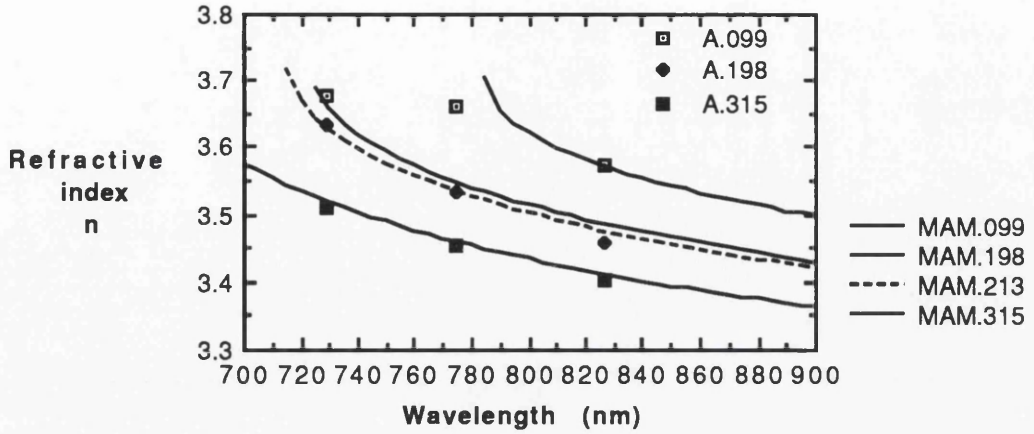

Fig.A1.4 Plot of refractive index data reported by Aspnes et al together with values calculated using the modified Afromowitz model.

Another model has been proposed by B.Jensen et al [4]. It involved a more rigorous potential band structure modelling. The model was shown to agree well with the data of ref.1 for aluminium fractions $x < 0.15$, but for higher concentrations the best fit was obtained for values of x significantly lower than that given by ref.1.

Chapter 6 showed how measured waveguide refractive indices could be used to obtain the material refractive index of the composite layers of a waveguide. The measured AlGaAs refractive indices reported in Chapter six are, by the author, considered more accurate than those published in refs. 1 and 3. This is mainly because every effort was made to keep the accuracy of the measurements as high as possible, particularly with respect to the determination of the exact aluminium content of the AlGaAs material. The Al-composition is regarded as the factor of highest degree of uncertainty in previously published reports.

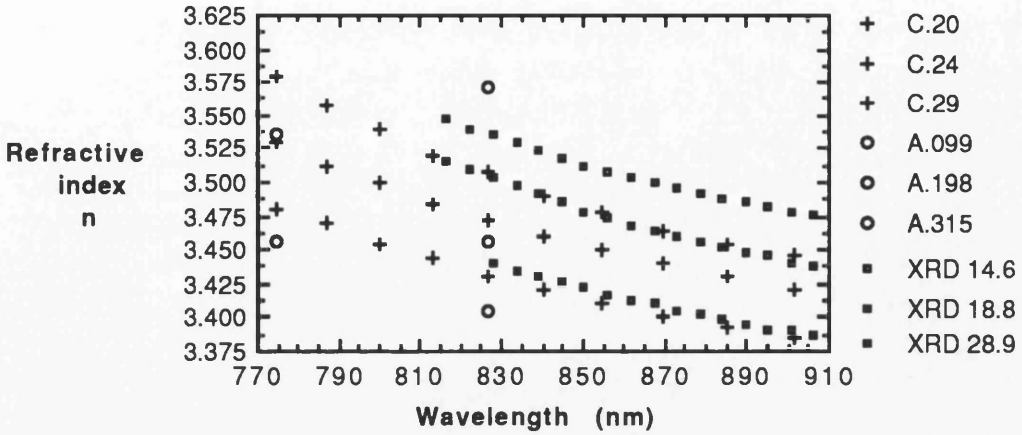

Fig. A1.5 Previously reported refractive indices for AlGaAs together with values reported here. C denotes Casey et al (ref.1), A denotes Aspnes et al (ref.3), with the aluminium fraction following the letter. XRD are values reported here, with the exact aluminium percentage indicated.

The results obtained in Chapter 6 is shown again in fig. A1.5. The results indicate that Casey et al overestimated the aluminium content of the AlGaAs material measured, but also that this discrepancy is smaller than suggested by the results of Aspnes et al. The difference in aluminium fraction between the data of ref.1 and the data presented here can be attributed to the uncertainty in the method used for the aluminium content estimate in ref.1, as suggested by the authors themselves.

---

[1]H.C.Casey Jr., D.D. Sell, M.B. Panish,"Refractive index of $Al_xGa_{1-x}As$ between 1.2 and 1.8 eV,"Appl. Phys. Letts. Vol. 24, No.2, 1974, pp 63-65.

[2]See also Chapter 2.

[3]D.E.Aspnes, S.M. Kelso, R.A. Logan, R. Bhat,"Optical properties of AlGaAs," J.Appl.Phys. Vol.60. No.2 1986, pp 754–767.

[4]B.Jensen,"Calculation of compound semiconductors below the bandgap", Ch.6, Handbook of Optical Constants of Solids, E.D. Palik, Ed. Vol 2, Academic Press Orlando ,1991, pp 141-147.

Appendix 2

This appendix contains program listings for the Turbopascal programs and subroutines that were written for some of the calculations in this thesis. The programs or subroutines are:

SteInp: This is a program for writing data from the console to a Turbopascal-readable format datafile.

SteOutp:This is a program used for retrieving data from a Turbopascal-readable format datafile.

FreqCnv: This program converts data on wavelength- refractive index and polarisation into electron energy, dielectric function and polarisation data, and writes the information to a file with extension (.eps). This file is in a form enabling it to be read by the single oscillator fitting program.

Osciltr: This is a single electron oscillator model fitting program. The program is based on a version of the χ^2 method to find the best fitting model parameters for a set of data. The background dielectric function in this program is a straight line approximation. A later version included an AlGaAs dielectric function generator based on the Modified Afromowitz Model and a reiterative loop-version of the above χ^2 fitting method. This was found to give better curve fitting for partly disordered material in particular.

Mod4lay: Modified four-layer slab waveguide program. This program solved Maxwells equations for a two-dimensional waveguide consisting of up to four composite layers, and used the results in a numerical procedure to obtain the refractive index of one of the layers when all the other parameters of the structure were known, including the waveguide index, the thicknesses of all the layers and the material refractive indices of all other layers than that for which it was solving. The program was based on a subroutine written by B.Bhumbra.

```
Program SteInp;

{*** Simple program to input values to file for later use ***}

Const
  MaxNoofResults = 10;
Type
  Name=String[2];
  ResultName = String[25];
  Results = Record
          Lambda:Real;
          RefracInd:Real;
          Field:Name;
          End;

Var
  ResultFile :File of Results;
  ResultRec :Results;
  NoofMeas, ResultNo,MaxResults,FileNo: Integer;
  LambdaR, RefrInd, LInp :Real;
  FileName :Resultname;
  RightAnswer:String[3];
  Exit:Boolean;
  TEM:Name;
{**** main program ****}



Function Exist(Filequery:Resultname):Boolean;

Var
Fil:file;

  begin
    Assign(Fil,Filequery);
    {$I-}
    Reset(Fil);
    {$I+};
```

```
   Exist := (IOResult=0)
 End;


Begin
ClrScr;
Writeln('This is a program to save refractive index values for varying');
Writeln('wavelengths into a file for later use by Conversion program Freqcnv');
Writeln('to make values suitable for Electron model program');
Writeln('          (Press any key to proceed)');

Repeat Until KeyPressed;

ClrSCr; Exit:=False;

Repeat
Writeln('What do you want to call the file? (drive\path\filename) ');
Readln(FileName);

If Exist(FileName) Then
 Begin
  Writeln('This file exists. Overwrite? Y/N');
  Readln(RightAnswer);
  If (RightAnswer ='y') Or (RightAnswer ='Y') Then
   Exit:=True;
 End
Else
 Exit:=True;

Until Exit;

Exit:=False;
Repeat
 Writeln('What Polarisation? TE/TM');
 Readln(TEM);
 If(TEM='TE') or (TEM='te') or (TEM='tm') or (TEM='TM') Then
 Exit :=True;
Until Exit;
```

```
 Writeln('How Many data points?');
 Readln(MaxResults);

  Assign(ResultFile,FileName);
  Rewrite(ResultFile);

{****    Input Section ****}


{**** NoofMeas :=0; ****}

With  ResultRec Do

Begin
 ClrScr;
For ResultNo :=1 To MaxResults do

  Begin
    Writeln('Entry number',ResultNo:4);
    Write('Type in wavelength in nm  ');
    Readln(Lambda);
       Write('Refractive Index? ');
{****     Writeln('Type in Refractive Index for ',Linp:7:1,' nm');****}
    Readln(RefracInd);
    Field:=TEM;
    Write(ResultFile,ResultRec);

  End;

End;

Flush(ResultFile);

Close(ResultFile);

End.
```

```
**********************************************************************
Program SteOutp;

{*** Simple program to read values from a file  ***}

Type
  ResultName = String[25];
  Results = Record
          Lambda:Real;
          RefracInd:Real;
          End;

Var
  InFile :File of Results;
  InputRec :Results;
  Inpointer,FileStop:Integer;
  LambdaIn, RefrIn, LIn :Real;
  FileName :Resultname;
  RightAnswer :String[3];
  Present:Boolean;

Function Exist(Filequery:Resultname):Boolean;

Var
Fil:file;

  begin
    Assign(Fil,Filequery);
    {$I-}
    Reset(Fil);
    {$I+};
    Exist := (IOResult=0)
  End;

{**** main program ****}

Begin
```

```
ClrSCr;

Present :=False;
Repeat

Writeln('Which file? (drive\path\filename) ');
Readln(FileName);

If Exist(Filename) Then
Present :=True;

Until Present;

Assign(InFile,FileName);

{*****Seek(InFile,FileSize(InFile)); ****}
{****FileStop := FilePos(InFile);   ****}

Reset(InFile);

{****     Read Section ****}

ClrScr;

With  InputRec Do

Begin

For InPointer :=1 To FileSize(InFile) do

  Begin
    Read(Infile,Inputrec);
    Writeln(Lambda:15:10,RefracInd:10:4);
  End;
End;
Close(InFile);
End.
```

```
**********************************************************************
Program FreqCnv;

{*** Simple program to read values from a file containing:***}
{*** Lambda, RI,TEM  and convert to 'frequency' (eV) and Permittivity***}

Type
 TempArray = Array[1..50]of Real;
 Name = String[2];
 ResultName = String[25];
 Results = Record
        Lambda:Real;
        RefracInd:Real;
        Field:Name;
        End;
 CResults = Record
         Cfreq:Real;
         Epsilon:Real;
         Transverse:Name;
         End;
Const
 Convert = 1239.8562;

Var
 InFile :File of Results;
 InputRec :Results;
 FieldTemp:Array[1..50] of Name;
 EpsilTemp,CfreqTemp:TempArray;
 EpsilFile:File of CResults;
 EpsilRec:CResults;
 EntryNo,Inpointer,FileStop,NoofMeas:Integer;
 LambdaIn, RefrIn, LIn :Real;
 CFileName,FileName :Resultname;
 RightAnswer:String[3];
 Present,Exit,Finish:Boolean;
```

```
Function  Exist(Filequery:Resultname):Boolean;

Var
Fil:file;

 begin
   Assign(Fil,Filequery);
   {$I-}
   Reset(Fil);
   {$I+};
   Exist := (IOResult=0)
 End;


{**** main program ****}

Begin
ClrSCr;

Present :=False; Finish :=False;
Repeat

Writeln('Which file contains Lambda,Refr.Ind,TEM? (drive\path\filename) ');
Readln(FileName);

If Exist(Filename) Then
 Present :=True
Else
 Begin
   Write('File does not exist. Try again? Y/N');
   Readln(RightAnswer);
   If (RightAnswer ='y') Or (RightAnswer ='Y') Then
    Present :=True
   Else
     If (RightAnswer ='n') Or (RightAnswer ='N') Then
      Begin
        Present :=True;
        Finish :=True;
```

```
    End;
  End;

Until Present;

If Not(Finish) Then
Begin

  Assign(InFile,FileName);


  Reset(InFile);



    {****      Read Section ****}

  ClrScr;
  EntryNo:=0;

  With  InputRec Do

  Begin

  For InPointer :=1 To FileSize(InFile) do

    Begin
      EntryNo:=EntryNo+1;
      Read(Infile,Inputrec);
      CfreqTemp[EntryNo]:=Convert/Lambda;
      EpsilTemp[EntryNo]:=sqr(RefracInd);
      FieldTemp[EntryNo]:=Field;

      Writeln(Lambda:15:10,RefracInd:10:4,Field:3);  {*** For initial Check***}


    End;
```

```
  End;


  Close(InFile);
  Present:=False;NoofMeas:=EntryNo;
  Repeat
   Writeln('Which File to write these values to? (Include ***.eps)');
   Readln(Filename);

   If Exist(Filename) Then
    Begin
     Present :=True;
     Writeln('File exists, choose another name? Y/N');
     Readln(RightAnswer);
      If (RightAnswer='n') Or (RightAnswer='N') Then
       Present:=False;
    End
   Else
    Present:=False;
  Until Not(Present);

  Assign(EpsilFile,FileName);
  Rewrite(EpsilFile);

  With EpsilRec Do
   Begin
    For EntryNo:=1 to NoofMeas Do
     Begin
      Cfreq:=CfreqTemp[EntryNo];
      Epsilon:=EpsilTemp[EntryNo];
      Transverse:=FieldTemp[EntryNo];
      Write(EpsilFile,EpsilRec);
      Writeln(EntryNo,Cfreq:15:8,Epsilon:10:4,Transverse:3);  {*** Check 2***}
     End;
   End;
  Close(EpsilFile);
 End;
End.
```

```
**********************************************************************
Program Osciltr;

{**Program using Chi-Square method for determining fitting **}
{**parameters for electron oscillator model.  Stein I Hansen March 1990 **}

Const
 Max = 100;

Type
 ResultName=String[25];
 ValArray=Array[1..50] of Real;
 Name = String[2];
 Narray =Array[1..50] of Name;
 CResults = Record
        Cfreq:Real;
        Epsilon:Real;
        Transverse:Name;
        End;



Var
  AA,BB,Sig,Xsig,BetaL,BetaH,Delta,Para1,Para2,GammaL,GammaH,OmegaL,
  ChiDiff,ChiSq,Sxx,Sxy,Syy,Skx,Sky,Sex,Sey,OmegaH,Temp,x:Real;
  InPointer,Dn,TopData,i,n,m,lines,Scale,dx,dy,PlotDensity:Integer;
  Exit,LeaveProg,PlotVal,TM,ReCalc,Finish,Present:Boolean;
  RightAnswer,CalcAnsw,PlotAnswer:Name;
  Freq,Epsil,Light,Heavy,Slope:ValArray;
  ModFile:ResultName;
  EpsilFile:File of CResults;
  EpsilRec:CResults;
  EntryNo,FileStop,NoofMeas:Integer;
  CFileName,FileName :Resultname;
  TEM:Narray;

{****     FUNCTIONS ****}
```

```
Function  Exist(Filequery:Resultname):Boolean;

Var
Fil:file;

 begin
   Assign(Fil,Filequery);
   {$I-}
   Reset(Fil);
   {$I+};
   Exist := (IOResult=0)
 End;


Function  Oscill(XGamma,XOmega,Xfreq:Real):Real;

Var
 SqGamma,SqOmega,Sqfreq,Xdiff,XDen:Real;

Begin
 SqGamma:=Sqr(XGamma);
 SqOmega:=Sqr(XOmega);
 Sqfreq:=Sqr(Xfreq);
 Xdiff:=SqOmega-Sqfreq;
 XDen:=Sqr(Xdiff)+Sqfreq*SqGamma;
 Oscill:=Xdiff*SqOmega/XDen;
End;


{***   Start of main program   ***}

Begin

LeaveProg:=False;
Repeat
```

```
 Sxx:=0; Sxy:=0; Syy:=0; Skx:=0; Sky:=0; Sex:=0; Sey:=0;  Dn:=0; TM:=False;


ClrSCr;

Present :=False; Finish :=False;
Repeat

 Writeln('Which file contains Material Permittivity?(.eps) (drive\path\filename) ');
 Readln(FileName);

If Exist(Filename) Then
 Present :=True
Else
 Begin
  Write('File does not exist. Try again? Y/N');
  Readln(RightAnswer);

  If (RightAnswer ='n') Or (RightAnswer ='N') Then
    Begin
     Present :=True;
     Finish :=True;
    End;
 End;

Until Present;

If Not(Finish) Then
 Begin

  Assign(EpsilFile,FileName);


  Reset(EpsilFile);
```

```
  {****      Read Section ****}

ClrScr;
Dn:=0;

With EpsilRec Do
 Begin
  For EntryNo:=1 to FileSize(EpsilFile) Do
   Begin
    Dn:=Dn+1;
    Read(EpsilFile,EpsilRec);
    Freq[Dn]:=Cfreq;
    Epsil[Dn]:=Epsilon;
    TEM[Dn]:=Transverse;
   End;
 End;

Close(EpsilFile);

TopData:=Dn;

If (TEM[1]='tm') Or (TEM[1]='TM') Then
TM:=True;

  {*** INPUT ALL KNOWN VARIABLES ***}

Exit:=False;
Repeat
 Write('Input straight line bias coefficients a  b   (aw+b) : ');
 Readln(AA,BB);
 Write('Input light hole linewidth and exciton peak frequency (eV): ');
 Readln(GammaL,OmegaL);
 If Not(TM) Then
  Begin
   Write('Input heavy hole linewidth and exciton peak frequency (eV): ');
   Readln(GammaH,OmegaH);
  End;
 Write(' Input estimated error for measurements : ');
```

```
 Readln(XSig);
 Sig:=Sqr(XSig);
 Writeln(' Are all values OK ?');
 Readln(RightAnswer);
 If (RightAnswer='y') Or (RightAnswer='Y') Then
  Exit:=True;
Until Exit;

  {*** START OF MANIPULATION OF DATA ***}

Dn:=0;
While Dn < TopData Do
 Begin
  Dn:=Dn+1;
  Temp:=Freq[Dn];
  Light[Dn]:=Oscill(GammaL,OmegaL,Temp);
  Sex:=Sex+Epsil[Dn]*Light[Dn]/Sig;
  Slope[Dn]:=Sqr(AA*Freq[Dn]+BB);
  Skx:=Skx+Slope[Dn]*Light[Dn]/Sig;
  Sxx:=Sxx+Sqr(Light[Dn])/Sig;

  {*** FILL TE ARRAYS ***}

  If Not(TM) Then
   Begin
    Heavy[Dn]:=Oscill(GammaH,OmegaH,Temp);
    Syy:=Syy+Sqr(Heavy[Dn])/Sig;
    Sxy:=Sxy+Light[Dn]*Heavy[Dn]/Sig;
    Sey:=Sey+Epsil[Dn]*Heavy[Dn]/Sig;
    Sky:=Sky+Slope[Dn]*Heavy[Dn]/Sig;
   End;
 End;

    {*** END OF ARRAY FILLING AND MANIPULATING ***}
    {*** START OF CALCULATIONS OF BETAx(s)     ***}

 Repeat
  ReCalc:=False;
```

```
 If TM Then
   Begin
    BetaH:=0;
    BetaL:=(Sex-Skx)/Sxx;
   End
 Else
   Begin
    Delta:=Sqr(Sxy)-Sxx*Syy;
    BetaL:=(Sxy*(Sey-Sky)+Syy*(Skx-Sex))/Delta;
    BetaH:=(Sex-Skx-Sxx*BetaL)/Sxy;
   End;

   {*** ESTIMATE GOODNESS-OF-FIT  ***}

ChiSq:=0; Dn:=0;

While Dn < TopData  Do
 Begin
   Dn:=Dn+1;
   ChiDiff:=Sqr(Epsil[Dn]-BetaL*Light[Dn]-BetaH*Heavy[Dn]-Slope[Dn]);
   ChiSq:=ChiSq+ChiDiff/Sig;
 End;

Para1:=(TopData-2)/2;
Para2:=ChiSq/2;

Q:=Gammq(Para1,Para2); {** Calling up probability procedure **}

 ClrScr;
 Writeln;
 writeln;
 writeln;
 writeln('       **** RESULT SECTION **** ');
 Writeln;
 writeln;
 Writeln('   Results are found to be as follows: ');
 Writeln;
 Writeln('     4*pi*BetaLight = ',BetaL:10:6);
```

```
Writeln('      4*pi*BetaHeavy = ',BetaH:10:6);
Writeln('      Accumulated inaccuracy is (Chi-Square): ',ChiSq:10:6);
Writeln('   Probability of correctness Q is:' (Q:10:6) );


{*****************************************************}

{*** SECTION TO RECALCULATE BETAx 's WITH DIFFERENT ERROR ***}

Writeln('Do you want to try calculation for different error?');
Readln(CalcAnsw);
 If (CalcAnsw='y') Or (CalcAnsw='Y') Then
  Begin
  ClrScr;
  ReCalc:=True;
   Writeln(' Input new error estimate (Previous error was: ',XSig:6:5,' )');
  Readln(Xsig);
  Sig:=Sqr(XSig);
  Sex:=0; Skx:=0; Sxx:=0; Sxy:=0; Syy:=0; Sky:=0; Sey:=0; ReCalc:=True;
  Dn:=0;
  While Dn < TopData do
    Begin
     Dn:=Dn+1;
     Sex:=Sex+Epsil[Dn]*Light[Dn]/Sig;
     Skx:=Skx+Slope[Dn]*Light[Dn]/Sig;
     Sxx:=Sxx+Sqr(Light[Dn])/Sig;

  {***  SUM UP TE ARRAYS ***}

     If Not(TM) Then
       Begin
         Syy:=Syy+Sqr(Heavy[Dn])/Sig;
         Sxy:=Sxy+Light[Dn]*Heavy[Dn]/Sig;
         Sey:=Sey+Epsil[Dn]*Heavy[Dn]/Sig;
         Sky:=Sky+Slope[Dn]*Heavy[Dn]/Sig;
       End;
    End;
  End;
```

```
  Until  (Not(ReCalc));

 End;  {*** End due to finish option above ***}

 Writeln('Do you want to leave program? y/n');
 Readln(RightAnswer);

 If (RightAnswer ='y') Or (RightAnswer ='Y') Then
   LeaveProg:=True;

Until LeaveProg;

End.
```

```
**********************************************************************
Function GammQ(a,x:Real):Real;

{*** Subroutines for calculation of probability that  ***}
{*** correct solution has been found***}


Var
 Gamser,gln:Real;

Begin
 If((x<0)Or(a<0)) Then
  Begin
   Writeln('Pause in GammQ,-Invalid arguments. ');
   Readln;
  End;

If(x<a+1) Then
 Begin
  Gser(a,x,Gamser,gln);
  GammQ:=1-Gamser;
 End
Else
 Begin
  Gcf(a,x,Gamser,gln);
  GammQ:=Gamser;
 End;

End;

{*** 1st Procedure used by Gammq  ***}

Procedure Gser(a,x:Real; Var Gamser,gln:Real);

Label 1;

Const
```

```
 itmax=100;
 eps=3e-7;

Var
 n:Integer;
 sum,del,ap:real;

Begin
 gln:=Gammln(a);
 If x<=0 Then
  Begin
   If x<0 Then
    Begin
     Writeln('Pause in Gser- x lesss than 0 ');
     Readln;
    End;
   Gamser:=0;
  End
 Else
  Begin
   ap:=a;  sum:=1/a; del:=sum;
   For n:=1 to itmax do
    Begin
     ap:=ap+1; del:=del*x/ap; sum:=sum+del;
     If (abs(del)<abs(sum)*eps) Then Goto 1
    End;
   Writeln('Pause in Gser - a too large, itmax too small');
   Readln;
1:  Gamser:=sum*exp(-x+a*ln(x)-gln)
  End
End;


{**** 2nd procedure for Gammq  ****}

Procedure gcf(a,x:Real; Var gammcf,gln:Real);

Label 1;
```

```
Const
 itmax=100;
 eps=3e-7;

var
 n:integer;
  gold,g,fac,b1,b0,anf,ana,an,a1,a0:real;

Begin
 gln:=gammln(a); gold:=0; a0:=1; a1:=x; b0:=0; b1:=1; fac:=1;
 For n:=1 to itmax do
  begin
   an:=1.0*n; ana:=an-a; a0:=(a1+a0+ana)*fac; b0:=(b1+b0+ana)*fac;
   anf:=an*fac; a1:=x*a0+anf*a1; b1:=x*b0+anf*b1;
   If a1<>0 Then
    Begin
     fac:=1/a1; g:=b1*fac;
     If(abs((g-gold)/g)<eps) Then Goto 1;
     gold:=g;
    end;
  end;
  Writeln('Pause in gcf,- a too large, itmax too small. ');
  Readln;
1:  gammcf:=exp(-x+a*ln(x)-gln)*g

end;
```

```
**********************************************************************
```

Program Mod4Lay:

```
{**** Calculates material index from effective index for ****}
{**** 3 or 4 layer slab.  Effective index is calculated ****}
{**** using eigenvalue equation obtained from solving ****}
{**** boundary conditions for TE and TM modes of ****}
{**** propagation in the slab ****}

{**** Modified program module written by B.S.Bhumbra  16/2/87 ****}
{**** is used in this program. Stein Hansen ****}

Const
   Ferror = 1e-7;
   Taccuracy = 1e-7;


Var
    N1, N2, N3, N4, Eta1, Eta2, Eta3, Eta4,
    LambdaInp, Lambda, Kprop, K1, K2, K3, K4, D2Inp, D2,
    D3Inp, D3, Neffmin, Neffmid, Neffmax, Fmin, Fmid, Fmax,
    Error, Perror, NeffInd, Ncal, Nest, Accuracy, Nmid, NPrev,
   Ntemp, NIncr : Real;
    Answer : String[2];
    LeaveProg, Exit, Foundroot, FirstTime, Three, Change, Four, TM, TE,
    TwoLoop, ThreeLoop, Nprop : Boolean;
    Mode, Count, Converge, Modeno, Nooflayer : Integer;

Function  FNeff(Neff:Real):Real;

  Var
    Sub1,Sub2,Sub3,Sub4 : Real;

  Begin
  K1 := Kprop*Sqrt(Neff*Neff-N1*N1);
  K2 := Kprop*Sqrt(N2*N2-Neff*Neff);
```

```
K3 := Kprop*Sqrt(Neff*Neff-N3*N3);
K4 := Kprop*Sqrt(Neff*Neff-N4*N4);
Sub3 := exp(K3*D3)*(Eta3*K3+Eta4*K4);
Sub4 := exp(-1*K3*D3)*(Eta3*K3-Eta4*K4);
Sub1 := Eta3*K3*(Sub3-Sub4);
Sub2 := Eta2*K2*(Sub3+Sub4);
Sub2 := Sub1/Sub2;
Sub1 := Eta1*K1/(Eta2*K2);
FNeff := K2*D2 - ArcTan(Sub1) -ArcTan(Sub2) -Mode*Pi;
End;
```

Function Index(Indest:Real):Real;

```
Begin
N2:=Indest;
If (N2<N3) Or (N2<N1) Or (N2<N4) Then
  Begin
  Writeln(' Estimated Refractive Index too low');
  Exit := True;
  Index := 10;
  End
Else
  Begin
  If N1>N3 Then
  Neffmin := N1+1e-10
  Else
  Neffmin := N3+1e-10;
  Neffmax := N2-1e-10;
  Exit := False;
  Fmax := Fneff(Neffmax);
  Fmin := Fneff(Neffmin);

  If ((Fmax>0) And (Fmin>0)) Or ((Fmax<0) And (Fmin<0)) Then
    Begin
    Index := 0;   {**Marker to show mode not propagating**}
    Exit := True;
    End;
```

```
    Foundroot :=False;
    End;

  While Not(Exit) Do
    Begin
    Neffmid :=(Neffmax + Neffmin)/2;
    Fmax := Fneff(Neffmax);
    Fmid := Fneff(Neffmid);
    Fmin := Fneff(Neffmin);

    If Fmid>0 Then Neffmin := Neffmid;
    If Fmid<0 Then Neffmax := Neffmid;
    If Abs(Neffmax - Neffmin)<Ferror Then
      Begin
      Exit := True;
      Foundroot := True;
      End;
    End;

    If Foundroot Then
    Index := Neffmid;

  End;

Begin  {***Main Program***}
ClrScr;
Writeln('Modified program 4lay to find guiding layer index in dielectric slab');
Writeln('consisting of three or four layers.');
FirstTime := True;
LeaveProg := False;
Repeat
  Change := False;
  Writeln;
  If FirstTime=False Then ClrScr;
  Writeln('Previous data (if any) shown in [ ].');
  Writeln('Type only "Enter" for no change.');
  Writeln;
  Exit := False;
```

```
Repeat

  Exit := False; Three := False; Four :=False;
  Writeln('Type 3 or 4 layers');
  Readln(Nooflayer);
  If Nooflayer =3 Then
     Begin
     Three := True;
     Exit := True;
     End;
   If Nooflayer =4 Then
     Begin
     Four :=True;
     Exit :=True;
     End;

Until Exit;

If Three Then
   Begin
   D3:= 0;
   Writeln('Type in thickness of guiding layer (in um)');
   If Not(FirstTime) Then
    Writeln('[',D2Inp:8:2,']');
   Readln(D2Inp);
   End
Else
   Begin
   Writeln('Type in thicknesses D2,D3 (D2=Guide,D3=Upper Cladding)');
   If Not (firstTime) Then
    Writeln('[',D2Inp:8:2,D3Inp:8:2,']');
   Readln(D2Inp,D3Inp);
   D3 := D3Inp*1e-6;
   End;

D2 :=D2Inp*1e-6;
Exit := False;
```

```
Repeat
  Writeln('What Polarization? TE/TM');
  Readln(Answer);
   If (Answer = 'TM') Or (Answer = 'tm') Or (Answer = 'te') Or (Answer = 'TE') Then
  Exit := True;
Until Exit;

TE := False; TM := False;

If (Answer = 'TM') Or (Answer = 'tm') Then
  TM := True
  Else
  TE := True;

Repeat
  Writeln('What no of modes to check for? (Max 4) ');
  Readln(Modeno);
  If Modeno <5 Then
    Begin
    Writeln('What accuracy?');
    Writeln(' Recommend use of 1e-4 (i.e. 0.0001) ');
    Readln(Accuracy);
    If Accuracy>Taccuracy Then
    Exit := True
    Else
    Writeln('Lower accuracy, please.');
    End;
Until Exit;

Exit:=False;
Repeat
  Writeln('All Values OK? Y/N');
  Readln(Answer);
   If (Answer = 'n') Or (Answer = 'N') Then
    Begin
    Exit:=True;
    Change := True;
    End
```

```
  Else
   If (Answer='y') Or (Answer='Y') Then
  Exit:=True;
Until Exit;

          {**** End Of Initial Input Part ****}



          {**** Repetitive Input Loop ****}

While Not(Change) Do
  Begin
  Exit := False;
  Writeln('Type in new wavelength (nm)');
   If Not(FirstTime) Then Writeln('[',LambdaInp:7:0,' ]');
  Readln(LambdaInp);
  Lambda:=LambdaInp*1e-9;

  If Three Then
  Repeat
    Writeln('Type in Cladding Layer Indices N1 And N3 (N3=Air?)');
    If Not(FirstTime) Then
     Writeln('[',N1:10:6,N4:10:6,' at ',LambdaInp:7:0,' nm ]');
    Readln(N1,N4);
    If (N1>=N4) Then
    Exit := True;
    N3 := N1;
  Until Exit
  Else
  Repeat
    Writeln('Type in Cladding indices N1,N3 and Top Layer Ind.N4 (Air?)');
    If Not(FirstTime) Then
     Writeln('[',N1:10:6,N3:10:6,N4:10:6,' at ',LambdaInp:7:0,' nm ]');
    Readln(N1,N3,N4);
    If ((N1<=N3) And (N3>N4)) Then
    Exit := True;
  Until Exit;
```

```
Exit := False;  {*** Waveguide Index Input Loop ***}
Repeat
  Writeln('Type in Waveguide Index at ',LambdaInp:7:0,' nm');
  If Not(FirstTime) Then
   Writeln('[ ',NeffInd:10:6,' ]');
  Readln(NeffInd);
  If ((NeffInd>N3) And (NeffInd>N1)) Then
  Exit := True
  Else
  Writeln('Not a proper value for guiding at this wavelength in this structure');
Until Exit;

Kprop:=2*Pi/Lambda;

If TM Then
  Begin
  Eta1:=1/(N1*N1); Eta2:=1/(N2*N2); Eta3:=1/(N3*N3); Eta4:=1/(N4*N4);
  End
Else
  Begin
  Eta1:=1; Eta2:=1; Eta3:=1; Eta4:=1;
  End;

Mode := 0; FirstTime :=False;  {*** All Parameters Obtained ***}

        {**** MAIN CALCULATION AREA ****}
ClrScr;
Writeln('Calculation in progress');
For Mode:=0 To (Modeno-1) Do
  Begin
   Nest:=(NeffInd+0.02);

   NIncr := 0.01;

   TwoLoop := False; ThreeLoop := False; NPrev := NeffInd;
   NProp := False;
```

```
Repeat
  Ncal:=Index(Nest);
  If Ncal=0 Then

    Begin
     Write('Mode ',Mode,' does not propagate');
    If NProp Then
      Begin
      TwoLoop := True;
      ThreeLoop := True;
      Writeln('- even for incremented guide index ',Nest:10:6);
      End;

    NProp := True;
    NPrev := Nest + (2*NIncr);
    Writeln(' Incrementing non-propagating mode with ',2*NIncr:10:6);
    End

  Else
  If Not(Ncal=10) Then

    Begin
    If Ncal > NeffInd Then
    TwoLoop := True
    Else
      Begin
      NPrev := Nest;
      Nest:= (Nest +NIncr);
      Writeln(' Incrementing guide estimate ',Nest:10:6);
      End;
    End

  Else
    Begin
    Writeln('Trouble in Calculation Procedure "Index" ');
    TwoLoop := True; ThreeLoop := True;
    End;
```

```
  Until TwoLoop;

  While Not(ThreeLoop) Do
    Begin
    Error := NeffInd - Ncal;
    If Abs(Error) > Accuracy Then
      Begin
      Writeln('Calculating');
      Nmid := (Nest+NPrev)/2;
      Ntemp := Index(Nmid);
      If (Ntemp = NeffInd) Or (Ntemp > NeffInd) Then
        Nest := Nmid
      Else
        NPrev := Nmid;
      Ncal := Ntemp;
      End

    Else
      Begin
      ClrScr;
      Write('Effective Index ',NeffInd:10:6,' yields Material Index  ');
       Writeln(Nest:10:6,' at ',LambdaInp:7:0,' nm.');
      ThreeLoop := True;
      End;

    End;

  End;

Writeln('Leave program Y/N   Change Structural Parameters C');
Readln(Answer);

 If (Answer='y') Or (Answer='Y') Then
  Begin
  Change:=True;
  LeaveProg := True;
  End;
 If (Answer='C') Or (Answer='c') Then
```

```
      Change := True;

      End;

   Until LeaveProg;

END.
```


GLASGOW UNIVERSITY LIBRARY